Universidade de Aveiro Departamento de Engenharia de Materiais e Cerâmica
2017

Olga Karavai

Mapeamento de parâmetros locais de corrosão usando SVET e SIET

Mapping local corrosion parameters using SVET and SIET

Universidade de Aveiro
2017
Departamento de Engenharia de Materiais e Cerâmica

Olga Karavai

Mapeamento de parâmetros locais de corrosão usando SVET e SIET

Mapping local corrosion parameters using SVET and SIET

Tese apresentada à Universidade de Aveiro para cumprimento dos requisitos necessários à obtenção do grau de Doutor em Ciência e Engenharia de Materiais, realizada sob a orientação científica do Doutor Mário Guerreiro Silva Ferreira, Professor Catedrático no Departamento de Engenharia de Materiais e Cerâmica da Universidade de Aveiro, e do Doutor António Alexandre da Cunha Bastos, Investigador no Departamento de Engenharia de Materiais e Cerâmica da Universidade de Aveiro.

Apoio financeiro da FCT, referência SFRH/BD/44475/2008, e do FSE no âmbito do III Quadro Comunitário de Apoio.

Dedicated to my husband for enormous inspiration and support.

o júri

Presidente — Reitor da Universidade de Aveiro

Prof. Doutor Christopher Michael Ashton Brett
professor catedrático, Faculdade de Ciências e Tecnologia, Universidade de Coimbra

Prof. Doutor Mário Guerreiro Silva Ferreira
professor catedrático, Universidade de Aveiro (orientador)

Doutor António Alexandre da Cunha Bastos
bolseiro de pós-doutoramento, Universidade de Aveiro (coorientador)

Prof. Doutor Carlos Manuel de Melo Pereira
professor auxiliar, Faculdade de Ciências, Universidade do Porto

Doutora Sviatlana Valeriyauna Lamaka
investigadora, Helmholtz-Zentrum Gessthacht, Alemanha

Doutor Silvar Kallip
investigador auxiliar, Universidade de Aveiro

Prof. Doutor João Carlos Salvador Santos Fernandes
professor auxiliar, Instituto Superior Técnico, Universidade de Lisboa

acknowledgments

I would like to thank my scientific supervisors Professor Mário Guerreira Silva Ferreira and Doctor António Alexandre da Cunha Bastos for having accepted a guidance of this work. I appreciate their immense help, transmitted knowledge, valuable advices, patience and time dedicated to this PhD thesis.

I acknowledge Department of Materials and Ceramic Engineering of University of Aveiro for having accepted me as a PhD student and Foundation of Science and Technology of Ministry of Science, Technology and Higher Education of Portugal for a PhD grant that permitted me to fulfil this work.

I would like to express my special appreciation and thanks to Professor Mikhail Zheludkevich giving the possibility to work in a unique and innovative research group, for immense support and assistance in my professional life, genuine caring and concern during my staying in Portugal.

I am fully grateful to Doctor Sviatlana Lamaka for the beginning of investigation activity and for continuous worthwhile guidance of my scientific work.

I give a lot of thanks to Maryna Taryba from Instituto Superior Técnico (IST, Lisbon, Portugal) for her help with development and characterization of the microsensors and to Doctor Maximilian Kopylovich from IST for synthesis of aluminium ionophores.

Professor Vladimir Egorov, Doctor Valiantsin Nazarau, Doctor Elena Zdrachek and Kseniya Andronchyk from Belarussian State University (Minsk, Belarus) are gratefully acknowledged for their help with the ion-selective electrodes and the treasured and interesting discussions of the obtained results.

The project of Marie Curie Actions SISET (Enhancing Scanning Electrode Technique, FP7-PEOPLE-IRSES-GA-2010-269282) is appreciatively acknowledged, as a large and important part of this thesis was made during the participation in it.

Many thanks to people from Department of Materials and Ceramic Engineering and from CICECO (Centre for Research in Ceramics and Composite Materials, now Aveiro Institute of Materials) who accompanied me in this research work.

I am particularly thankful to Kiryl, Ricardo, João, Frederico, Alena, Silvar, Ana, André, Aleksey, Maksim, Jorge, Andrey, Cheo, Nuno, Richard and Yuliya for companionship, comprehension and good moments spent together in laboratory and at the University.
I am grateful to Tatsiana and Sergey for their friendship, support and faith in me during the dissertation preparation.

I wish to thank my parents, parents-in-law and my whole family who encouraged and assisted me during the PhD studies.

palavras-chave corrosão localizada, microsensores electroquímicos, distribuição de espécies químicas

resumo

A corrosão localizada, i.e., corrosão confinada a locais específicos, é difícil de prever e controlar. Em geral, ocorre como resultado de heterogeneidades tanto no metal como no ambiente corrosivo. Uma das características da corrosão localizada é o desenvolvimento de ambientes específicos junto das zonas activas. Na prática, o micro-ambiente junto da superfície metálica é diferente do do seio da solução, variando com o tempo e com as condições do sistema em estudo.

Técnicas electroquímicas localizadas baseadas na utilização de micro-eléctrodos são convientes para medir a distribuição de potencial, intensidade de corrente e espécies químicas em solução junto de zonas activas, poros ou defeitos. Muito do trabalho que existe publicado sobre microeléctrodos em corrosão refere-se a trabalho exploratório que permanece numa etapa preliminar. A aplicação de microeléctrodos em estudo de corrosão numa base rotineira é ainda rara.

Este trabalho apresenta o desenvolvimento e aplicação de microeléctrodos como ferramentas experimentais capazes de aceder a reacções electroquímicas locais em substratos metálicos imersos em soluções agressivas. As técnicas electroquímicas tradicionais usadas no estudo de corrosão dão resposta média do processo global em toda a superfície da amostra sem distinguir efeitos locais e a química local. Não são, portanto, adequadas para a descrição detalhada dos mecanismos de corrosão localizada, de processos de inibição e, por vezes, para a selecção dos métodos de protecção mais adequados. É importante conhecer parâmetros locais, como pH, efeitos micro-galvânicos, concentração de espécies oxidantes (como O_2) e agressivas (como Cl^-), formação de filmes superficiais.

Neste trabalho usou-se a técnica do eléctrodo vibrante de varrimento (SVET) para medições locais de corrente iónica em solução. A técnica detecta a distribuição de potencial em solução, associada à corrente iónica. Para a análise de espécies químicas envolvidas no processo corrosivo, foram usados microsensores electroquímicos no modo SIET (Técnica de Varrimento de Eléctrodo Selectivo de Iões).

Foram desenvolvidos e caracterizados microeléctrodos sensíveis a pH, oxigénio dissolvido e catiões metálicos (nomeadamente, Mg^{2+}, Zn^{2+} e Cu^{2+}). Trabalhou-se também no desenvolvimento de microeléctrodos sensíveis a Al^{3+}, embora com menos sucesso. Os microeléctrodos foram utilizados na investigação da corrosão e inibição em defeitos induzidos em revestimentos protectores aplicados sobre ligas de alumínio e de magnésio, e na detecção da micro-distribuição de espécies químicas em solução perto de eléctrodos de zinco, cobre e de um par galvânico Zn-Fe.

Este trabalho revela também as limitações e dificuldades na aplicação destas técnicas ao estudo de corrosão devido à inerente reactividade do processo corrosivo, com formação de produtos de corrosão e grandes variações de pH, O_2 e força iónica ao longo da superfície de amostra.

Apesar das dificuldades, os resultados aqui apresentados demonstram que o mapeamento por SVET/SIET fornece informações muito úteis para a quantificação de processos electroquímicos à micro-escala. Os dados são de primordial importância para a modelação e simulação de mecanismos de corrosão, selecção de novos inibidores de corrosão e desenvolvimento de revestimentos anticorrosivos “inteligentes”.

Keywords localized corrosion, electrochemical microsensors, chemical species distribution

abstract

Localized corrosion, i.e., corrosion confined to local regions, is difficult to predict and control. In general, it appears as a result of heterogeneities, either in the metal or in the corrosive environment. One of the phenomenological features of localised corrosion is the development of specific environments close to active sites. In practice, the micro-environment near the metallic surface is different from that of the bulk medium and varies with time and conditions of the system under study.

Localized electrochemical techniques based on the use of microelectrodes are well suited for *in situ* sensing the distribution of potential, current and chemical species in active zones, pores or defects. Most of the published work dealing with microelectrodes in corrosion is mainly exploratory and their use in a regular basis is still rare in corrosion research.

This work presents the development and application of microelectrodes as experimental tools capable to assess local electrochemical reactions on metallic substrates immersed in aggressive solutions. Traditional electrochemical techniques used in corrosion research give the average response of the global activity of the whole surface not discriminating local effects and local chemistry. Therefore they are unable per si to properly characterize localized phenomena and the corresponding corrosion, inhibitive mechanisms and, sometimes, even to select the best protection methods. It is important to know local parameters such as pH, micro-galvanic effects, concentration of oxidizing (like O_2) and aggressive (like Cl^-) species, and formation of surface films.

The Scanning Vibrating Electrode Technique (SVET) was used for local measurements of ionic currents in solution. The technique detects the potential distribution in solution associated to ionic currents in solution. For the analysis of the chemical species involved in the corrosion process, electrochemical microsensors were used in SIET (Scanning Ion Selective Electrode Technique) mode.

Microelectrodes sensitive to pH, dissolved oxygen and metal cations (namely, Mg^{2+}, Zn^{2+} and Cu^{2+}) were developed and characterized. Work was also done with microeloectrodes sensitive to Al^{3+}, but with less success. Then, they were used for investigating the reactivity on defects and corrosion inhibition on coated aluminium and magnesium alloys, detecting the micro-distribution of chemical species in solution close to the corroding surface of Zn, Cu and a Zn-Fe galvanic couple specimens.

Limitations and difficulties exist for the use of these techniques in corrosion research due to the inherent reactivity of corroding metals, with the formation of corrosion products and sharp changes of pH, O_2 and ionic strength along the samples surface.

In spite of the difficulties, the results presented here demonstrate that the SVET/SIET mapping gives useful information for the quantification of electrochemical processes at the micro-level. The data are of prime importance for the modelling and simulation of corrosion mechanisms, selection of new corrosion inhibitors and development of ‘‘smart” coatings that suppress the corrosion processes.

Contents

Júri iv
Acknowledgments v
Resumo vi
Abstract viii
Contents 1
Abbreviations and symbols 6
List of Figures 8
List of Tables 15
Preface 17
STATE OF ART
1 Phenomena of localized corrosion of metals 19
1.1 Corrosion process and its reactions 19
1.2 Localized corrosion 21
1.2.1 Galvanic corrosion 23
1.2.2 Pitting corrosion 25
1.2.3 Crevice corrosion 26
1.3 Strategies of corrosion control 27
1.4 Organic coating failures as sites for localized corrosion 29
1.5 Concluding remarks 31

2 Localized electrochemical techniques in corrosion research 33
2.1 Introduction 33
2.2 SRET and SVET 38
2.2.1 Historical outline 38
2.2.2 SRET 40
2.2.3 SVET 41
2.2.4 Applications in corrosion research 44
2.3 SECM 45
2.3.1 Principles of operation in amperometric mode 46
2.3.2 SECM application for amperometric detection of chemical species 47
2.4 SIET 49
3 Potentiometric microelectrodes 55
3.1 Potentiometry 55
3.2 Types of potentiometric microsensors 56
3.3 Components of ion-selective membrane solution 59
3.4 Basic theory 60
3.5 Main characteristics of ISEs 63
3.5.1 Detection limit 63
3.5.2 Potentiometric selectivity coefficients 64
3.5.3 Response time 65
3.5.4 Potential stability 66
3.6 Important ISMEs requirements for application in localized corrosion studies 67
3.7 Microelectrodes sensitive to relevant corrosion species 68
3.7.1 pH-SMEs 68
3.7.2 Mg^{2+}-SMEs 72
3.7.3 Zn^{2+}-SMEs 74
3.7.4 Cu^{2+}-SMEs 77
3.7.5 Al^{3+}-SMEs 79
3.8 Concluding remarks 80
EXPERIMENTAL
4 Experimental procedures 81

4.1 Materials 81
4.2 Reagents 82
4.2.1 Reagents for ISEs 83
4.3 Samples preparation 84
4.3.1 Coated samples 84
4.3.2 Metallic wires 85
4.4 Equipment setup 85
4.4.1 SVET apparatus 85
4.4.2 Potentiometric (SIET) and amperometric modes 87
4.4.3 Apparatus for ISEs testing 88
4.5 Microelectrodes fabrication 88
4.5.1 Microelectrodes for SVET 88
4.5.2 Glass capillary microelectrodes 89
4.5.3 Copper sensitive solid state microelectrode 91
4.6 Macroelectrodes preparation 92
4.7 Measurements 93
4.7.1 Characterization of ISMEs 93
4.7.2 Testing the response of ISEs 95
4.7.3 Amperometric detection of oxygen 96
4.7.4 Mapping 97

RESULTS

5 Mapping local currents, pH and oxygen in localized corrosion processes 99
5.1 Spatial distribution of current density, pH and oxygen above Zn-Fe galvanic couple 99
5.1.1 Distribution of current density 100
5.1.2 The distribution maps of pH 104
5.1.3 The distribution maps of dissolved O_2 106
5.2 Spatial distribution of current density, pH and oxygen above the sol-gel coated AA2024-T3 with artificial defects 108
5.3 Spatial distribution of current density, pH and oxygen above the sol-gel coated AA2024-T3 during inhibition 109
5.4 Concluding remarks 114

6 Mg^{2+}-SME for corrosion applications 115
6.1 Characterization of Mg^{2+}-SME 116
6.2 Monitoring the local spatial distribution of pH, Mg^{2+} and ionic current density 117
6.3 Studying of corrosion inhibition in microdefects on coated AZ31 alloy 118
6.4 Concluding remarks 124
7 Zn^{2+}-SME for corrosion studies 125
7.1 Development and characterization of Zn^{2+}-SME 125
7.2 Application of Zn^{2+}-SME to corrosion studies 131
7.2.1 Galvanically coupled Zn-Fe electrodes 131
7.2.2 Zinc wire corroding in chloride media 133
7.2.3 Final remarks 140
7.3 Optimization of the membrane composition for Zn^{2+}-SME applicable for corrosion related studies 140
7.3.1 Selection of Zn^{2+} ionophores 140
7.3.2 Screening of Zn^{2+}-SEs 143
7.3.3 Study of Zn^{2+}-SEs response at natural pH and in 0.05M NaCl 147
7.3.4 Cocktails for Zn^{2+}-SMEs 152
7.3.5 Concluding remarks 154
8 Development of a membrane cocktail for Al^{3+}-SME 155
8.1 Aluminium ions in solution 156
8.2 Overview of Al^{3+}-SEs 159
8.3 Selection of Al^{3+} ionophores 162
8.4 Screening of Al^{3+}-SEs 164
8.4.1 Membranes compositions 164
8.4.2 Response of Al^{3+}-SEs at different pH 165
8.5 Effect of membrane components on Al^{3+}-SEs response at natural pH and in 0.05M NaCl 170
8.5.1 Membranes compositions 170
8.5.2 Effect of ionophore nature 172
8.5.3 Influence of ion-exchanger nature 172
8.5.4 Effect of plasticizer and ionophore content 174
8.6 Cocktails for Al^{3+}-SME 177

8.7 Concluding remarks 177
9 Two potentiometric sensors for Cu^{2+} determination in corrosion processes 179
9.1 Generalities about copper corrosion and inhibition 179
9.2 Glass-capillary Cu^{2+}-SME based on TBTDS ionophore 182
9.2.1 Caracterization of Cu^{2+}-SME 182
9.2.2 Probing copper inhibition by BTAH with Cu^{2+}-SME 183
9.3 Copper(II) ion sensitive solid state microelectrode based on copper selenide 188
9.3.1 Response of the Cu{CuSe} microelectrode 188
9.3.2 A word about working mechanism 189
9.3.3 Probing copper corrosion and inhibition with Cu{CuSe} microelectrode 191
9.4 Concluding remarks 195
10 Discussion 197
10.1 Work overview 197
10.2 SVET/SRET and SIET applications in corrosion studies 198
10.3 Development of membrane compositions for the ISMEs 200
10.3.1Screening tests of ISEs 200
10.3.2Membrane resistance of ISMEs 201
10.3.3ISMEs response evaluation 202
10.4 SIET particularities regarding to corrosion studies 204
11 Conclusions and future work 207
References 211

Abbreviations and symbols

AC	alternating current
AEI	Applicable Electronics Inc.
AFM	Atomic Force Microscopy
ASET	Automated Scanning Electrode Technique
BTAH	benzotriazole
C	concentration
CE	counter electrode
D	diffusion coefficient
DC	direct current
E	potential/voltage
ETH 500	tetradodecyl ammonium tetrakis(4-chlorophenyl)-borate
F	Faraday constant, 96485 C mol^{-1}
GPTMS	(3-glycidoxypropyl)-trimethoxysilane
ISE	ion-selective electrode
ISME	ion-selective microelectrode
IUPAC	International Union for Pure and Applied Chemistry
KTClPhB	potassium tetrakis(4-chlorophenyl) borate
LEIS	Local Electrochemical Impedance Spectroscopy
M	metal
ME	microelectrode
n	number of electrons for the electrochemical reaction

NaFMPhB	sodium tetrakis[3,5-bis(trifluoromethyl)phenyl] borate
NaTPhB	sodium tetraphenyl borate
NPhOE	2-nitrophenyl octyl ether
OCP	open circuit potential
POT	poly(3-octylthiophene-2,5-diyl)
PVC	polylvinyl chloride
p*X*	$-\log a_x$, where $X = H^+, Mg^{2+}, Zn^{2+}, Cu^{2+}, Al^{3+}$
r	micro-disc radius
R	universal gas constant, 8.314 J K^{-1} mol^{-1}
RE	reference electrode
SECM	Scanning Electrochemical Microscopy
SIET	Scanning Ion-selective Electrode Technique
SISET	Project “Enhancing Scanning Ion-selective Electrode Technique”
SKP	Scanning Kelvin Probe
SKPFM	Scanning Kelvin Probe Force Microscopy
SRET	Scanning Reference Electrode Technique
SVET	Scanning Vibrating Electrode Technique
T	absolute temperature, K
TAP	titanium diisopropoxide bis(acetylacetonate)
TBTDS	tetra-*n*-buthylthiuram disulfide
TDDA	tridodecylamine
THF	tetrahydrofuran
TPOZ	zirconium (IV) tetra-propoxide
UME	ultramicroelectrode
WBE	Wire Beam Electrode
WPI	World Precisions Instruments, Ltd.

List of Figures

Figure 1. Scheme of oxidation and reduction during corrosion. Adapted from [9]..... 20

Figure 2. Schematic summary of the various forms of corrosion [1]..... 22

Figure 3. Autocatalytic process occurring in a pit. Taken from [28]. 25

Figure 4. Scheme of strategies for corrosion control. 28

Figure 5. Scheme of the filiform-corrosion cell. Taken from [46]. 30

Figure 6. Methods used for study and monitor corrosion. 34

Figure 7. Techniques used to study localized corrosion at the micro/nanometer range: (a) SRET; (b) SVET; (c) LEIS; (d) SIET; (e) SECM; (f) WBE; (g) SKP; (h) AFM; (i) SKPFM; (j) microcapillary cell; and (k) microdroplet cell. Adapted from [64]. 35

Figure 8. Potential and current distributions above nickel-steel couple determined by Copson. Taken from [83]. 39

Figure 9. Element of equipotential surfaces. Taken from [83]. 39

Figure 10. A schematic view of the potential and current distribution above the surface of a local anode. Adapted from [58]..... 42

Figure 11. Scheme of current density measurements limitations by SVET. Adapted from [136]..... 43

Figure 12. Operating principles of SECM. A) Hemispherical diffusion of O leads to a steady-state current, $\boldsymbol{iT}, \infty$; B) Hindered diffusion of O leads to $\boldsymbol{iT} < \boldsymbol{iT}, \infty$; C) Feedback diffusion of O leads to $\boldsymbol{iT} > \boldsymbol{iT}, \infty$..... 46

Figure 13. Schematic cross sections of ME configurations. (a) Nomenclature of ME parts; (b) Na^+-sensitive ME; (c) recessed Na^+-sensitive ME; (d) liquid membrane micropipette electrode; (e) coated wire ME; (f) flow through ISE; (g) tubular flow-through glass electrode, (h) planar sensor made by microelectronic technology; (i) ISFET sensor. Taken from [73]. 58

Figure 14. Schematic diagram of a potentiometric cell assembly with a membrane electrode and a double junction reference electrode. Taken from [218]. Lower – Cell scheme, where single vertical lines indicate phase boundaries, and double vertical lines indicate a liquid-liquid interface. 61

Figure 15. Determination of the lower detection limit of ion-selective electrode [228]. .. 64

Figure 16. Definition and determination of response time of ISE according to IUPAC recommendations. Taken from [228]. 66

Figure 17. a) Schematic drawing and b) an optical photo of the solid-contact ion-selective microelectrode. c) SEM image of the tip apex. Taken from [230]. 70

Figure 18. The configuration of solid state Zn^{2+}-SME. Taken from [249]. 76

Figure 19. Prepared samples of AA2024-T3 alloy with two defects in the coating, with edges masked by beeswax+colophony– (a); Zn-Fe couple with scotch tape – (b), and Zn wire – (c). 85

Figure 20. Scheme of interaction between different modules of SVET apparatus controlled by ASET software. Taken from ASET guide. The numbers are labeled in the text. 86

Figure 21. SVET cell (a) and probe vibrating with an amplitude with the double of the tip size (b). 87

Figure 22. Photographs of SIET arrangement, a) and a homemade reference electrode, b). 88

Figure 23. Silanization of glass surfaces with trimethylchlorosilane (upper) or N-trimethylsilyldimethylamine (lower) [76]. 89

Figure 24. Photographs of the silanization chamber, a); the glass micropipettes: view under the microscope during front filling from spare broken capillary, b); a 25 µm column of membrane cocktail at the tip, c); a ready to use microelectrode, d). 90

Figure 25. Schematic picture of Cu^{2+} sensitive solid state microelectrode. 91

Figure 26. Glass raschig rings fixed on the glass plate for producing PVC membranes. 92

Figure 27. Calibration curves of Mg^{2+}-selective microelectrode in pure solutions of Mg^{2+} and Na^{+} for determining selectivity coefficient of Mg^{2+}-SME to Na^{+} [230]. 94

Figure 28. Amperometric microsensor for detection of dissolved oxygen in solution. 97

Figure 29. Voltammogram for the reduction of dissolved oxygen in 0.05M NaCl. The scan rate polarization was 30 mV s^{-1}. 97

Figure 30. Photograph of dual head support with microsensors at 35 µm and an analysing cell. 98

Figure 31. Scheme of the Zn-Fe galvanic cell (a) and the optical photograph of the sample surface with indicated measured areas (b). 100

Figure 32. Distribution of ionic currents measured by SVET in XY (a) and in XZ (b) planes in 5 mM NaCl solution above Zn-Fe galvanic couple. 101

Figure 33. Distribution of potential in 5mM NaCl solution (vs bulk) in XY plane at 100 µm with grid points of measurement (a), 120 µm (b) and in XZ plane above the Zn-Fe couple after 2h of immersion. The colour scale is the same one for (a), (b) and (c). 102

Figure 34. Potential differences between the two XY planes of Figure 33, (a), and in XZ plane, (b), above Zn-Fe couple immersed in 5mM NaCl. 103

Figure 35. Distribution maps of ionic currents calculated from SRET measurements in 5 mM NaCl above Zn-Fe galvanic couple in XY plane (a) and in XZ plane (b). 104

Figure 36. The typical dynamic response (upper) and calibration curve (lower) of the pH-SME based on Hydrogen ionophore I cocktail B to commercial buffers 105

Figure 37. Distribution of pH in XY (a) and XZ (b) planes in 5 mM NaCl solution above Zn-Fe galvanic couple. 106

Figure 38. Distribution of dissolved oxygen concentration ($[O_2]$, M) in XY (a) and XZ (b) planes in 5 mM NaCl solution above Zn-Fe galvanic couple. 107

Figure 39. Image of sol-gel coated AA2024-T3 with 2 artificial defects and indicated regions of measurements, (a); SVET current density map after 30h of immersion in 0.05M NaCl, (b); variation of pH 100 µm above the surface, (c), and dissolved oxygen concentration at 50, 100 and 2000 µm above the sample surface (d). 109

Figure 40. Sample surface with indication of the two artificial defects and the position of measurement lines. 110

Figure 41. (a) SVET map obtained 19 h after immersion in 0.05M NaCl and minutes before the addition of cerium nitrate; (b) SVET map obtained 19 h after the addition of cerium nitrate to the solution at a concentration of 10 mM. Maps position is indicated in Figure 40. 111

Figure 42. Line scans of ionic current, pH and dissolved oxygen reduction current, obtained at 50 µm (100 µm for SVET) above the surface, before and 20 h after addition of cerium nitrate to the solution. Lines position is indicated in Figure 40. 112

Figure 43. Ionic currents, pH and O_2 reduction current measured in the z direction above the two defects before (a) and 20 h after (b) the addition of cerium nitrate. 113

Figure 44. Calibration plots for Mg^{2+}-SME in different media. 116

Figure 45. pH-dependent response of Mg^{2+}-SME. C(Mg^{2+}) = 0.01M [270]. 117

Figure 46. Optical photograph of scanned area of 1.53 x 1.85 mm^2, (a), pMg, (b), and pH, (c), and distribution of local ionic current density, (d), recorded during immersion of AZ31B alloy coated with thin sol-gel film in 0.05M NaCl solution. 118

Figure 47. Optical micrographs (a, b, c, d) and local ionic currents maps (e, f, g, h) after immersion of AZ31 alloy coated with sol-gel film in 0.05M NaCl during 5 hours with different inhibitors: e – blank sample, f – 0.01M NaF, g – 0.01M $Ce(NO_3)_3$, h – 0.01M 1,2,4-triazole. 120

Figure 48. Optical micrograph (a), pH (b) and currents (c) maps after 7.5h of immersion coated AZ31 in 0.05M NaCl. 122

Figure 49. Optical micrograph (a), pH (b) and pMg (c) maps after 6.5h of immersion coated AZ31 in 0.05M NaCl, 0.01M 1,2,4-triazole [62,270]. 122

Figure 50. Optical micrograph and pH observation during immersion of coated AZ31 in solution of 0.05M NaCl, 0.01M 1,2,4-triazole. 123

Figure 51. Optical micrograph (a) and SVET maps (µA cm^{-2}) after 1 day (b) and 3 days (c) of immersion coated AZ31 in 0.05M NaCl + 0.01M 1,2,4-triazole. 124

Figure 52. Response of Zn^{2+}-SME based on membrane cocktail Zn-c1 with different column length (40 µm and 120 µm). 126

Figure 53. Response of Zn^{2+}-SME based on membrane cocktail Zn-c2 with different column length (40 µm and 120 µm). 127

Figure 54. Response of Zn^{2+}-SME based on membrane cocktail Zn-c3 with different column length (40 µm and 120 µm). 127

Figure 55. Response of Zn^{2+}-SME based on membrane cocktail Zn-c4 with different column length (40 µm and 120 µm). 128

Figure 56. Response of Zn^{2+}-SME based on membrane cocktail Zn-c2 with 120 µm of column length in the presence of 0.05M NaCl. 129

Figure 57. The dynamic response (upper) and calibration plots (lower) of Zn^{2+} -SME based on membrane cocktail Zn-c5. 130

Figure 58. Distribution maps of Zn^{2+} activity in XY (height 10 µm) (a) and XZ (b) planes near the Zn-Fe galvanic couple after 15h of immersion in distilled H_2O. 131

Figure 59. Optical image of the Zn-Fe couple (a). Distribution of pZn in XY (b, c) and in XZ planes (d) near Zn-Fe galvanic couple immersed in 5mM NaCl during 2h (b), 36h (c) and 48h (a, d). 132

Figure 60. Photograph of zinc wire after 24 hours of immersion in 5mM NaCl (a). Maps of pH (blue lines and labels) and of pZn (red lines and labels) taken 100 µm above the surface and ploted over the sample photograph (b). 134

Figure 61. Diagram of distribution Zn^{2+} species in H_2O generated by PHREEQC for 1m M of Zn^{2+}. 1, 2, 3 and 4 correspond to the sites in Figure 60 (a) and Table 11. 137

Figure 62. Diagram of Zn^{2+} species (pZn 3.89) in 5mM NaCl without CO_2 (a) and with CO_2 (b) generated by Hydra&Medusa. 138

Figure 63. Diagram of Zn^{2+} species for initial pZn 1 in 5mM NaCl generated by Hydra&Medusa. 138

Figure 64. Stability diagram of Zn^{2+} containing species in 5mM NaCl with 1M (blue) or 10^{-5}M (red) of total zinc concentration in presence of dissolved CO_2 generated by GWB. .. 139

Figure 65. Studied zinc-ionophores structures. 141

Figure 66. Response to pH of Zn^{2+}-SEs with different ionophores measured in 10^{-2}M $Zn(NO_3)_2$ (black solid symbols) and 10^{-3}M $Zn(NO_3)_2$ (red open symbols). 145

Figure 67. Response of Zn^{2+}-SEs to pH at 10^{-2}M $Zn(NO_3)_2$ background. 146

Figure 68. Calibrations plots of Zn^{2+}-SEs based on Zn-S4-2A and Zn-1C membranes..... 146

Figure 69. Electrode function of the Zn^{2+}-selective electrodes with different Zn ionophores. 149

Figure 70. Electrode functions of the Zn^{2+}-selective electrodes based on the Zn-S4 inophore with two ion exchangers: KTClPhB (Zn-S4-2A*) and NaFMPhB (Zn-S4-3A). 151

Figure 71. Calibrations plots of Zn^{2+} -SME based on membrane cocktails with different content of the ionophore Zn-c5 (7% of Zn-S4) and Zn-c6 (10% of Zn-S4) at 5mM NaCl background. 153

Figure 72. Response of the developed Zn^{2+}-SMEs based on Zn-S5 ionophore with different ion exchangers: (a) - $Ca(TOBS)_2$ and (b) - KTClPhB. 153

Figure 73. Distribution of Al(III) species in 10^{-5}M (a), 0.001M (b), 0.1M (c) and 1M (d) hypothetically homogeneous Al(III) solution as a function of pH. The shaded area indicates the approximate pH range of oversaturation with regard to gibbsite, $Al(OH)_3$(s). Taken from [334]. 157

Figure 74. The pH of beginning of $Al(OH)_3$ precipitation for different initial concentrations of total Al^{3+} in solution calculated from Equation 8.2. 158

Figure 75. Ideal response of selective electrodes to one-charged (M^+), two-charged (M^{2+}) and three-charged (M^{3+}) cations. 159

Figure 76. Structures of the studied Al^{3+} ionophores. 163

Figure 77. Response of Al^{3+}-ISEs to pH at 10^{-2}M $Al(NO_3)_3$ (solid black symbols) and at 10^{-3}M $Al(NO_3)_3$ (open red symbols) background 166

Figure 78. Electrode functions of Al^{3+}-SEs based on Al-M, Al-S0, Al-S5, Al-S6 and Al-S7 ionophores. 167

Figure 79. Effect of ion-exchanger on electrode functions of the Al^{3+}-SEs based on the Al-S6 ionophore and plasticized by NPhOE. 167

Figure 80. Influence of ion-exchanger on response of the Al^{3+}-SEs based on Al-S8 and Al-S9 ionophores to aluminium calibration solutions at pH≈3 (black squares) and at pH≈4 (blue circles). (Exact pH values are shown on graphs). 168

Figure 81. Influence of plasticizer on response of the Al^{3+}-SEs based on Al-S9 ionophore to aluminium calibration solutions at pH≈4 (exact pH values are indicated on graphs). 169

Figure 82. Response of the Al^{3+}-SEs: 1- in solutions with Al^{3+} ions, 2 – in solutions without Al^{3+} ions but with corresponding pH (pH values are listed in Table 8, Section 4.7.2.2). 173

Figure 83. Response of the Al^{3+}-SEs at 0.05 M NaCl background: 1- in solutions of Al^{3+} ions, 2 – in solutions without Al^{3+} ions but with corresponding pH value listed in Table 8, Section 4.7.2.2. 176

Figure 84. The dynamic response (upper) and calibration plots (lower) of glass-capillary Cu^{2+}-SME in different media. 183

Figure 85. Photograph of the cell composed by Cu-Pt galvanic couple, reference electrode and a Cu^{2+}-selective microelectrode. 184

Figure 86. Optical photographs of Cu wire that is connected to Pt after 5 minutes (a) and up to 2 hours 30 minutes (c) of immersion in 5 mM NaCl. Activity of Cu^{2+} measured by Cu^{2+}-SME 10 µm above the surface at different times of immersion (b). 186

Figure 87. Optical photographs of Cu wire that is connected to Pt with an artificial scratch after 35 minutes (a) and up to 3 hours 40 minutes (c) of immersion in 5 mM NaCl + 1 mM BTAH. Activity of Cu^{2+} measured 10 µm above the surface at different times of immersion (b)..... 187

Figure 88. The dynamic response (upper) and calibration plots (lower) of Cu{CuSe} microsensor in different mediums. 189

Figure 89. Optical image of Cu wire connected to Pt wire beneath the holder (a) and distribution of pCu 50 µm above the surface (b) after 3 hours of immersion in 0.05M NaCl. 191

Figure 90. Influence of BTAH on the response of Cu{CuSe} microelectrode at 0.05M NaCl background. 192

Figure 91. Copper activity measured 100 µm above the surface at different immersion times in 0.05M NaCl (a) and corresponding optical images of the copper wire (b, c, d, e and f)..... 194

Figure 92. Optical photograph of Cu wire with scratched surface (a) and copper activity measured 100 µm above the surface at different times of immersion in 0.05M NaCl after the pre-exposure in 1 mM BTAH + 0.05M NaCl solution (b)..... 195

Figure 93. Summary of realizations made during this PhD work. 198

List of Tables

Table 1. Types of galvanic corrosion couples. Adapted from [26]. 24

Table 2. Localized techniques used in corrosion research. 36

Table 3. Characteristics of pH-sensitive commercial cocktails [237]. 69

Table 4. Examples of different Cu^{2+}-selective microsensors found in literature. 78

Table 5. Description of used materials. 81

Table 6. Reagents. 82

Table 7. Reagents used for membranes preparation. 83

Table 8. Measured pH of Zn^{2+} and Al^{3+} calibration solutions. 95

Table 9. Composition of prepared membrane cocktails for Zn^{2+}-SME based on TBTDS ionophore. 126

Table 10. Comparison of response of Zn^{2+}-SMEs based on preparead cocktails. 128

Table 11. Results of potential, pH and pZn measurements in single sites above Zn wire immersed in 5mM NaCl. 135

Table 12. Characteristics of chosen Zn^{2+}-selective electrodes. 142

Table 13. Prepared membranes for preliminary screening of Zn^{2+}-selective electrodes. 143

Table 14. Studied membranes of Zn^{2+}-selective electrodes. 147

Table 15. The effect of the membrane composition on the selectivity of Zn^{2+}-SEs, where E_1 – potential in 0.01 M $Zn(NO_3)_2$ with pH=5.14; E_2 – potential in 0.05 M NaCl with pH=5.22. 150

Table 16. Membrane cocktail compositions for Zn^{2+}-SME being studied. 152

Table 17. The pH of beginning of $Al(OH)_3$ precipitation for different initial concentrations of total Al^{3+} in solution calculated from Equation 8.2. 158

Table 18. Comparison of found Al^{3+}-selective electrodes. 160

Table 19. Prepared membranes for preliminary screening of Al^{3+}-selective electrodes. . 164

Table 20. Prepared membranes for Al^{3+}-SEs. 171

Table 21. The effect of the ion-exchanger on the selectivity of Al^{3+}-selective electrodes, where E_1 – potential in solution of 0.01 M Al^{3+} with pH=3.70; E_2 – potential in HNO_3 solution with pH=3.68; E_3 – potential in 0.05 M NaCl solution with pH=3.67. 174

Table 22. The effect of the plasticizer on the response of Al^{3+}-SEs, where E_1 – potential in solution of 0.01 M Al^{3+} with pH=3.70; E_2 – potential in HNO_3 solution with pH=3.68; E_3 – potential in 0.05 M NaCl solution with pH=3.67. 175

Table 23. Membrane cocktail compositions for Al^{3+}-SMEs being studied. 177

Table 24. Tests made during corrosion and inhibition of copper connected to platinum. 193

Preface

This PhD thesis consists of 11 chapters. The state of art, basic theory and techniques are described in the Chapters 1-3. Thus, Chapter 1 “Phenomena of localized corrosion” presents an introduction to metallic corrosion, localized phenomena and corrosion control, which is the main research field considered here; Chapter 2 gives an overview of electrochemical techniques used for studying localized corrosion with emphasis on SVET/SRET, SECM and SIET; and Chapter 3 deals with the theory of potentiometric measurements, types of ion-selective microelectrodes and their analytical characteristics. After the introductory part Chapter 4 describes the experimental procedures and methods.

Results are presented in Chapters 5 to 9. Chapter 5 is dedicated to the use of SVET/SRET, potentiometric pH selective microelectrode (pH-SME) and an amperometric O_2 microsensor for describing the local chemistry during corrosion of two technologically important cases: i) Zn-Fe galvanic couple and ii) corrosion and inhibition on defects on a coated AA2024-T3 aluminium alloy. The characterization and application of a Mg^{2+}-selective microelectrode (Mg^{2+}-SME) for the study of corrosion and corrosion inhibition of magnesium alloy AZ31B is analyzed in Chapter 6. Chapter 7 reports about the development and characterization of a Zn^{2+}-SME. Its application for the investigation of corrosion of zinc wire and a Zn-Fe galvanic couple is demonstrated. Chapter 8 is dedicated to the screening of ion-selective electrodes for Al^{3+}. While the focus of this work was microelectrodes, for Zn^{2+} and Al^{3+} macroelectrodes were used to find optimal conditions of operation for applying to the microsize. The work includes screening experiments to evaluate the influence of the membrane components on the electrode sensitivity to target ions under relevant pH and NaCl background conditions. Chapter 9 describes the development and testing of two Cu^{2+}-SMEs of different type. It is divided in 3 parts: the first presents some generalities about copper corrosion and inhibition and next two

present the response of a glass microelectrode and a metal/metal salt microelectrode and their application to some model corrosion conditions.

Each chapter in the thesis ends with a small summary. A generalized discussion of the results is given in Chapter 10. Conclusions and proposal for future work can be found in Chapter 11.

The work of this PhD thesis was partialy included in the implementation of the following scientific projects:

i) POCI/CTM/59234/2004 - "Development of new nanostructured hybrid sol-gel coatings modified with organic inhibitors for corrosion protection of metallic substrates".
ii) Integrated European project NMP/CT/2005/011783 – "Advanced environmentally friendly nanostructured corrosion protection coatings" (MULTIPROTECT).
iii) PTDC/CTM/66041/2006 – "Sensing the micro-distribution of chemical species in solution close to active metals".
iv) Marie Curie Actions Programme FP7-MCA-PIRSES-GA-2009-269282 – "Enhancing Scanning Ion-Selective Electrode Technique" (SISET).

The participation in the first two projects justifies the choice of the metallic substrates, the sol-gel based protective coatings and the choice of metal cations to be detected during the PhD studies. Application of geochemical modelling software for corrosion studies appears in the frame of the third project. The involvement in the fourth project, SISET, permitted to achieve significant insights in the development and testing of ISEs due to the synthesis of novel ionophores and choice of membrane optimization strategies.

Part of the results obtained during the PhD studies was included in the following papers:

1. S.V. Lamaka, *O.V. Karavai*, A.C. Bastos, M.L. Zheludkevich, M.G.S. Ferreira "Monitoring local spatial distribution of Mg^{2+}, pH and ionic currents", Electrochem. Commun. 10 (2008) 259-262.
2. A.C. Bastos, *O.V. Karavai*, S.V. Lamaka, M.L. Zheludkevich, M.G.S. Ferreira "Micro-sensores potenciométricos e amperométricos para o estudo da corrosão", Corros. Prot. Mat., Nº2, 28 (2009) 42-47.
3. *O.V. Karavai*, A.C. Bastos, M.L. Zheludkevich, M.G. Taryba, S.V. Lamaka, M.G.S. Ferreira "Localized electrochemical study of corrosion inhibition in microdefects on coated AZ31 magnesium alloy", Electrochim. Acta 55 (2010) 5401-5406.
4. A.C. Bastos, M.G. Taryba, *O.V. Karavai*, M.L. Zheludkevich, S.V. Lamaka, M.G.S. Ferreira "Micropotentiometric mapping of local distributions of Zn^{2+} relevant to corrosion studies", Electrochem. Commun. 12 (2010) 394-397.
5. A.C. Bastos, *O.V. Karavai*, M.L. Zheludkevich, K.A. Yasakau, M.G.S. Ferreira "Localized measurements of pH and dissolved oxygen as complements to SVET in the investigation of corrosion at defects in coated aluminium alloy", Electroanalysis 2 (2010) 2009–2016.
6. A.C. Bastos, M.C. Quevedo, *O.V. Karavai*, M.G.S. Ferreira "On the application of SVET to corrosion research", J. Electroanal. Chem. (2017) *under revision.*

Chapter 1

1 Phenomena of localized corrosion of metals

1.1 Corrosion process and its reactions

Metals and alloys are present in all areas of human activity due to their physical and chemical properties. Particularly in the last two centuries they have been extensively used in transportation, infrastructures, machinery and tools. And it is possible to associate the increasing use of metals with the world's economic growth. It's, however, a major concern to maintain the metallic assets in a proper state during service in different, many times extreme, conditions. In spite of the huge efforts that had been dedicated to the protection of metals, this problem is still very actual.

The spontaneous instability of metallic materials in the terrestrial environment is the reason for the natural process of corrosion. Corrosion is the destructive result of electrochemical reactions between a metallic material and its environment [1–3]. This process returns the metal to its original state in nature as mineral. Thus, corrosion has also been called as "extractive metallurgy in reverse" [4]. Another more general definition exists, contemplating all materials, not only metals [5], but given the nature of this work the traditional definition is preferred.

Metallic corrosion is still one of the most significant processes in the degradation of materials and goods leading to annual losses around 3-5% of the gross national product in industrialized countries [3,6,7], causing in addition environmental and safety hazards [3,7,8].

Corrosion in aqueous environment is the most common corrosion processes because water is omnipresent in the Earth's crust (oceans, rivers, lakes, rain, dew, etc.) and is used in all ranges of purposes, from supporting life as potable water, to multiple industrial tasks, including heat exchange and waste transport. Moisture in the air and water in the soil also account for aqueous corrosion. In all these cases, water is rarely pure. Due to various salts and dissolved gases in it and their dissociation, the water becomes conductive and acts as an electrolyte [8].

When metal corrosion begins its atoms loose electrons and go into the solution in the form of metal ions:

$$M \rightarrow M^{n+} + ne^{-} \qquad (1.1).$$

This half-reaction is called oxidation because involves the increase of oxidation number of the reacting species. By definition, the place where it occurs is called an anode. The electrons generated at the anode travel to the cathode via an electronic path through the metal, until the place where they are used up in reduction half-reactions (Figure 1).

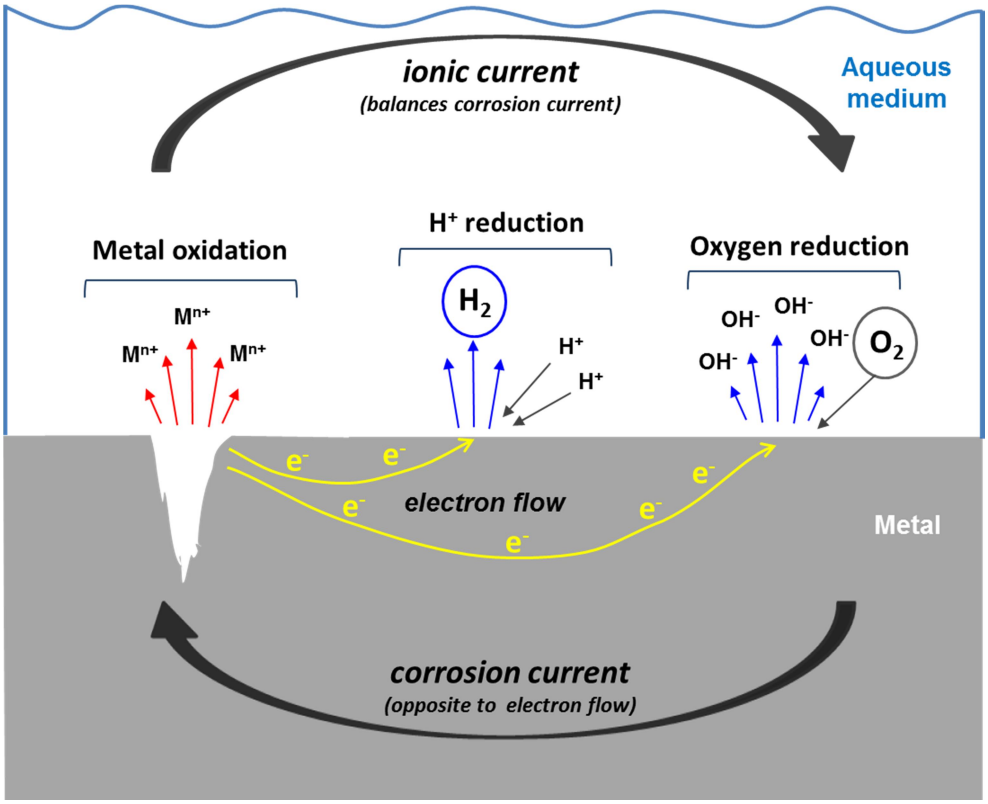

Figure 1. Scheme of oxidation and reduction during corrosion. Adapted from [9]**.**

It should be noticed that although the anodic reactions of metal dissolution are relatively simple, the cathodic process is more complicated. Two common reduction reactions (Figure 1) are dissolved oxygen reduction

$$O_2 + 2H_2O + 4e^- \rightarrow 4OH^- \quad (1.2)$$

and hydrogen ion reduction in acidic medium

$$2H^+ + 2e^- \rightarrow H_2 \uparrow \quad (1.3)$$

In basic medium or at sufficiently negative corrosion potentials the water reduction takes place:

$$2H_2O + 2e^- \rightarrow H_2 \uparrow + 2OH^- \quad (1.4)$$

If metal ions exist in solution , their reduction or deposition may occur [8]:

$$M^{n+} + me^- \rightarrow M^{(n-m)+} \quad (1.5),$$

$$M^{n+} + ne^- \rightarrow M \quad (1.6)$$

The oxidation and reduction half-reactions must proceed simultaneously and at the same rate. The balance between these reactions results in a mixed potential, or corrosion potential, the values differing for each metal/electrolyte system [1].

Thus, corrosion creates a spontaneous flow of electrons from the anodic to the cathodic sites (without applying any external potential), which is balanced by an equal ionic current in the electrolyte thereby completing the electrical circuit (Figure 1).

1.2 Localized corrosion

Corrosion can be present in many forms (Figure 2). Corrosion may be uniform (general), when it occurs over all metal surface at often predictable rate, or localized, when anodic and cathodic sites are well separated [10]. Most of the corrosion in technological applications is local, i.e., confined to small zones. Localized corrosion is a misfortune for industry because the metal may look undamaged on the outside while developing discrete pits and cracks on the inside that can cause loss of fluids, reactants or products in extractive and production industry, the collapse of bridges, aircrafts failures, breakup of ships stressed in storms, etc. [6,7].

Localized corrosion is a more complex form of corrosion due to the small dimensions, and self-acceleration of the attack [2,3,8,11]. It appears, in general, as the result of heterogeneities, either in the metal or in the environment to which it is exposed [2]. Based on the conditions of attack, several forms of localized corrosion can be distinguished [1–4,7,8,10]: g*alvanic corrosion* results from the coupling of dissimilar metals or alloys, sometimes the dissimilar metals are part of the same alloy, and a selective corrosion, or *dealloying* may occur; typical of passive systems *pitting* and *crevice corrosion* generally happen in the presence of chloride ions*, filiform corrosion* is a special case of aeration cell; *hydrogen embrittlement* results from the incorporation of atomic

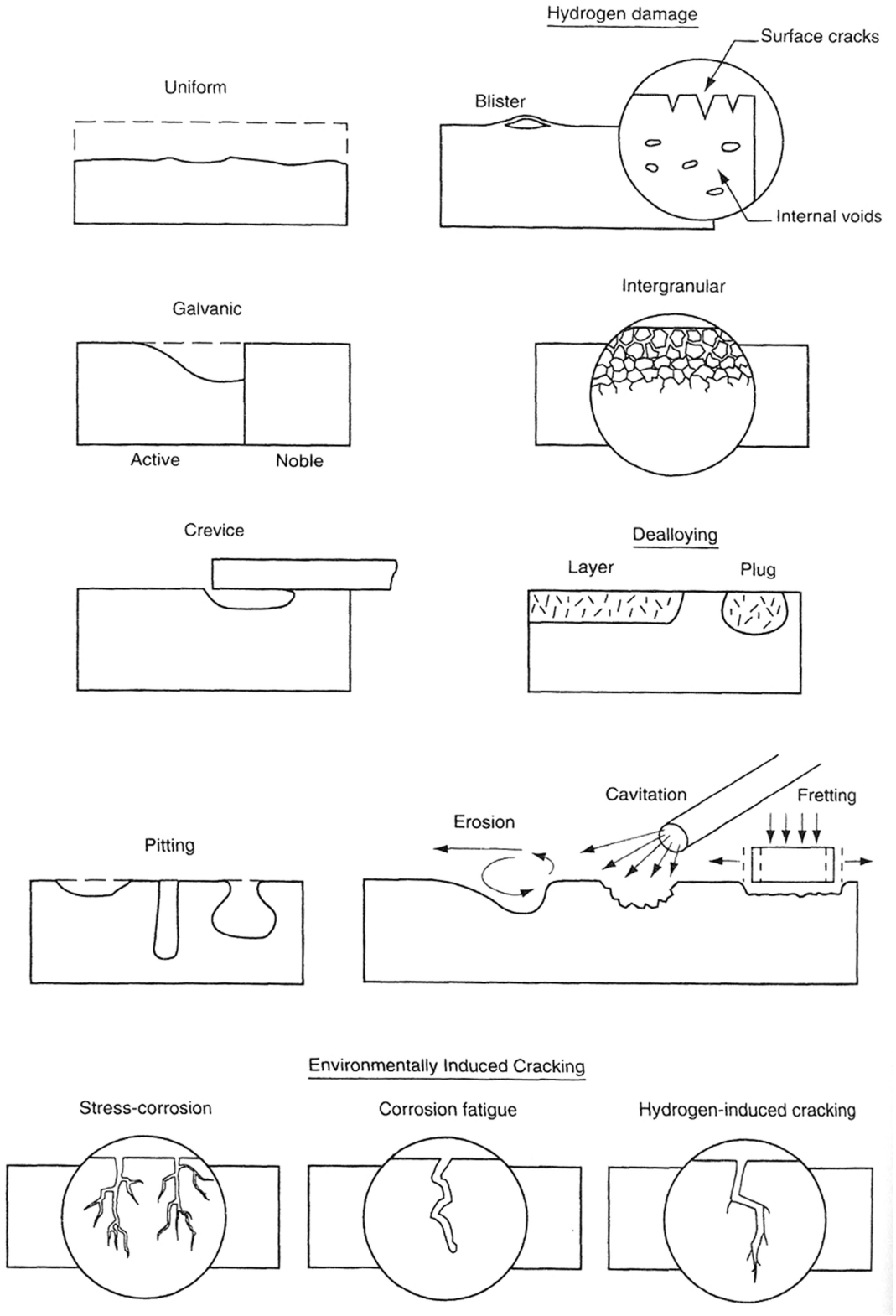

Figure 2. Schematic summary of the various forms of corrosion [1].

hydrogen into the metallic matrix; s*tress corrosion cracking* and *corrosion fatigue* are forms of attack associated to permanent or cyclic states of mechanical tension; *intergranular corrosion* occurs preferentially at grain boundaries; *erosion corrosion*, *cavitation corrosion and fretting corrosion* appear together with mechanical action on the surface and fluid flow effects.

Galvanic, pitting and crevice corrosion are responsible for a significant part of failures and require more attention and depper research [11–13].

1.2.1 Galvanic corrosion

Galvanic corrosion takes place when two different metallic materials become electrically connected (galvanically coupled) and in contact with a common electrolyte [1,9]. The potential of the couple lies between the potential values of both metals when uncoupled. The potential difference between the coupled and uncoupled situations (anodic overpotential) is the driving force for the oxidation of the less noble material (the one with more negative potential when uncoupled). The shift in potential of the more noble metal will also reduce its tendency to dissolve and promotes reduction reactions to proceed therein. The more active metal or alloy becomes the anode and the more noble metal or alloy becomes the cathode in the couple.

For predicting galvanic relationships a galvanic series of metals and alloys is used. Such a series is an arrangement of metals and alloys according to their potentials measured in a given environment. As the potential of a metal or alloy is affected by their metallurgical conditions, environmental factors, changes in temperature, presence of corrosion products and other surface layers, no unique value can be given for a particular material rather an interval of values exists. The most common galvanic series has been constructed from measurements in seawater [14] and, with certain exceptions, is broadly applicable to other aqueous media. According to it, graphite and platinum are at the higher potential (more noble or cathodic) end of the series, while zinc and magnesium are at the lower potential (more active or anodic) end.

It is this principle that forms the scientific basis for using zinc and magnesium as sacrificial anodes to protect the steel, in a process called cathodic protection [7,8]. The use of cathodic protection to reduce or prevent corrosion is a successful technique of long-lasting use in marine structures, naval ships, pipelines, bridges, steel sheet piling, and tankages, under soil and in the sea water.

It should be noticed that dissimilar metal contact can be found not only between two metallic pieces as plates and screws, but also among the constituents of alloy. Impurities, intermetallics and different phases can create microgalvanic couples with the alloy matrix. For example, Cu, Si, Fe, Mn, Mg and Zn are elements commonly used to tune

aluminium alloys composition to achieve desired properties. Such inhomogeneity of the alloys results in appearance of localized corrosion activity which was a subject of study in many research works [15–25]. Thus, aluminium alloys with Cu-enriched S-phases and magnesium alloys containing rare-earth elements are highly susceptible to microgalvanic corrosion [15,20,21].

According to Tomashov [26], depending on the character of electrochemical heterogeneity of the metal surface, galvanic corrosion couples can be differentiated by dimensions of cathodic and anodic sites and also by their degree of uniformity distribution (position) – Table 1.

Table 1. Types of galvanic corrosion couples. Adapted from [26].

Types of corrosion couples			Examples of heterogeneity causing the couples	Character of surface deterioration	
Type	**Dimensional characteristics**	**Characteristics of position**			
First	Macrocouples of structural dimensions (more than 1 mm).	Couples of fixed position.	Contact between different metals. Differential aeration.	Local corrosion of different sections in a structure or detail.	Local ↓ General
Second	Microcouples in crystal structure dimensions (0.1µm-1mm).	Couples with possible gradual change in position from anode to cathode.	Differences in composition or orientation of various crystallites. Presence of inclusions, grain boundaries, etc.	Micro, nonuniform deterioration in macroscale (sometimes considered uniform).	
Third	Submicroscopic couples in dimensions of crystal lattice (10-1000 Å).	Couples with constantly changing positions between anodes and cathodes (fluctuating couples).	Presence of defects (dislocation of atoms) in crystal lattice. Different locations of individual atoms. Heat fluctuations.	Complete uniform external deterioration.	

The activity of couples of the first type (macrocouples) is generally characterized by the stabilized distribution of active areas over the corroding surface in time which exhibits clearly defined local corrosion. Corrosion couples of the second type (microcouples) are characterized by the extreme nonuniformity of distribution of the anodic and cathodic areas. The couples of the third type (submicrocouples) constantly change their position between anodes and cathodes and it can be arbitrarily considered that the anodic and cathodic processes are distributed over the whole corroding surface (uniform or general corrosion).

1.2.2 Pitting corrosion

Pitting corrosion is a form of extremely localized attack by which a piece can be seriously damaged while the overall metal loss is usually negligible. In the extreme case, it appears as a deep, tiny hole in an otherwise unaffected surface. The initiation of a pit is associated with the breakdown of the passive film on the metal surface [12,27,28]. It occurs mainly as a result of the action of aggressive anions [27–29], and it is particularly insidious because it frequently happens in environments which are close to provide passivity.

Figure 3 illustrates the mechanism of pitting attack on aluminium, which is, apparently, similar for steel. A pit is initiated by the adsorption of activating anions, particularly chlorides, on certain defects of oxide film, such as slag inclusions or precipitates of secondary phases.

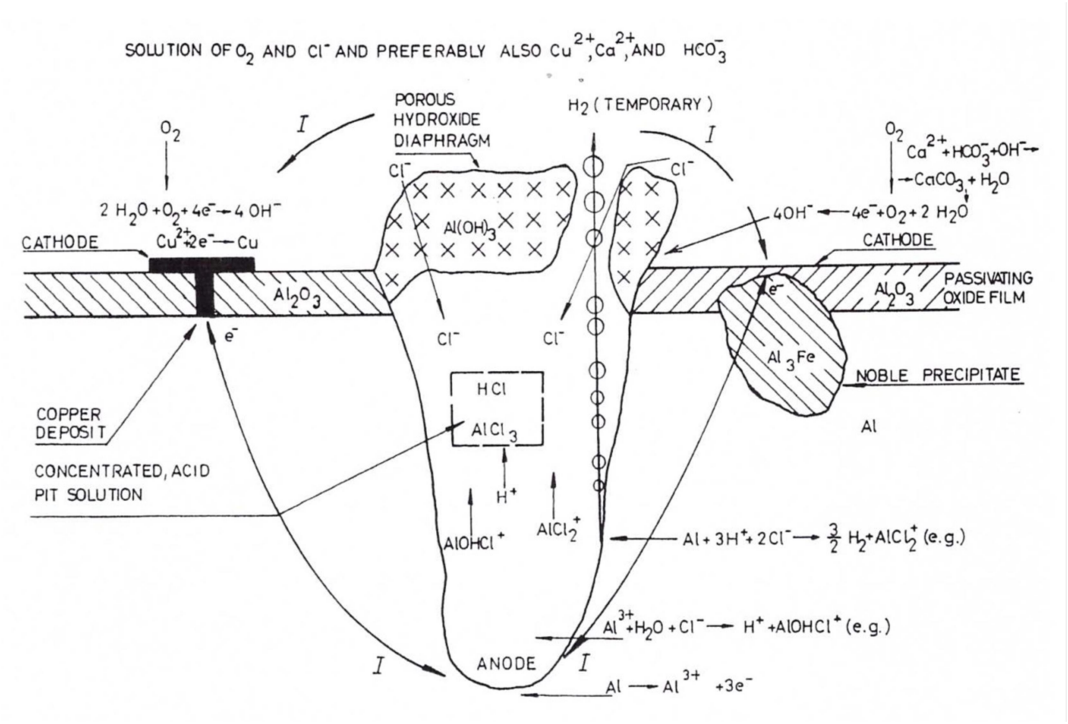

Figure 3. Autocatalytic process occurring in a pit. Taken from [28].

When the chloride ions penetrate the film, the formation of oxide-chloride product and a subsequent local dissolution of oxide film begin. As soon as a pit has been formed, it grows autocatalytically. The self-stimulating conditions occur due to following features [28]:

i) enrichment of chloride ions in the pit by migration with the corrosion current, generated by the pit cell;

ii) the generation of an acid solution in the pit, by the hydrolysis of metal ions that go to solution, and a consequent local rise in the passivation potential;
iii) high conductivity in the concentrated salt solution in the pit;
iv) limited O_2 access, partly due to its low solubility in the concentrated pit solution;
v) the formation of a crust of hydrate, counteracting the dilution of pit solution by diffusion and convection and hence strengthening the factors i)-iv);
vi) cathodic protection by the corrosion current around the pit;
vii) passivation by alkali formed in the cathode reaction, particularly in the presence of calcium hydrogen carbonate;
viii) deposition of more noble metals, such as copper, on local cathodes, increasing their efficiency, so the cathode potential is maintained above the pitting potential.

The phenomenon is more serious in systems which can cause major changes of the environment within the pit, when an autocatalytic increase in corrosion rate can appear [12,28,29]. Pits may also assist in brittle failure, fatigue failure, stress corrosion cracking, and corrosion fatigue by providing sites of stress concentration.

Pitting corrosion is characterized by the following features [12]:

- The attack is concentrated into discrete areas. Pits are sometimes isolated and sometimes close together, giving the area of attack a rough appearance.
- Pits usually initiate on the upper surface of the horizontally placed parts.
- An extended initiation period is usually required before visible pits appear.
- Stagnant solution conditions lead to pitting.
- Stainless steels, aluminium, and their alloys are particularly susceptible to pitting. Most failures of stainless steels occur in neutral-to-acid chloride solutions. Aluminium and carbon steels pit in alkaline chloride solutions.
- Most pitting is associated with halide ions (chlorides, bromides) and hypochlorites, which are particularly aggressive. Cupric, ferric, and mercuric halides are extremely aggressive because their cations are cathodically reduced and sustain attack.

1.2.3 Crevice corrosion

Crevice corrosion occurs in sites were a gap is wide enough for liquid to penetrate but too narrow for the liquid to flow. As a consequence a concentration cell is formed between the inner side, which is oxygen poor, and the outside, where oxygen is readily available [8,12,30]. Inside the crevice the low oxygen concentration brings the local

potential into the negative direction making it anode with respect to the outside. The mechanism is believed to be similar to that of pitting.

Crevices may be produced by design or accident. Crevices caused by design occur at gaskets, flanges, rubber O-rings, washers, bolt holes, rolled tube ends, threaded joints, lap joints, riveted seams, overlapping screen wires, and anywhere close-fitting surfaces are present. Occluded regions are also formed under tubercles, deposits, and below sediments or biological growth (biologically influenced corrosion). Similarly, unintentional crevices such as cracks, seams, and other metallurgical defects could serve as sites for corrosion.

1.3 Strategies of corrosion control

A great number of different approaches exist to prevent and control the corrosion of metallic structures. In the process they act over one of the following:

- the metal;
- the environment;
- the separation of the material from the corrosive medium through surface coatings.

Figure 4 illustrates the most common strategies for corrosion control. The corrosion prevention should be started in the project phase by the selection of appropriate materials, a clever structure design and choise of favourable location. Then, in service, the metallic structures and equipments can be protected by many ways depending on the actual operating conditions, cost and easy of implementation. Examples can be changing the working environment by avoiding the presence of O_2 and other oxidizing species, reducing the concentration of aggressive species, decreasing the temperature and controlling air humidity [6,10,31].

A corrosion inhibitor is a chemical compound (usually soluble or volatile) that is added to the environment in order to reduce the rate of metal corrosion [10]. The corrosion inhibitor usually makes the metal passive by providing an insulating film on the anode, the cathode, or both.

In anodic protection the metal to be protected is turned an anode. The potential is brought in the positive direction till the passivation region, where a passive layer can be created on the surface. This only works if the metal can be passivated in the medium of interest. The most common application is in storage tanks of sulphuric acid for the chemical industry. Cathodic protection involves the reversal of electric current flow within the corrosion cell by making the metal to be protected a cathode. The metal potential became more negative than the corrosion potential. If this potential is in the immunity

region, there is no thermodynamic possibility for metal oxidation and the metal stays protected. The use of cathodic protection to reduce or eliminate corrosion is successfully applied in marine structures, pipelines, naval ships, bridges, steel piling, tankages, and other steel structures buried in soil and immersed in water [7,32].

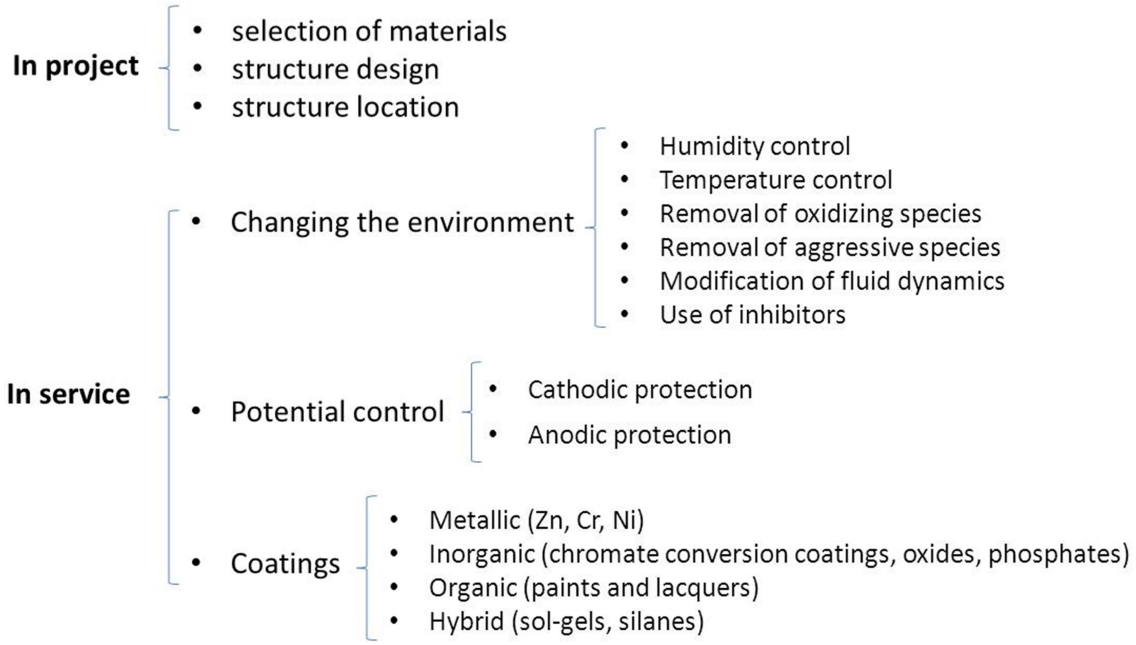

Figure 4. Scheme of strategies for corrosion control.

Application of coatings in its variuos forms is the most simple, versatile and widespread method to control corrosion [1,6,32]. Metallic coatings can be formed by metals that are more noble than the substrate (examples for steel are Cr, Ni, Cu) or by those that are less noble (i.e. Zn, Cd, Al) than the substrate [1,7,10,33]. In all cases, the coating provides a barrier between the metal and the corrosive environment and thus reduces corrosion, provided its own corrosion rate is low. However, if the metal base is exposed to the environment, its corrosion is accelerated by a galvanic connection with a large cathode, if the coating is more noble, while for less noble coating the metal substrate is galvanically (cathodically) protected.

An organic coating, i.e. paint or lacquer, acts as a physical barrier preventing the aggressive environment from reaching the substrate; it also acts as an electrical barrier providing high resistance between anodes and cathodes after corrosion starts; finally, it may contain corrosion inhibitors that provide additional protection.

There are two types of inorganic non-metallic coatings: conversion coatings and contact coatings [10]. Conversion coatings are obtained by a controlled corrosion reaction of the metal to be coated in a suitably chosen solution. Conversion coatings therefore

always contain cations from the substrate itself, and can be obtained by anodizing, phosphatizing or chromatizing. Contact coatings, on the other hand, are prepared by a deposition process, such as plasma vapour deposition or electroplating, that do not involve a chemical reaction of the substrate. The chemical composition of such coatings is therefore independent of the substrate. Non-metallic inorganic contact coatings made of materials not related to the substrate include: enamel coatings, cement coatings and ceramic coatings.

Hybrid coatings are a novel class of materials composed of both inorganic and organic moieties, where two different phases with complementary physical and chemical properties are mixed. The inorganic component confers enhanced mechanical properties while the organic component provides an increased flexibility and functional compatibility with organic paint systems. One example is hybrid inorganic–organic sol–gel coatings, prepared by either linking of the organic and inorganic groups by stable chemical bonds or embedding the organic component into an inorganic material, or vice-versa [34,35]. An advantage of the organically modified inorganic composites is the possibility to prepare thick, crack-free coatings that can provide an effective barrier to corrosive agents. Moreover, the hybrid films can be dopped with inhibitor containing nanoparticles that improve the corrosion protection [35–38].

Recent trends in the application of protective coatings deal with designing of multi-level self-healing protective systems, that combine damage prevention and repair mechanisms, including the capture of corrosive species, corrosion inhibition and water displacement from active sites originated by local failures in protective films [39,40]. Such so called “smart” coatings are based on the controlled release of active anticorrosion species from micro or nanocontainers incorporated in the coating matrix [41]. For example, the release of inhibitors happens only after a stimulus from the environment, like, for example, changes in local pH, provoked by the onset of corrosion.

1.4 Organic coating failures as sites for localized corrosion

An organic coating acts mainly as a physical barrier preventing the aggressive environment from reaching the surface. The protection is effective until the coating loses its integrity. It may occur at film defects (i.e., pores, pinholes, voids) resulting either from insufficient surface preparation (poor surface profile, presence of contaminants), or improper film application (inappropriate angle and distance during spreading, inhomogeneous thickness), or in service, by mechanical damaging and wearing, followed by local exposure of the base metal [32,42]. In the presence of an electrolyte the coating starts to fail via localized corrosion reactions. The loss of film protective properties results

from filiform corrosion, blister formation, cathodic delamination and anodic undermining [10,42–46].

Filiform corrosion initiates at small, sometimes microscopic, scratches or defects in the organic coating related to presence of salts on the surface before paint application and high humidity environment [43,46]. The pattern of attack is characterized by the appearance of fine filaments spreading in random directions. Filaments may propagate in one direction over relatively long distances. Filiform corrosion proceeds with the same general characteristics on steel, aluminium, and magnesium. It occurs on painted plain carbon steel and aluminium sheet, coated steel cans, aluminium foil laminated packaging and other lacquered metallic items placed in areas with high humidity. The driving force for filiform corrosion is the voltage generated by differential aeration between its active head, which is deaerated and acidic, and a filamentous tail, which is aerated and alkaline [46]. A general diagram illustrating the mechanism of filiform corrosion is shown in Figure 5. Separation of anode and cathode is essential for filiform corrosion to occur. As the filiform track proceeds, the coating and metal are disbonded and the coating is lifted. The presence of oxygen is a requirement for filiform-corrosion tracks to propagate. Oxygen is supplied to the cathodic regions behind the head of the track by diffusion through the corrosion products in the tail or by cracks in the coating uplifted by the passage of the head.

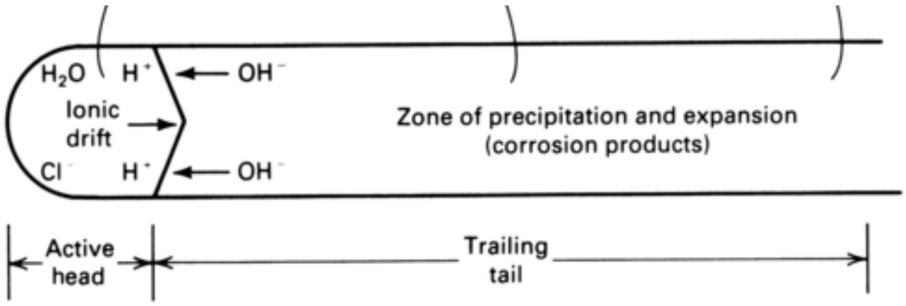

Figure 5. Scheme of the filiform-corrosion cell. Taken from [46].

Filiform corrosion does not directly affect the mechanical integrity of the structure. However, it is visually unpleasing and causes progressive degradation of the protective organic coating, which may lead to the start of more damaging forms of corrosion.

Blistering of paint films is an osmotic phenomena occurring due to the semi-permeability of organic coatings [10,42]. In places where salt contaminants are present at the interface between the metal and the paint film concentrated electrolyte is created by diffusing of water through the film. An osmotic pressure provokes more water to be transported inside. As a result, the film locally detaches from the substrate and a blister is formed. Depending on film physical and mechanical properties either the blisters grow

with time detaching ever-larger areas of the paint or, because of the internal pressure, the film cracks directly exposing the substrate. In any case the paint loses its protective properties.

Cathodic delamination is a loss of adhesion that results from pH increase due to a cathodic reaction at the metal-coating interface. For example, during the atmospheric corrosion of a coated steel, oxygen can diffuse through the paint and react not only at the defect site, but also at the adjacent paint-metal interface, making it slightly cathodic with respect to the defect [43,47]. A corrosion cell starts to form. As rust increasingly covers the defect area, the access of oxygen to the metal surface decreases. The defect area thus becomes progressively anodic relative to the paint-covered metal. The underfilm reduction of oxygen leads to an increase of the pH at the metal-coating interface which affects the bonding between paint and substrate and, as a consequence of this, to a loss of adhesion of the paint and its detachement. The same mechanism might occur when a coated metal is subjected to cathodic polarization (ex: in cathodic overprotection) and during blisters growth.

Anodic undermining is anodic dissolution of metal or its oxide leading to the loss of coating adhesion [45]. In contrast to cathodic delamination, the edges of a blister are anodic. Coating defects may cause anodic undermining, but in most cases it is associated with a corrosion sensitive site under the coating, such as a particle remaining from a cleaning or blasting procedure, or a scratch on the metal surface. These sites become active once the corrosive medium reaches the metal surface. The initial corrosion rate is low. With time, the osmotic pressure increases the soluble corrosion products that stimulate blister growth and the blister will also propagate due to the anodic reaction at its edge. Coated aluminium is very sensitive to anodic undermining, while steel is more sensitive to cathodic delamination [43].

1.5 Concluding remarks

Many forms of localized attack (crevice corrosion, pitting, intergranular attack, stress-corrosion cracking) are believed to share the same mechanism since they have in common regions with restricted mass transport, i.e., an occluded geometry of the corrosion cell. The mechanism of localized corrosion process has been considered to include initiation and propagation stages [12,27,29,30,48,49]. During the initiation period the entire surface remains passive and after an induction time localized attack is formed due to small variations in species (oxygen, hydrogen and/or chloride ions) concentration [12,50]. It has been generally accepted that the reason of propagation of corrosion at localized sites is the development of a specific extremely aggressive micro-environment

inside them [12,27,30,50]. Hence, the local solution composition changes significantly during the break of passivity in pits [12,27,29].

Similar changes in environment can be developped at dissimilar metals contacts [21,51] and in damaged areas of protective coatings [10,42,48]. It should be noted that not only electrochemical corrosion reactions are responsible for the change in the local composition of the environment. Metallic ions from the metal dissolution affect the adjacent electrolyte by taking part in reactions of acid-base, precipitation and complexation nature [27,52,53]. Thus, the local environment at the metallic surface differs from that of the bulk medium. Variables like pH, micro-galvanic effects, concentration of oxidizing and aggressive species, variations in ionic strength, deposits, hydrodynamics and temperature are determinant for the control of localized corrosion. In practice, the aqueous micro-environment is a collection of variables that can change with time and conditions, so the definition and characterization of it is important but can be quite complex.

The spatiotemporal distribution of the above mentioned variables in the micro-environment is an essential aspect in understanding and predicting metals behaviour [13]. Many scientists have mentioned about the importance of knowing local chemistry. But despite this importance little is known about it. Moreover, if the effectiveness of protective coatings is to be increased by additional functionalities, it is also essential to develop improved methods for detecting the micro size failures and predict the service life of the new coated materials.

Chapter 2

2 Localized electrochemical techniques in corrosion research

2.1 Introduction

Many methods and techniques have been applied to study and monitor corrosion [6,7,54–57] and Figure 6 gives an overview of the most significative. Electrochemical techniques can probe the thermodynamic and kinetic aspects of corrosion, including the rate of corrosion and therefore, are among the most widely used, being very suitable and versatile [55,56]. These techniques allow corrosion engineers and scientists to predict the performance of materials, plan corrosion mitigation strategies, and understand the effects of changes in production process and environment conditions. Traditionally these techniques use electrodes of millimetre or centimetre size and give the average response of the whole sample area, what makes impossible the differentiation of local anodes and cathodes on a metal surface. It is also difficult for traditional methods to describe the local processes at defects of coatings. In order to investigate these kinds of processes at the microscale, techniques with local spatial resolution are applied [57–61].

In the last three decades, a lot of effort has been made to design new equipment for the analysis of corrosion phenomena with spatial resolution [57,59,62,63]. The main results of these attempts are SRET (Scanning Reference Electrode Technique), SVET (Scanning Vibrating Electrode Technique), LEIS (Local Electrochemical Impedance Spectroscopy), SIET (Scanning Ion-selective Electrode Technique), SECM (Scanning Electrochemical Microscopy), SKP (Scanning Kelvin Probe), AFM (Atomic Force Microscopy),

- **Visual inspection**
- **Gravimetric methods**
- **Physical and chemical analysis**
- **Spectroscopic and surface characterization**
  - Scanning electron microscopy (SEM)
  - X-ray microanalysis (EDS/WDS)
  - Transmission electron microscopy (TEM)
  - X-ray photoelectron spectroscopy (XPS)
  - Auger electron spectroscopy (AES/SAM)
  - Mossbauer spectroscopy
  - X-ray diffraction
  - Infrared and Raman spectroscopy
- **Atomic force microscopy (AFM)**
- **Scanning tunnelling microscopy (STM)**
- **Optical methods**
  - Optical microscopy
  - Ellipsometry
  - Reflectance measurements
- **Thermometric and calorimetric methods**
- **Radiochemistry and isotopes**
- **Acoustic methods**
- **Electrochemical methods**
  - OCP monitoring
  - Polarization resistance
  - Polarization curves
  - Cyclic voltammetry
  - Electrochemical impedance spectroscopy (EIS)
  - Electrochemical noise
  - Microelectrodes and scanning probe techniques
  - Sensors
- **Spectroelectrochemical methods**
- **Others**

Figure 6. Methods used for study and monitor corrosion.

SKPFM (Scanning Kelvin Probe Force Microscopy), WBE (Wire Beam Electrode), Microdroplet and Microcappilary cells (Figure 7).

These localized electrochemical techniques can provide information on the surface chemical composition, structure, topography, defects, mechanical and electronic properties, and kinetic data about the corrosion process at nano and/or microscale (Table 2). Thus, scanning probe techniques (SRET, SVET, LEIS, SIET, SKP, SKPFM, and SECM) used to investigate the behaviour of immersed samples, measure the local distribution of one or several corrosion parameters. The experiments might be performed at OCP (open circuit potential) or under potential or current control. However, many scanning methods do not allow assessment of the local corrosion currents on the metallic surface.

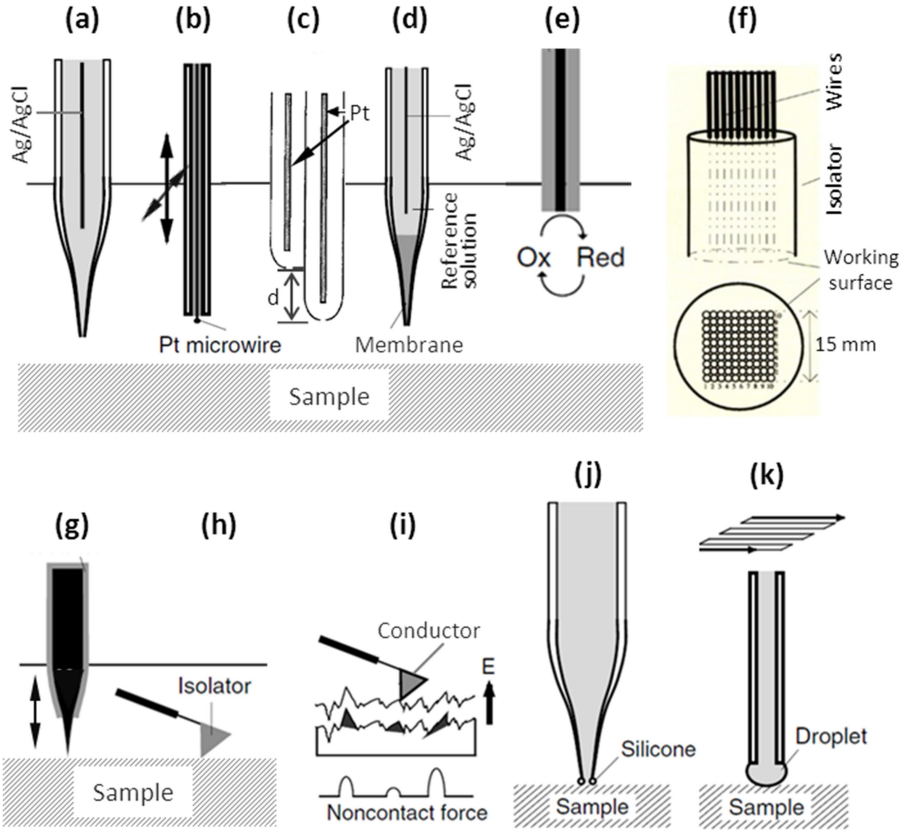

Figure 7. Techniques used to study localized corrosion at the micro/nanometer range: (a) SRET; (b) SVET; (c) LEIS; (d) SIET; (e) SECM; (f) WBE; (g) SKP; (h) AFM; (i) SKPFM; (j) microcapillary cell; and (k) microdroplet cell. Adapted from [64].

The SRET measures either the local electrode potential (if the probe is connected to the sample) or the potential distribution in solution (if the probe is connected to another RE at fixed position). The potential in solution arises from the flow of ions produced on the surface during chemical/electrochemical reactions and allows quantifying the local current density from the electrical field and the solution conductivity [82].

Table 2. Localized techniques used in corrosion research.

Technique	Description	Reference
AFM	Measures mechanical contact forces, Van der Waals forces, capillary forces, chemical binding, electrostatic forces, magnetic forces, Casimir forces, solvation forces, etc. during scanning the surface by a sharp tip placed on the end of the cantilever. Changes in tip oscillation provide information on surface topography and surface atomic structure. It is well suited for (sub)micrometer scale studies of dissolution and dealloying, of effect of adsorbed species structure on state of surface (inhibition and passivation), of surface defects role in passivity breakdown and of surface heterogeneities role in pit initiation.	[65–67]
LEIS	Measures potential differences in solution that result from local current distributions while applying an AC potential perturbation to the substrate. The local AC current flow through the electrolyte just above the substrate surface is then obtained to determine local impedance values.	[68–70]
Microcells	Potentiostatic or potentiodynamic measurements, galvanostatic measurements, and cyclic voltammetry, can be applied to the microscopic delimited surface areas of substrate.	[58,81, 82]
SECM	The most common mode of application is based on measurement of electrode currents (at a tip or at a substrate) as function of various parameters, including tip-substrate distance and tip or substrate potentials. Applied for imaging and study of early stages of localized corrosion, electroactive defect sites in passive films, local initiation of pits, degradation of coating properties and chemical identification of species.	[73–75]
SIET (ISME)	The potential of ISME is measured versus reference electrode under zero current conditions in the cell and is used to determine the activity of a given ion in solution according to Nernst equation or upon a calibration, i.e. to acquire chemical information about solution composition.	[76,77]
SKP	Measures distribution of Volta potential differences between tip and substrate through insulating dielectric media, such as air or polymeric films. Provides direct access to corrosion potentials. It enables direct information about distribution and activity of local cathodes and anodes and how these are affected by substrate composition and inhibitors in the solution. Successfully applied for investigating atmospheric corrosion and coating delamination.	[55,74, 75]
SKPFM	Simultaneously provides topographic and Volta potential maps of the surface. Involves scanning the sample in tapping mode to determine the topography. The metal-coated or doped silicon cantilever is then lifted a fixed distance from the surface, and the tip is rescanned in “lift” mode. On the rescan an AC voltage is applied to the tip, which stimulates oscillations of the cantilever in the presence of an electric field. Similar to SKP but with higher spatial resolution.	[80,81]
SRET	Measures either local electrode potential or potential differences in solution related to the flow of current and allows quantifying the local current densities from the potential measurements.	[82–84]
SVET	Makes use of a probe vibration and a lock-in amplifier to measure local potential differences associated with ionic currents in solution.	[84,85]
WBE	It consists of a number of small wires (4-100 typically) to mimic a large electrode but providing local quantities. Potentiostatic or potentiodynamic measurements, galvanostatic measurements, and cyclic voltammetry, can be applied to WEs of small area.	[86–88]

The SVET is a more sensitive method for measuring the potential difference due to the use of a lock-in amplifier. SVET and SRET show the potential and current distribution in solution without identifying the nature of the responsible species.

The SECM is a powerful technique for probing electrochemical reactions in the corrosion process due to its high spatial resolution and sensitivity to characterize the topography and redox activities at the metal/electrolyte solution interface. It is also capable for the direct identification of chemical species in localized corrosion processes. Depending on the type of the sensing probe, the SECM can be broadly split into amperometric, if an ultramicroelectrode (UME) is used, and potentiometric, if the probe is an ion-selective microelectrode (ISME).

The electrochemical microsensors, i.e. ISMEs and voltammetric microsensors, have been used for gathering microscale chemical information in solution since the middle of the 1950s [76,89–92]. Application of electrochemical microsensors for spatial species detection during corrosion process has been implemented at least since the beginning of the 1970s [12]. Several akin methodologies were described in literature: micropotentiometry [93–97], potentiometric SECM [98–100], LICT (Local Ion Concentration Technique) [101], SIET (Scanning Ion Selective Technique) [102–105], MIFE (Microelectrode Ion Flux Estimation) and SERIS (Self-Referencing Ion-Selective probes) [106] on one side, and microamperometry [96,97], SLCP (Scanning Diffusion Limited Current Probe) method [107] and amperometric SECM [108,109] on the other side. To avoid misunderstandings in terminology, the acronym “SIET” is used in this work to indicate ISMEs based methods, and therefore the acronym SECM is considered for an amperometric technique, in which a faradaic current at an UME is measured when it is held or moved in a solution in the vicinity of a substrate surface.

The development of AFM by Binning, Quate and Gerber in 1986 and related techniques has enabled the evaluation of physical and chemical properties at submicrometer scale. AFM permits *in situ* measurements of various types of contact forces to provide quantitative information regarding the topography of a surface.

SKP is a noncontact technique that maps distribution of Volta potential differences (VPD) in the vicinity of the corroding specimen in the presence of a film or a drop of electrolyte or in humid air. The application of SKP to corrosion is due to Stratmann [78]. VPD can be correlated with the corrosion potential [78]. The standard SKP, however, has not high enough spatial resolution necessary for probing the submicroscopic defects. To overcome this, SKPFM, which combines SKP and AFM, has been used [81]. The VPD correlation to the electrochemical activity of metals can be used for analysis of the corrosion susceptibility and localized corrosion behaviour of metals and alloys. Nevertheless, compared to the standard SKP technique, SKPFM is prone to much more artefacts, which are often not taken into account in the interpretation of the results [80].

Moreover the resolution of these two methods is strongly dependent on the distance between the tip and coating/metal interface, what requires the preparation of special model samples with ultrathin coatings and specially prepared defects [110].

The small-area techniques (WBE, microcapillary and microdroplet cells) provide the possibility of application the common electrochemical techniques, for example, potentiostatic or potentiodynamic measurements, galvanostatic measurements and cyclic voltammetry in microscopic areas of the surface. Local corrosion currents can be evaluated directly.

Although a significant progress in the localized chemical analysis of surfaces has been achieved in the last decades, success in micro-scale measurements providing information about the chemical nature and concentration of species on the solution side of the interface is much more modest. Meanwhile, the knowledge of the micro-spatial distribution of the ions is of great importance for understanding the intricate mechanisms of the processes in electrochemistry, corrosion [103,105,111,112], coating science [113–117], biochemistry and biology [118–120]. That is why the focus will be given to techniques based on electrochemical microsensors (SIET and amperometric mode of SECM) capable to achieve spatial species distribution during local corrosion processes. SRET and SVET will also be used as complement tools to more clearly present the results of the cases studied.

2.2 SRET and SVET

2.2.1 Historical outline

The early idea of measuring potential variations in the solution close to metallic surface appeared at the end of 1930s in works of Thornhill and Evans [121,122] and Agar and Evans [123]. For investigating water line corrosion of zinc, iron and steel a manually scanned reference electrode ending in a Luggin tubulus was used. This electrode measured the potential in solution as a function of position relative to other reference electrode fixed at several centimetres away from the sample surface. The flowing current in solution was obtained from the measured equipotential lines with 10% agreement to that measured by weight loss [123].

Following the same concept in 1943 Copson determined the distribution of galvanic corrosion in nickel-steel plate immersed in tap water [83]. The steel plate was 305 mm x 813 mm x 6.4 mm with 10% nickel cladding (0.64 mm thick) on one side. The machining exposed a 305 x 203 mm^2 area of steel in the middle of the plate, remaining 305 x 305 mm^2 of nickel areas on each side. The plate was immersed horizontally and inclined at an angle of 30° to provide complete immersion without touching the tank. The potential

measurements were made with a moving saturated calomel electrode with a Luggin tubulus in a vertical plane intersecting the plate along its longitudinal axis versus a saturated calomel electrode mounted in a fixed position in the centre of the bare steel area. The potential distribution in solution is presented in Figure 8 together with equipotential lines.

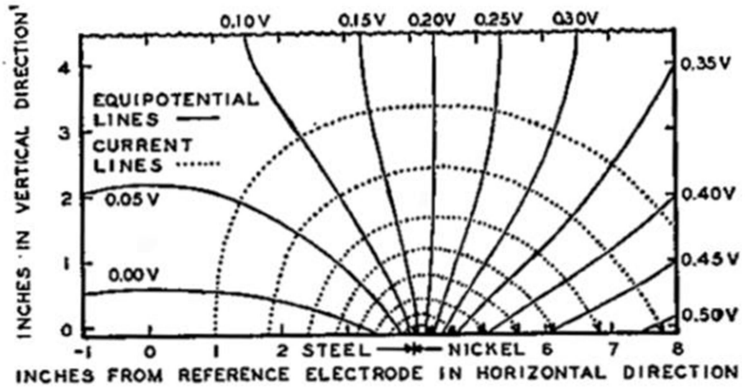

Figure 8. Potential and current distributions above nickel-steel couple determined by Copson. Taken from [83].

The equipotential lines actually represent the section of a set of equipotential surfaces cut by the vertical plane. To know the approximate current distribution above the sample, calculations were done based on an element of the equipotential surfaces presented in Figure 9.

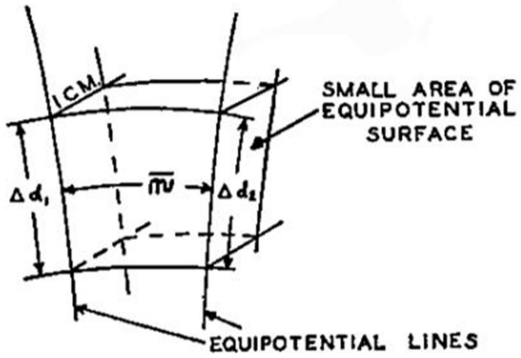

Figure 9. Element of equipotential surfaces. Taken from [83].

The current density i flowing between the two equipotential surfaces of lengths Δd_1 and Δd_2, extending for 1 cm perpendicularly to the vertical plane and separated by distance $\bar{n}$, is given by

$$i = k\frac{(\Delta d_1+\Delta d_2)\Delta V}{2\bar{n}} \qquad (2.1)$$

where k is the medium conductivity and ΔV is the potential difference between the equipotential surfaces. If the equipotential surfaces are divided into small areas such as the ratio of their length to the distance between them is unity, i.e.

$$\frac{\Delta d_1+\Delta d_2}{2\bar{n}} = 1 \quad (2.2)$$

then the Equation (2.1) reduces to

$$i = k\,\Delta V \quad (2.3)$$

The segments of equipotential lines complying with Equation (2.2) can be seen on Figure 8. The dotted lines show current density components in vertical plane, and the current value on each segment is the same. The current lines intersect the equipotential lines at right angles.

In the general case, the potential difference (ΔV) measured between two points distanced by (Δd) in a solution with a resistivity ρ ($\rho = 1/k$) is related to the local current density passing between them through equation [85,124]:

$$i_{local} = \frac{\Delta V}{\rho \cdot \Delta d} \quad (2.4)$$

Other scientists have applied this concept to evaluate equipotential lines and current densities in solutions around galvanic couples of copper-zinc [125] and copper-magnesium [126] and during localized corrosion of stainless steel [82,127] and aluminium alloys [128].

Over the years there have been two ways for making local potential measurements [57,82]. In the first method, similar to that of Evans, potential data are collected by an electrometer that measures the potential difference between the scanning (either a noble metal wire or a reference electrode with a Luggin capillary) and the fixed reference electrode. In the second method the scan is made with two noble metal electrodes at a constant and known small separation distance [127,129]. As this bi-electrode set-up is moved across the sample surface, the measured potential difference between the two wires then is multiplied by the solution conductivity in order to readily obtain the current densities.

2.2.2 SRET

The term SRET was coined in 1981 by Isaacs and Vyas in a review [82], where the principles, advantages and several cases of potential mapping in solution were described. The expansion of SRET application in corrosion studies had occurred in the 1980s due to improvement of data recording [82,128,130,131] and introduction of computer control into the experimental set-up [132–135].

In spite of becoming a valuable approach for *in situ* determination of local corrosion activities, SRET has limited sensitivity and resolution while measuring rather small local potentials [82]. SRET sensitivity to local current distributions depends on tip/sample separation distance, which can be minimized by reducing the tip size [82,129]. Smaller probe diameter also provides better resolution. However, decreasing the tip size increases the electrical noise due to high tip impedance [82]. To avoid this problem, investigators commonly coat the probe tip with platinum black to increase the surface area exposed to solution. In addition, stepper motors are chosen instead of servomotors to pick up less noise. Nevertheless, the current density values given by SRET present significant noise, which became even more notable with increasing solution conductivity [136]. This can be overcome by making the probe vibrate, what was proposed by Isaacs and Ishikawa [85], and in fact was already being done in biology. That is the principle of the Scanning Vibrating Electrode Technique (SVET).

2.2.3 SVET

SVET is based on instruments known as *Vibrating Probes* that originally were applied in biology between 1950s and 1980s for measuring ionic currents produced by living cells and tissues [137–141]. One of them is an equipment from Applicable Electronics Inc. (AEI), USA [142]. It was developed during the 1980s in the Marine Biological Laboratory (Massachusetts, USA) by Scheffey group [141,143]. Improvements of this system and its commercialization by Shipley [142] and Karplus [144] (former technicians at Marine Biological Laboratory) promoted the expansion of the technique in the biology and life sciences areas as well as in the corrosion field. A few other systems were developed in different laboratories later [145–148]. Nowadays several commercial instruments are available in the market. The ones from Applicable Electronics Inc., USA and from Uniscan Instruments Ltd., UK [149] were commercialized firstly, lately VersaSCAN SVET from Princeton Applied Research, USA [150] and SCAN-LAB workstation from Bio-Logic SAS, France [151] became also available.

2.2.3.1 Working principles

The objective of the SVET is the same as of the SRET, the measurement of potential gradients that develop between anodic and cathodic areas as a consequence of current flow in solution (see Figure 1). A schematic view of the potential and current distribution above the surface of a local anode is shown in Figure 10. Current lines intersect the potential lines perpendicularly.

When a small probe is vibrated at a certain frequency above the sample surface, the potential difference (ΔV) between the two positions of vibration (Δd) in the electrolyte is measured. Typically, in the SVET from AEI the probe is vibrated in two

directions, perpendicularly and parallel to the surface, to determine individual components of the electrical field. The vibrating probe converts the measuring signal into AC voltage with the same frequency as the vibration. A lock-in amplifier extracts the component related only to the vibration frequency and filters any other interference increasing the signal to noise ratio [85]. Thus the sensitivity to small current values compared to SRET is higher.

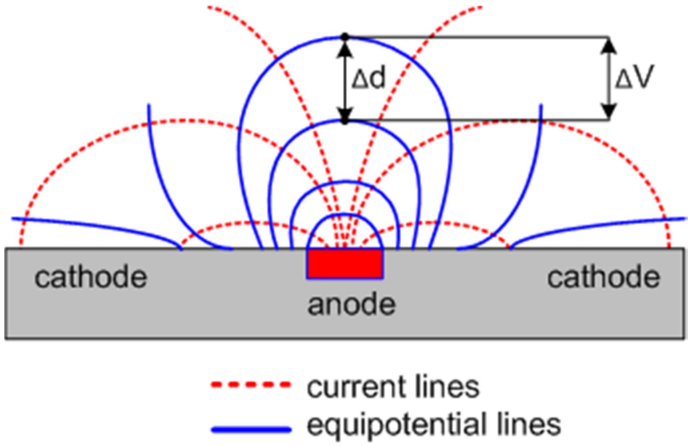

Figure 10. A schematic view of the potential and current distribution above the surface of a local anode. Adapted from [58].

In order to quantitatively use the measured potential gradients for getting the local current densities, a prior calibration procedure is necessary. For this purpose the probe is usually placed at a known distance from a point current source, which can be a polarized metal wire or a glass capillary filled with an electrolyte and a Pt wire inside. The local current density, i, at a distance, r, from the point source of current, I, is given by the following equarion [141]:

$$i = \frac{I}{4\pi r^2} \qquad (2.5).$$

The system measures the potential differences and determines the factor of proportionality for current density, i. This factor depends on solution conductivity, frequency and amplitude of probe vibration.

To scan a sample, the technique uses a 3D computerized stepper-motors system that controls the movement of the probe above the surface. A map of localized currents is obtained when scanning the sample in (X, Y) plane at a fixed probe - sample separation distance. The resulting data allows the location of anodic and cathodic sites, areas of low/high activities or even defects in a coating. In other words SVET visualizes corrosion processes on metal substrates and therefore is very suitable for receiving *in situ* data at microscale.

2.2.3.2 Limitations of SVET

Besides pioneering works of Isaacs related to the theoretical aspects of SVET measurements [85,152–154], its resolution, sensitivity and limitations were investigated in others studies [136,141,155–157]. For example, some important restrictions are described by Bastos *et al.* when it is intended to extract quantitative information from SVET results [136]. Thus, for determination of current flowing on the sample surface in order to get a corrosion rate value, the currents in all positive (alternatively, negative) points should be integrated, from where the sample current results. The total current then is divided by sample's area giving sample's current density. Obtained in such way positive and negative currents should be self-compensated. This procedure, however, seldom provides acceptable values due to four main reasons:

i) As measurements are carried out at a distance from the sample surface, the technique doesn't count the current that flows between anodes and cathodes below that distance, as it is schematized on Figure 11a.

ii) A current, that arises and crosses the measurement plane, returns to the surface crossing the plane once more in opposite direction. The current return can occur out of the mapped region, and therefore it is not measured (Figure 11b). This is the case of much localized intensive anodic currents, surrounded by larger cathodic areas with small current values.

iii) The noise level for SVET in typical solutions of 0.01-0.1 M NaCl is about 1 µA cm^{-2}. This means that smaller current values are not detected.

iv) The current flows in three directions, but usually the current density component in Z is used (Figure 11b), which implies the measured current is almost always being underestimated, and rarely positive and negative currents are self-compensated.

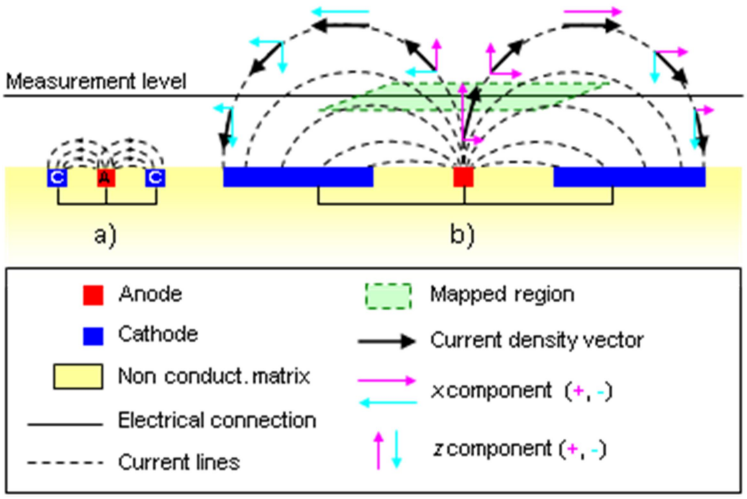

Figure 11. Scheme of current density measurements limitations by SVET. Adapted from [136].

Due to these limitations SVET is not an appropriate method for estimating corrosion rates, because the obtained values will present high level of uncertainty. SVET should be considered as semi-quantitative method for local corrosion visualization and imaging.

2.2.4 Applications in corrosion research

Reviews about scanning microprobe techniques were performed in 2000s by Grundmeier *et al.* [58], Kaesche [158] and Lillard [84]. They assessed the historical outline as well as basic principles, technical developments and detailed description of numerous applications of SRET and SVET. In biology, SVET was used in plant cytology [106], animal embryology [159], and also for some medical applications [160,161]. In corrosion research the SVET has been used extensively, either as a unique method or in combination with others techniques, to investigate passive systems [162], galvanic couples [146,163,164], cut-edges of pre-painted systems [103], corrosion inhibitors [37,96,165–168], coating defects [152,169–171] and self-healing effects [113,170,172].

Isaacs has used SVET to characterize defects in ion vapor-deposited aluminium on steel in a borate solution (pH 8) [152]. The SVET enables to locate defects in the coating indicated by areas of high anodic or cathodic activity. To accomplish this, the surfaces were mapped at potentials where hydrogen or oxygen evolution readily occurs on steel and not aluminium. These potential regions were determined by generating the potentiodynamic polarization curve for bare steel and bare aluminium in borate solution. Once a defect was located, a local potentiodynamic polarization curve for the defect was made by ramping the potential of the electrode and measuring the current from the defect locally with the probe. The polarization measurements of the defect sites showed that they were not a result of exposed steel but were caused by the presence of inclusions. Energy dispersive spectroscopy of the areas of anodic activity located by SVET found that these sites were, in fact, inclusions in the coating primarily comprising Si, Ca, and Ti.

Kallip and co-wokers showed a promising approach for high-throughput screening of corrosion inhibitors based on SVET and a multi-electrode cell [168]. The method has the advantage of saving time and materials. The cell is constituted by wire electrodes from different metallic materials embedded in insulating resin and not connected. SVET measurements were carried out above each metal electrode to monitor the local currents in solution. When inhibitors are added to the test electrolyte their protection efficiency can be evaluated for the different materials in a single experiment. Two ways of inhibition efficiency evaluation were described. It was concluded that the use of the integrated values of ionic currents is in principle more reliable than the maximal currents. In the cases of low uniform and strongly localized corrosion, the maximal anodic ionic current

can give additional information such as the degree of localization of the attack. This method is sufficient and fast for preliminary selection when a large number of metals/inhibitors/concentrations have to be analysed.

Another noteworthy application of SVET was given by Thébault *et al.* [172]. Local cathodic inhibition has been observed on the cut-edge of galvanized steel immersed in 0.03M NaCl solution. The SVET measurements and polarization curves were complement with numerical simulation. The current distribution measurements over the cut edge of galvanized steel have revealed three distinct kinetic regions: an anode localized over the zinc surface, a region of partial inhibition of the oxygen reduction and the cathodic area on the opposite side of the steel. The cathodic zone was covered by loose white corrosion products which appear to have simply been deposited on the surface, probably due to precipitation in the bulk solution. A wavy line of dense particles separated the inhibition zone and the cathodic zone. The inhibition was attributed to the formation of a zinc-based oxide film at the steel surface, formed during the very early stages of the immersion when the current densities were at a maximum and controlled by an increase of the interfacial pH. The numerical simulation correlated well with the experimental results.

2.3 SECM

SECM was introduced in the end of 1980s by Bard and co-workers [74,75,173] following previous work from Engstrom *et al.* [174–176]. During the next decade the SECM studies were dedicated mainly to proof-of-concept till the appearance of the first commercial instrument in 1999, then SECM has evolved substantially [177]. In 2000s the SECM turned into a powerful electrochemical technique used to study heterogeneous and homogeneous reactions, for high-resolution imaging of the chemical reactivity and topography of different interfaces, and for microfabrication. Due to availability of various operational modes to characterize electrochemical activities SECM has proved useful for a wide range of interdisciplinary research. Current application of it includes studies of single biological cells, corrosion research, electrocatalysis and combination with others localized techniques [73]. A comprehensive review about the different aspects of SECM was published by Bard and Mirkin in 2001 [177] with a second edition in 2012 [73]. It describes in detail the principles, instrumentation, tip preparation, imaging methods and theory, together with de description of most important applications of SECM in different areas of research.

2.3.1 Principles of operation in amperometric mode

SECM amperometric methods are based on the measurement of electrode currents (at a tip, i_T, or at a substrate, i_S) as function of various parameters, including tip-substrate distance (d) and tip or substrate potentials (E_T or E_S) [73]. The amperometric tip is an UME that can be positioned in the vicinity of the sample surface. The UME is an electrode with a radius of the order from a few nanometers to 25 µm, fabricated as a conductive disk of metal or carbon in an insulating sheath of glass or polymer (Figure 12). The electrochemical cell also contains a reference electrode, such as silver/silver chloride electrode, and an auxiliary electrode that completes the circuit via power source.

The behaviour of UMEs in the bulk solution (a few tip diameters from the substrate) has been well investigated [90,178]. When a negative polarization is applied, a reduction of electroactive species O from solution takes place at the tip (Figure 12A)

$$O + ne^- \rightarrow R \qquad (2.1)$$

resulting in current flow. The transport of species O to the electrode surface occurs mainly by diffusion. To reduce or eliminate migration currents, supporting electrolyte is added to solution. Then, the diffusion of O leads to a steady-state current at the tip, $i_{T,\infty}$, independent of small changes of applied potential. For a UME disc it can be calculated as follows [73]

$$i_{T,\infty} = 4\,n\,FD\,r\,C \qquad (2.6),$$

where n - number of electrons for the electrochemical reaction 2.1; F – Faraday constant; D – diffusion coefficient of species O; r – radius of the UME tip; C – concentration of species O in the solution.

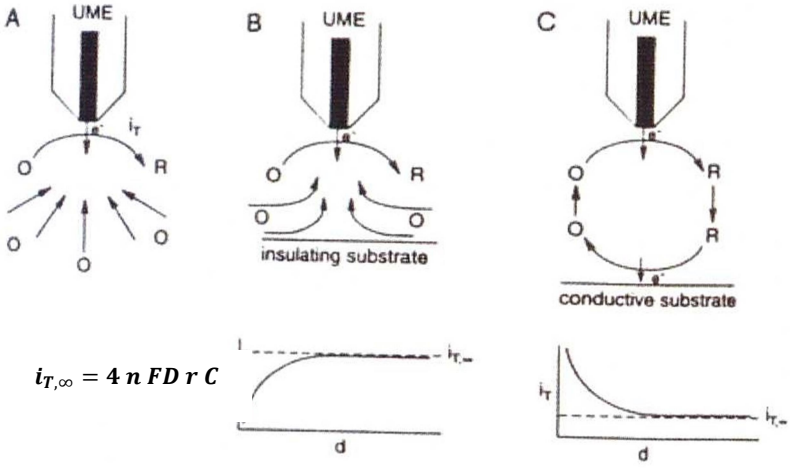

Figure 12. Operating principles of SECM. A) Hemispherical diffusion of O leads to a steady-state current, $i_{T,\infty}$; B) Hindered diffusion of O leads to $i_T < i_{T,\infty}$; C) Feedback diffusion of O leads to $i_T > i_{T,\infty}$.

A plot of i_T vs. *d*, i.e. when an UME moves in Z direction, is called an approach curve. At close proximity of a sample surface the tip current is perturbed. If the tip is moved toward the surface of an insulating substrate, the tip current decreases compared to $i_{T,\infty}$ because the tip sheath blocks diffusion of O from the bulk solution to the tip (Figure 12B). The closer the tips goes to substrate the smaller the i_T becomes (this is called *negative feedback*). In another case, with a conducting substrate polarized at a potential, where the species R can be oxidized back to O (Figure 12C), the current i_T increases as the tip approaches the surface. An additional diffusion flux of O to the tip is produced and the smaller the value of *d*, the larger i_T will be (*positive feedback*). In the limit, when the UME approaches the surface, i.e., $d \to 0$, electron tunnelling can occur and the tip current will be very large, i.e. $i_T \to \infty$. When the tip is shifted in the X-Y plane above the substrate at a fixed height, the tip current variation represents changes in topography or conductivity (or reactivity). This is the basis of the most frequently used *feedback mode* of SECM operation, which was described by Kwak and Bard, along with the apparatus and theory, in a series of papers in 1989 [74,75,173].

Other set of SECM operation modes is called *generation-collection* [177]. In the tip generation– substrate collection mode (TG/SC), the tip is used to generate a reactant that is detected at a substrate electrode. TG/SC mode is usually used in studies of homogeneous chemical reactions, where the reaction of species R (as it transits between tip and substrate) causes a decrease in the substrate current. When the substrate is a generator and tip is a collector (SG/TC), the tip travels within a thin diffusion layer generated by the substrate electrode. The SG/TC mode was first used to study concentration profiles near an electrode surface without scanning and imaging [174–176]. There are some shortcomings which limit the applicability of SG/TC mode when investigating large substrates: a) the process at a large substrate is non-steady state; b) a large substrate current may cause significant iR-drop; and c) the collection efficiency, i.e., the ratio i_T/i_S, is low. The tip generation – substrate collection mode is advisable for kinetic measurements, while SG/TC mode is used for monitoring enzymatic activity, species detection, corrosion reactions and others heterogeneous processes at the substrate surface.

2.3.2 SECM application for amperometric detection of chemical species

Several reviews and monographs about SECM applications in corrosion research can be found in literature [62,179–182]. These works describe and summarize SECM imaging of early stages of localized corrosion, electroactive defect sites in passive films, local initiation of pits by local generation of aggressive ions such as Cl^- and Br^-, degradation of coating properties and improvement in information acquisition through SECM integrated with other techniques. SECM capability for the direct identification of

chemical species (their nature and concentration) in localized corrosion processes has been seldom implemented in routine studies, despite this is of great interest for corrosion scientists. Several examples of such SECM application will be given below.

The SECM amperometric detection of chemical species is based on the substrate generation – tip collection mode. The tip current is measured at fixed potential, at which electroactive species will undergo redox reaction. The measured current is diffusion limited and proportional to the concentration of analyte in solution (Equation 2.6). Thus, the concentration distribution of various species, relevant for corrosion, such as metal cations (Fe^{2+}, Fe^{3+}, Zn^{2+}, Cu^{2+}, Ni^{2+}, etc.), O_2, and H_2 can be measured above active regions by using SECM tips or an appropriate amperometric microsensor [89,90].

Kupper and Schultze used amperometric microsensors (Pt microdisk electrodes, 20 µm tip) while studying the electrodeposition of a Cu-Ni alloy [107]. They combined chronoamperometry with scanning and positioning sets and called the method "Scanning Diffusion Limited Current Probe". The detection of local concentration of Cu^{2+} or Ni^{2+} at constant height z above the surface, vertical concentration profiles normal to the electrode surface and time resolved concentration measurement were done. Simultaneous local concentration measurement of Cu^{2+} and Ni^{2+} ions was performed with potential/time programs at two deposition potentials.

Tada *et al.* determined the Zn^{2+} distribution in 0.01M NaCl above a zinc-steel couple [108]. The sensor was a scanning zinc disk electrode (Ø 0.5 mm) embedded in glass capillary of 1.6 mm diameter. It was observed, that during galvanic corrosion, marked changes in the Zn^{2+} concentration were confined to a thin solution layer ca. 1.0 mm thick above the couple surface. A high Zn^{2+}concentration region in the range of 5–18 mM occurred around the zinc layer, while above the steel surface distant from the zinc layer, the concentration of Zn^{2+} was almost zero during galvanic corrosion. On this surface, the precipitation of zinc corrosion products due to the hydrolysis reaction of Zn^{2+} was noticed. Authors stated that according to the distribution of the Zn^{2+} concentration, Zn^{2+} suppressed the increase in pH due to the cathodic reaction on the steel surface near the zinc layer, where almost no corrosion products formed.

Microelectrodes (ME) as amperometric sensors for dissolved oxygen have been used for decades in biology, medicine, analytical chemistry and environmental sciences [89,90,92,183]. Small size "Clark-type" oxygen sensors are reliable and the most commonly used devices for measuring oxygen content [184]. They are based on an integrated three-electrode cell insulated in glass. A semipermeable membrane protects the Pt tip against interference from the medium. After diffusing through a KCl solution oxygen is then reduced at the Pt disc. The stability of the signal was later improved by Revsbech by using an internal silver guard cathode [185]. Such microsensors are rather

complicated in fabrication, despite being miniaturized. An alternative is platinum or gold recessed discs [186,187].

One of early works about measuring dissolved oxygen at metal/liquid interfaces using microelectrodes was reported by Lewandowski in 1989 [188]. Tests were performed in artificial seawater with biotic and abiotic systems in order to evaluate the effect of electrochemical and/or biological reaction products on the conditions at the metal surface.

Bastos *et al.* measured concentration profiles of dissolved oxygen and Fe^{2+} while studied degradation of pure iron in naturally aerated 0.1M NaCl solutions [109]. The used UME tip was a 10 µm Pt wire positioned 20, 40, 100 or 200 µm above the sample. During the immersion of pure iron in a neutral aqueous solution, the potential of the UME tip was set to either detect the Fe^{2+} ions originating from the electrodissolution of iron at the anodic sites on the metal surface, or the depletion of oxygen in the electrolyte in the proximity of the corresponding cathodic sites. The effects of tip position to measured current values were discussed.

Among new types of voltammetric probes the ones designed by Silva and co-workers appear to be very attractive for corrosion studies [189]. Boron-doped nanocrystalline diamond (B-NCD) films obtained by the hot filament chemical vapor deposition technique on top of sharp electropolished ≈1 µm tungsten wires are robust, stable and rather reversible amperometric MEs for detection of Zn^{2+}(aq) and dissolved O_2 with high spatial resolution. The B-NCD microelectrodes exhibited a working potential window of about 3.5 V in 5 mM NaCl, with low background current and good chemical inertness. The linear relationship between zinc concentration and zinc reduction current was found in 10^{-5} M–10^{-2} M concentration interval of $ZnCl_2$ in 5 mM NaCl background. Measurements above Fe–Zn galvanic couple immersed in 5 mM NaCl demonstrated the decrease of O_2 near both metals and zinc cations production at the anode. The main observed drawback of B-NCD microelectrodes consisted in a significant deposition of metallic zinc during Zn^{2+} detection.

2.4 SIET

SIET (Scanning Ion Selective Electrode Technique) is just another name of a set up for potetiometric measurements with ion selective microelectrodes. SIET measures the ions activities while potentiometric microelectrodes are moved at a constant distance over the active surface immersed in solution. A two electrodes electrochemical cell, composed of a reference electrode and an ion-selective microelectrode, under zero current conditions, is used to perform potentiometric measurements.

The use of potentiometric microelectrodes has been known for more than 50 years as demonstrated by the large number of applications in different research areas [76,89,90]. Before ion-selective microelectrodes became interesting for corrosion scientists, the glass-capillary microelectrode with liquid membrane was introduced by life scientists [190]. Similar techniques, Microelectrode Ion Flux Estimation (MIFE) and Self-Referencing Ion-Selective probes (SERIS) have been used in microbiology for studying membrane-transport processes [106]. The MIFE and SERIS estimate ion fluxes by vibrating the ion-selective microelectrode with a frequency of 0.3 to 0.05 Hz. Since then, microbiologists have kept developing pipette preparation, instrumentation and experimental approaches for micropotentiometric research [183,191,192]. Today, glass-capillary microelectrodes are well established analytical devices. The principles of experimental work with microelectrodes are summarized in references [76,77,193]. A brief chronology of ISMEs development, potentiometric theory, as well as microelectrodes sensitive to relevant corrosion species are described in Chapter 3. Applications of ISMEs in electrochemistry and corrosion are now presented.

Lately, measurements with glass capillary and all-solid-state micro- and nano-electrodes became an actively developing area [77,103,105,111,112,194,195]. Profiles and gradients of concentration of pH, Ca^{2+}, K^{+}, NH_4^{+}, Cl^{-} by potentiometric sensors above biological specimens [118–120,195–197] and potentiometric SECM mapping of Zn^{2+}, K^{+}, NH_4^{+} and Cl^{-} in model systems have been reported [179,198].

In corrosion, Park *et al.* used pH-selective microelectrodes to measure hydroxide ion concentration fields produced by electrochemical reduction of oxygen on 10 and 25 µm Pt disk electrodes [102]. The results were compared with calculations of OH^{-} concentration from oxygen solubility in water. The largest differences between the experimental and theoretical hydroxide concentrations occurred at the center of the disks with the difference of pH 0.18 for 10 µm disks and pH 0.07 for 25 µm disks. The pH microelectrode was also used to verify the distribution of hydroxide ions generated above Al_3Fe-Al 6061 galvanic couple at the rest potential in 0.6 M NaCl. The detected buildup of hydroxide ion over Al_3Fe provided evidence for cathodic reaction over the intermetallic. The last can lead to the dissolution of the aluminium matrix around the intermetallic and pitting initiation.

Tada *et al.* studied the pH variation using a scanning tungsten pH electrode in a zinc-steel galvanic couple immersed in 0.01M NaCl [95]. The couple consisted of a steel substrate with a 3 µm-thick layer of zinc electroplated at its centre. During galvanic corrosion, marked changes in pH occurred in a thin layer of solution ca. 1.5 mm over the couple surface. As the surface was approached, the pH over the zinc layer decreased slightly from ca. 5.6 in the original bulk solution, while the pH over the steel surface distant from the zinc layer increased to ca. 11.5. The area of low pH was detected not

only over the zinc layer, but also over the steel surface adjacent to the zinc. Zinc corrosion products precipitated in the region of high pH.

The utilization of scanning potentiometric microsensors in corrosion research is very often accompanied by other techniques, i.e. SRET/SVET, SEM/EDS, EIS, etc. [103,105,171,199,200]. Thus, chloride ions, pH and potential distributions were investigated by Luo *et al.* in pitting on nickel and steel [93,94]. Alvarez-Pampliega and co-workers mapped pH, Cl^- or Na^+ distribution simultaneously with monitoring current density by SVET over the cut-edge of aluminium-rich metal-coated steel [200]. Depletion of Cl^- in anodic sites and its accumulation in cathodic sites, along with an increase of Na^+ concentration in anodic sites and Na^+ decrease in cathodic sites over the steel were observed. The described Cl^- distribution, explained by the formation of Cl^- and OH^- containing corrosion products and charge compensation effects, was partly confirmed by ex situ analysis of corrosion products performed by SEM-EDX and Raman spectroscopy [200].

In another work Ogle *et al.* combined SVET measurements with local pH measurements when studying a cut-edge of a pre-painted metal system (coil-coating) [103]. Local anodic and cathodic current densities corresponded with that anticipated from mixed potential theory; the current densities over Fe regions were cathodic while current densities over the electro galvanized Zn were anodic. Measurements of pH above the sample indicate that the Fe regions were predominately alkaline (pH 10) in comparison to the near neutral Zn region (pH 7.6). The alkaline pH over the iron electrode and the precipitation of Zn in this region was consistent with cathodic reduction of oxygen dissolved in water. Current density maps at the OCP after a period of immersion revealed the lack of activity at the Fe surface where hydrated Zn oxide films had precipitated. This fact was further confirmed through local polarization curves generated with SVET. Thus, it was concluded that Zn corrosion products act as cathodic inhibitors further protecting the electro galvanized steel.

A combination of SVET and pH-SIET was applied by Ding and Hihara to investigate localized corrosion of aluminium-based metal matrix composites (MMCs) [105]. The studied material was a particulate 6092-T6 Al, reinforced with 20 vol. % of B_4C, SiC, and Al_2O_3 immersed in 0.5M NaCl. According to the results, the extent of localized corrosion on the MMCs appeared to increase with decreasing reinforcement resistivity. Corrosion looked to be greatest on the MMC reinforced with B_4C, followed by that reinforced with SiC, and least on the MMC reinforced with Al_2O_3. Combined SVET and SIET measurements revealed that sites supporting anodic currents were generally accompanied by local solution acidification, whereas sites supporting cathodic currents were accompanied by local solution alkalinization. For the MMCs reinforced with B_4C and SiC, SVET revealed that corrosion initiated at anodic sites, which become cathodic over time. The authors

explained the observed anodic-cathodic transformation behavior by amphoteric properties of aluminium oxides, by the formation of microcrevices resulting from residual reinforcement particles in corroded matrix, and by the possible galvanic action between the 6092-T6 Al matrix and the B_4C and SiC particles. The localized anodic and cathodic regions were many times larger than the individual reinforcement particle size. For the Al_2O_3-reinforced MMC, localized corrosion coincided with regions showing some cathodic activity and alkalinity.

Recently local pH measurements together with SVET and EIS measurements were applied for studying corrosion and inhibition processes by Lamaka *et al.* on ZK30 magnesium alloy with complex protective coatings [199] and by Taryba *et al.* on coated galvanized steel [171]. In the latter paper mapping of the ionic current density and pH distribution was performed quasi-simultaneously according to the methodology described earlier by the authors [201]. To do that the vibrating probe of SVET and the pH-selective microelectrode were brought up together. The 1.5 s time lag between reading SVET and SIET signals was required due to the response time of the pH-selective probe. Such approach was utilized by the authors to assess the self-repair processes in defects on "smart" coatings applied to galvanized steel [171]. Thus, model weldable primer coatings for galvanized steel were modified with submicron containers loaded with corrosion inhibitors. Defects of 50 μm × 50 μm were created in the coatings by using a focused ion beam, and the samples were immersed in a NaCl 0.05M solution. EIS revealed that the addition of containers filled with organic inhibitors do not damage the barrier properties of weldable model primers applied to galvanized steel substrates. The SVET–SIET measurements clearly identify zones of cathodic and anodic activity, both in the maps of pH and ionic current distributions for all samples. On the reference sample the intense acidification over the defect shows that Fe^{3+} species are formed together with Zn^{2+} species, which was confirmed by the chemical EDS analysis. Thus, iron was clearly identified in the anodic zones, when strong acidification was measured. The addition of inhibitors in form of containers in the coating led to the passivation of sacrificial Zn with the detrimental dissolution of Fe as a result. The study revealed, that the corrosion activity on the coated sample was very low, indicating the self-healing ability of the containers loaded with the corrosion inhibitor. The electrochemical results highlight the importance of the combined use of integral and localized electrochemical techniques to extract information for a better understanding of the corrosion processes and corresponding repair of active microscopic defects formed on thin coatings containing inhibitor filled containers.

Summarizing, these examples demonstrate the complementary use of the localized electrochemical techniques (SRET, SVET, SECM and SIET) to detect local changes of current density, dissolved oxygen and pH. This information provided important insights into the mechanism of localized corrosion processes. However, the mapping of specific metallic cations by potentiometric microsensors in real corroding systems is not a routine so far. Meanwhile, there is a clear demand for such measurements since they can provide experimental evidence of different phenomena, such as self-healing of protective coatings, which is a hot item nowadays [39,96].

Chapter 3

3 Potentiometric microelectrodes

3.1 Potentiometry

Potentiometry is a branch of electroanalytical chemistry, in which potential between an indicator electrode and a reference electrode under conditions of no current flow in the cell is used to determine the activity or concentration of a given ion in solution. This potential is typically measured by a potentiometric probe, which has an inert body with an ion-selective membrane as recognition element at its end and an electrochemical half-cell equivalent.

Potentiometric probes are the oldest form of electrochemical sensors. Ion-selective electrodes (ISEs) have being used to detect a great variety of chemical species, in chemical analysis, in clinical analysis, environmental and life sciences. It is a fast and simple method. Other advantages of ISE are high selectivity of the potentiometric signal and sensor passivity toward the analysed sample in contrast to amperometric probes, which can alter the redox state of the species and create mass transport in the solution.

The history of ISEs development has begun in 1906 with the introduction of the pH-sensitive glass membrane electrode by Cremer [202]. Due to its exceptionally wide concentration response, excellent selectivity, simplicity and low cost, it is still the example of the ideal analytical tool. The next significant achievement was reported by Eisenmann in 1957 with the preparation of the well-functioning sodium-selective glass electrode [203]. Since the 1950s several research groups studied the behaviour of diverse membrane materials searching for high selectivity and near Nernstian response. In the

1960s lanthanum fluoride crystal-based F^--selective electrode was developed by founders of the Orion company, Frant and Ross, [204] following attainments of Pungor and co-workers in fabrication of highly selective iodide electrodes. The commercial success of LaF_3-crystal-SE led to intensive scientific activity in designing new ISEs with enhanced characteristics. Significant contributions were made by Ruzicka, Shatkay, Bloh, Freiser, Thomas and specially Simon's group from ETH Zurich (Eidgenössische Technische Hochschule Zürich). For example, following a suggestion by Shatkay *et al.*, Thomas *et al.* improved polyvinylchloride (PVC) membranes through a simplified preparation procedure of PVC films [205,206]. This method, together with the discovery of sensitivity of nonactin and valinomycin (neutral carrier organic molecules) toward NH_4^+ and K^+ ions in the ETH Zurich centre [207] resulted in the invention of almost universal form of ion selective electrode. That early years of ISE handling together with the leaders vignettes are reviewed by Durst [208].

In the following 20 years, tremendous results were achieved by a number of research groups around the world [209,210]. Ion-selective electrodes for more than 50 different ions were developed [210], microelectrodes were introduced for in vivo measurements [76], and, as a significant development for everyday life, potentiometry has become the standard technique in the clinical analysis of ions, including Na^+, K^+, Ca^{2+}, and Cl^- [211].

3.2 Types of potentiometric microsensors

While analytical chemists and electrochemists were focusing on designing new inophores and searching for more selective membrane compositions, life scientists and corresponding companies aimed to implement ISEs into clinical applications. Facing the dimensions of biological cells and tissues and the small volume of analysed samples they took steps toward miniaturization of ISE. The first ISEs of microdimensions were produced in 1950s from available types of sensitive glasses, but these early H^+-, Na^+- and K^+-selective electrodes were complicated and their fabrication was frequently beset with problems [76,212].

In the early 1970s the technologies developed by the semiconductor electronic industry were applied to the manufacture of other type of miniaturized ISEs. Bergveld was the first to notice that metal oxide field effect transistors could be combined with ion-selective materials to detect activity of different ions [213]. The device was named ion-selective field effect transistor (ISFET). Such promising approach for mass production of microsensors was, however, not very successful due to incompatibility of materials used in electronics with wet conditions of chemical analysis.

Metallic electrodes, or electrodes of second type, also can be used as potentiometric sensors. Their miniaturization was started in 1950s by Mauro, who prepared a Cl^- selective minielectrode (15 mm length wire) by cementing AgCl on silver wire and measured chloride concentration inside squid giant axons [89]. In 1977 Saunders and Brown reported an electrochemical method for fabrication of Ag/AgCl microelectrodes [214]. A silver wire (125 µm in diameter) was sharpened by anodizing under voltage control, etched in NaCN alkaline solution and electrochemically coated by AgCl in 100mM HCl. In 1992 Denuault *et al.* reported Cl^--sensitive microdisc electrodes used in SECM for ion flux measurements [215]. The Ag/AgCl-microdisc (10 and 50 µm in diameter) electrodes were also prepared by electrochemical anodizing.

In 1970s advances in ISEs fabrication from liquid membranes (based on different organic carriers) resulted in their commercialization in the form of electrode preparation kit, consisting of conventional size electrode body, organic liquid membrane and internal reference solution. Walker seems to be the first to introduce a liquid membrane into a glass micropipette for investigation of intracellular ion activities [190]. The organic solution inside the micropipette tip formed a measuring membrane, which separated the internal filling solution from the sample solution. Submicron size ISE could be fabricated in this way. Within a decade, these liquid-membrane microelectrodes had completely replaced ion-selective glass ME in many laboratories, because of the universal procedure for making another ion-detecting microelectrode.

Carrier-based microelectrodes now exist that can measure the activity of H^+, Li^+, Na^+, Mg^{2+}, Ca^{2+} and other ions [76,77]. Classical ion-exchanger ISMEs for measuring K^+- and Cl^--activity are other examples of liquid-membrane microelectrodes in common use.

Today, existing ISEs can be classified according to the nature of the ion-selective membrane or the shape and size of the electrode arrangement. According to Denault *et al.*, the main membrane types of electrodes are [73]:

1 Glass membrane electrodes (e.g., H^+, Na^+, K^+, Ag^+-selective glass electrodes);

2 Liquid or polymeric ion-selective membrane electrodes:

   a) Classical ion-exchangers (with hydrophobic cations and anions providing mobile positively and negatively charged sites, respectively), for example, K^+- and Cl^--selective electrodes;

   b) Liquid ion-exchanger based electrodes (with positively or negatively charged sites acting as ion carriers), for example, Ca^{2+}- and NO_3^--selective electrodes;

   c) Neutral carrier based liquid membrane electrodes (with uncharged complex ligands), for example, Na^+, K^+, NH_4^+, Ca^{2+}, and Cl^--selective electrodes;

3 Solid-state electrodes:

a) Crystalline electrodes, for example, F^-, CN^-, Pb^{2+}, Cu^{2+}, and Cd^{2+}-selective electrodes;

b) Sb/Sb oxide, Ir/Ir oxide, and Pd hydrid for sensing H^+;

c) Ag/Ag halides based electrodes for sensing Cl^-, I^-, and Br^-.

Currently thin-layer technology, as well as screen printing and other thin film fabricating methods, are used for making microsize cells, flat form electrode assemblies and arrays of sensing elements in modern technologies [77,89,90,216–218]. Various types of potentiometric microsensors are summarized in Figure 13.

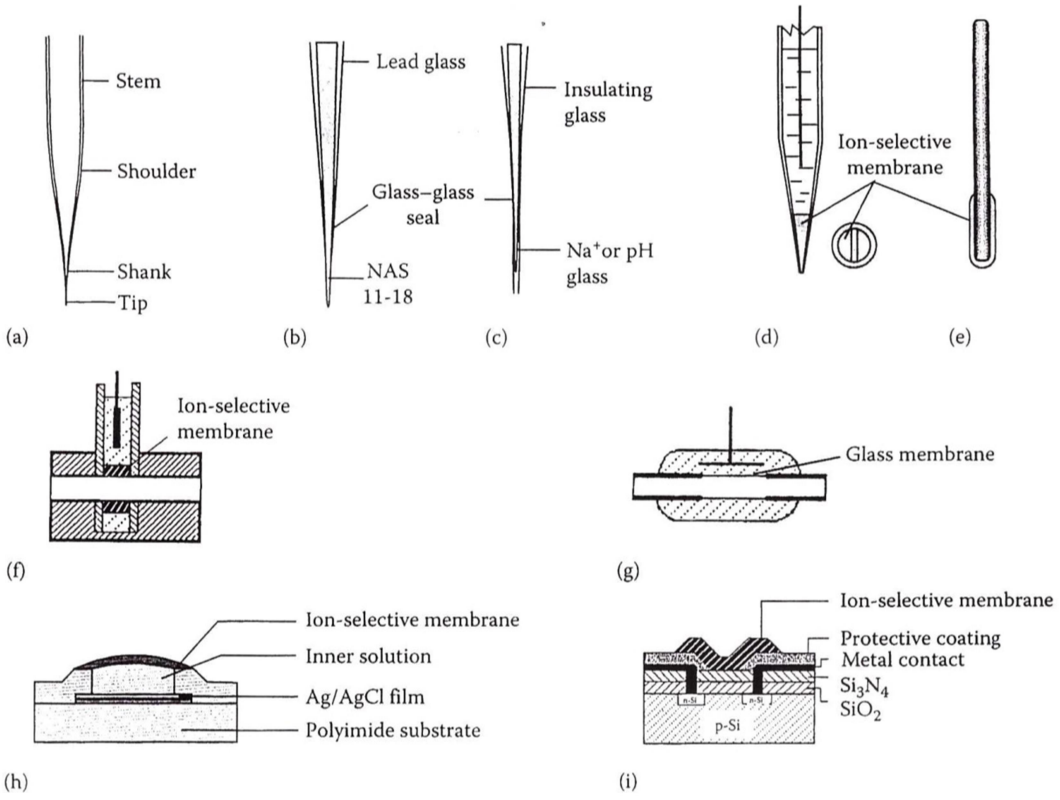

Figure 13. Schematic cross sections of ME configurations. (a) Nomenclature of ME parts; (b) Na^+-sensitive ME; (c) recessed Na^+-sensitive ME; (d) liquid membrane micropipette electrode; (e) coated wire ME; (f) flow through ISE; (g) tubular flow-through glass electrode, (h) planar sensor made by microelectronic technology; (i) ISFET sensor. Taken from [73].

Being very suitable for specific applications, the potentiometric microelectrodes are very delicate tools, which require particular care and attention during work. ISMEs share with the macro counterparts many advantages: i) non-desturbing; ii) relatively cheap; iii) do not change sample composition; iv) suitable for flow systems; v) allow the determination of ion gradient and transport; vi) easy automated. In addition, ISME can vii) measure small volumes of solution; and viii) provide spatial distribution at the microscale.

Unfortunately, they also possess several disadvantages: i) can show limited linear range comparing to their macro versions; ii) ionic strength sensitive; iii) require special equipment because of high noise and high resistance; iv) have short lifetime; and v) some types have poor mechanical robustness.

The diversity of developed kinds of microelectrodes is explained by the fact that each electrode arrangement was designed for a specific application. In the case of microsensors to perform scanning measurements of localized chemical reactions with high spatial resolution, the most suitable ones are MEs of type (d) due to their universal fabrication procedure and type (e) due to their mechanical robustness.

3.3 Components of ion-selective membrane solution

The term “membrane” generally refers to a continuous layer, solid or liquid, with controlled permeability. The membrane for micropipette ISME is an organic mixture of several components, and that is why it is called a cocktail. Different ion-selective cocktails have been elaborated [76] and are commercially available (for instance, from Sigma-Aldrich-Fluka [219]) as organic solutions in small vials ready for electrode preparation.

A typical cocktail consists of a low-viscosity *organic solvent* (60-90 wt. %), such as 2-nitrophenyl octhyl ether (NPhOE) or bis(2-ethylhexyl)sebacate, in which *an inophore* (5-10 wt. %) and *lipophilic additives* (1-20 wt. %) are dissolved.

The most important component in determining the electrode characteristics (e.g. slope, selectivity, limit of detection) is an *ionophore*. The ionophore is a selective and reversible complexing agent (ligand) capable of transporting a given ion across a membrane phase excluding all ionic species. The selectivity comes from the fitting of the ion of interest in the host-guest chemistry of the inophore. The ionophore may be an ion-exchanger, neutral carrier or charged carrier. The first neutral carriers were natural compounds, valinomycin and nonactyn, introduced into the liquid membrane by Simon’s group from ETH Zurich for measuring potassium and ammonium ions activities [207]. This discovery generated the design of various synthetic acyclic and macrocyclic ionophores such as crown ethers and, more recently, calixarene derivatives [210]. The selection of suitable neutral carriers for ion sensing can be facilitated by structural studies on the interaction between carriers and ions [220]. Ligands used as an ionophore should ideally fulfill certain conditions. They should be selective toward the target ion over other ions, they should have rapid exchange kinetics and should be sufficiently lipophilic to prevent leaching into solutions surrounding the membrane sensor [76,221].

The *solvent* for liquid cocktails is usually the same substance that is being used as a plasticizer in fabrication of conventional PVC-based membrane ISE [76,205,222]. The high content of the solvent in membranes significantly affects a number of parameters

influencing the properties of the sensor [76,209,221,223]. This is due to the plasticizers effect on the dielectric constant of the membrane, the mobility of the ionophore molecules, and the state of the ligands [223]. Thefore it can substantially affect selectivity, stability and lifetime of the sensors [209].

The performance of most cation-selective neutral carrier based membranes can be enhanced by the addition of *lipophilic additives*, such as, tetraalkylammonium tetraaryl borate, potassium tetrakis(4-chlorophenyl)borate (KTClPhB), or tetradodecylammonium tetrakis-(4-chloropheyl)borate (ETH 500). The analytical response of any ISE is caused by potential jump originated due to the distribution of primary ions between the analysed solution and the membrane boundary layer. For this potential jump to be dependent only on the concentration of primary ion in the analysed solution, the amount of the primary ion in the membrane phase should be constant, and no others ions should be present there in. This can be achieved by addition of lipophilic ionic additives into membrane. Being ion-exchangers in their chemical nature, they reduce or eliminate entering of lipophilic ions from of the sample inside the membrane, which would otherwise compete with the ionophore in interaction with cation of interest. These additives also reduce electrode response time, lower the electrical membrane resistance [221,224], and improve cation sensitivity and selectivity [76]. Their content in the membrane phase is calculated relative to the ionophore, usually in mole per cent.

In addition to selectivity, a major goal in developing neutral carrier-based liquid membranes is to reduce the resistance of the ISME. This is achieved by adjustment of the membrane composition, i.e. changing solvent, ionophore concentration and the nature of lipophilic salts (ion-exchangers) [224]. The final optimum cocktail is therefore obtained by varying the composition of each component to find electrodes with the best performance. Different individual chemicals for membrane cocktails (ionophores, additives and solvents) are commercially available [219]. A carefull review about performance characteristics of ISE based on more than 500 ionophores selective to ca. 50 different ionic species can be also useful when choosing a membrane composition for a particular application [210].

3.4 Basic theory

The principles of modern potentiometry can be found in many books and reviews [209,217,220,221,225–227]. IUPAC recommendations on nomenclature of ISE [228], time response [228–230] and selectivity [231,232] are also available. In this section the basis of potentiometry is described regarding its application for gathering microscale chemical information by scanning techniques.

The scheme of the common electrochemical cell for potentiometric measurements is shown in Figure 14. The cell potential is the sum of a number of local potential differences generated at the solid-solid, solid-liquid, and liquid-liquid interfaces within the cell between the two reference electrodes. Since no current passes through the cell, the cell potential, E_{cell}, is given as [225]

$$E_{cell} = E_{ref} - E_{ref(int)} + E_{mem} + E_{lj} \quad (3.1),$$

where E_{ref} – potential of RE immersed into sample solution; $E_{ref(int)}$ – potential of internal RE from ISE; E_{mem} – membrane potential; E_{lj} – liquid junction potential due to interface between the sample and a RE.

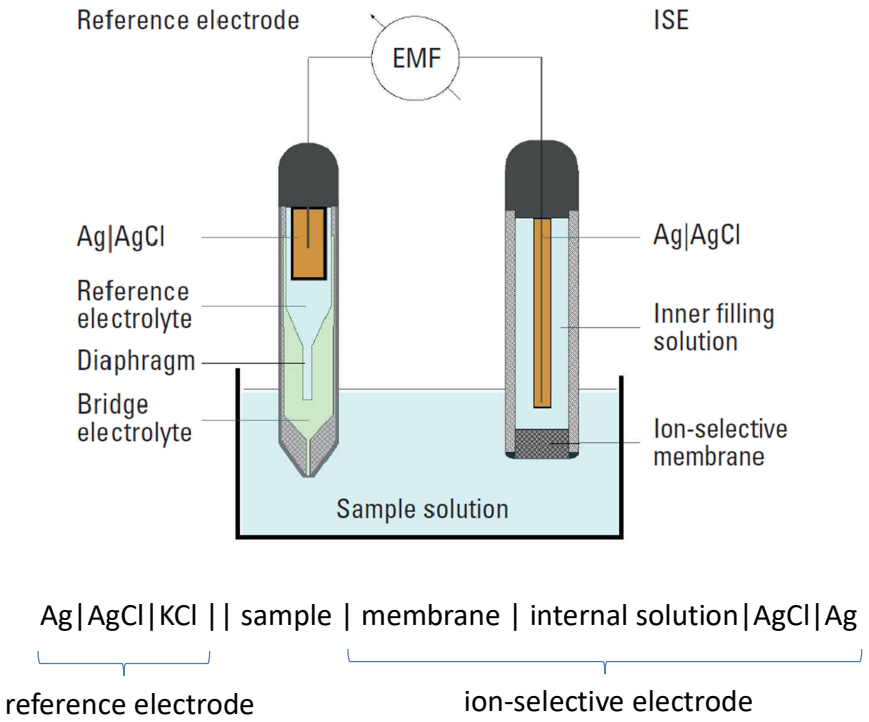

Figure 14. Schematic diagram of a potentiometric cell assembly with a membrane electrode and a double junction reference electrode. Taken from [218]. Lower – Cell scheme, where single vertical lines indicate phase boundaries, and double vertical lines indicate a liquid-liquid interface.

The response of ISE is based on the distribution of charged species (cations and anions) between the analysed solution and the membrane boundary layer. This process leads to space separation of charges and to formation of a double electric layer at the membrane-solution interface. The observed potential jump at the membrane-solution interface is caused only by the ions distribution process, occurred when there is a

difference in ions activity on opposite sides of the membrane; no reduction-oxidation processes take place as in the case of other types of electrode.

If the liquid junction potential and reference electrode potentials are maintained constants, any change in the cell potential can be attributed to the membrane potential. The relationship between cell potential, E_{cell}, and the activity of the analyte ion i, a_i, is log-linear and is described mathematically by the Nernst equation [225,228]:

$$E_{cell} = constant + S\, log\, a_i \quad (3.2),$$

where *constant* includes the potentials of the REs and the liquid junction potentials; S is the Nernstian slope defined as

$$S = 2.303 \frac{RT}{z_i F} \quad (3.3),$$

with R – universal gas constant; T– absolute temperature, K; F – Faraday constant; z_i – charge number of ion $\boldsymbol{i}$. The activity is related to the concentration by,

$$a_i = C_i \cdot f_i \quad (3.4),$$

where C_i– is the concentration of ion $\boldsymbol{i}$; f_i - activity coefficient of ion $\boldsymbol{i}$, here calculated from Debye-Huckel theory utilizing the modifications of Robinson and Guggenheim and Bates [233]:

$$-log f_i = z_i^2 \left(\frac{A\sqrt{I}}{1 + B a_i^{\circ} \sqrt{I}} - 0.2I \right) \quad (3.5),$$

where *A* is a constant, depending on temperature and dielectric constant of solvent (equals to 0.5115 unit volume for water at 25°C [233]); I is the ionic strength of the medium, given by

$$I = \frac{1}{2} \sum_i C_i \cdot z_i^2 \quad (3.6),$$

B is a constant, depending on temperature and dielectric constant of solvent (equals to 0.3291 unit volume for water at 25°C [233]); a_i° is the approximate effective ionic radius of ion $\boldsymbol{i}$, Å (values for various ions can be found in reference [233]).

Equation 3.2 shows that E_{cell} varies 59 mV per decade change of the activity of a monovalent ion. A plot of E versus $log\, a_i$ should be a straight line with slope = 59 mV. Calibration of the electrode against a range of standard solutions should ideally yield a slope of 59 mV (at 25°C) per decade change in the activity of a monovalent ion. In practice, however, the ideality is not observed because under most conditions interfering ions (ions giving the same response as the ion of interest) are present in the analysed solution. Hence contributions to the overall cell potential made by each interfering ion, $\boldsymbol{j}$, must be taken into account. In the presence of interferences the electrode potential is described by the Nickolsky-Eisenman equation, a modified Nernst equation [225]:

$$E_{cell} = constant + 2.303\frac{RT}{z_i F}\log(a_i + \sum_j K_{i,j}^{Pot} a_j^{z_i/z_j}) \quad (3.7),$$

where $K_{i,j}^{Pot}$ is the selectivity coefficient of ion ***i*** toward ion ***j*** (see Section 3.5.2). Equation 3.7 is a general equation, and applies to all types of ion-selective electrodes.

Important ISEs characteristics are i) linear response range of calibration curve (and detection limit), ii) slope, iii) selectivity to foreign ions, iv) response time, v) potential stability, vi) reproducibility, vii) working pH range, viii) life time and ix) membrane resistance.

3.5 Main characteristics of ISEs

3.5.1 Detection limit

The ISEs typically exhibit linear response in limited concentration range, usually between 10^{-1} and 10^{-6}M [77], what results in the appearance of regions in the calibration graph (in low or high concentrations), where the ISE is not sensitive to the concentration changes of the ion of interest (sometimes called primary ion or target ion) (Figure 15). The borders of these regions are named higher and lower detection limits. According to IUPAC [228], the lower detection limit (DL) is the lowest ion activity that can be detected with confidence. The theoretical detection limit usually depends on the nature of ion-selective membrane material. For ionophore-based electrodes it is determined by the stability constant for the ionophore-target ion complex.

By analogy with definitions assumed for other analytical methods, a limit of detection could be defined as the concentration for which, under the specified conditions, the cell potential deviates from the average cell potential in region I of the calibration plot by a multiple of the standard error of a single measurement of the cell potential in this region I (Figure 15). The multiple value depends on a statistical significance level selected. Usually 3 is used [234].

In practice, due to the logarithmic response of potentiometric ISE, a simpler and more convenient way of DL definition can be applied. This method is actually recommended by the IUPAC [228]. Thus, the practical DL is determined by the intercept of the two asymptotes of the calibration response curve (Figure 15). If the measurements of the electrode function below the detection limit is problematic (too long response time, bad reproducibility, etc.) a line parallel to the x-axis should be drawn through the mean potential value determined in the solution of lowest concentration, instead of linear fitting of some data in the curved region of the calibration plot.

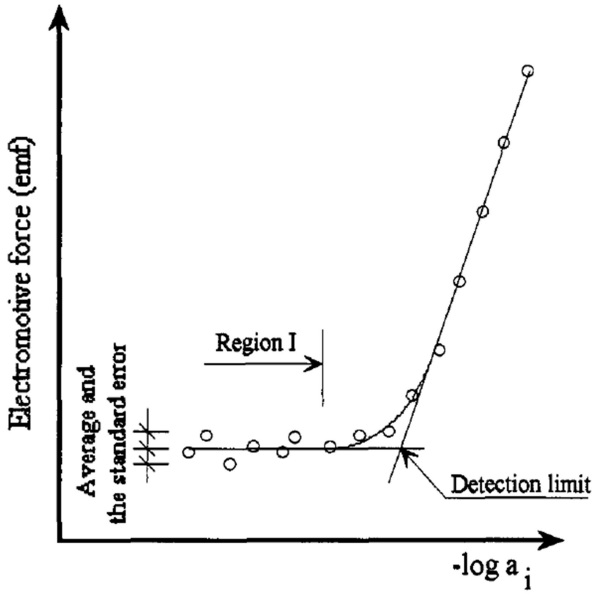

Figure 15. Determination of the lower detection limit of ion-selective electrode [228].

3.5.2 Potentiometric selectivity coefficients

The potentiometric selectivity coefficients, $K_{i,j}^{Pot}$, define the ability of an ion-selective electrode to distinguish a target ion, ***i,*** from others (interfering) ions, ***j***. The smaller the value of $K_{i,j}^{Pot}$ the greater the electrode preference for the primary ion, i.e. the higher is its selectivity.

According to IUPAC recommendations, the selectivity coefficients can be determined by the following methods [226,228]:

i) Fixed Interference Method (FIM), in which the cell potential is measured in mixed solutions of different activities of the primary ions and a constant level of the interfering ions. The cell potential values obtained are plotted vs. the logarithm of the activity of the primary ion. The intersection of the extrapolation of the linear portions of this plot indicates the value of a_i which is to be used to calculate potentiometric selectivity coefficient from the Nikolsky-Eisenman equation as follows:

$$K_{i,j}^{pot} = \frac{a_i}{a_j^{z_i/z_j}} \tag{3.8}$$

ii) Separate Solution Method (SSM), in which the potential difference in separate solutions of ***i*** and ***j*** of the same activity is measured. The value of potentiometric selectivity coefficient in SSM is calculated as follows:

$$logK_{i,j}^{pot} = \frac{(E_j - E_i)z_i F}{2{,}303\ RT} + log\frac{a_i}{a_j^{z_i/z_j}} \quad (3.9)$$

FIM is preferable since its conditions are closer to real situations, when both ions coexist in the same solution. On the other hand, the SSM is rather simple and fast, especially suitable for comparing the selectivity of a novel ISE based on different membrane compositions.

Problems can arise if the interfering ions exhibit non-Nernstian response and if ions of unequal charge are involved [226,232]. In this case the Matched Potential Method (MPM), independent of Nikolsky-Eisenman equation, is recommended by IUPAC [232]. According to this method, at first a known activity ($a_i^{'}$) of the primary ion solution is added to a reference solution with fixed activity of the primary ion, a_i, and the corresponding changes in potential are recorded. Next, a solution of interfering ions with known activity, a_j, is successively added to the reference solution until the same potential change is observed. Selectivity measure, $k_{i,j}^{MPM}$, called a selectivity factor, is then defined as the ratio of the primary ion activity and the interfering ion activity which gives the same potential change in a reference solution [231]:

$$k_{i,j}^{MPM} = \frac{a_i' - a_i}{a_j} \quad (3.10)$$

The MPM can be applied to ISE of any type because it is not based at any model assumption. As a consequence, $k_{i,j}^{MPM}$ loses its predictive ability about cell potential measured with solutions other than those for which it was determined [231]. Values of $k_{i,j}^{MPM}$ in general depend on the experimental conditions [231], that is why term “factor” and a small letter are frequently used instead of “coefficient” and a capital letter.

3.5.3 Response time

According to IUPAC recommendations [228], the response time, τ_{lim} ($\Delta E/\Delta t$), is the time which elapses between the instant when an ISE and a RE are brought into contact with a sample solution (or at which the activity of the ion of interest in a solution is changed) and the instant at which the cell potential/time slope ($\Delta E/\Delta t$) reaches a limiting value (e.g. 1 mV/min or 0.017mV/s) (Figure 16).

Another value of response time, i.e. τ_{95}, the time needed to obtain 95% of total potential jump, can be also determined for comparison, as this value (together with τ_{90}) is often found in literature [229].

The response time is one of the critical parameters of the ISEs in continuous analysers and *in situ* monitoring. It is affected by membrane properties and also by the experimental conditions used, for instance, the amount of convection at the electrode

surface, the way of concentration changings, and the electronics used for potential measurements [77]. While for solid and most liquid membrane electrodes of conventional size, the rate-limiting step is the ion transport in the stagnant solution layer close to the ISE, the response time of microelectrodes with high internal resistance, never reflects transport processes toward or within the membrane, instead it reflects the *RC* time constant of the measuring circuit or of the ISME itself [77]:

$$E_{cell}(t) = E_{cell}(\infty) \pm [E_{cell}(\infty) - E_{cell}(0)]e^{-t/RC} \quad (3.11)$$

where $E_{cell}(0)$ is the cell potential prior to the change in activity; $E_{cell}(\infty)$ is the cell potential at very long time after change in activity (once the potentiometric response has stabilized); *R* is the internal resistance of the electrochemical cell, *C* is the capacitance of the amplifier input.

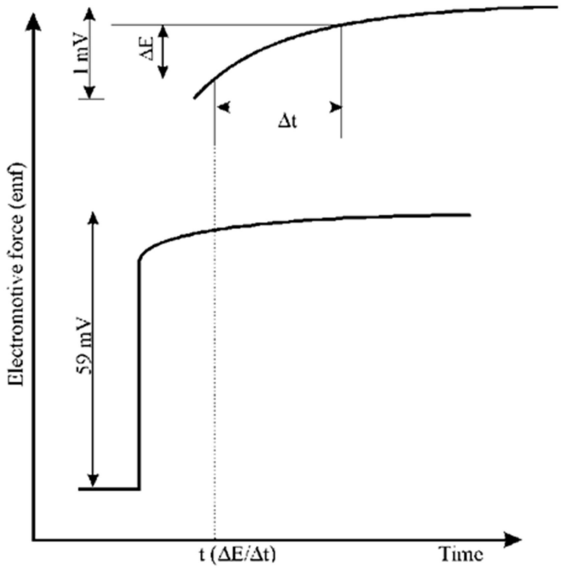

Figure 16. Definition and determination of response time of ISE according to IUPAC recommendations. Taken from [228].

3.5.4 Potential stability

The potential stability of ISEs is determined by the potential drift and potential reproducibility. The IUPAC defines drift as "the slow non-random change with time in the potential of an ion-selective electrode cell assembly, E_{cell}, maintained in a solution of constant composition and temperature" [228]. The determination of the drift is carried out by a linear graph fitting the data set recorded during a given period of time in a solution of constant composition and temperature. The slope of the graph (E vs time) is

called drift. The standard deviation of the measured data is defined by random E_{cell} deviations around the graph line.

Potential reproducibility is the standard deviation of cell potential collected in a series of measurements in solutions of different concentrations of ion of interest (after removal and washing and/or wiping of the electrodes). The electrode memory, or hysteresis, can occur when there is a difference between the first observed value of cell potential in a solution of ion of interest and a second recorded value of cell potential in the same solution after exposing the electrode to a different concentration of ion of interest**.** If the electrode does have a distinct hysteresis, the reproducibility will be poor. Nonetheless, it is believed that normal, reversible responses are measured, when sufficient time is allowed for the system to return to its initial condition.

The ISE with well optimized membranes, used in flow analysing assays for clinical applications, have standard deviations in E_{cell} smaller than 0.1 mV, which results in less than z_i·0.4 % error in activity determination [77]. Ion-selective microelectrodes usually have worst characteristics due to chemical (e.g. cocktail affinity to the micropipette surface) or electrical (high membrane resistance) factors.

3.6 Important ISMEs requirements for application in localized corrosion studies

As it follows from the literature data, corrosion processes of steel, Mg and Al alloys in NaCl solution as corrosion medium are accompanied by the following chemical alterations:

- appearance of dissolved metal ions in the solution, the concentrations of these ions can vary from the trace levels to ~10^{-2}M (in anodic zones) [12];
- change of the pH value due to the hydrolysis of dissolved metal ion (in the anodic zones) and to water or oxygen reduction (in the cathodic zones) [52,53]; the ultimate pH values depend on the alloy nature and can vary from 2 in the anodic zone to 12 in the cathodic zone [12,53];
- since the corrosion process leads to space charge separation (positively charged ions produced at the anode and negatively charged ions at the cathode) (see Chapter 1), it generates the fluxes of the background electrolyte ions, so Na^+ and Cl^- concentrations in the solution vary close to active sites [99].

It should be noticed that, to obtain reliable results, a number of special requirements to analytical characteristics of ISMEs should be fulfilled. According to the specificity of SIET, the most essential electrodes parameters for their successful application in corrosion study are the following:

1. For any ISME:

- size of the membrane surface (for instance, the diameter of the orifice of the glass micropipettes) – smaller tip provides higher spatial resolution;
- electrical resistance of the membrane – high resistance disables voltmeter sensitivity to small signal values;
- response time - low response time is needed to obtain scans consisted of about 400-2500 experimental points within an appropriate timescale;
- selectivity against Na^+ cations – should be high enough, as NaCl is among the most used corrosive media.

2. For metal cation-selective MEs:

- pH working range – should be rather wide, as far as pH in the corrosion zone can vary greatly;
- robustness to alternation of the medium pH from acidic to alkaline and vice-versa.

Nevertheless, ISMEs should have a low detection limit, a near Nernstian slope, and small selectivity coefficients. The most crucial parameters for metal cation selective MEs are the low detection limit and high selectivity against Na^+ ions. As far as the concentrations of metal ions can vary in wide range, very good potential reproducibility is not a very critical parameter for these microelectrodes.

3.7 Microelectrodes sensitive to relevant corrosion species

In fact, electrolyte species (mainly H^+/OH^-(pH), K^+, Na^+, Cl^-, SO_4^{2-}) as well as cations of all technical metals are relevant chemical species to be detected in local corrosion processes, however here the focus is given to development and state of art of potentiometric microelectrodes sensitive to pH, Mg^{2+}, Zn^{2+}, Cu^{2+} and Al^{3+} ions. The aim of this Section is to substantiate a choice of an appropriate for SIET measurements microsensor configuration (type and membrane composition) or a strategy to achieve that.

3.7.1 pH-SMEs

pH is a very important parameter to characterize any environment or to explain complex reactions taking place in aqueous medium. The redox reactions associated with corrosion are also invariably linked with local changes in pH. The increasing use of pH electrodes as a research tool has led to various technical developments for fabrication of pH-SME. The pH-SMEs have been designed based on three types of commercially available pH sensors: glass membrane electrodes, ionophore-based membrane electrodes, and solid-state electrodes.

The glass membrane pH-sensitive microelectrodes, as their macroversions, have fast ion-exchange capacity, are not sensitive to redox species and, hence, are often used in life and environmental sciences [76,89,217]. However, they possess low selectivity against alkali metal ions, high membrane resistance, intricate fabrication procedure and are fragile, which restricts their use in many situations [76,77,89,210].

3.7.1.1 Liquid membrane glass micropipette pH-SMEs

Liquid membrane glass micropipette electrodes for pH are quite popular among researchers because of their well-established construction process [95,98,102–106,118,120,171,196,199,201,235]. The common procedure starts with micropipettes drawing from glass capillaries using an especial pulling machine. The obtained micropipettes are then cleaned, dried and covered with silane layer (so called silanized) inside and outside. After they are filled with an internal solution, a column of liquid membrane is introduced at the tip. An Ag/AgCl wire is introduced inside the micropipette and works as internal RE. The tip diameter, depending on the melting properties of glass and requirements of experiment, varies from 0.1 µm to 10 µm [76].

A large number of various ionophores for non-glass pH-sensitive electrodes was investigated [210]. In spite of a variety of existing H^+-sensitive ionophores, only one cocktail for fabrication of glass micropipettes pH-SMEs is now commercially available [219]. This cocktail is Hydrogen ionophore I cocktail B, based on tridodecylamine (TDDA, hydrogen ionophore I) [235,236], since another liquid cocktail, based on 4-nonadecylpyridine (hydrogen ionophore II), was recently discontinued. Their composition and characteristics are presented in Table 3. The first cocktail operates in pH intervals from 5.5 to 12.0, and the second one workes in pH intervals from 2.0 to 9.0 [237]. All glass capillary H^+-SMEs that have been used mostly for local corrosion studies are based on the two above mentioned cocktails.

Table 3. Characteristics of pH-sensitive commercial cocktails [237].

Cocktail name	Composition	Linear range, pH	Slope, mV/ pH	Response time, s	$logK^{Pot}_{H+,Na+}$
Hydrogen ionophore I cocktail B	10.00 wt. % TDDA, 0.70 wt. % KTClPhB, 89.30 wt.% NPhOE	5.5-12.0	58.0±0.04	τ_{90}≤5	-10.4
Hydrogen ionophore II cocktail A	6.00 wt. % 4-nonadecylpyridine, 1.00 wt. % KTClPhB, 93.00 wt.% NPhOE	2.0-9.0	57.1±0.8	τ_{90}≈0.6	-9.6

3.7.1.2 Solid-contact and solid-state pH-SMEs

Glass capillary microelectrodes have two main drawbacks, possible leakage of the liquid membrane and fragility. Novel solid contact pH-MEs with ionophore based membranes, presented by Lamaka and co-workers, are free of these problems [230]. The designed pH-SME was based on an insulated needle-shaped Pt-Ir wire with an exposed apex (Figure 17). The apex tip was firstly plated with a gold layer (0.7–1.2 µm thick), followed by a conductive polymer (poly(3-octylthiophene-2,5-diyl), POT) film (1.5–2.0 µm tick) and, finally, by a pH sensitive PVC-based membrane (3-4 µm thick).

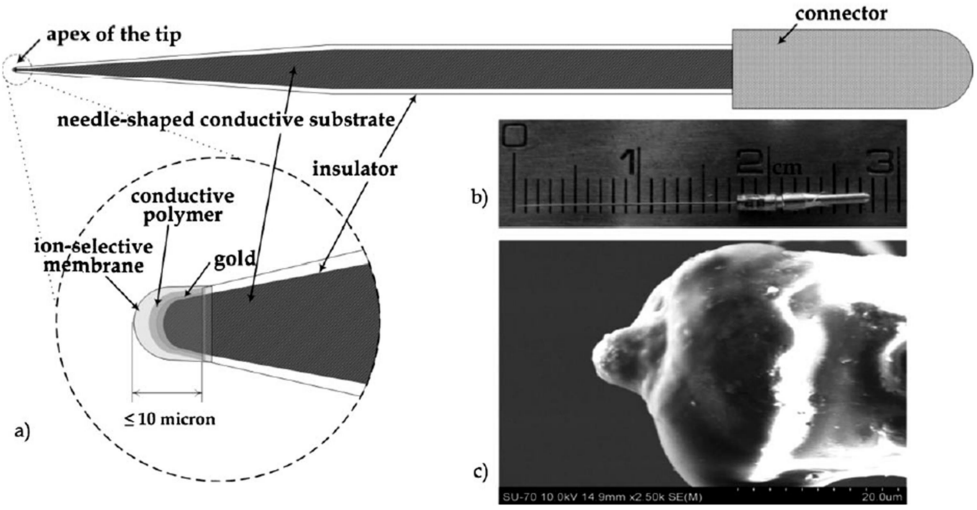

Figure 17. a) Schematic drawing and b) an optical photo of the solid-contact ion-selective microelectrode. c) SEM image of the tip apex. Taken from [230].

The pH-sensitive membrane was composed of 25 wt.% PVC, 10 wt. % TDDA, 55.5 wt.% NPhOE and 9.5 wt.% (90 mol.%) KTClPhB dissolved in tetrahydrofuran (THF). The length of the ion-sensitive part of the ME was less than 10 µm. The pH-SME showed linear response in 4.8-12 pH interval with the slope of 56.8 – 55.8 mV/decade during the first three days of microelectrode exploitation. The 0.05 M NaCl solution did not influence the potential of the solid contact pH-SME. The measured response time was τ_{lim} = 0.96±0.02 s and τ_{95} = 0.33±0.01 s, however, after 4 days of continuous usage its values increased up to 2.8 s and 1.8 s respectively. The developed pH-SMEs were applied for mapping of a Al-Cu galvanic couple embedded in epoxy resin and immersed in 0.01M NaCl solution. Well defined regions of cathodic reaction with alkalization of solution over copper (up to pH 11.2) and anodic dissolution of aluminium with local acidification of solution (down to pH 4.0) were detected with good spatial resolution. The fabrication procedure yield in two thirds of successful MEs preparation, as defects in POT and/or PVC layers may occur, which could not be noticed in an optical microscope during deposition of functional layers

but may be revealed by SEM/EDS observation. The microelectrodes with defects showed highly unstable and drifting potential in the first calibration.

Solid-state microelectrodes include metal, metal oxide, carbon fiber, and optical fiber types [217]. Typically they show rather wide pH responses, are mechanically robust, have low resistance and are more or less free from cation interferences, what makes them rather widespread [93–95,100,101,112,238–240].

Horrocks *et al.* described the fabrication and application of antimony SECM tips for pH measurements in different model chemical systems [100]. The microelectrodes were made of melted antimony in a Pyrex tube (outer diameter, 7 mm; inner diameter, 1 mm). The antimony filled capillaries were then pulled twice in order to produce smaller tips of antimony fiber, polished and bevelled. The response of the antimony microdisc electrode to pH was tested in phosphate buffers. The slopes of calibration curves were typically between 40 and 50 mV/pH unit. Measurements of pH profiles and maps 33 µm above a 25-µm Pt disc were carried out in pH 7.0 phosphate buffer. Also corrosion of silver iodide (40 µm target) in 0.1M KCl and 1mM KCN solution was investigated by 15 µm antimony ME. In both cases the pH-sensitive antimony MEs were able to detect local pH changes caused by electrochemical reactions. As the tips were also used as voltammetric probes, their pH function deteriorated, resulting in potential drift and decreased slope. However, the problem was solved by returning the electrode potential to 0 V for a few seconds before switching to potentiometric mode. The original pH response was then completely restored. The presence of redox species also affected the antimony ME response.

Luo *et al.* used 10 µm tungsten wires embedded in a glass body for the study of localized corrosion [93,94]. The calibration curve from -0.38 to 9.28 pH presented 4 intervals with different slope: -0.4-1.4 pH with S=31.8 mV/pH, 1.4-4.7 pH with S=37.27 mV/pH; 4.7-7.9 with S= 20.07 mV/pH, and 7.9-9.3 pH with S=17.5 mV/pH. In addition, the behaviour of an individual probe slightly varied due to manufacturing process, it was necessary to determine a specific working curve for each pH-SME. Nonetheless, the tungsten pH-SMEs were applied for analysis of local conditions inside the simulated pits on nickel and natural pits on stainless steel [93], as well as for the study of influence of chlorination of saline environments on localized corrosion of stainless steel [94].

A tungsten/tungsten oxide pH microsensor type was used by Tada *et al.* for investigation of spatial distribution of pH during galvanic corrosion of a Zn/steel couple immersed in 0.01M NaCl [95]. The microelectrode had sub-Nernstian response with values of 35-45 mV/pH. The authors referred that such behaviour was caused by the presence of dissolved ions and dissolved oxygen, as well as surface area phenomena [95].

Iridium oxide based microsensors for pH were produced by deposition of hydrous iridium oxide onto carbon fiber microelectrodes by the group of Wipf [112]. The obtained microelectrodes (overall diameter ≈ 40 µm) exhibited two linear regions of

potentiometric response between pH 2-6 and pH 6-12, with the slope varying from 59 to 80 mV/decade, depending on the preparation method [112]. The electrodes responded to pH changes within 50 ms, and an equilibrium value was reached within 30 s. By using these MEs as probes in the scanning electrochemical microscope, dynamic pH changes (profiles and maps) were measured at substrates where electrochemical (oxidation and reduction of H_2O_2, hydrogen evolution) or enzymatic (glucose oxidase) reactions involving proton transfer occurred.

Among the variety of developed H^+-sensitive microelectrodes, the glass micropipette MEs with liquid membrane seem to be easier to handle (only optical microscope and manipulators are required) and faster to prepare (ready-to-use commercially available cocktail). Moreover, they have the smallest tips (1-5 µm), what enables higher spatial resolution. Thus, glass capillary pH-SMEs based on commercially available cocktails were chosen for SIET applications in this work.

3.7.2 Mg^{2+}-SMEs

Magnesium is widely distributed in the earth crust and dissolved in the sea, where it occurs in combination with other elements in the oxidized state of Mg^{2+}. It is the eighth element in order of terrestrial abundance [241]. This metal presents no toxicity and can be shaped and worked by all known methods [242,243]. Its applications include construction and transport, metallurgy and electronics, pharmacology and medicine. Magnesium is a vital chemical element for all living cells, because it is a major regulator of enzymes functions and a number of cellular properties and processes [76]. As a consequence, measurements of magnesium activity in biology and physiology are important for understanding its role in living organisms.

The initial development of molecules exhibiting high selectivity for Mg^{2+} was rather difficult [76]. Between 1970s and 1980s several classes of synthetic carriers together with some naturally occurring ionophores and antibiotics have been investigated. However, the attempts to utilize the selectivity of the studied carriers in membrane solutions were not successful [76]. The first direct determination of intracellular Mg^{2+} activity was performed by Lanter *et al.* in 1980 using a glass pipette ISME [244]. The membrane for Mg^{2+}-SME was based on a lipophilic neutral carrier N, N'-diheptyl-N,N'-dimethylsuccinamide (ETH 1117). The Mg^{2+}-SME had good analytical characteristics and was suitable for intracellular activity measurements. Its main drawback consisted in relatively low selectivity against K^+ and Na^+ ($logK^{Pot}_{Mg2+,K+} = -1.4$, $logK^{Pot}_{Mg2+,Na+} = -1.1$) what was taken into account by performing calibrations with a typical intracellular background and by using the Nicolsky-Eisenman equation [244].

A new magnesium selective ionophore, that supposed to possess higher selectivity properties against alkali and alkaline-earth metal cations, was N,N''-octamethylenbis(N'-heptyl-N'-methyl-methylmalonamide) (ETH 5214). It was presented in 1989 by Hu and co-workers for liquid membrane based Mg^{2+}-SME [245]. A membrane optimized for intracellular measurements consisted of 10% of ionophore ETH 5214, 3 wt. % of KTClPhB and 87 wt.% of NPhOE. The glass micropipette (1 µm tip) Mg^{2+}-SME based on this membrane, showed linear response from pMg 1 to pMg 6 with slope of 29.3 mV/decade. The measured response time, τ_{90}, was ≤ 3 s. The selectivity coefficients determined by SSM, for Na^+ and K^+were -2.3- and -2.2 respectively. This ISME was superior to one based on ETH 1117, but still care had to be taken to adjust the K^+ activity in calibration solutions [245].

Schaller and co-workers presented another neutral carrier for Mg^{2+}-SME, N-heptyl-N',N'-bis{8-[[3-(heptylmethylamino)-1,3-dioxopropyl]amino]octyl}-N-methyl-propanedia-mide (ETH 7025) [246]. Apart from this ionophore, the membrane contained two ion exchangers KTClPhB and tetrakis-(4-chlorophenyl)borate tetradodecyl ammonium (ETH 500), NPhOE and PVC. The authors believed that the addition of PVC could improve the properties of ISMEs, but a more suitable PVC solvent, cyclohexanone, should be used instead of a common tetrahydrofuan (THF). Two membrane compositions (type A – 10% wt. ETH 7025, 60 mol. % KTClPhB, 5 wt. % ETH 500 and type B – 10% wt. ETH 7025, 150 mol. % KTClPhB, 1 wt. % ETH 500) with PVC were prepared by adjusted experimental procedure. The Mg^{2+}-SMEs with membrane A showed the best selectivity against K^+ ions ($logK^{Pot}_{Mg2+,\mathrm{K+}} = -3.1$) and were used for measuring intracellular magnesium activities, while the Mg^{2+}-SMEs with membrane B had better selectivity against Ca^{2+} ($logK^{Pot}_{Mg2\ ,\mathrm{Ca2}} = -0.7$) and consequently worked for both intra- and extracellular measurements [246]. Comparing the data with the Mg^{2+}-SME, based on ETH 5214, one can notice, that ETH 7025-based ME performed better. However, there was necessary to add the second lipophilic ion exchanger into membrane solution to lower the resistance of ME, caused by the presence of PVC matrix.

Consequently, the membrane solution, based on neutral carrier ETH 5214 was commercialized [219]. The cocktail for Mg^{2+}-SME, named "Magnesium ionophore II cocktail B" consists of 10% wt. of magnesium ionophore ETH 5214, 3 wt. % KTClPhB, 62 wt. % NPhOE and 25 wt. % chloroparaffin. According to the Fluka catalogue [237], its analytical characteristics are the following – slope 29.7±0.2 mV/activity decade, detection limit pMg = 6.4, pH range 3.5-9.5 and τ_{95}<3 s.

Recently, as for pH, a solid contact Mg^{2+}-SME, based on the ionophore ETH 5214, was presented by Lamaka *et al.* [230]. The ion-sensitive membrane was composed of 7.0 wt.% ETH 5214, 2.1 wt.%. (35 mol. %) KTClPhB, 43.2 wt. % NPhOE, 17.4 wt. % chloroparaffin and 30.3 wt.% PVC. This membrane was deposited over a layer of

conductive polymer (POT), obtained on the gold plated apex of an insulated needle-shaped Pt-Ir wire. The final tip sized was less than 10 µm. The Mg^{2+}-SME was linear from 1.7 to 6.3 pMg with slope of linear regression of 29.6±0.4 mV/decade and had very fast response time values (τ_{lim}=2.58±0.05 s and τ_{95}=1.10±0.05 s), what makes it attractive enough for performing localized potentiometric scanning measurements in biomedical and corrosion science applications. However, no information about its selectivity against sodium or other ions was reported. The potential stability of the Mg^{2+}-selective microelectrode is similar to that of the pH-SME, i.e. the intensive use of ME affects their life time, decreases the linear slope and increases the response time. The applicability of solid contact Mg^{2+}-SME was demonstrated in a model experiment, which involved scanning of a local source of magnesium cations. The source of Mg^{2+}, simulating release of magnesium ions from a biological microobject or from a corroding microdefect on a magnesium based substrate, was a glass capillary filled with agar stabilized 0.01M $MgCl_2$ solution and mounted in a polished epoxy holder. The activity profile was measured 15 µm above the source in 0.01M NaCl. As in the case of such solid contact ISMEs for pH, only about two thirds of all produced microelectrodes were functional, due to existence of initial defects in POT and/or PVC layers. The microelectrodes with defects showed highly unstable and drifting potential during the first calibration and were discarded.

This review of Mg^{2+}-SMEs shows that the glass micropipette ISME with commercial membrane cocktail for Mg^{2+} seems to be the most advantageous to be implemented into SIET for corrosion applications, because of its analytical characteristics and simplicity.

3.7.3 Zn^{2+}-SMEs

The detection and quantification of Zn^{2+} is of interest to many different areas. Zinc is a metal of great technological importance being mostly used in galvanising of steel, batteries, brass metallurgy, die casting, as metal sheet and in chemical compounds for a broad range of industries. It also plays a significant role in living organisms and in a number of human metabolic processes. In corrosion research Zn^{2+}-SMEs have been used in a few studies.

As it is mentioned in Section 2.3.2, the spatial distribution of Zn^{2+} ions during galvanic corrosion was observed by Tada *et al.* using an amperometric minisensor (0.5 mm zinc disc electrode) [108]. Another amperometric microsensor, based on B-NCD for Zn^{2+} was reported by Silva *et al.* [189]. However, direct amperometric detection of Zn^{2+} in solution could suffer from several difficulties. A major drawback consists in the deposition of metallic zinc on the surface of the B-NCD tip microelectrodes [189], as well as on Pt-disc microelectrodes [247]. This may eventually lead to the blockage of the electrode, because the active area of microsensor is continuously modified during the measurements. Consequently, the changed microelectrode size disturbs current

proportionality to the original area of disk electrode surface (see Section 2.3.1). Another problem, related to the use of Pt-microelectrodes for the detection of zinc species, is the presence of dissolved oxygen in an aerated aqueous solution, as oxygen reduction potential and water itself overlap the reduction of zinc [247]. For these reasons, a potentiometric Zn^{2+} selective microsensor would be more suitable for measuring local distribution of zinc ions.

One of the first reported zinc-selective microelectrodes was described in 1995 by Wei and co-workers together with the theoretical introduction of potentiometric SECM [198]. Liquid membranes for glass micropipette MEs consisted of 5-7 wt% N-phenyliminodiacetic acid N,N-dicyclohexylbisamide (synthesized neutral carrier), 15-70 mol.% of KTClPhB, and 93-95% NhPOE. The response of the Zn^{2+}-SMEs was linear between 10^{-1}-10^{-5}M with slope of ≈ 27 mV/decade. The tip diameter varied from 1 to 20 µm. The selectivity and others analytically important characteristics of the Zn^{2+}-SMEs were documented by Toth *et al.* [248]. The $logK^{Pot}_{Zn2+,Me+}$ is around -3.1 for Na^+ or K^+ and below -4 for Mg^{2+} and Ca^{2+} for membrane composition of 5 wt% N-phenyliminodiacetic acid N',N'-dicyclohexylbisamide, 70mol.% of KTClPhB, NPhOE [248]. The response time value was not indicated in that article. Two configurations of Zn^{2+}-SMEs were fabricated and applied for studying a model zinc source system [198]. The source of Zn^{2+} ions was a microdisc amalgam electrode of 25 µm in diameter (target), at which Zn^{2+} reduction at -1.15 V vs Ag/AgCl RE from 0.84 M $Zn(NO_3)_2$ solution took place. The first type of Zn^{2+}-SMEs was a conventional ISME pulled from single-barrel borosilicate glass tubes. This ME was used for measurements of concentration profiles and for estimating a tip-to-target separation distance from them. However, the distance determined by concentration profile requires the establishment of steady-state conditions at the target. This difficulty was overcome by using another type of Zn^{2+}-SMEs, produced from double-barrel glass micropipettes. While one pipette channel was filled by the membrane cocktail and worked as a Zn^{2+}-SME, the second one served as a Ag/AgCl reference microelectrode and was also used as a distance sensor. Double-barrel tips with separate Ag/AgCl RE and a ISME have been fabricated and applied previously for the measurements of intracellular activities in order to avoid membrane potential of the cell [76]. Moreover, such type of dual-channel ME minimizes problems related to the simultaneous measurements of iR drop in systems with current flowing, since the RE is only a few micrometers away from the potentiometric ME [215].

The same neutral ionophore was used by Varga and co-workers for designing a solid contact micropipette electrode [249]. In this ME, the internal reference electrode was replaced by a 33 µm carbon fiber coated by a conductive polymer film, which was dipped into the ion-selective cocktail (Figure 18). The micropipette electrodes were made from two glass pipettes. The glass pipette with larger internal diameter held a 5-10 mm cocktail column, and the thinner one with carbon fiber inside was introduced into the

lumen of the first. A thin copper wire was used for electrical connection and mercury or silver epoxy paste provided contact between the carbon fiber and the copper wire. The tip of ME was either 3 or 7 µm. The cocktail consisted of 5 wt% N-phenyliminodiacetic acid N',N'-dicyclohexylbisamide, 1.8 wt% of KTClPhB, 80% NPOE, 13% PVC (for larger tips to provide mechanical stability).

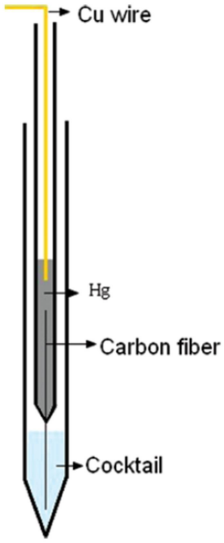

Figure 18. The configuration of solid state Zn^{2+}-SME. Taken from [249].

The internal resistance of the Zn^{2+}-SME with a tip of 3 µm in diameter was in the range of 40.9 MΩ/mm. The designed ME had a linear range of 10^{-4}-10^{-1}M with slope of 27.7 mV/decade. Response time or selectivity was not reported. However, the Zn^{2+}-SME was implemented for potentiometric SECM measurements. Effects of distance on the electrode potential were studied by using a glass micropipette filled with a solution of 0.1M $ZnSO_4$ + 0.1M KCl as a source of zinc ions (substrate). The variation of the electrode potential with the tip-substrate distance recorded above the centre of the source was used to convert the electrode potential readings to concentration values. The zinc concentration profiles were measured above the Zn and Fe galvanic couple. The Zn^{2+}-SME (7 µm tip) was scanned over a surface of small size Zn and Fe discs, both inserted in an epoxy resin holder and connected at the back. The detection of Zn ionic species was clearly observed when the ISME tip passed above the zinc disc, whereas no signal could be measured either above the surrounding epoxy resin or the iron disc.

In spite of these two works, not more was found about potentiometric Zn^{2+}-SMEs. Both articles were based on the same synthesized ionophore, which obviously, is not commercially available. Moreover, the prepared Zn^{2+}-SMEs showed rather small linear range and no records about their response time were found.

3.7.4 Cu^{2+}-SMEs

Copper is a mineral and an important element to our everyday life. Copper and its alloys have been used for thousands of years. It is a major industrial metal because of its high ductility, malleability, thermal and electrical conductivity and resistance to corrosion. The major applications of copper are in electrical industry, construction, transportation, industrial machinery, telecommunications, and also in alloys (for example in aluminium alloy AA2024). Copper also plays an essential role in biological systems and in the environmental field; it is a vital element for most animals. Thus copper detection is an important task for scientists.

The electrochemical approach to chalcogenide glass preparation offered exceptional possibilities for producing Cu^{2+}-selective electrodes [250–252]. These materials in form of thin films are very suitable for all solid state potentiometric sensors or for ISFET technology [253]. Several examples of Cu^{2+}-sensitive microsensors based on chalcogenide glasses were found [253–255] (Table 4).

One of them is a Cu/CuSe microelectrode, described by Papeschi *et al.* [255]. The microsensor was prepared by cathodic deposition of Se and subsequent formation of a thin layer of CuSe on a copper wire insulated with thin layer of lacquer. The chalcogenide coatings on copper as well as on silver are obtained by cathodic deposition of selenium onto the metal base, where it reacts to give the corresponding selenide [256,257]. The process occurs in 0.1M Na_2SeO_3 solution whose pH is adjusted to about 6 with sulphuric or hydrochloric acid. The obtained Cu/CuSe microelectrodes were used in the "vibrating probe method" for measuring net temporal and spatial fluxes of Cu^{2+} in Olea europaea roots. The described microsensors showed near Nerstian slope toward Cu^{2+} in the concentration range from 2 to 6 pCu, had fast response time (<0.5 s) and good selectivity with respect to Ca^{2+}, Mg^{2+}, NH_4^+, Na^+ and K^+ (Table 4).

Kupper and Schultze presented a coated wire microsensor based on copper sulfide of complex composition [258] (Table 4). The crystalline sensor material was embedded in a polymer membrane, which was deposited on a microdisc platinum electrode. Electrochemical characterization of the obtained microsensor showed an excess of sulphur within the solid membrane layer as sulfidic and polysulfidic species. The prepared Cu^{2+}-SMEs showed good reproducibility and were highly selective against Zn^{2+} and Ni^{2+} ions. The microsensor was applied for locally resolved concentration measurements during electrolytic copper deposition. The weakness of the reported Cu^{2+}-SME was an unusual linear slope of 50 mV/pCu. The reasons of that were discussed in terms of different valences of copper atoms.

Table 4. Examples of different Cu^{2+}-selective microsensors found in literature.

Type of ME	Membrane	Size	Characteristics[#]	Selectivity, X, $logK^{Pot}_{Cu2+,X}$	Reference
ISFET	Cu-Ge-Se-Sb	film of 0.4-1 μm	S = 28 mV/ pCu; LR = 3-5.5 pCu; DL - 10^{-6} M; $\tau \approx 5$ s;	Na^+ -5.3 Fe^{3+} -1.3 Ni^{2+} -4.2	[253]
thin film	Cu-As-Se	15-30 nm	S = 27-30 mV/ pCu; LR = 2-5 pCu; DL - $0.8\cdot10^{-6}$ M; $\tau \approx$10-20 s;	Fe^{3+} 0.4 H^+ -3.5 Ni^{2+} -5.7	[254]
wire	Cu/CuSe	Tip Ø 25; 50; 75 μm	S = 26 mV/ pCu; LR = 10^{-3}-$5\cdot10^{-5}$ M; DL - 10^{-6} M; $\tau <$ 0.5 s;	Na^+ -5.7 Mg^{2+} -3.6 K^+ -7.4	[255]
wire	polymer embedding CuS_x – crystallites	Tip Ø 20-30 μm	S = 50 mV/ pCu; LR = 1.0-10^{-4} M; DL - 10^{-6} M; $\tau_{90} \approx$ 10 s;	Interfering species: dissolved O_2, C (Cl^-) ≥ 10^{-3}M	[258]
ISFET	macrocyclic carrier*, NPhOE, KTClPhB, PVC	film of 90-130 μm	S = 29.5±1 mV/ pCu; LR = 10^{-2}-10^{-6} M; DL - $5.62\cdot10^{-7}$ M; $\tau \approx$ 14 s;	Na^+ ≈-4.2 Interfering ions: Mg^{2+}, Ca^{2+}	[259]
ISFET	p-tert-butylcalix-[9]arene	film	S = 24 mV/ pCu; LR = 10^{-2}-$10^{-4.5}$ M; DL - 10^{-5} M; $\tau <$ 1 s;	K^+ -4.9 Ca^{2+} -2.8 Pd^{2+} -1.6	[260]
ISFET (checker)	charged carrier, DOP, PVC	not mentioned	S = 28.1 mV/ pCu; LR = 10^{-3}-10^{-7} M; DL - $6.3\cdot10^{-8}$ M; τ_{95} = 8 s;	Ag^+ 0.0 Fe^{3+} -4.9 Zn^{2+} -4.7	[261]

*- see text for details; [#]S – slope; LR – linear range, DL – detection limit, τ – response time.

Solid-state electrodes based on chalcogenide glasses are now well established sensors, but unfortunately Fe^{3+}, Ag^+ and other ions are serious interferences (see Table 4 and references cited there).

A number of various carrier types has been investigated as potential ionophores for Cu^{2+}-SE [210]. Among them attractive selectivity toward Cu^{2+} revealed macrocyclic and noncyclic carriers containing sulphur atoms [210]. Following this concept, Marques de

Oliveira and co-workers synthesized a dithiomacrocyclic neutral carrier, (4-phenyl-11-decanoyl-1,7-dithia-11-azacyclotetradecane-4-sulfide), which they successfully used in all-solid-state PVC-membrane for ISFET [259]. The fabricated microsensor exhibited good linear response, low detection limit (Table 4) and high selectivity toward variety of other cations [259].

Several others ISFETs with carrier based PVC membranes were described recently [260,261]. However, no reports about Cu^{2+}-sensitive potentiometric microelectrodes based on liquid membrane cocktails were found in literature.

3.7.5 Al^{3+}-SMEs

The detection and quantification of aluminium is important in areas as diverse as the health and life sciences, environmental and pollution research, industrial production, surface engineering and materials degradation. In all of them aluminium can be found in aqueous media in ionic form. In spite of the importance of aluminium neither pontentiometric, nor amprerometric microsensors have been described in literature. Dozens of neutral carrier based membrane compositions have been reported during last decades for fabrication of conventional ISE for aluminium cations. But only one substance as aluminium ionophore, morin (aluminium ionophore I), was commercialized by Fluka [219] based on Al^{3+}-selective electrode in PVC matrix presented by Gupta [262]. Even though, an ISE for routine analysis of Al^{3+} is not available on the market due to existence of several limitations in the reported sensors. As this chapter is dedicated to microelectrodes, an overview of Al(III)-selective electrodes will be given in Chapter 8.

Among other types of microelectrodes used for aluminium determination in solution one can find different optical sensors. For example, a fiber-optic imaging sensor based on immobilized morin was used for investigation of localized corrosion behaviour of a galvanic aluminium-copper couple in NaCl solution by Szunerits and Walt [263]. A stable aluminium sensor was constructed by covalently attaching morin to the distal end of an imaging fiber, previously modified with (3-aminopropyl)-triethoxysilane and a poly(acrylamide-*co*-N-acryloxysuccinimide) layers. Morin forms a highly fluorescent complex with Al^{3+}, which could be imaged with the optical fiber bundle (350 μm in diameter) to localize regions of corrosion on the surface of the metal. The optical sensor allowed the *in situ* visualization of localized corrosion over time by monitoring the release of Al^{3+}. However, this approach has some limitations. The method is not a truly nonperturbing one, because the metal surface of interest is not freely exposed to the surrounding solution as the sensor is placed over it. Other important limitation is the irreversible response of the Al^{3+}-sensitive sensor due to the formation of a chelate on the modified fiber end. The imaging fibre needed to be regenerated by dipping it into EDTA solution to dissociate the complex. Ultimately, to quantify the aluminium concentration a

kinetic approach should be used, in which the fluorescence signal is measured after a constant time period, 5 minutes in this case.

3.8 Concluding remarks

Potentiometric microsensors can be a good option to assess chemical information about different objects in small sample volumes and with high spatial resolution, but careful choise of electrode material and type is necessary.

In spite of the body of work already published dealing with microsensors, much of it was just exploratory or remains in a preliminary stage in terms of their regular applications in corrosion research. Time and efforts are needed to develop and test the qualities and response of such microelectrodes, particularly in real corrosion situations, when the processes evolve relatively fast, change location and the appearance of corrosion products interferes with the approximation of the probes to the metal surface.

During the PhD work, microelectrodes sensitive to pH, dissolved oxygen and metal cations (namely, Mg^{2+}, Zn^{2+}, Cu^{2+} and Al^{3+}) will be developed and used for SIET measurements. Their fabrication approaches as well as characterization and suitability for testing real corrosion systems will now be demonstrated and discussed.

Chapter 4

4 Experimental procedures

This chapter presents the materials and reagents used in this work as well as the equipment and experimental methodology.

4.1 Materials

The metallic samples tested in this work were plates of aluminium alloy AA2024-T3 and cast magnesium alloy AZ31 and wires of zinc, copper and iron. Their composition and dimensions are described in Table 5. The AA2024-T3 and AZ31 alloys were donated by Airbus (Germany) and Alubin (Israel), respectively. The wires were supplied by Goodfellow (USA).

Table 5. Description of used materials.

Metal/Alloy	Type	Dimensions	Nominal composition	Reference
AA2024-T3	plates	2.5 x 4 cm^2	3.8-4.9 wt.% Cu, 1.2-1.8 wt.% Mg; < 1wt.% Cr, Fe, Mn, Si, Ti, Zn, others; Al balance	[264]
AZ31	plates	2.5 x 4 cm^2	3 wt.% Al, 1 wt% Zn; Mg balance	[264]
Zn	wire	Ø1.0 mm	≥99%	
Fe	wire	Ø1.0 mm	≥99%	
Cu	wire	Ø1.5 mm	99.99%	
Pt	wire	Ø1.0 mm	≥99%	

4.2 Reagents

The reagents used are shown in Table 6. Other compounds, which were used occasionally, are given in the context of their application.

Table 6. Reagents.

Formula / short name	Name
NaCl	sodium chloride
KCl	potassium chloride
KH_2PO_4	potassium dyhydrophosphate
HNO_3	nitric acid, concentrated
$Mg(NO_3)_2$	magnesium nitrate
$Zn(NO_3)_2 \cdot 6H_2O$	zinc nitrate hexahydrate
$ZnCl_2$	zinc chloride
$Cu(NO_3)_2$	copper nitrate
$CuCl_2$	copper chloride
$Al(NO_3)_3$	aluminum nitrate
HF	fluoric acid, concentrated
HCl	hydrochloric acid, concentrated
HNO_3	nitric acid, concentrated
NaOH	sodium hydroxide, grains
$Ce(NO_3)_3 \cdot 6H_2O$	cerium (III) nitrate hexahydrate
Na_3PO_4	trisodium phosphate
$C_2H_3N_3$	1,2,4-triazole
$C_6H_5N_3$ / BTAH	benzotriazole
GPTMS	(3-glycidoxypropyl)-trimethoxysilane
TAP	titanium diisopropoxide bis(acetylacetonate)
TPOZ	zirconium (IV) tetra-propoxide
$C_6H_{10}O_3$	ethyl acetoacetate
$C_5H_8O_2$	acetylacetone
i-C_3H_6OH	2-propanol
C_2H_5OH	ethanol

All substances used were purchased from Sigma-Aldrich and were of *puriss* or *purum* grade. The solutions were prepared with deionized water (≈18MΩ cm).

4.2.1 Reagents for ISEs

Table 7 presents chemicals used for membrane preparation of ISEs and ISMEs. Ionophores (commercial and custom synthesized) for membranes of Zn^{2+} and Al^{3+} selective electrodes will be reported in Chapters 7 and 8 respectively.

Table 7. Reagents used for membranes preparation.

Name	Acronym	The main purpose of use	Supplier (Ref.)
N,N'-dimethyltrimethylsilylamine	-	silanizing agent	Fluka (41716)
Hydrogen ionophore I cocktail B	-	membrane for pH-SME	Fluka (95293)
Hydrogen ionophore II cocktail A		membrane for pH-SME	Fluka(95297)
Magnesium ionophore II cocktail B	-	membrane for Mg^{2+}-SME	Fluka (63101)
tetra-*n*-butylthiuram disulfide	TBTDS	Zn^{2+} or Cu^{2+} ionophore	Fluka (96491)
sodium tetraphenyl borate	NaTPhB	ion exchanger 0	Fluka
calcium 2,3,4-trioctyloxybenzenesulfonate	$Ca(TOBS)_2$	ion exchanger 1	BSU (Minsk)
potassium tetrakis(4-chlorophenyl) borate	KTClPhB	ion exchanger 2	Fluka
sodium tetrakis[3,5-bis(trifluoromethyl)-phenyl] borate	NaFMPhB	ion exchanger 3	Fluka
bis(2-ethylhexyl)phosphate	BEHP	ion exchanger 4	Fluka
tetradodecyl ammonium tetrakis(4-chlorophenyl)borate	ETH 500	ion exchanger 5	Fluka
2-nitrophenyloctyl ether	NPhOE	plasticizer A	Fluka
dibutyl phthalate	DBP	plasticizer B	Fluka
tris(2-ethylhexyl)phosphate	TEHP	plasticizer C	Fluka
bis(1-butylpentyl)adipate	BBPA	plasticizer D	Fluka
2-nitrophenylpenthyl ether	NPhPE	plasticizer E	Fluka
Tetrahydrofuran	THF	PVC solvent	Fluka
poly(vinyl chloride), high molecular weight	PVC	membrane matrix	Fluka

The commercial membrane components were of Selectophore grade purity. Commercial buffer solutions with pH 2 to 14 were used for calibration of pH-selective electrodes.

4.3 Samples preparation

4.3.1 Coated samples

4.3.1.1 Sol-gel synthesis

The organic–inorganic film was synthesized via the sol-gel route, mixing two different sols. A silane-based alkosol was combined with another alkosol containing titania (for AZ31 alloy) or zirconia (for AA2024-T3 alloy) precursors in order to obtain the hybrid sol. The first silane-based alkosol was prepared by acid (HNO_3, pH 0.5) catalysed hydrolysis of GPTMS in 2-propanol solution (1:1 volume ratio). The second alkosol was prepared by acid catalysed hydrolysis of TPOZ (70 wt. % in 2-propanol) in ethylacetoacetate (for AA2024-T3) or TAP (70 wt. % in 2-propanol) in acetylacetone (for AZ31). The final sol–gel solution (with 2:1 volume ratio of the first and the second sol, respectively) was stirred under ultrasonic agitation for 1 h and aged for 1 h. More details on the synthesis can be found in [38,265] for AA2024-T3 and in [266] for AZ31.

4.3.1.2 Substrate preparation

Aluminium alloy AA2024-T3 samples were etched using an industrial 3-steps cleaning procedure: (1) alkaline cleaning in 48 ± 2 g L^{-1} Metaclean T2001^{TM} (CVH Chemie-Vertireb GmbH & Co. Hannover KG, Germany) at 65 ± 5 ^{o}C for 20 ± 5 min, followed by (2) alkaline etching in 65 ± 5 g L^{-1} Turco Liquid Aluminetch N2^{TM} (Henkel, Germany) at 60±5^{o}C for 45±15 s and completed by (3) acid etching in 180±10 mL L^{-1} Turco Liquid Smutgo NC^{TM} (Henkel, Germany) at 25±7^{o}C for 8 ± 2 min. The samples were thoroughly washed in distilled water between each cleaning step. Then they were dried in a flow of warm air.

Magnesium alloy plates (AZ31) were polished by sand paper in ethanol changing grade sequentially from 1200 to 2500, then chemically etched by 12% HF during 15 min at room temperature and rinsed with deionized water. The cleaned AZ31 substrates were dried at 105°C during 1 h.

4.3.1.3 Sol-gel application

The sol–gel films on metallic substrates were applied by a dip-coating procedure. Then the samples were cured in the oven for 1 h. The coated samples were kept in a desiccator when not in use.

4.3.1.4 Samples mounting

Pieces of 1x1 cm^2 of coated alloys samples were cut and glued directly to an epoxy base (1 cm height, 3 cm in radius). The edges were masked by beeswax+colophony (3:1 wt. ratio) leaving a small open window (approximately of 2 mm^2) (Figure 19 a). Then round-shaped artificial defects down to the metal substrate were produced in the coating by a metallic needle. Sometimes scratches were used. The scratches, about 150 µm in width and variable length, were made by a thin scalpel. A scotch tape (15 mm width) was attached around the epoxy holder providing a reservoir for the testing solutions (as in Figure 19 b for a wire electrode).

4.3.2 Metallic wires

Metallic wires of Zn, Fe and Cu were embedded in cylinder shaped (1 cm height, 3 cm in radius) epoxy mounts as single or couple electrodes (Figure 19 b, c). Before each experiment the electrode surface was restored by polishing the sample with SiC sand paper, changing the grade sequentially from 800 to 2500, in distilled water. A scotch tape (15 mm width) was attached around the epoxy holder providing a reservoir for the testing solutions (Figure 19 b).

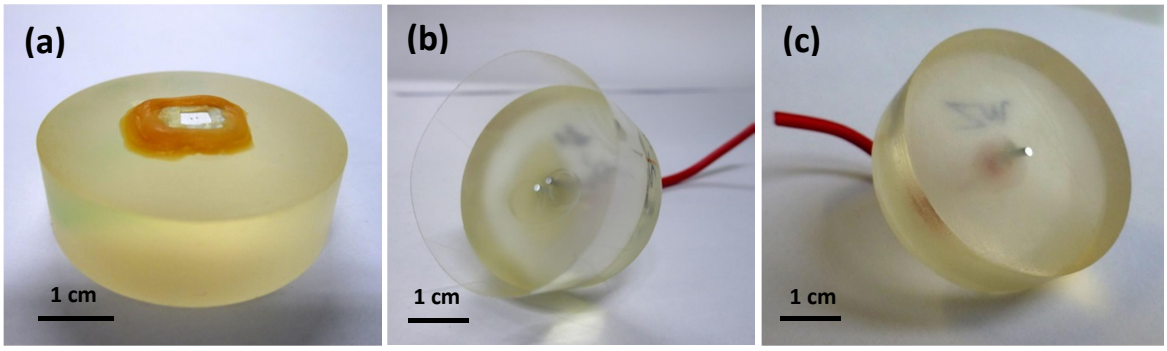

Figure 19. Prepared samples of AA2024-T3 alloy with two defects in the coating, with edges masked by beeswax+colophony– (a); Zn-Fe couple with scotch tape – (b), and Zn wire – (c).

4.4 Equipment setup

4.4.1 SVET apparatus

For the SVET measurements commercial equipment from Applicable Electronics Inc. (AEI, USA) controlled by the ASET 2.0 (Automated Scanning Electrode Technique) software from ScienceWares Inc. (USA) was used. Figure 20 shows a schematic view of the equipment, consisting of a 2 channels lock in amplifier (PSDA-2) (1), a pre-amplifier

(2), two piezoelectric oscillators in isolated box (3), responsible for probe vibration, a motion control panel (4), probe motors (5), a computer (6), a monitor (7), the sample (8) and a video camera (9). An anti-vibration table, a Faraday cage and an uninterruptible power supplay (UPS) with power peak filtering are optional but recommended parts, which substantially improve the system operation.

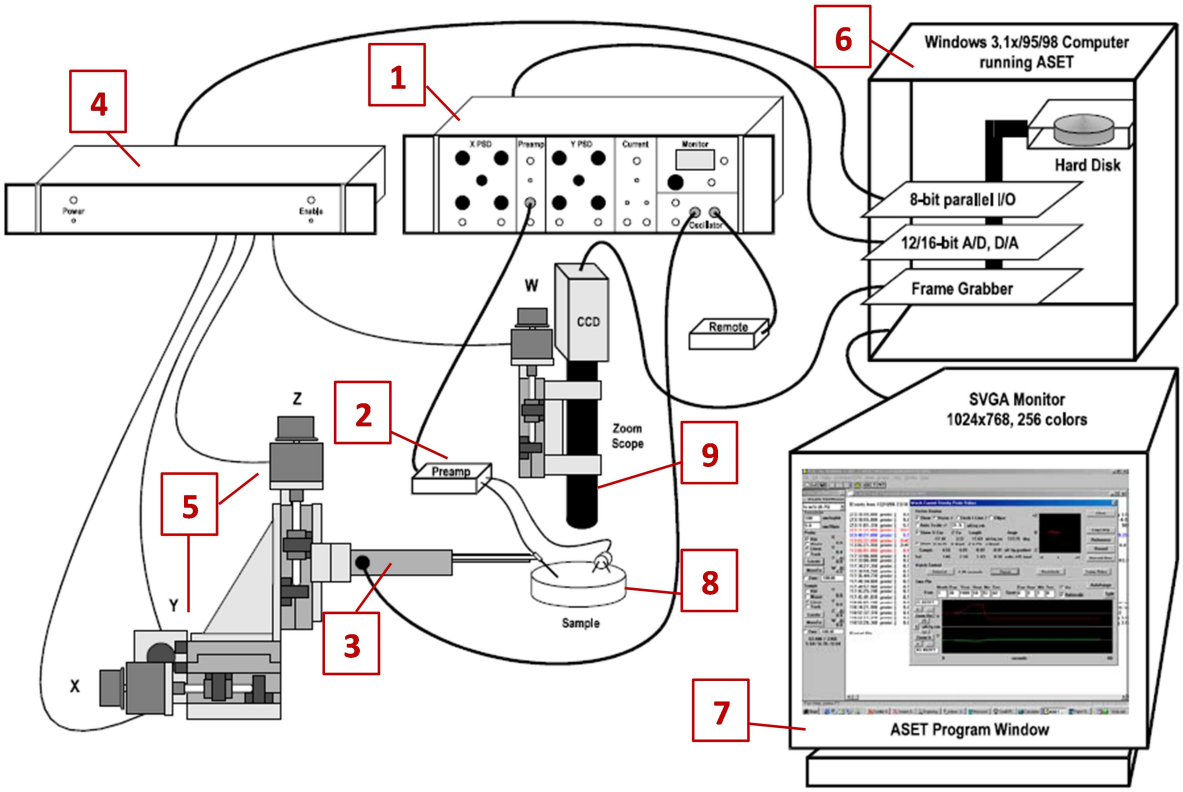

Figure 20. Scheme of interaction between different modules of SVET apparatus controlled by ASET software. Taken from ASET guide. The numbers are labeled in the text.

The electrochemical cell setup (Figure 21) includes a Pt vibrating microprobe, one ground and one reference electrode and a sample glued to an epoxy holder. A 3D computerized stepper-motors system is used to position and move the microprobe over the sample. A light source and a video camera with a magnification up to 400 times are located over the sample.

The probe was usually located 100 µm above the sample surface and vibrated in two directions, one parallel (X axis) and another perpendicular (Z axis) to the surface at different frequencies and amplitude double of the tip diameter. Signals were processed by the two channels lock-in amplifier. Only signals from the field normal to the surface (Z axis) were used in the present study. The measured potentials were converted by software to ionic currents. A prior calibration with a point current source driving 60 nA at 150 µm from the vibrating probe was made as described elsewhere [141,143].

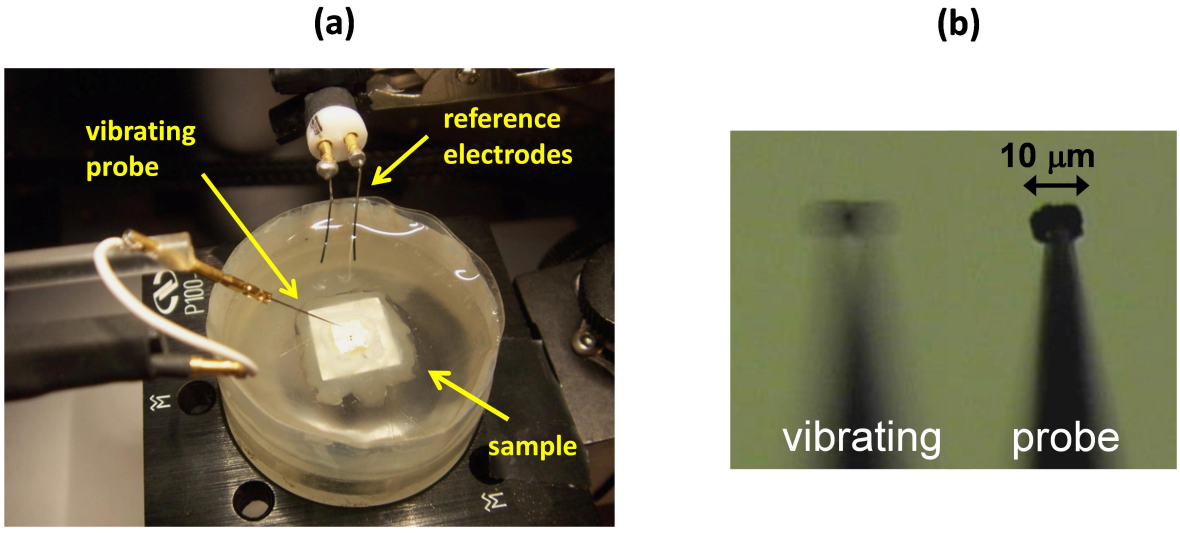

Figure 21. SVET cell (a) and probe vibrating with an amplitude with the double of the tip size (b).

4.4.2 Potentiometric (SIET) and amperometric modes

The set-up used was basically the same previously described manufactured by AEI (USA) and controlled by ASET 2.0 software. A two electrode electrochemical cell under zero current conditions was used to perform potentiometric measurements. The potentiometric cell was composed of a reference electrode and an ion-selective microelectrode. The IPA2 two channels amplifier with input resistance $>10^{12}\Omega$ was used to measure potential. An additional pre-amplifier head (gain 1 or 10 and input resistance $>10^{15}\Omega$) was used for measuring small changes in signal values of potentiometric microsensors (Figure 22, a). A homemade Ag/AgCl, 0.05M NaCl mini-electrode with the inner solution stabilized by 3% agar-agar was used as external reference electrode (Figure 22, b). The size of its orifice was around 2 mm.

For detection of dissolved oxygen the IPA2 amplifier worked in the amperometric mode. A two electrode cell also was used with a homemade Ag/AgCl reference electrode and a 10 µm Pt wire as amperometric sensor. An additional pre-amplifier head (with switch between pico or nano amperes) was used. The working microelectrode and the corresponding pre-amplifier were mounted in the same 3D positioning system used for SVET and SIET.

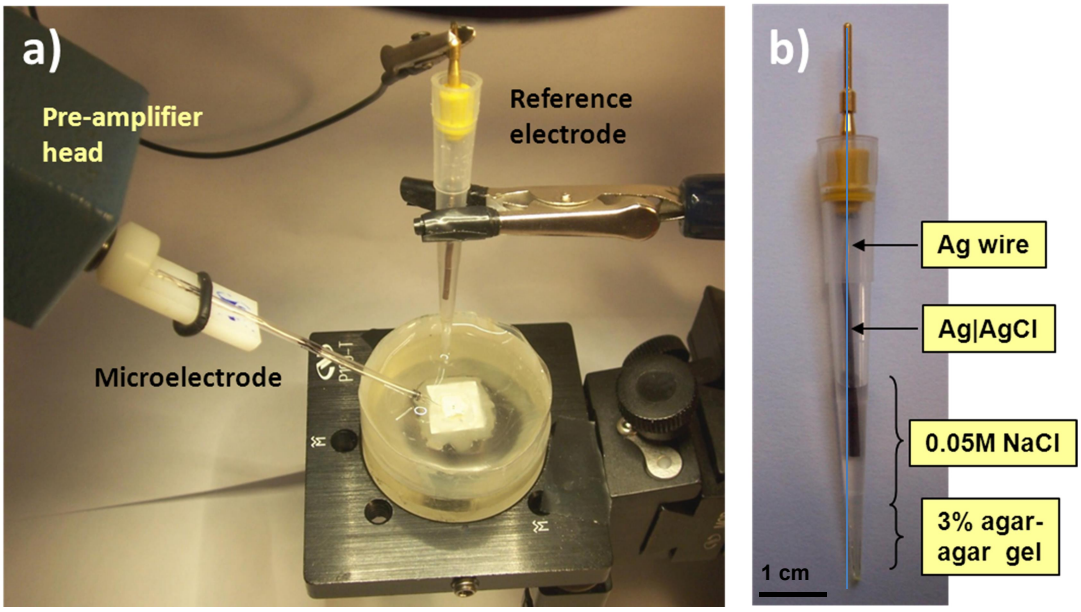

Figure 22. Photographs of SIET arrangement, a) and a homemade reference electrode, b).

4.4.3 Apparatus for ISEs testing

Ion-selective macroelectrodes (further only referred as electrodes) with plasticized membranes were used for a number of tests. The measurements were performed either using 8-channels pH-meter/ion-meter Ecotest-120 (Econix, Russia) and Ag/AgCl, saturated KCl - reference electrode EVL-1M3.1 (Izmeritel, Belarus) or by Sevenmulti Mettler Toledo AG meter (Switzerland) with its Ag/AgCl, saturated KCl - reference electrode (InLab® Reference, № 51343190, Mettler Toledo, Switzerland). A Sevenmulti Mettler Toledo AG meter (Switzerland) with combined pH-electrode (InLab® Expert Pro, № 51343101, Mettler Toledo, Switzerland) was also used to control pH in calibration solutions.

4.5 Microelectrodes fabrication

4.5.1 Microelectrodes for SVET

The microelectrodes used in SVET were Pt (80%)-Ir (20%) wires from MicroProbes Inc., USA [267] insulated with parylene C® (chemical vapour deposited poly(*p*-xylene) film) except for the very tip. For the SVET measurements the tip was covered with a platinum black deposit plated with an aqueous solution of 0.02M H_2PtCl_6 (Merck) + $2 \cdot 10^{-4}$M $Pb(CH_3COO)_2$ (Riedel-de Haen, Ref. 32307). For plating, a current of -200 nA was applied for 5 minutes followed by 10-20 spikes at -1500 nA. The final SVET tip is usually 10-20 µm in diameter.

4.5.2 Glass capillary microelectrodes

The ISMEs (namely, pH-SME, Mg^{2+}-SME, Zn^{2+}-SME, Cu^{2+}-SME and Al^{3+}-SME) for SIET were made of single-barreled, standard-wall (330 µm) borosilicate glass capillaries (TW 150-4, WPI, USA) with an outer diameter of 1.5 mm. A P-97 Flaming/Brawn Micropipette Puller (Sutter Instruments, USA) was used to shape the cone tip. The diameter of the tip was 1.5 ± 0.3 µm.

The obtained micropipettes should be properly treated before filling with a liquid membrane cocktail. The liquid membrane cocktail consists of a mixture of organic substances, dissolved in a solvent that is immiscible with water. Since a glass surface is highly hydrophilic (it can have up to 4.6 free hydroxyl groups per 10 nm^2 of glass [76]) water would rapidly displace the membrane cocktail from the untreated tip of a micropipette. Thus, the free hydroxyl groups on the glass surface are made to react with organic silicon compounds (so called silanization procedure), so that the covered glass surface becomes hence hydrophobic (Figure 23).

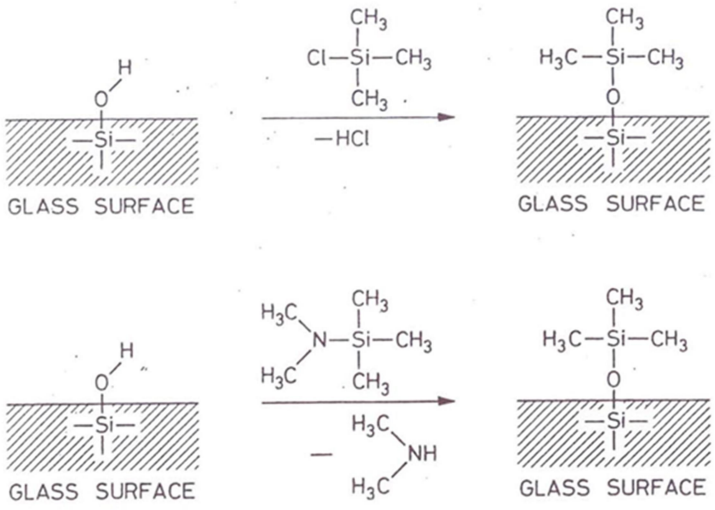

Figure 23. Silanization of glass surfaces with trimethylchlorosilane (upper) or N-trimethylsilyldimethylamine (lower) [76].

This principle of silanization was introduced by Walker [190] and over the years has been modified [76]. In this work the vapour method of silanization was used, as it makes possible fast and technically simple simultaneous preparation of many dozens micropipettes. The glass capillaries firstly were dried overnight at 150°C in a glass preparation chamber (Figure 24, a) and then silanized by injection a 200 µl of N,N'-dimethyltrimethylsilylamine at 200°C with further heating for more 30 minutes. After slow cooling inside the oven the silanized glass micropipettes were taken out and kept in a desiccator during ca. 30 days for which the silanized layer was considered to be stable.

The ion-selective microelectrodes were prepared before each experiment. Firstly, micropipipettes were back-filled with an inner reference solution by a syringe with a flexible needle. Secondly, they were front-filled with a liquid membrane cocktail by capillary action and small suction using an optical light microscope (1113AMH Binocular Microscope, VanGuard, USA) with two 3D micromanipulators (Figure 24, b, c). Properly fabricated ISME should have no air bubbles in the tip either from the inner solution side or from the outside.

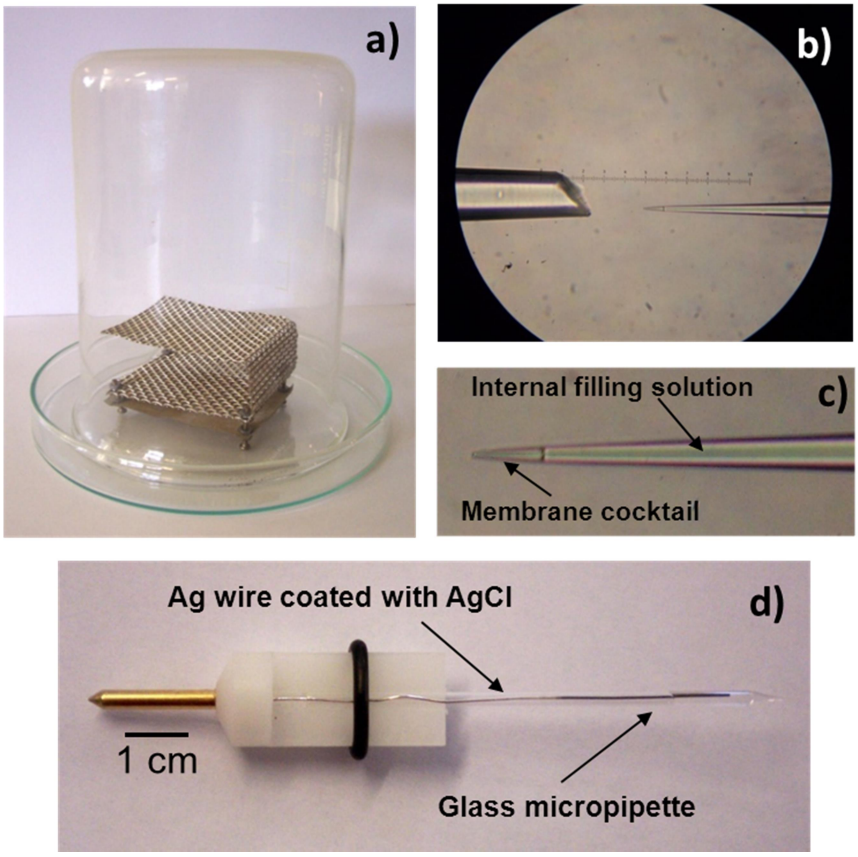

Figure 24. Photographs of the silanization chamber, a); the glass micropipettes: view under the microscope during front filling from spare broken capillary, b); a 25 µm column of membrane cocktail at the tip, c); a ready to use microelectrode, d).

Finally, a Ag/AgCl wire embedded in a Teflon support with rubber ring for capillary fixation was inserted into the internal electrolyte from the back side of the pipette to provide inner reference electrode electrical contact (Figure 24, d).

4.5.2.1 Liquid membrane cocktails preparation

The **pH-SME** was based on the commercial cocktail – Hydrogen ionophore I cocktail B (Fluka, Germany). The composition of cocktail is described in Table 3. The inner

reference solution contained 0.01M KH_2PO_4 + 0.1M KCl. The used column length was the one recommended by Fluka catalogue [237], which is 25-30 µm.

The **Mg^{2+}-SME** was also based on a commercial available cocktail – Magnesium ionophore II cocktail B (Fluka, Germany). It contained 10% of magnesium ionophore II – N,N''-octa-methylenbis(N'-heptyl-N'-methyl-methylmalonamide), 3% KTClPhB, 62% NPhOE and 25% chloroparaffin. The internal reference solution consisted of 0.1M $MgCl_2$. The used column length was 35-40 µm, the one recommended by Fluka catalogue [237].

The membrane cocktails for **Zn^{2+}-SMEs, Al^{3+}-SMEs** and **Cu^{2+}-SMEs** (of 100 µl) were prepared by weighing an appropriate amount of an ionophore and adding an appropriate quantity of an ion exchanger and solvent into a polypropylene vial. Then the components were thoroughly mixed using an ultrasonic bath (ca. 15 minutes). Column lengths of 40 and 120 µm were tested for Zn^{2+}-SME and 120 µm for Cu^{2+}-SMEs and Al^{3+}-SMEs. The compositions of internal reference solutions and prepared cocktails are reported in the next chapters corresponding to each type of ISME.

4.5.3 Copper sensitive solid state microelectrode

The solid state Cu^{2+}-selective microelectrode (Figure 25) was made of Pt-Ir wire used in SVET (Figure 21). Firstly, a platinum deposit was plated at the tip from an aqueous solution (0.02M H_2PtCl_6 + $2 \cdot 10^{-4}$M $Pb(CH_3COO)_2$) at a current of -200 nA for 5 minutes followed by a current of -500 nA for 10 minutes. Secondly, copper was deposited with a solution of 0.2M CuCN (Fluka, Ref. 61176) + 0.6M NaCN (Sigma-Aldrich, Ref. 71431) + 0.1M Na_2CO_3 (Fluka, Ref. 71352) and pH 11-12 [268] at -100 nA for 60 minutes. Finally, to make the electrode sensitive to Cu^{2+} a layer of copper selenide was obtained on the copper surface by cathodic deposition (current of -100 nA for 30 minutes) from 0.1M Na_2SeO_3 solution adjusted to pH 6 with sulphuric acid, as described in reference [255].

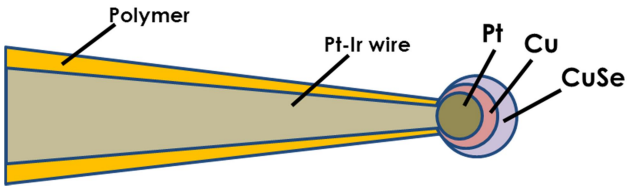

Figure 25. Schematic picture of Cu^{2+} sensitive solid state microelectrode.

4.6 Macroelectrodes preparation

While the focus of this work was microelectrodes, electrodes of conventional type for Zn^{2+} and Al^{3+} were studied to find optimal conditions of operation to apply to the microsize.

Zinc- and aluminum-selective electrodes were fabricated according to the following procedure. All membrane components (PVC, plasticizer, ionophore and ion-exchanger) were weighed precisely and dissolved in THF. The obtained mixture was poured into a glass raschig ring fixed on a glass plate (Figure 26) and the solvent was allowed to evaporate overnight. Membrane discs (approximately 0.5 mm thick and 1 cm in diameter) were cut out from the master membrane and glued on the top of poly(metylmetacrylate) tubes with PVC:THF = 1:15 mixture. A Ag/AgCl wire connected to a BNC-end cable was screwed to provide electrical contact.

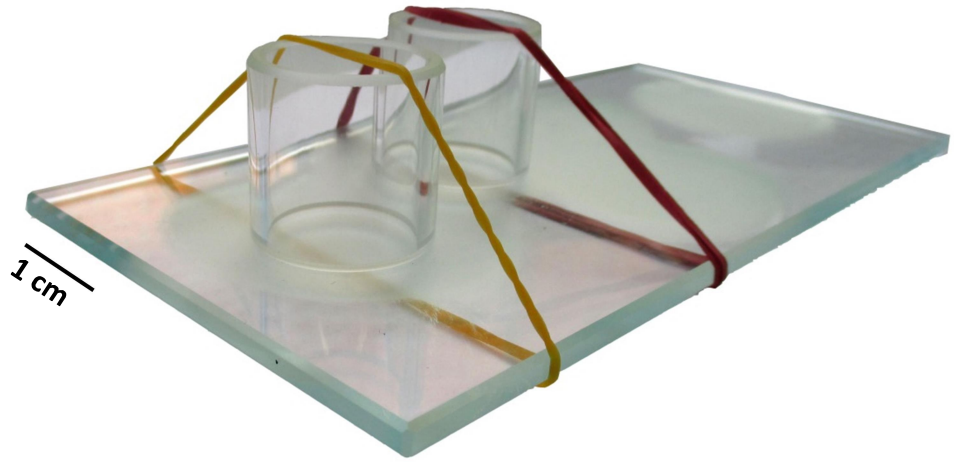

Figure 26. Glass raschig rings fixed on the glass plate for producing PVC membranes.

The compositions of the produced membranes for Zn^{2+}- and Al^{3+}-selective electrodes are presented in Chapters 7 and 8 respectively.

Obtained Zn^{2+}-selective electrodes were preconditioned in 10^{-2}M $Zn(NO_3)_2$ during 24h and filled with 10^{-3}M $Zn(NO_3)_2$ + 10^{-2}M KCl solution. The Al^{3+}-selective electrodes were preconditioned in 10^{-2}M $Al(NO_3)_3$ during 24h and filled with 10^{-3}M $Al(NO_3)_3$ + 10^{-2}M KCl solution.

4.7 Measurements

4.7.1 Characterization of ISMEs

4.7.1.1 Calibrations of ISMEs

Before calibration ISMEs were immersed in a dilute solution of target ion (usually 10^{-4}M) during ca. 20 minutes for preconditioning. The potentiometric microelectrodes were calibrated by measuring the potential in each calibration solution during 3-5 minutes versus a homemade Ag/AgCl/0.05M NaCl mini-electrode with the inner solution stabilized by 3% agar-agar (Figure 22 b). The activities of ions in the calibration solutions were calculated according to the Debye–Huckel theory [233] using Equations 3.4-3.6 (Chapter 3).

The pH-SMEs were calibrated using commercial buffer solutions with pH values from 2 to 14. The calibration plots of Mg^{2+}-SME, Zn^{2+}-SME, Cu^{2+}-SME and Al^{3+}-SME were determined in solutions with concentrations of metal ion from 10^{-6}M to 10^{-1}M with and without NaCl background solution.

Before use the important characteristics of produced ISMEs were determined according to IUPAC requirements [228]. Before and after each experiment the response of ISMEs was checked by three calibration solutions with concentrations close to the one to be measured. The ISMEs with slope less than 90% of Nernstian value were discarded.

4.7.1.2 Determination of response time of ISMEs

The determination of response time and selectivity coefficients of ISMEs (next Section 4.7.1.3) was carried out by colleagues from Instituto Superior Técnico (IST), Lisbon, Portugal, in the frame of the project SISET (Marie Curie Actions, FP7-PEOPLE-IRSES-GA-2010-269282).

Two different approaches were used for quantification of the response time, τ_{lim} and τ_{95}. The response time of the microelectrode, τ_{lim}, is the time elapsed between the instant when the microelectrode was brought into contact with the solution and the instant at which the potential/time slope ($\Delta E/\Delta t$) reaches a limiting value 1 mV/min (by IUPAC recommendation [228]). The time needed to obtain 95% of the total potential change, τ_{95}, was also determined for comparison, as this value is often found in the literature.

The values of response time, τ_{95} and τ_{lim}, were measured using a ‘‘dual drop cell” described elsewhere [230]. The cell contained two drops (ca. 1 µl each one) of solutions with different activities placed in very close proximity to each other (ca. 100 µm) and connected to a Ag/AgCl reference mini-electrode by a salt bridge. The ion-selective

microelectrode was moved by the PC-controlled motors from one drop of solution to the other. The two response times were obtained from the potential vs time curve.

4.7.1.3 Determination of selectivity coefficients to Na^+ by modified SSM

The selectivity coefficients of the Mg^{2+}-SME and Zn^{2+}-SME to Na^+ ions were determined by the modified SSM, which involves calibration of the electrode in solutions of the main and then of the interfering ion in order to determine graphically a standard cell potential value for a = 1 M, $E^0_{M^{z+}}$ [228,231].

Exemplifying for the Mg^{2+}-SME, Figure 27 shows the graphical determination of $E^0_{Na^+}$ and $E^0_{Mg^{2+}}$, which are used in Equation 4.1 to calculate $logK^{pot}_{Mg^{2+},Na^+}$ [230]:

$$logK^{pot}_{Mg^{2+},Na^+} = (E^0_{Na^+} - E^0_{Mg^{2+}})\frac{z_{Mg^{2+}}F}{RT\ ln10} \quad (4.1)$$

where $z_{Mg^{2+}}$ is the charge of Mg^{2+}, F, R and T have their usual meaning. This Equation is a simplification of the Equation 3.9 for $a_{Mg^{2+}} = a_{Na^+} = 1$.

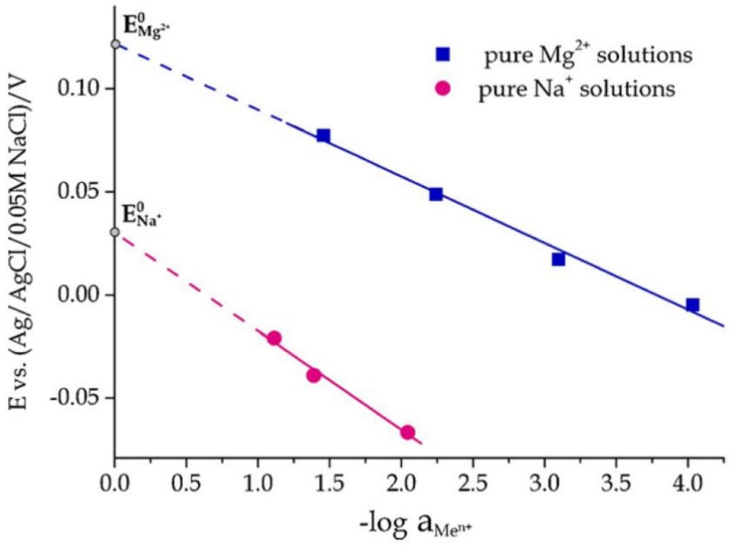

Figure 27. Calibration curves of Mg^{2+}-selective microelectrode in pure solutions of Mg^{2+} and Na^+ for determining selectivity coefficient of Mg^{2+}-SME to Na^+ [230].

4.7.1.4 Detection limit and potential stability of ISMEs

The detection limit was determined as the intersection point of the lines fitted to the linear segments of the calibration curve. When it was not possible to define the linear segment, a line was drawn parallel to the X-axis through the point of potential value with the lowest measured concentration.

The potential stability of an ISME was observed after the preconditioning during approximately 0.5 hour. If a tested ISME showed no potential drift, it was after calibrated and used for the corrosion studies. If the potential of the ISME was not stable, a new microsensor was prepared.

4.7.2 Testing the response of ISEs

4.7.2.1 Preliminary tests

Given the importance of the pH working range and knowing that many ISE candidates may respond to pH, the pH response of **Zn^{2+}-selective electrodes** was evaluated. For this, the electrode under evaluation and a calibrated pH glass-electrode were immersed in solution of $Zn(NO_3)_2$ (10^{-2}M and 10^{-3}M) at 0.015M HNO_3 background that yielded pH≈2. NaOH solutions with different concentrations (from 1M to 10^{-3}M) were added dropwise in order to change the pH of the testing solution by approximately 0.5 pH unit up to pH 9, which was controlled by the pH glass-electrode while the Zn^{2+}-SE potential was being registered. Measurements at two concentrations of primary ion allow simultaneous checking of electrode function slope at different pH values. The electrodes, which potential was stable in the widest pH range and which showed theoretical slope, were further calibrated in a series of $Zn(NO_3)_2$ solutions with concentrations from 10^{-5} M to 10^{-1} M.

A similar procedure was used for **Al^{3+}-selective electrodes**. The calibration was performed in a series of $Al(NO_3)_2$ solutions with concentrations 10^{-1}, 10^{-2}, 10^{-3}, 10^{-4} and 10^{-5} M at pH ≤ 4.2 (adjusted by HNO_3).

4.7.2.2 Study of ISEs response at natural pH and in 0.05M NaCl

It is worth to notice, that both zinc and aluminium salts undergo hydrolysis in solution causing pH changes. Hence, pH of calibration solutions was measured by a combined pH-electrode (InLab® Expert Pro, № 51343101, Mettler Toledo, Switzerland) and the results are presented in Table 8.

Table 8. Measured pH of Zn^{2+} and Al^{3+} calibration solutions.

C (M^{n+}), M	Measured pH	
	Zn^{2+}	Al^{3+}
10^{-1}	4.61	3.17
10^{-2}	5.19	3.71
10^{-3}	5.22	4.16
10^{-4}	5.25	4.65
10^{-5}	5.32	5.02

In the case of zinc calibration solutions the pH remains in the same range and only the pH of 10^{-1}M $Zn(NO_3)_2$ solution is slightly lower. This means that the calibration described in Section 4.7.2.1 is valid, especially if it is done up to 10^{-2}M (or below 10^{-2}M).

The selectivity of Zn^{2+}-SEs against Na^+ was evaluated from the potential difference $\Delta E_{12} = E_1 - E_2$, where E_1 – is the potential measured in 10^{-2}M Zn^{2+} solution with the natural pH caused by metal cation partial hydrolysis and E_2 is the potential measured in 0.05M NaCl solution with pH strictly adjusted to the pH of 10^{-2} M Zn^{2+} solution. The larger ΔE_{12} is the more sensitive is the electrode to Zn^{2+} comparing to others.

Table 8 also shows that the pH of aluminium calibration solutions changes around 2 units of pH. As a consequence, the response of Al^{3+}-SEs to Al^{3+} was measured in two series of solutions: first, in Al^{3+} calibration solutions with concentrations 10^{-1}, 10^{-2}, 10^{-3}, 10^{-4} and 10^{-5} M at natural pH and, second, in solutions of HNO_3 without Al^{3+}, with pH strictly adjusted to the values of the Al^{3+} calibration solutions (Table 8).

The selectivity of Al^{3+}-SEs against H^+ and Na^+ was estimated in a similar way as for Zn^{2+}-SEs. The potential was measured in three solutions: 1) 10^{-2}M Al^{3+} solution with natural pH value caused by metal cation partial hydrolysis (E_1); 2) solution of HNO_3 with pH value adjusted to the pH of 10^{-2} M Al^{3+} solution (E_2) and 3) 0.05M NaCl solution with pH value adjusted to the pH of 10^{-2} M Al^{3+} solution (E_3). Then the potential differences, $\Delta E_{12} = E_1 - E_2$ and $\Delta E_{13} = E_1 - E_3$, are proportional to the selectivity of the electrode against H^+ and Na^+, respectively. The bigger the calculated ΔE is the more sensitive is the electrode to Al^{3+}.

4.7.3 Amperometric detection of oxygen

The amperometric detection of dissolved oxygen in aqueous solution is based on the following reaction, occurring at the microelectrode tip [90,177]:

$$O_2 + 2H_2O + 4e^- \rightarrow 4OH^- \qquad (4.2)$$

when it is polarized at a potential where the O_2 reduction is controlled by diffusion. A two electrode cell was used for measuring profiles and maps of dissolved oxygen over corroding samples. The working microelectrode was a platinum micro-disc (Figure 28) in a glass body (CH Instruments, USA, Ref. CHI100) and a homemade Ag|AgCl electrode worked as counter and as reference electrode (Figure 22, b).

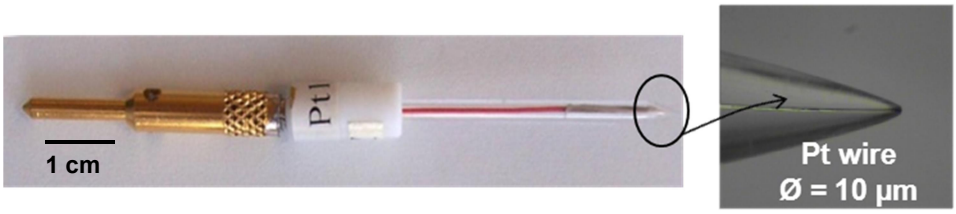

Figure 28. Amperometric microsensor for detection of dissolved oxygen in solution.

Given the small currents to be measured (pico to nano amperes) the RE could maintain its integrity and a fairly stable potential, especially if the measurements were not too long. The tip potential was fixed at -0.7 V vs Ag|AgCl, well inside the region of diffusion control (Figure 29).

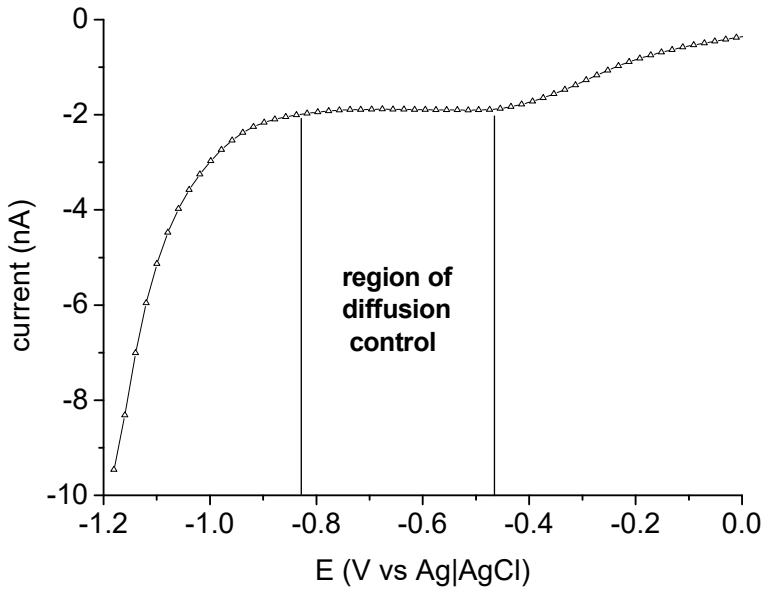

Figure 29. Voltammogram for the reduction of dissolved oxygen in 0.05M NaCl. The scan rate polarization was 30 mV s^{-1}.

The measured tip current is proportional to the concentration of dissolved oxygen in solution according to Equation 2.6 (Section 2.3.1).

4.7.4 Mapping

The local activities of ions and the ionic current densities were mapped sequentially. A move-wait-measure scheme was employed. The time of acquisition for each SIET data point was larger or equal of τ_{95} of the corresponding ISME. The sampling

time for each SVET data point required about 0.5 s. More details are reported further, since adjustments of system working parameters are required for each analysed sample.

Simultaneous detection of two kinds of species (two ions activities) was performed using a dual head stage holder which allows bringing together two probes at any micro distance (Figure 30).

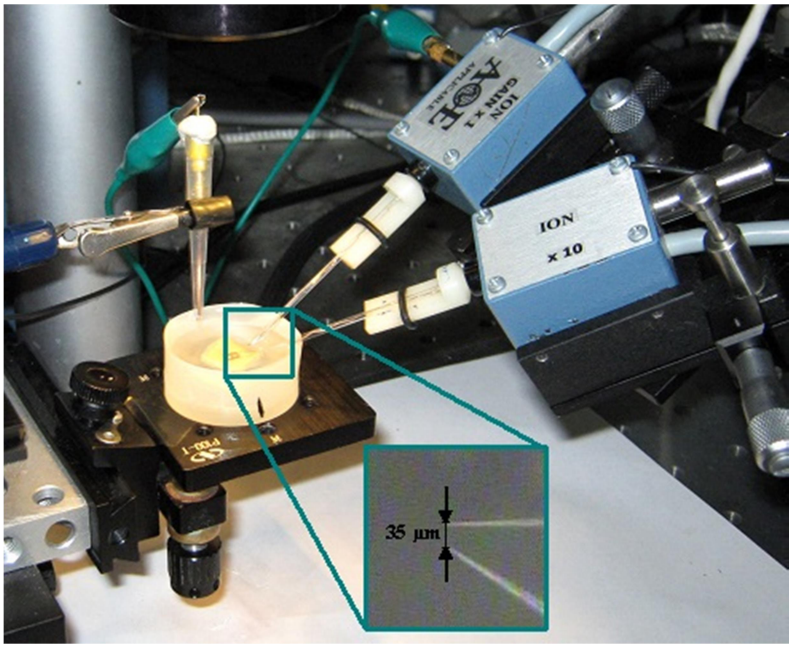

Figure 30. Photograph of dual head support with microsensors at 35 µm and an analysing cell.

Chapter 5

5 Mapping local currents, pH and oxygen in localized corrosion processes

In this chapter, SVET, potentiometric pH-SME and an amperometric O_2 microsensor were applied for describing the local chemistry during corrosion of two technologically important cases: i) Zn-Fe galvanic couple and ii) corrosion and inhibition on a coated 2024-T3 aluminium alloy. SRET was also used for studying the Zn-Fe couple.

Technologically, the Zn-Fe galvanic coupling is very important in the sacrificial protection of steel in offshore structures, ships, bridges, tanks, etc. [7,8], and in the galvanizing industry.

The 2024-T3 aluminium alloy is very important in the aeronautic sector, being commonly used for skinning and in structural frames due to the low density combined with high strength [269]. The good mechanical properties result from alloying elements such as copper which has a side effect of producing intermetallic particles in the alloy matrix creating a myriad of small cathodes inducing micro-galvanic coupling all over the surface, particularly in the presence of chloride solutions.

5.1 Spatial distribution of current density, pH and oxygen above Zn-Fe galvanic couple

Figure 31 (a) shows a scheme of the galvanic cell. It consisted of pure Zn and pure Fe wires of 1 mm diameter embedded in epoxy matrix, electrically connected from the back. Figure 31 (b) shows the position of maps of SRET, SVET, pH and O_2 in planes normal

and parallel to the surface. The distribution maps of potential, ionic currents, pH and dissolved O_2 over zinc-iron galvanic couple were collected in 5mM NaCl. Maps in XY plane parallel to surface were measured at 100 µm above the sample. Maps in XZ plane normal to the surface were made between 100 and 3000 µm for SVET, from 50 to 3000 µm for SRET and from 50 to 2000 µm for pH and O_2 measurements.

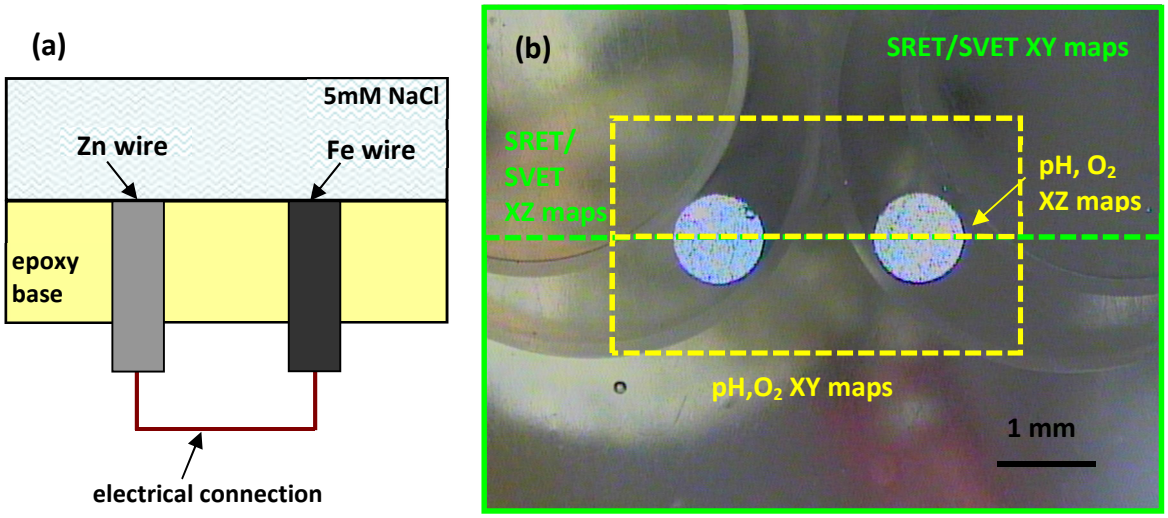

Figure 31. Scheme of the Zn-Fe galvanic cell (a) and the optical photograph of the sample surface with indicated measured areas (b).

5.1.1 Distribution of current density

5.1.1.1 Distribution of current density as given by SVET measurements

The Scanning Vibrating Electrode Technique (SVET) measures current density in solution (by actual measurements of potential as presented in Section 2.2.3). Maps of current density above Zn-Fe couple are shown in Figure 32. Both maps on Figure 32 allow visualizing the active areas with spatial resolution.

Positive currents (in red) correspond to anodic currents, in this case, from zinc oxidation

$$Zn \rightarrow Zn^{2+} + 2e^{-} \qquad (5.1)$$

and negative currents (in blue) correspond to cathodic processes, here considered to be the O_2 reduction (Reaction 1.2).

The map normal to the sample (Figure 32 (b)) shows that the electrode processes affect the solution at distance up to 2000 µm. The currents correspond to the migration current flowing in solution and all ions can take part.

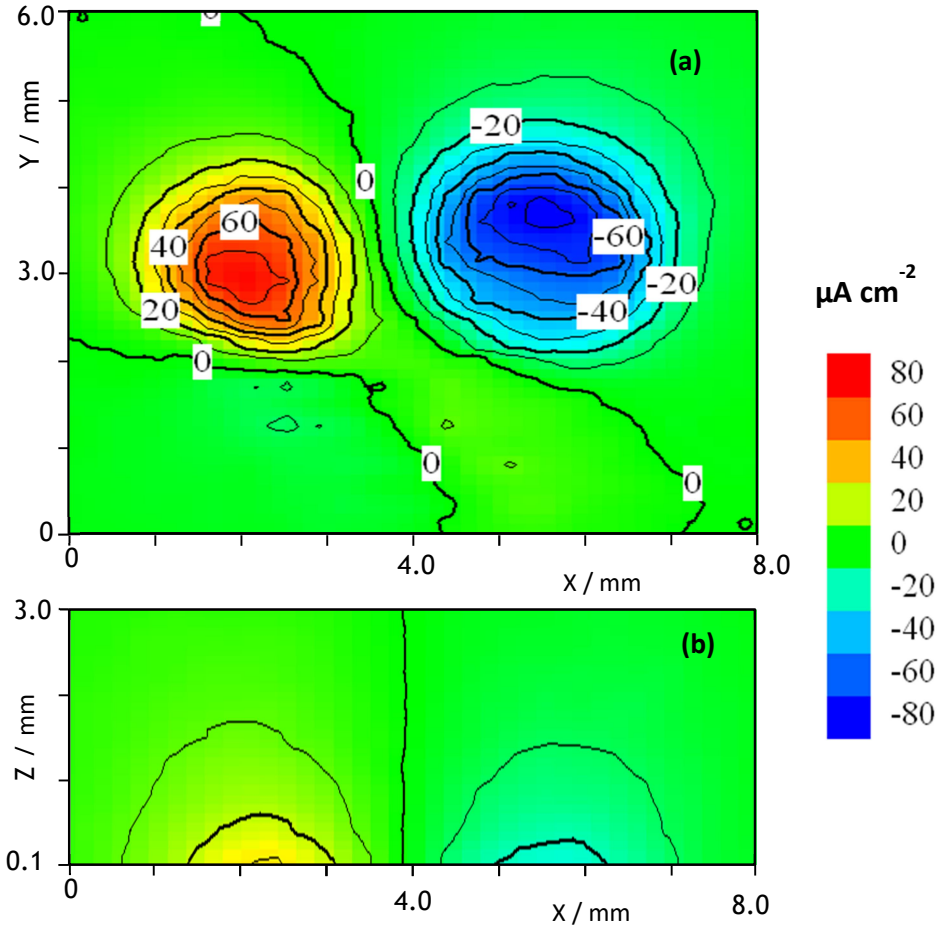

Figure 32. Distribution of ionic currents measured by SVET in XY (a) and in XZ (b) planes in 5 mM NaCl solution above Zn-Fe galvanic couple.

Naturally, as the solution becomes more concentrated (more charge carriers, more conductive) larger is the noise, lower is the migration current and smaller is the electrical field in solution.

5.1.1.2 Distribution of current density as calculated from SRET measurements

The distribution of potential in solution can be measured by SRET. For this a glass micropipette (2 µm in diameter) filled with 5mM NaCl and containing a Ag/AgCl wire was used as scanning microelectrode. The reference electrode was a homemade Ag/AgCl, 5 mM NaCl mini-electrode with the inner solution stabilized by 3% agar-agar (Figure 22 b). The reference mini-electrode was fixed inside the cell, a few millimeters away from the galvanic couple. The electrodes were connected to the SIET preamplifier which moved by the same positioning system used for SVET (Section 4.4.2). The measurements were controlled by the ASET software which registered the potential in points inside the selected area for mapping after an acquisition time of 0.2 s.

Figure 33 shows the potential in solution in the vicinity of the Zn-Fe couple. Figure 33 (a) shows the potential in the plane parallel to the surface at 100 µm (including points of data acquisition), while Figure 33 (b) shows a similar map at 120 µm above the surface. Figure 33 (c) is the potential in a plane normal to the surface. The values are given with respect to the bulk solution where no effect from the processes on the sample exists. For that the potential of the first point in the map (top, left), close to bulk conditions, was subtracted in all points. What remains is the potential difference with respect to the bulk. Positive values appear above the anode (excess of Zn^{2+}) and negative above the cathode (excess of OH^-). A difference of 9 mV was found between the most anodic and the most cathodic areas and is related to the current flowing in solution.

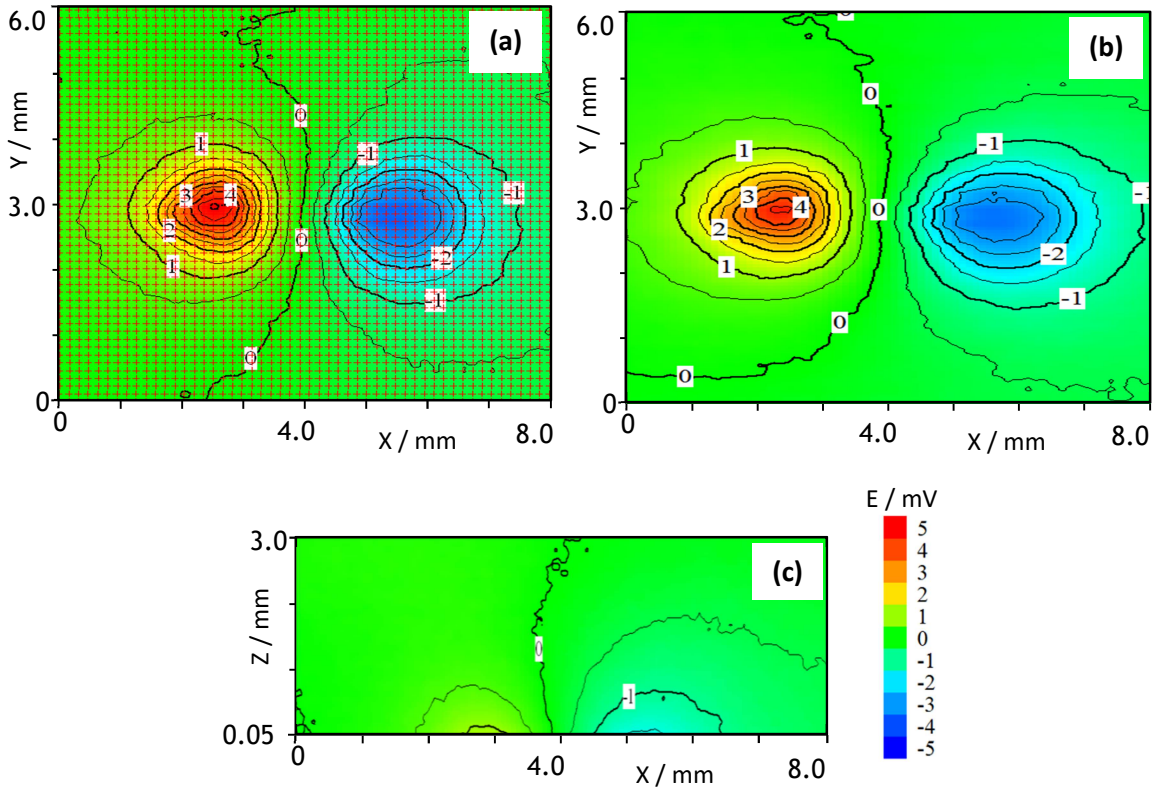

Figure 33. Distribution of potential in 5mM NaCl solution (vs bulk) in XY plane at 100 µm with grid points of measurement (a), 120 µm (b) and in XZ plane above the Zn-Fe couple after 2h of immersion. The colour scale is the same one for (a), (b) and (c).

Having a potential map and knowing the solution conductivity it is possible to estimate the current densities in solution using Equation 2.4. Thus, subtracting the potential of the points with the same (x; y) coordinates in map (b) and map (a) will give the potential difference (ΔE, mV) between two points separared by 20 µm in the Z axis. In the case of XZ map, the ΔE can be calculated by subtracting the two points in nearest lines parallel to the sample surface, measured with 50 µm steps. Figure 34 shows the obtained

values of ΔE for XY (a) and for XZ (b) planes. The ΔE was used to calculate the current density with Equation 2.4 for Δd = 20 μm and k (5mM NaCl, 23°C)= 5.8x10^{-4} S cm^{-1}.The calculated currents are shown in Figure 35 in XY plane (a) and in XZ plane (b).

In the obtained XY and XZ current densities maps (Figure 35) anodic and cathodic areas are detected but with lower resolution compared to SVET maps. The XY current scan, in general, is characterized by a rather significant noise presence, even though the potential maps (Figure 33) look very good.

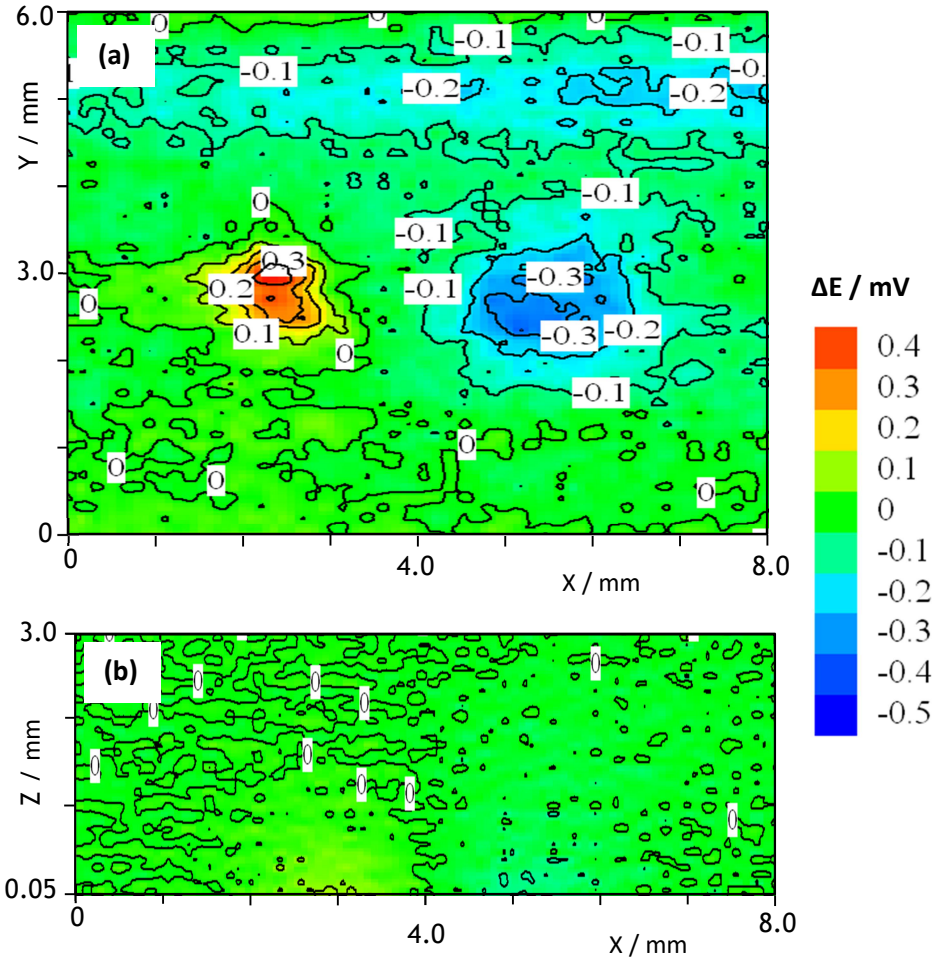

Figure 34. Potential differences between the two XY planes of Figure 33, (a), and in XZ plane, (b), above Zn-Fe couple immersed in 5mM NaCl.

The calculation of current densities from XZ map presented less artifacts and noise effects than the one from XY planes, since the data for XY plane were recorded in two measurements 15 minutes apart, and eventually the system was changing during this time.

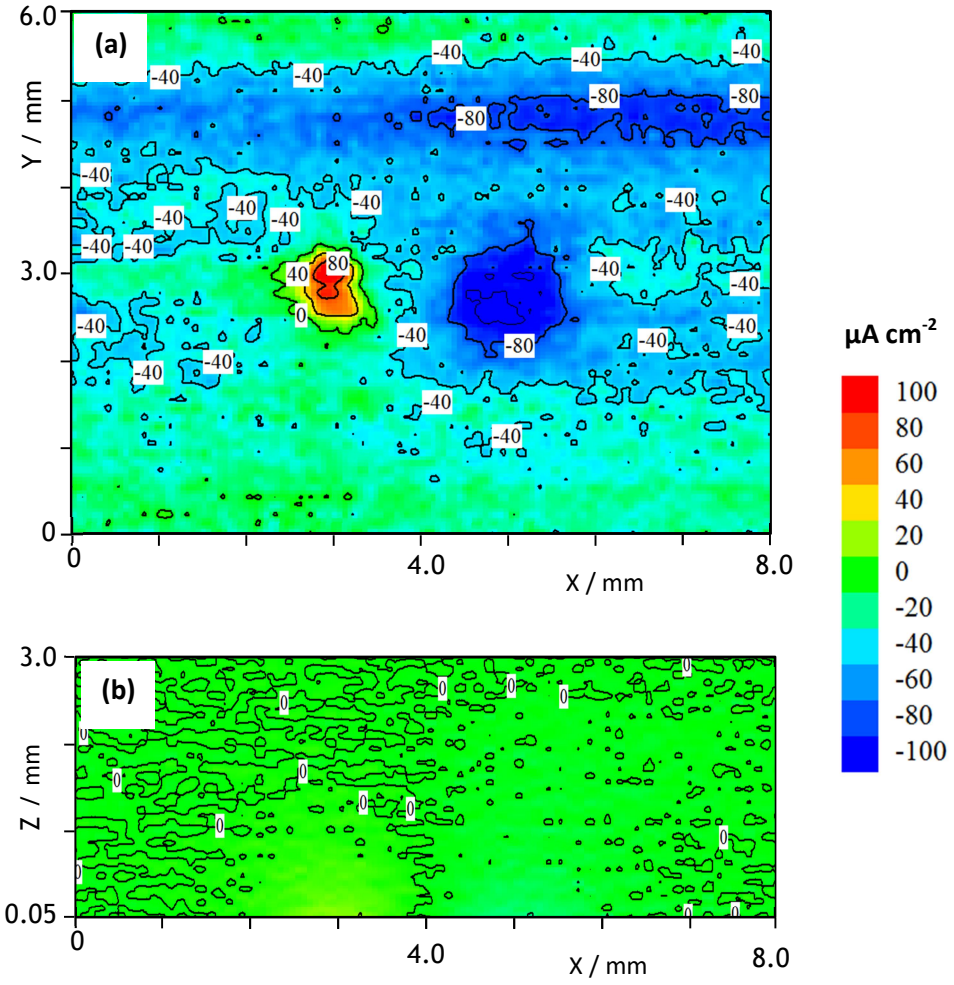

Figure 35. Distribution maps of ionic currents calculated from SRET measurements in 5 mM NaCl above Zn-Fe galvanic couple in XY plane (a) and in XZ plane (b).

The SVET can provide invaluable information regarding the localization of currents and their magnitudes but no chemical information is given about the nature of the species involved in the process. Two important parameters that can be obtained to complement SVET are the local distribution of pH and dissolved oxygen in solution.

5.1.2 The distribution maps of pH

5.1.2.1 Response of pH-SME

The response of pH-SME based on Hydrogen ionophore I cocktail B (Fluka, Germany) to commercial buffer solutions is shown in Figure 36. The linear range of calibration plot is from pH 5 to pH 13 with slope of 55.1±1.4 mV/decade. The response time for the pH-SME was τ_{95}=0.30 s and τ_{lim}=1.3 s [270], meeting the requirement for fast responding microelectrodes to be used for mapping corrosion systems.

The response of pH-SMEs prepared from silanized glass micropipettes and based on commercial cocktail, was stable and corresponded to the characteristics described in the Fluka catalogue [237] (See Table 3).

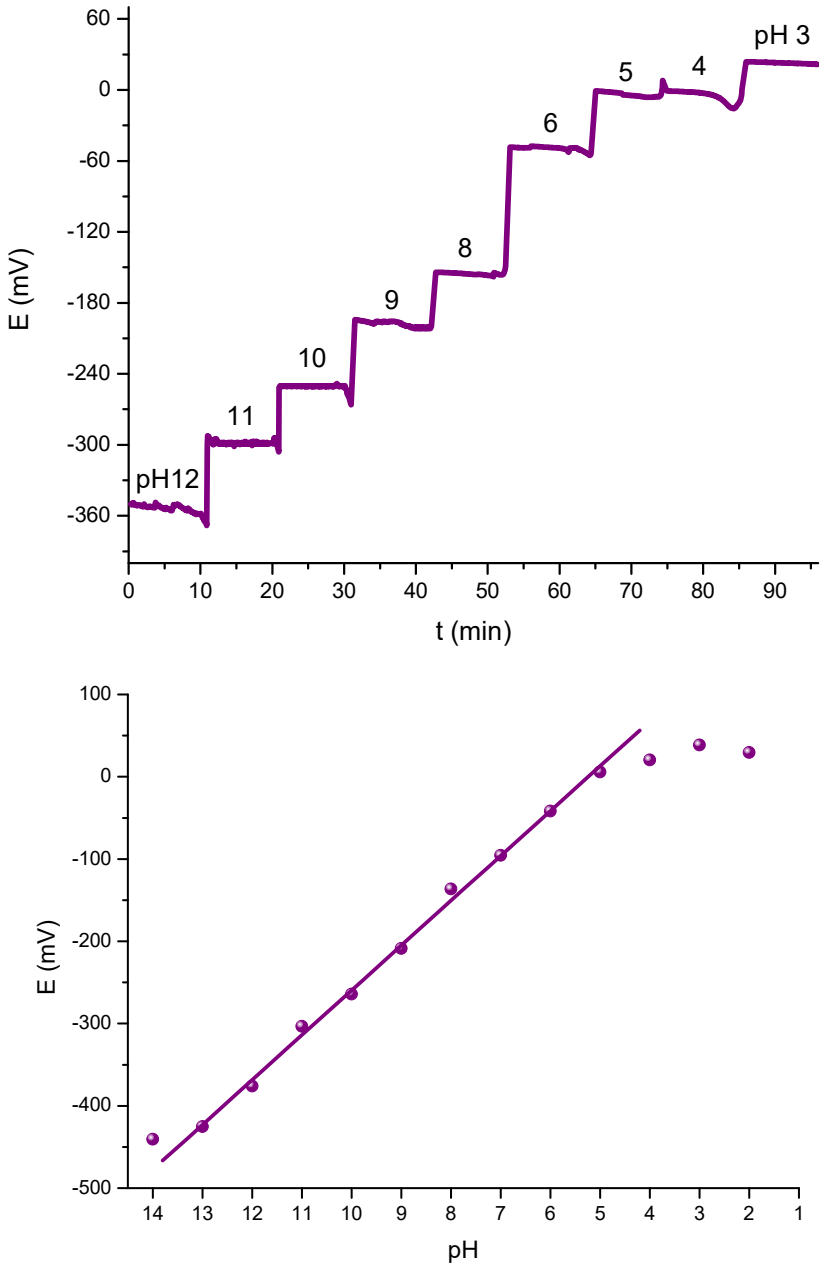

Figure 36. The typical dynamic response (upper) and calibration curve (lower) of the pH-SME based on Hydrogen ionophore I cocktail B to commercial buffers.

5.1.2.2 The distribution maps of pH

The local pH measured in XY and XZ planes above Zn-Fe couple are shown in Figure 37 (a) and (b) respectively. The high pH, up to 10.5, was detected above the iron surface, while over the zinc the pH remained nearly constant, equal to pH of bulk 5.6 (Figure 37 (a)).

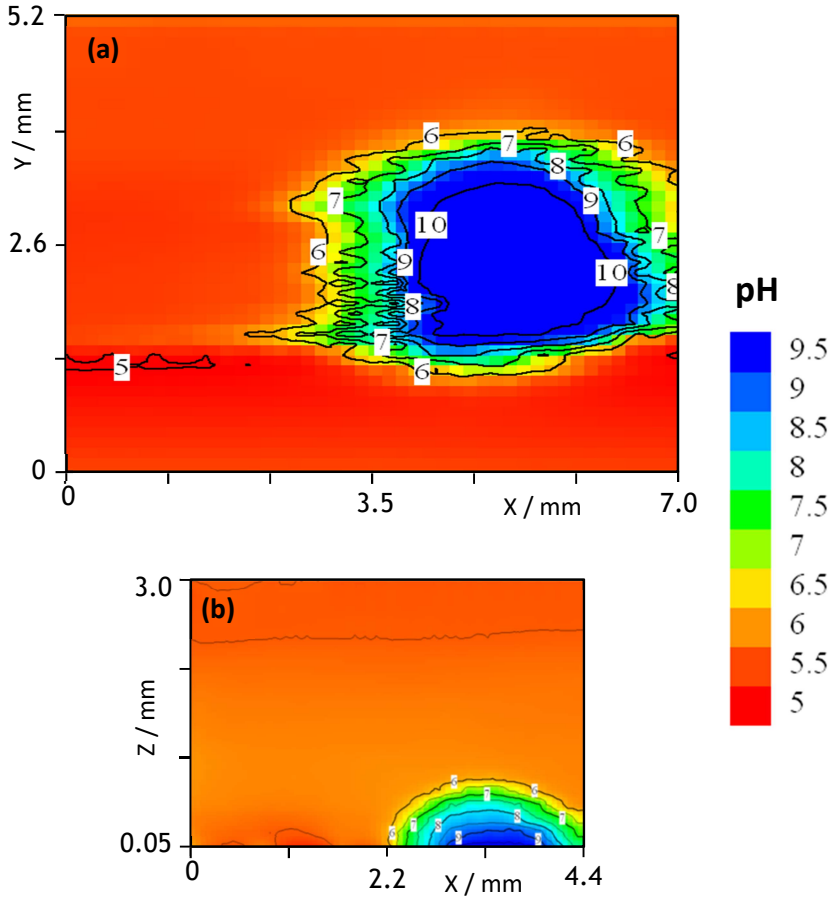

Figure 37. Distribution of pH in XY (a) and XZ (b) planes in 5 mM NaCl solution above Zn-Fe galvanic couple.

5.1.3 The distribution maps of dissolved O_2

The measured local dissolved oxygen concentration XY and XZ maps are shown in Figure 38 (a) and (b) respectively. The concentration of dissolved oxygen was lower above iron, and almost constant above the zinc wire (Figure 38). These results confirm the association of the alkaline pH and oxygen consumption with the cathodic reaction.

The amperometric detection used in this work to measure dissolved oxygen has some experimental limitations. The bulk value of oxygen concentration in Figure 38 is 1.4×10^{-4} M while 2.6×10^{-4} M is normally reported [271]. The discrepancy can be explained

due to the number of electrons in Reaction 1.2, *n*, to be less than 4 and in the Equation 2.6 for the diffusion controlled limiting current at a microdisc [177]. However, even taking into account that values of *n* equal to 2.64 and 2.8 were found in practice [186], the experimental value is still too low. Other reasons for that may be a tip radius smaller than the one considered in the calculation and the possibility of side oxidation reactions that, occurring at the same tip potential, would decrease the current measured by the system. The poisoning of the platinum surface by impurities might happen which decreases the active area and can lead to its deactivation at long timescales. The possibility of $Zn(OH)_2$ precipitation also exists when the tip, with local high pH due to Reaction 1.2, passes close to the anodic sites (sources of Zn^{2+}). This poisoning problem is usually solved through the use of oxygen semi-permeable membranes [272] or by periodically cleaning the electrode by cycling the tip potential between the value of oxygen and hydrogen evolution [186]. In this work cycles between -2 and +1.5 V vs Ag|AgCl were performed before measurement.

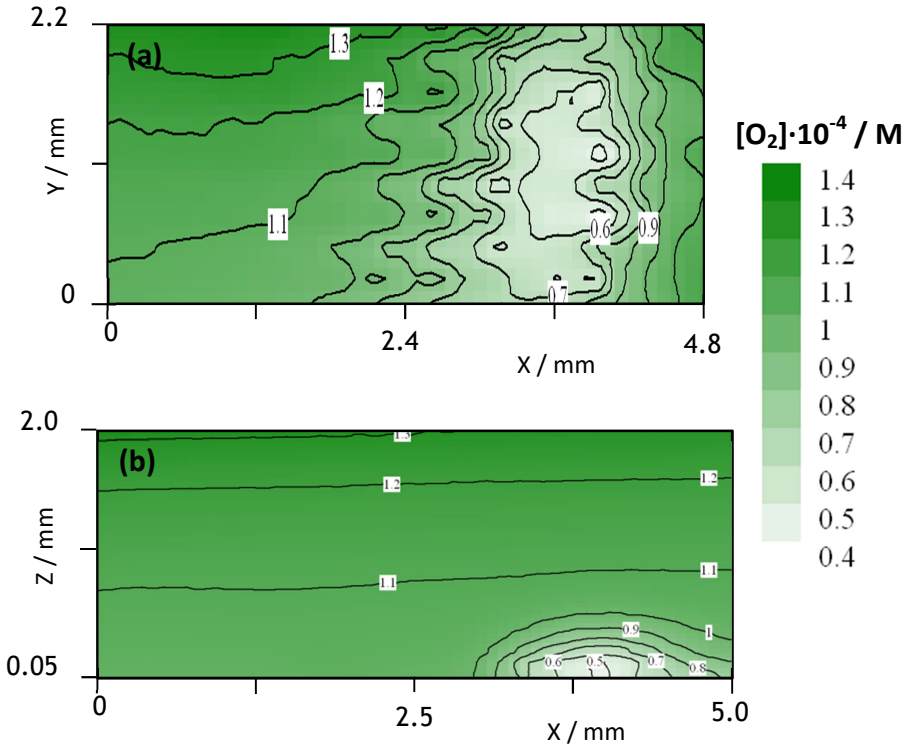

Figure 38. Distribution of dissolved oxygen concentration ($[O_2]$, M) in XY (a) and XZ (b) planes in 5 mM NaCl solution above Zn-Fe galvanic couple.

The current densities, pH and dissolved oxygen concentration maps measured above the Zn-Fe galvanic couple immersed in 5mM NaCl are in good agreement showing clearly the placement of oxidation and reduction reactions and the local changes in environment produced by the corrosion process.

Thus, the three techniques can be used in complementary way for the description of corrosion systems.

5.2 Spatial distribution of current density, pH and oxygen above the sol-gel coated AA2024-T3 with artificial defects

Another example of the complementary use of the 3 techniques (SVET, potentiometric detection of pH and amperometric detection of O_2) is the corrosion at defects of coated metals. This is important to assess, for example, for the performance of protective coatings. This section shows results for AA2024-T3 covered by a sol-gel film with two artificial defects.

Figure 39 shows the sample surface after 30h of immersion in 0.05M NaCl. Two black spots on the Figure 39 (a) correspond to two round artificial defects, which are separated by precipitated corrosion products. The Figure 39 (b) is a current density map measured by SVET at 100 µm above the surface. Localized activity was detected only above the defects, while the rest of the surface remained protected by the sol-gel film. The left defect was mainly cathodic and the right defect has anodic and cathodic activity.

pH measured in a line 100 µm above the surface shows an increase above the cathodic area and a decrease above the anodic area. O_2 measured 2000 µm above the surface shows a constant value which is considered to be the bulk value. As the probe approaches the surface less current is measured close to the cathodic areas because these deplete the O_2 to be sensed by the tip probe. The closer the tip is to the cathodes the lower is the measured current.

It is assumed that reactions responsible for the above observations are as follows.

Anodic process on the AA2024 can be attributed mainly to the dissolution of aluminium from the alloy matrix, and dissolution of magnesium from S-phase intermetallics (Al_2CuMg) according to Reaction 1.1 [15,17]. The flux of metal cations (Al^{3+} and Mg^{2+}) from surface to bulk solution is measured by SVET as positive currents.

Close to anodic regions, hydrolysis of metal cations (mainly Al^{3+}) may acidify locally the solution according to:

$$M^{n+} + mH_2O \rightarrow M(OH)_m^{(n+m)+} + mH^+ \qquad (5.2)$$

leading to the slight decrease in pH detected in Figure 39 (c).

The cathodic process is the reduction of oxygen dissolved in solution according to Reaction 1.2. The OH^- flux from metallic surface to bulk solution is measured by SVET as negative currents and increases the local pH measured by the pH microelectrode. The local consumption of oxygen leaves less reactant at the Pt tip of O_2 microsensor.

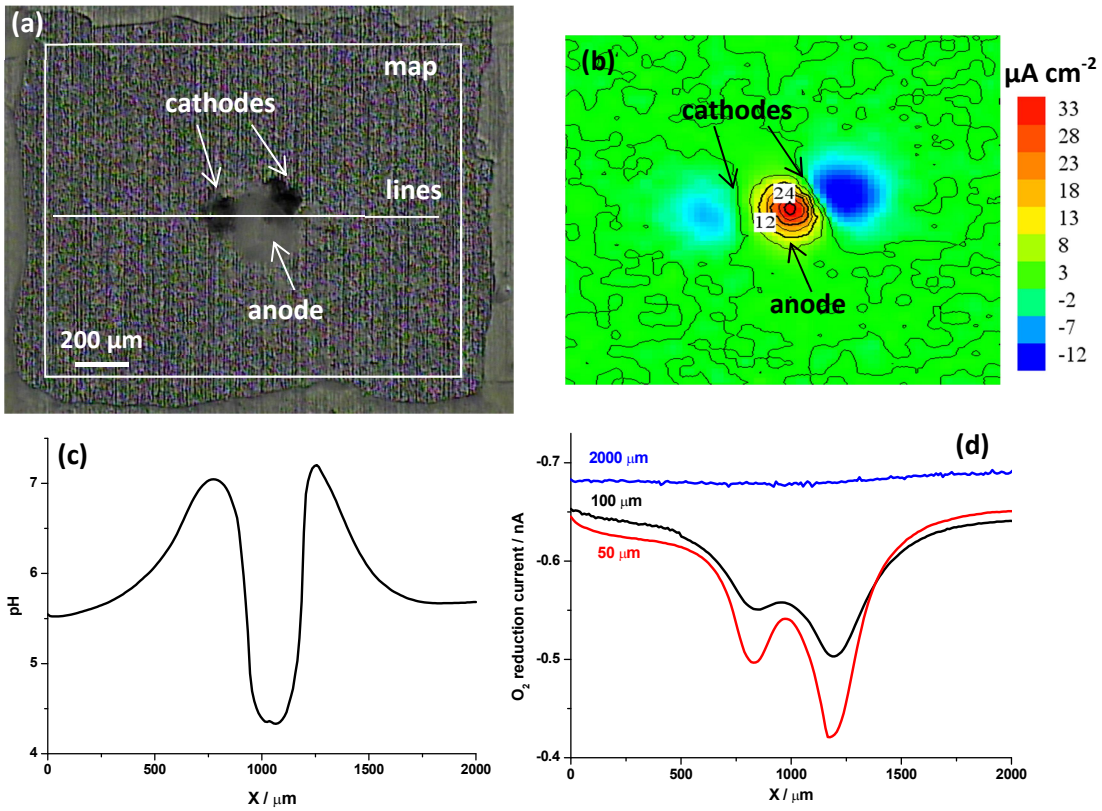

Figure 39. Image of sol-gel coated AA2024-T3 with 2 artificial defects and indicated regions of measurements, (a); SVET current density map after 30h of immersion in 0.05M NaCl, (b); variation of pH 100 µm above the surface, (c), and dissolved oxygen concentration at 50, 100 and 2000 µm above the sample surface (d).

The hydrogen evolution according to Reaction 1.3 may also be possible in places of lower pH, for instance, close to the anode, where H^+ ions are generated as a result of Al^{3+} hydrolisys.

As for the Zn-Fe case, the distributions of current densities, pH and O_2 are all in good agreement. The highest cathodic activity in the right defect is consistent with the larger O_2 reduction current drop in it and the higher measured pH.

5.3 Spatial distribution of current density, pH and oxygen above the sol-gel coated AA2024-T3 during inhibition

The same sol-gel coated system was used to study the corrosion inhibition effect of a compound added to the solution. The medium was made inhibitive by addition of crystals of $Ce(NO_3)_3 \cdot 6H_2O$ to the solution of 0.05M NaCl until reaching a concentration of 10 mM in Ce^{3+}, because Ce^{3+} ions are known as inhibitor for aluminium, ferrous and zinc alloys [273–278].

The objective was to simulate the effect of inhibitor after being released from the coating and verify the ability of SVET and SIET to probe self-healing properties of protective systems [39,40]. In a real situation the compound would be in the film either directly dispersed or inside micro- or nano-containers. The release would occur upon the opening of the containers triggered by local environment changes, like pH for example.

Figure 40 shows the tested sample: AA2024 coated with sol-gel and two defects. The small numerous dark spots scattered throughout the alloy surface are a result of the cleaning process that removed the intermetallic precipitates from the surface leaving small holes, later filled by the sol-gel film.

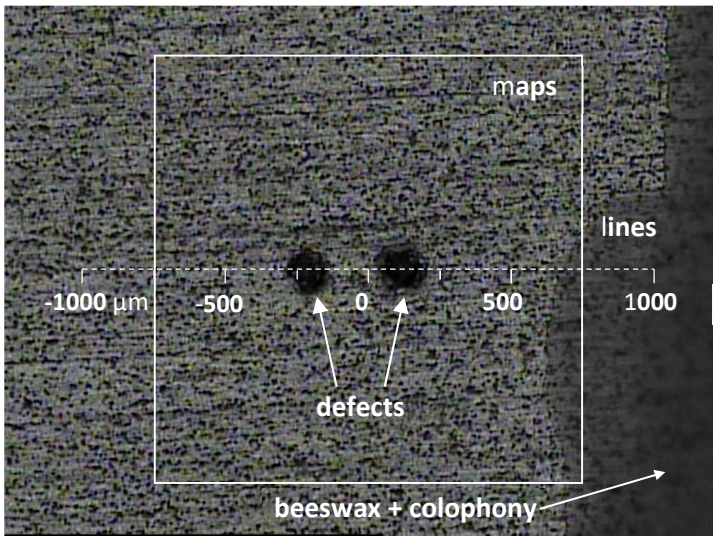

Figure 40. Sample surface with indication of the two artificial defects and the position of measurement lines.

SVET detected the corrosion activity 2 hours after immersion, initially as very small currents that increased in magnitude with time until a steady value. The map of Figure 41 (a) was obtained after 19 hours of immersion in 0.05 M NaCl. The anodic and cathodic regions stayed in the same position since the beginning. Negative currents were measured on the left defect and positive currents on the right defect.

As in previous case (Section 5.2), the positive currents are associated with an upward net flux of cations attributed mainly to the dissolution of aluminium and magnesium from the alloy (Reaction 1.1). The negative currents are associated with an upward net flux of OH^- originated from the reduction of dissolved oxygen (Reaction 1.2).

After this measurement cerium nitrate was added to solution in order to estimate its inhibition capability. Figure 41 (b) shows the current map measured 19 hours after the addition of cerium nitrate. No activity was detected then. This means that the inhibitor successfully stopped the corrosion process at the defects. The corrosion inhibition by

cerium nitrate is attributed to the blocking of the cathodic process by precipitation of cerium hydroxide in the cathodic sites [165,278–280],

$$Ce^{3+}(aq) + 3OH^{-}(aq) \rightarrow Ce(OH)_3(s) \downarrow \quad (5.3)$$

Cerium oxides, namely CeO_2 and Ce_2O_3, may be formed as well [165,279,280]. Once the original cathodic sites become blocked, the anodic and cathodic reactions will take place in the area still active. The blocking of the new cathodic sites reduces even more the active area and the process continues until all area becomes covered.

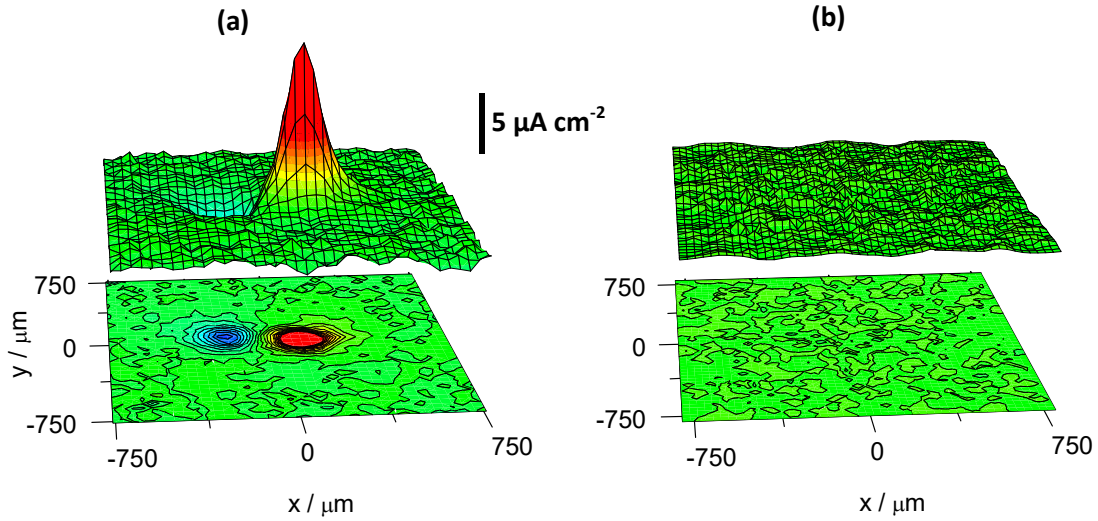

Figure 41. (a) SVET map obtained 19 h after immersion in 0.05M NaCl and minutes before the addition of cerium nitrate; (b) SVET map obtained 19 h after the addition of cerium nitrate to the solution at a concentration of 10 mM. Maps position is indicated in Figure 40.

Figure 42 shows the variation of the ionic current, pH and reduction current of dissolved oxygen in lines above the artificial defects at a constant height from the surface immediately before and after 20 hours of inhibitor addition.

The height was 50 µm for pH and O_2 measurements and 100 µm for SVET. SVET lines show the negative and positive currents above the cathodic and anodic defects, respectively. The pH in solution had a significant increase close to the cathode and no variation was detected above the anode. The measured current due to oxygen reduction (negative by definition) was constant except at positions near both defects where it was smaller. In the inhibited medium the three quantities (red lines), ionic current, local pH and O_2 reduction current, showed the same values encountered in the bulk solution; no local changes existed, confirming that the corrosion process was halted by the inhibitor.

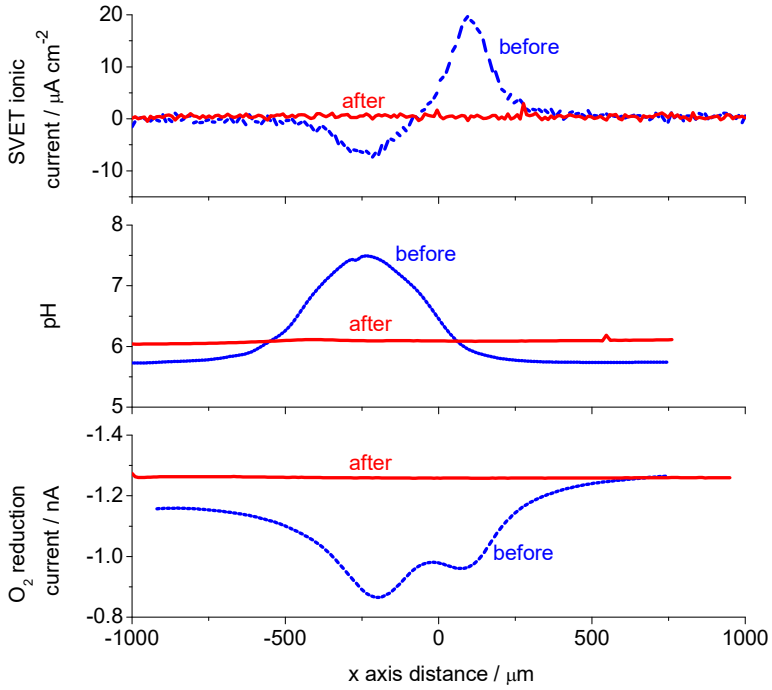

Figure 42. Line scans of ionic current, pH and dissolved oxygen reduction current, obtained at 50 µm (100 µm for SVET) above the surface, before and 20 h after addition of cerium nitrate to the solution. Lines position is indicated in Figure 40.

Figure 43 shows the three quantities measured over each of the two defects, at different distances to the surface along the z axis, before and after the addition of inhibitor. The minimum height probed was 50 µm for pH and O_2, and 100 µm for SVET. It was observed the same tendency as before: in the uninhibited medium, SVET showed positive currents above the right defect and negative currents above the left defect, pH increased in the left defect and oxygen current decreased close to both defects. Values changed with the distance to the surface but above 300-400 µm they became constant and similar to those in the bulk solution. 20 hours after addition of inhibitor the measured values were constant, regardless the position of measurement and the distance to the surface.

However, given that SVET measures the net response, a small anodic current could also exist in the cathodic region detected by SVET, being masked by the larger cathodic current (or vice versa). This shows the importance of complementing SVET with other techniques, capable to perform chemical speciation.

The measurements of pH presented in Figures 42 and 43 show an increase in the left defect, consistent with cathodic activity and with an upward flux of hydroxyl ions

detected as negative currents by SVET. Reactions 1.2 and 1.3 can be responsible for the local alkalization.

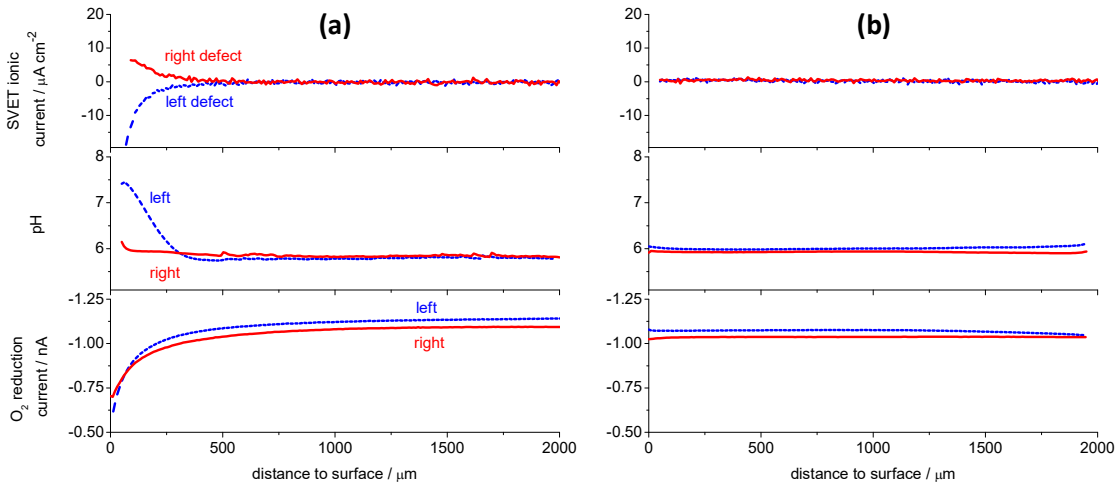

Figure 43. Ionic currents, pH and O_2 reduction current measured in the z direction above the two defects before (a) and 20 h after (b) the addition of cerium nitrate.

The micro-amperometric measurement of local oxygen distribution was used to clarify the cathodic process. The decrease of reduction current measured near the defects means less oxygen to react at the microdisc due to its consumption to "feed" Reaction 1.2 at the defects. The confirmation of Reaction 1.2 does not discard Reaction 1.3 but, given the pH of the exposure solution (≈6) and being the corrosion potential close to -0.6 V vs Ag|AgCl, its contribution should be negligible. Besides, no gas evolution was observed in the cathodic defect.

Surprisingly, oxygen depletion was detected on the anodic defect as well. The drop of oxygen concentration in the two defects contradicts the initial assumption given by SVET of a sole cathode and a sole anode. In fact, one defect is predominantly cathodic and the other is predominantly anodic but cathodic activity exists in both, since the metal substrate is at a potential around -0.6 V vs Ag|AgCl, potential where oxygen can be reduced. This shows the importance of complementing SVET with other techniques. Given that SVET measures the net response, a small anodic current could also exist in the left defect, being masked by a larger cathodic current. The detection of Mg^{2+} or Al^{3+} in solution would provide that extra information.

5.4 Concluding remarks

Results presented in this chapter showed the suitability of SVET, SIET and microamperometry to study localized corrosion and inhibition processes in a Zn-Fe galvanic couple and in defects of protective coatings applied on AA2024. These techniques can give a very good picture of the localized processes taking place over time. Ionic currents given by SVET permitted to visualize the temporal and spatial evolution of the anodic and cathodic processes in active sites. Measurements of local pH and local oxygen reduction current complement SVET in the characterization of the local environment in the solution above active zones.

The local pH and oxygen content measurements are important in corrosion studies; however, they can be not sufficient in case of studying complex systems. The detection of metal ions (Mg^{2+} or Al^{3+}, as in case of AA2024) in solution, resulting from localized corrosion reactions, would give extra information about the corrosion and inhibition processes.

Chapter 6

6 Mg^{2+}-SME for corrosion applications

Magnesium is the lightest of the technical metals and its alloys have quite special properties, like high stiffness/weight ratios, good vibration and shock absorption ability, relatively high thermal and electrical conductivity, good cast ability, and high damping capacity [2,242]. Magnesium and magnesium alloys are also nonmagnetic. More than half of the annual magnesium production is used as alloying element in aluminium alloys [242] and nodular cast iron. The rest is used principally as castings in the aerospace and general transport industries, with some wrought products in specialized applications. Recently, die cast magnesium alloys have found application in computer disk drives and magnetic card readers at supermarket checkouts.

Because of their high strength/weight ratios, magnesium alloys are of particular interest to the aerospace and transport industries which have provided a great stimulus to the development of magnesium alloys over the last 50 years. Magnesium alloys are not as popular as aluminium alloys and the main reason is their lower corrosion resistance. In order to better understand the corrosion process of magnesium based materials and devise better protection measures, it is important to be able to detect magnesium ions resulting of the electrochemical reactions on the immersed sample surface.

In this chapter a Mg^{2+}-selective microelectrode (Mg^{2+}-SME) is used in the study of the corrosion and corrosion inhibition of magnesium alloy AZ31B.

6.1 Characterization of Mg^{2+}-SME

The Mg^{2+}-SME was prepared in the laboratory with the Magnesium ionophore II cocktail B (Fluka, Germany) (See section 4.5.2.1).

The calibration plots are shown in Figure 44. The response in Mg^{2+} solutions is linear from 1.2 to 4.7 pMg ($-loga_{Mg2+}$) with the slope 31.4±0.9 mV/decade, close to Nernstian value. Figure 44 does not show it but the linear range goes, in fact, down to 6.0 pMg, as was shown later [270]. In the presence of 0.005M NaCl the slope is also close to the theoretical value, i.e. 30.3±0.4 mV/decade and the plot is linear from 1.3 to 4.4 pMg. With 0.05M NaCl background the slope is 28.5±0.7 mV/dec in 10^{-4}-10^{-1}M $Mg(NO_3)_2$ range. Although 0.05M NaCl background limits the linear range of response to 1.3 - 4.6 pMg, it does not influence the stability of the Mg^{2+}-SME potential.

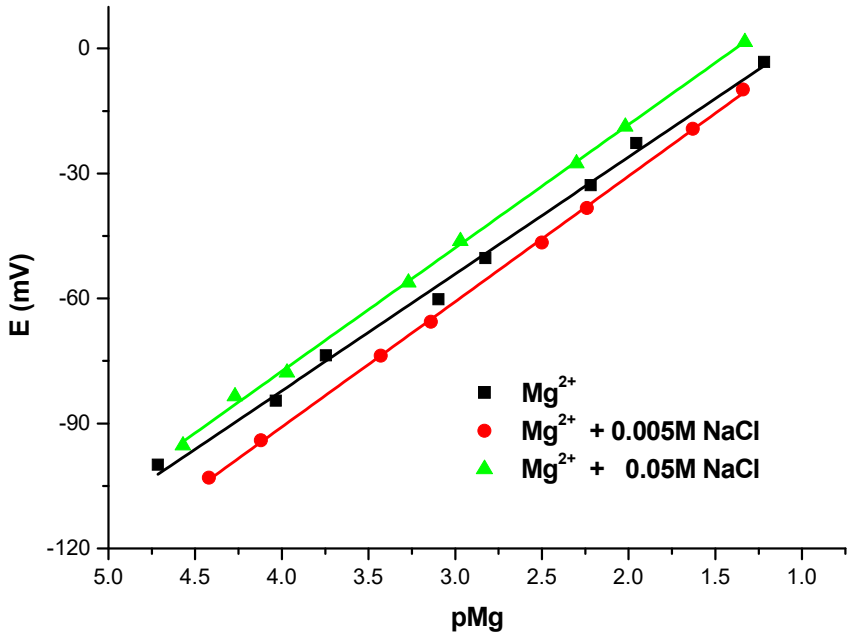

Figure 44. Calibration plots for Mg^{2+}-SME in different media.

The logarithm of potentiometric selectivity coefficient against Na^+ ions determined by the modified SSM [231] was $logK^{Pot}_{Mg2+,Na} = -3.1$ [270]. The potential of Mg^{2+}-SME was found to be stable in the pH range from 3 to 9 (Figure 45) and after that it becomes more negative as a result of the decrease of Mg^{2+} concentration by reaction with OH^-, which complies with the stability constants of $Mg(OH)^-$ and $Mg(OH)_2$ complexes [233]. This allows tracking Mg^{2+} concentration in anodic zones where dissolution of magnesium occurs. The measured response time of Mg^{2+}-SME was τ_{lim}=2.9 s and τ_{95}=1.6.

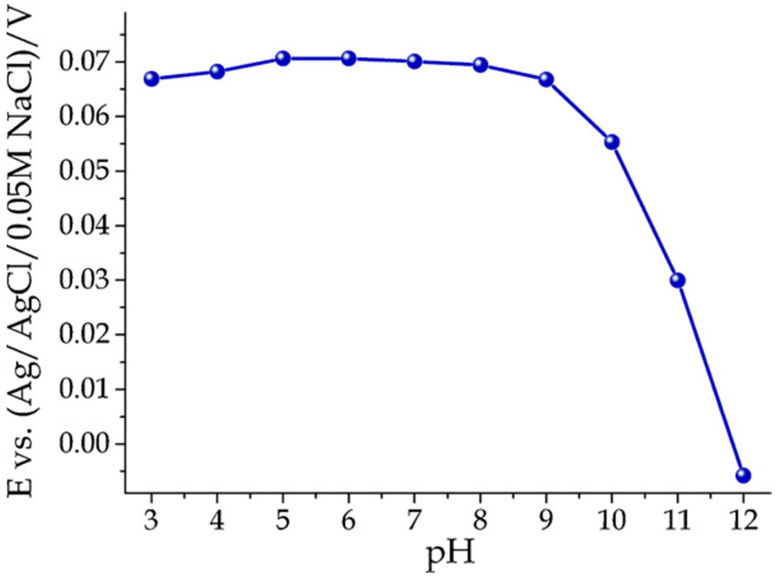

Figure 45. pH-dependent response of Mg^{2+}-SME. C(Mg^{2+}) = 0.01M [270].

6.2 Monitoring the local spatial distribution of pH, Mg^{2+} and ionic current density

A AZ31 magnesium alloy (3% Al, 1% Zn, Mg balance) coated with a sol-gel film with 5 defects was exposed to 0.05M NaCl. Black spots in Figure 46 (a) correspond to artificial defects made in the coating by a sharp needle. The diameter of the three smaller defects is about 150 µm, the size of others two is ca. 200 x 280 μm^2 and 170 x 320 μm^2.

The local activities of H^+ and Mg^{2+} were mapped sequentially 10 µm above the surface on a 25x25 grid and the ionic current density was mapped on a 30x30 grid at height 100 µm. These grids generated 625 and 900 data points respectively. The time of acquisition for each SIET data point was about 2 s, resulting in a total scan time of about 35 min which also includes the time for the electrode to move from point to point. The data-sampling time for each SVET data point required about 0.5 s resulting in a total scan time of ≈ 11 min. The maps were recorded after about 5 hours of immersion.

Figure 46 shows the results obtained for simultaneous local mapping of current density, pH and pMg. Corrosion reactions in micro-defects result in development of cathodic (blue colour on the map Figure 46, d) and anodic (red colour on the map) processes as measured by SVET. Three defects became cathodic, one anodic while one demonstrates mixed activity working as a cathode and as an anode at the same time. The cathodic regions correspond to the Reaction 1.2 of water reduction with local alkalinization of solution (Figure 46 c). The SIET mapping of the same corroded defects was performed using an Mg^{2+}-selective microelectrode. The pMg map reflects the low concentration of Mg^{2+} in the cathodic regions due to predominance of OH^- ions which

lead to formation of $Mg(OH)_2$ (Figure 46 b). The regions of anodic activity, scanned by the Mg^{2+}-selective microelectrode, clearly show increased activity of Mg^{2+}-cations due to anodic metal dissolution (Reaction 1.1) in these zones.

All three maps are in good agreement. The cathodic and anodic distribution in each defect is completely coherent with the distribution of Mg^{2+} and H^+ ions.

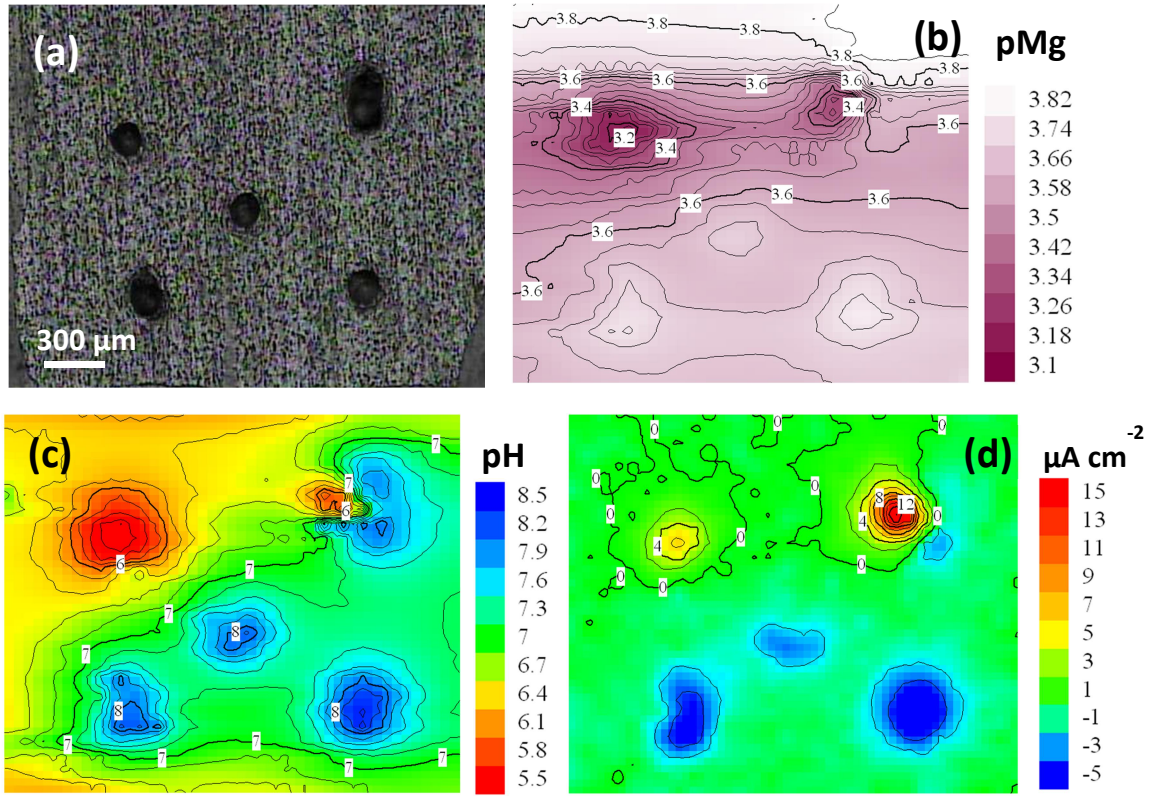

Figure 46. Optical photograph of scanned area of 1.53 x 1.85 mm^2, (a), pMg, (b), and pH, (c), and distribution of local ionic current density, (d), recorded during immersion of AZ31B alloy coated with thin sol-gel film in 0.05M NaCl solution.

6.3 Studying of corrosion inhibition in microdefects on coated AZ31 magnesium alloy

The inhibition of corrosion processes in micro defects of sol-gel films on AZ31 magnesium alloy was studied in chloride media. The defects, scratches and holes, in the coating were made artificially by a scalpel and a metallic needle respectively.

Three compounds were chosen as potential inhibitors for AZ31: 1,2,4,-triazole, F^- and Ce^{3+} ions. Fluoride compounds are used to form conversion coatings on pure magnesium and its alloys as pre-treatments for subsequent coating. MgF_2 and MgF(OH) are considered to be present in the surface layer after immersion in HF solutions [281–

283]. The fluoride containing film passivates the metallic surface and reveals promising corrosion resistance properties. Therefore F^- ions added to aggressive solution can be a good inhibitor because of the formation of insoluble compounds with Mg^{2+} released from the defects. Ce^{3+} ions, like other rare earth elements, are well known inhibitors for aluminium, ferrous and zinc alloys [273–278]. The cerium-containing conversion layers are also used for Mg alloys [284,285]. Particularly it should be mentioned that Ce^{3+} ions are able to provide corrosion protection in a rather wide pH range from 5.5 to 12. Derivatives of triazole, specifically 1,2,4,-triazole, and their mixtures are among the most popular organic inhibitors for light alloys [286–289]. Normally 1,2,4-triazole adsorbs in zones of metal dissolution forming stable complexes.

The SVET was used here as a main method for fast screening of the selected inhibitors in order to reveal the most efficient one. Figure 47 presents SVET maps obtained after 5h of immersion in the electrolytes containing different inhibitors. The reference sample (a) (no inhibition, 0.05M NaCl) is characterized by strong corrosion undermining the coating and spreading out from the defects (2 narrow scratches at the before measuring). Two well-defined zones appear in the places of defects. One defect becomes predominantly anodic and the other is cathodic. Strong hydrogen evolution appears in both anodic and cathodic zones. Normally, in the case of Mg-based alloys, due to corrosion potentials typically around -1.5V (vs saturated calomel electrode), the main cathodic reaction is the water reduction (Reaction 1.4), with hydrogen evolution and local alkalinisation [290]. Reduction of dissolved oxygen will also take place but the total amount of current is small compared to Reaction 1.4 [291]. The main anodic reaction is

$$Mg \rightarrow Mg^{2+} + 2e^- \quad (6.1).$$

But several authors also refer the possibility of reaction 6.2 [20,291–294]

$$Mg \rightarrow Mg^{+} + e^- \quad (6.2).$$

followed by hydrolysis of Mg^+,

$$Mg^{+} + H_2O \rightarrow Mg^{2+} + OH^- + 1/2\ H_2 \quad (6.3)$$

which produces hydrogen evolution in the anodic sites. Thus, the origin of the gas evolution in the “anodic” defect may be Reaction 1.4, Reaction 6.3 or both. Indeed, debates about the occurrence of reaction 6.2 and 6.3 are still ongoing in the scientific community. The arguments against Mg^+ formation and other possible explanations of hydrogen evolution reaction can be found in papers from Birbilis group [290,295].

The second sample (b) was tested in electrolyte containing 0.01M NaF. The surface seems only slightly affected around the scratch area. No hydrogen release is observed. The corrosion current densities are also significantly decreased being almost two orders of magnitude lower compared to 0.05M NaCl.

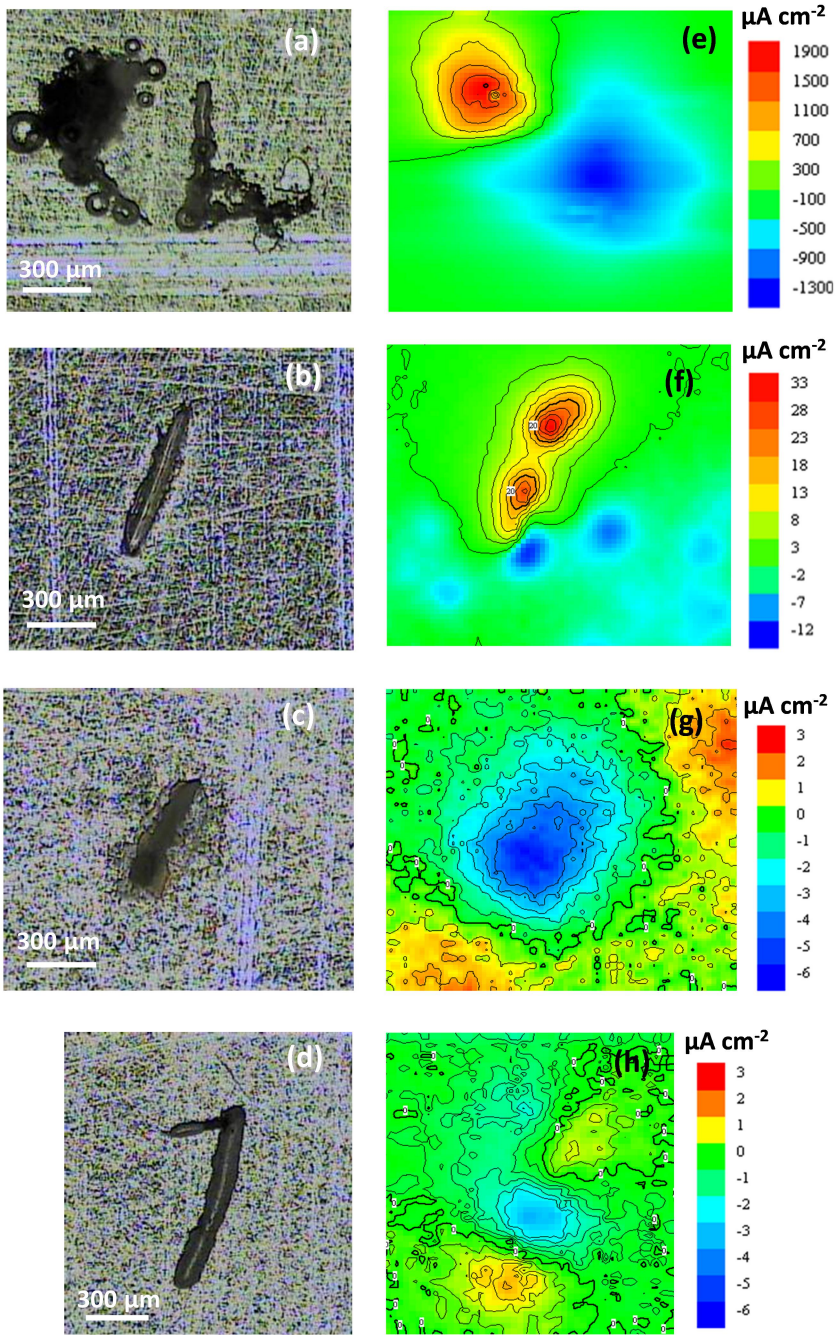

Figure 47. Optical micrographs (a, b, c, d) and local ionic currents maps (e, f, g, h) after immersion of AZ31 alloy coated with sol-gel film in 0.05M NaCl during 5 hours with different inhibitors: e – blank sample, f – 0.01M NaF, g – 0.01M $Ce(NO_3)_3$, h – 0.01M 1,2,4-triazole.

The third specimen (c) was tested in presence of $Ce(NO_3)_3$. Only minor delamination of the coating starting from the scratch area can be seen. No hydrogen bubbles are detected, whereas precipitation of corrosion product occurs in the scratch. The local currents are also significantly decreased in this case, being even lower according to the scale than in the case of fluoride containing electrolyte. Addition of 1,2,4-triazole

also significantly decreases the corrosion processes (d). The coating remains visually unchanged without any signs of the corrosion activity outside the defect or under the coating near the scratch. The measured corrosion current densities are almost 3 orders of magnitude lower than in the case of reference sample. Compared to the blank sample, all three tested compounds decreased the corrosion activity about 100-1000 times and suppressed hydrogen evolution. In the case of cerium and fluoride ions some processes are detected outside the defects while with 1,2,4-triazole only the damaged zone corrodes. Also the currents values in 0.01M 1,2,4-triazole are the smallest ones indicating the lowest corrosion activity and the highest protection. Thus 1,2,4-triazole is the most effective inhibitor for AZ31 among the tested ones.

It is well known that most of the corrosion inhibitors are pH dependent [1,10]. Therefore SIET with pH-SME and Mg^{2+}-SME was used in order to understand how pH and Mg^{2+} activity change during the corrosion processes in the defects when the corrosion inhibitor is present. Sol-gel coated alloy samples with round defects (holes with diameter of about 200 µm) were prepared for these measurements. Simultaneous detection of pH and Mg^{2+} activity was performed using a dual head stage holder with two probes situated 35 µm one from another (Figure 30). A move-wait-measure scheme was employed for scanning at 100 µm above the surface. The time of data acquisition was 3 s for potentiometric measurements and 0.3 s for vibrating probe.

The corrosion reactions in micro-defects on sol-gel coated AZ31 result in the development of cathodic and anodic processes that are detected by SVET (Figure 48 c). Some defects show only anodic or cathodic currents while in others both processes can be detected. The regions of anodic activity clearly show increased activity of Mg^{2+} cations due to anodic metal dissolution in these zones as reported in Section 6.2. The high local pH (up to 11.2, Figure 48 b) of the electrolyte near the defect can seriously affect the efficiency of the used corrosion inhibitors.

The effect of 1,2,4-triazole on the evolution of the pH and Mg^{2+} concentration above the corroding defects was investigated. Results of simultaneous measurements of pH and pMg are shown in Figure 49. In presence of the inhibitor local pH distribution on coated AZ31 varies close to the deffects between 5.8 and 4.8 (Figure 49 b).

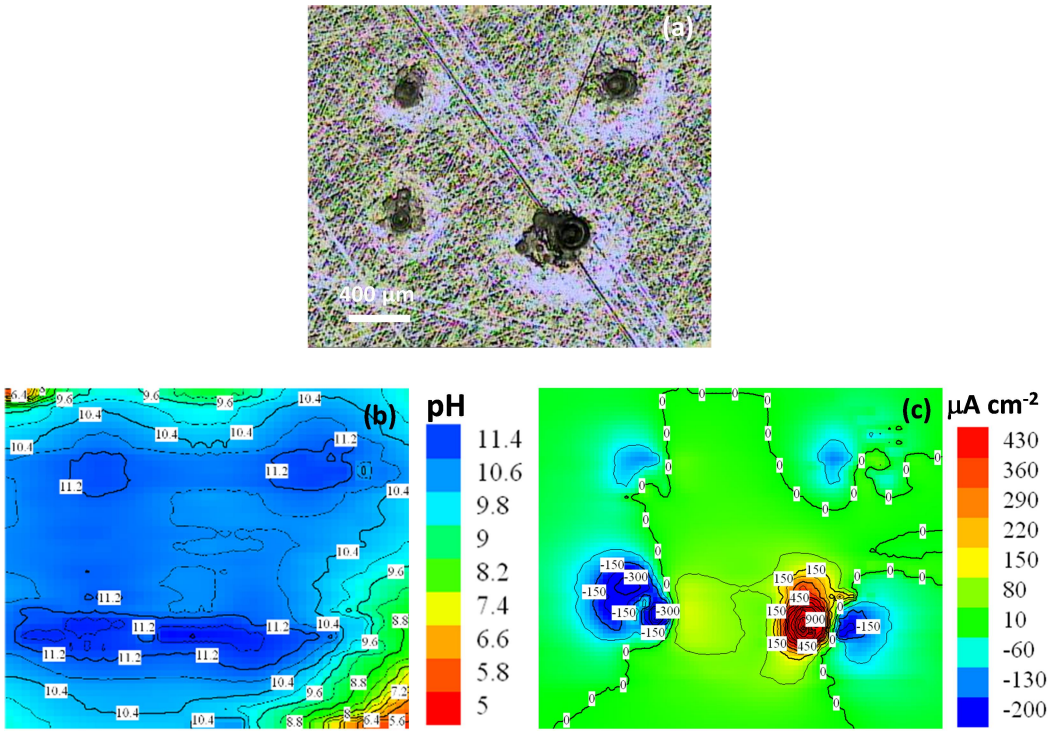

Figure 48. Optical micrograph (a), pH (b) and currents (c) maps after 7.5h of immersion coated AZ31 in 0.05M NaCl.

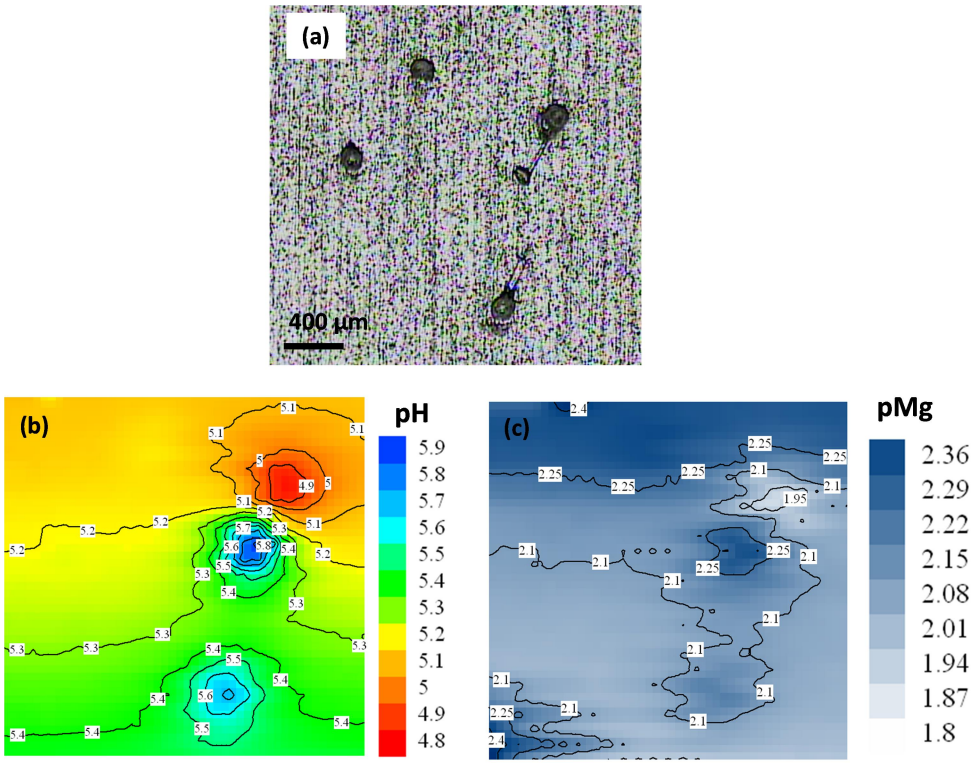

Figure 49. Optical micrograph (a), pH (b) and pMg (c) maps after 6.5h of immersion coated AZ31 in 0.05M NaCl, 0.01M 1,2,4-triazole [62,270].

The Mg^{2+} activity distribution (Figure 49 c) shows that the dissolution of the metal occurs in lower pH zone, while depletion of Mg^{2+} concentration is observed in regions with higher pH.

In contrast to strongly corroding sample without inhibitor where pH reaches 11.4 (Figure 48 b) both in anodic and in cathodic zones, the use of 1,2,4-triazole keeps pH in rather narrow range: 5.3±0.5 (Figure 49 b), thus, the presence of 1,2,4-triazole in electrolyte keeps the corrosion rate very low (as shown by SVET, Figure 47 d) and the solution is only slightly affected by the corrosion process.

Monitoring the pH above the defects for more than 10 hours shows a stable system (Figure 50). Values of OH^- activity rise slowly and with quite little increment in the initial zones although one more active zone of higher pH appears above the upper left defect after 8.5 hours. The presented results demonstrate that 1,2,4-triazole is able to inhibit corrosion processes in the micro-confined defects on coated magnesium alloy AZ31. The inhibition action suppresses the increase of local pH in the defects keeping almost constant values and ensuring continuous inhibition.

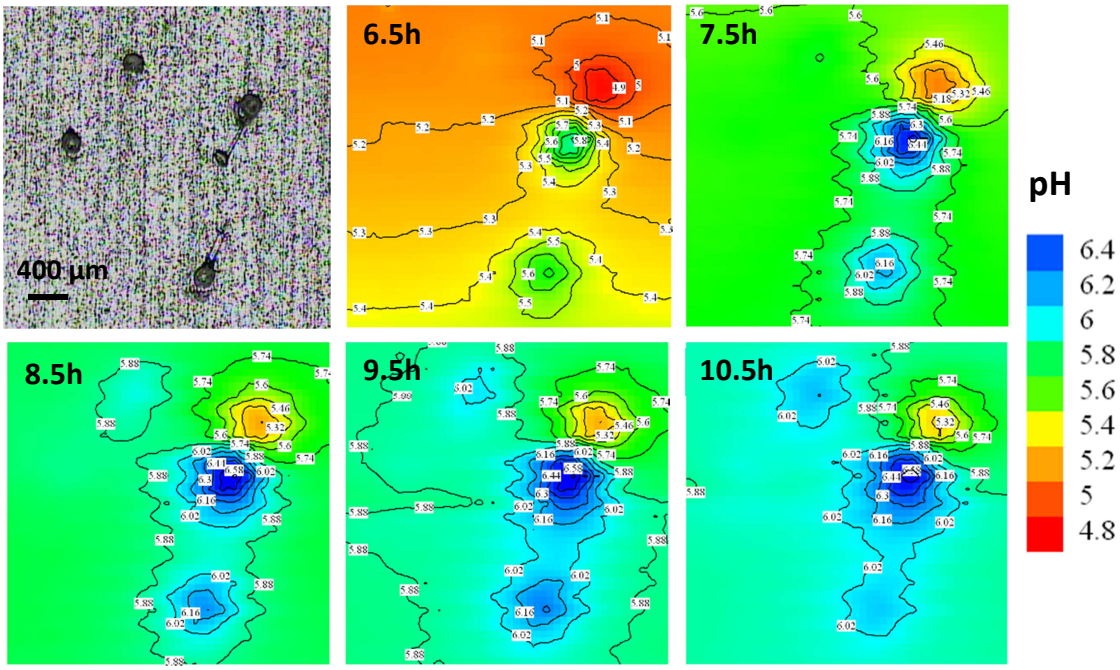

Figure 50. Optical micrograph and pH observation during immersion of coated AZ31 in solution of 0.05M NaCl, 0.01M 1,2,4-triazole.

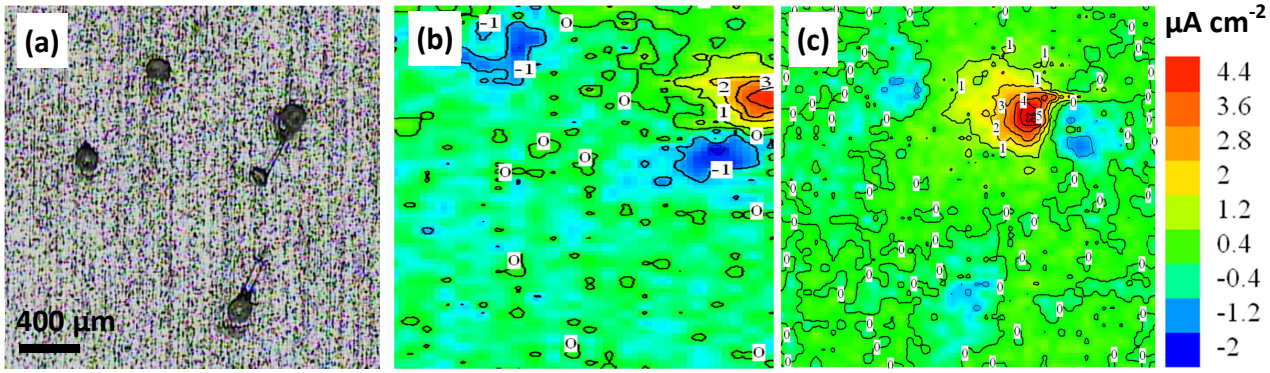

Figure 51. Optical micrograph (a) and SVET maps (µA cm^{-2}) after 1 day (b) and 3 days (c) of immersion coated AZ31 in 0.05M NaCl + 0.01M 1,2,4-triazole.

After 24 hours of immersion the corrosion activity in the defects was checked by SVET (Figure 51). The current density map presents three active zones (as in pH and pMg maps) – one slightly anodic and two slightly cathodic. Values of current density are very low being 2-3 orders of magnitude below the current densities in reference electrolyte. Even after 3 days of immersion the corrosion currents stay almost constant and small proving lasting and effective inhibition by 1,2,4-triazole (Figure 51 c).

6.4 Concluding remarks

The analytical characteristics of a Mg^{2+}-SME, based on a commercial membrane cocktail, confirm its suitability for corrosion studies. The mapping of local activity of magnesium ions dissolved due to corrosion on coating defects was measured successfully by SIET.

The combination of SVET and SIET is demonstrated here as a tool to investigate corrosion and inhibition processes in defects on coated magnesium alloys. The corrosion process on AZ31 coated with hybrid sol-gel film was studied by SVET in 0.05M NaCl solution with F^-, Ce^{3+} and 1,2,4-triazole as potential inhibitors. 1,2,4-triazole showed the highest inhibition efficiency and is a strong candidate as corrosion inhibitor in protective coatings for the AZ31 alloy.

Another possible application of Mg^{2+}-SME in localized corrosion processes is the detection of dissolution of Mg-containing intermetallics from aluminum alloy AA2024. The measurement of Mg^{2+} with the Mg^{2+}-SME was attempted but the experiments were unsuccessful. This means that either oxidation doesn't occur in the anodic zone, or if it takes place, it generates Mg^{2+} in an amount lower than the detection limit of the Mg^{2+}-SME.

Chapter 7

7 Zn^{2+}-SME for corrosion studies

In this chapter a Zn^{2+}-selective microelectrode (Zn^{2+}-SME) is developed and described. Its application in the study of the corrosion of pure zinc and a Zn-Fe galvanic couple is demonstrated.

7.1 Development and characterization of Zn^{2+}-SME

Not many works can be found in literature about potentiometric Zn^{2+}-SMEs (see Section 3.7.3). In addition, there are no ready-to-use membrane cocktails selective to Zn^{2+} available in the market. Therefore, it was decided to adapt a composition from macroelectrodes. Kojima and Kamata reported a composition with very attractive analytical characteristics, namely, low detection limit ($4.2 \cdot 10^{-7}$ M), relatively fast response time (2 s at 100-fold increase of Zn^{2+} concentration and 10 s at 100-fold decrease of Zn^{2+} concentration), quite small coefficients of selectivity toward alkali and alkaline-earth ions (for example, $logK^{Pot}_{Zn2+,Na+} = -3.3$) and working pH range from 3.5 to 6.5 [296]. The membrane consisted of 5.4 wt. % tetra-*n*-buthylthiuram disulfide (TBTDS), 12.3 mol. % KTClPhB, 53.6 wt. % NPhOE and 40.2 wt. % PVC.

This membrane composition was adapted for microelectrodes by excluding the PVC matrix. Also as only one composition was reported in [296]; it was decided to investigate the influence of the quantity of the ionophore and the ion exchanger on the electrode response at the micro-level. Thus, 4 membrane cocktails for Zn^{2+}-SME were prepared (Table 9).

Table 9. Composition of prepared membrane cocktails for Zn^{2+}-SME based on TBTDS ionophore.

Component	Membrane cocktail			
	Zn-c1	Zn-c2	Zn-c3	Zn-c4
TBTDS, wt. %	7.0	10.0	5.4	10.0
KTClPhB, mol.%	15.0	25.0	12.3	75.0
NPhOE, wt. %	up to 100	up to 100	up to 100	up to 100

The response of each obtained Zn^{2+} membrane cocktail was tested at two column lengths of membrane cocktail, i.e. 40 µm and 120 µm. The internal reference solution was 10^{-1}M $ZnCl_2$. Calibrations were made in $ZnCl_2$ solutions with and without 0.05M NaCl background. The dynamic calibration curves were recorded in order to evaluate the signal stability and the electrodes' life time (possible leakage and robustness). The results are presented in Figures 52-56 and Table 10 compares the response of all cocktails.

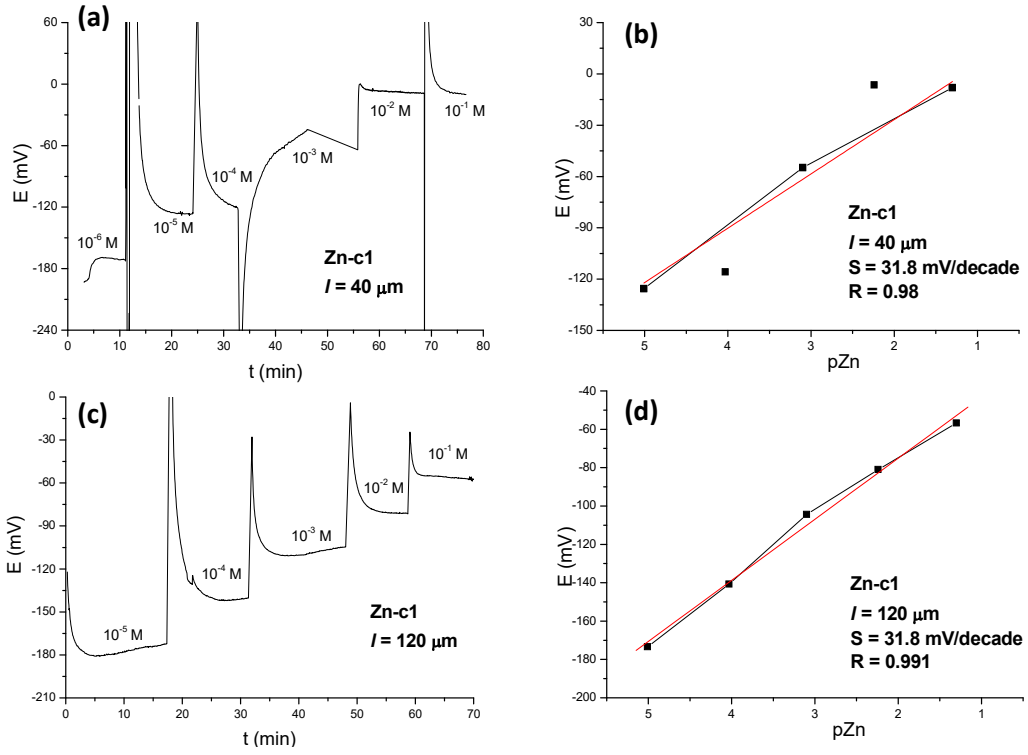

Figure 52. Response of Zn^{2+}-SME based on membrane cocktail Zn-c1 with different column length (40 µm and 120 µm).

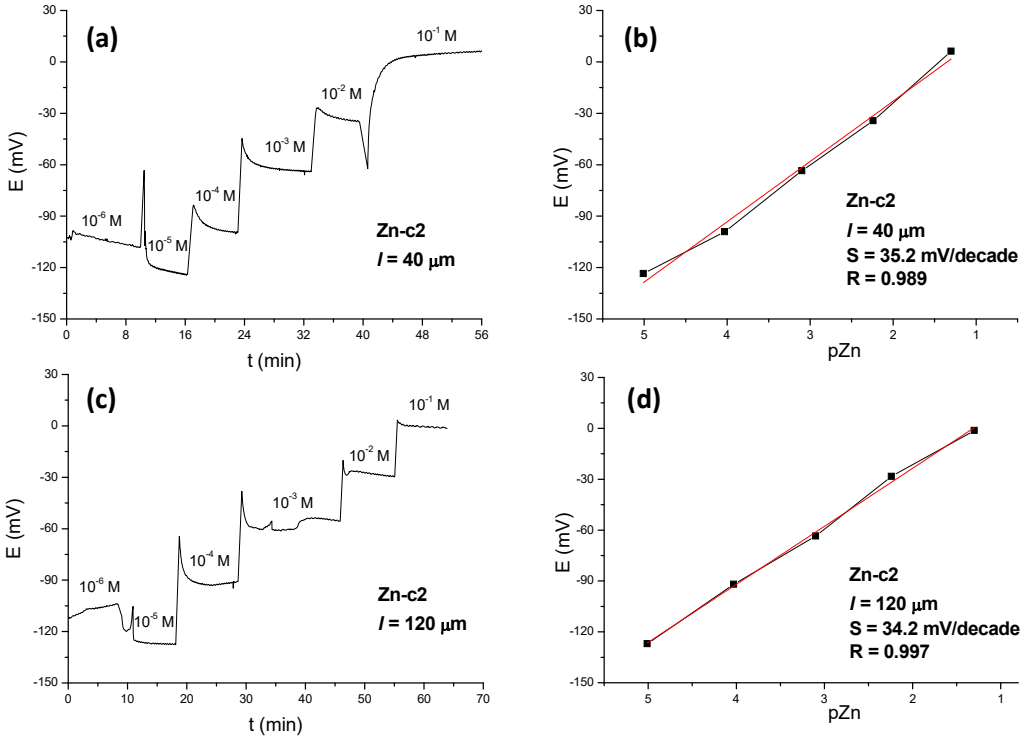

Figure 53. Response of Zn^{2+}-SME based on membrane cocktail Zn-c2 with different column length (40 µm and 120 µm).

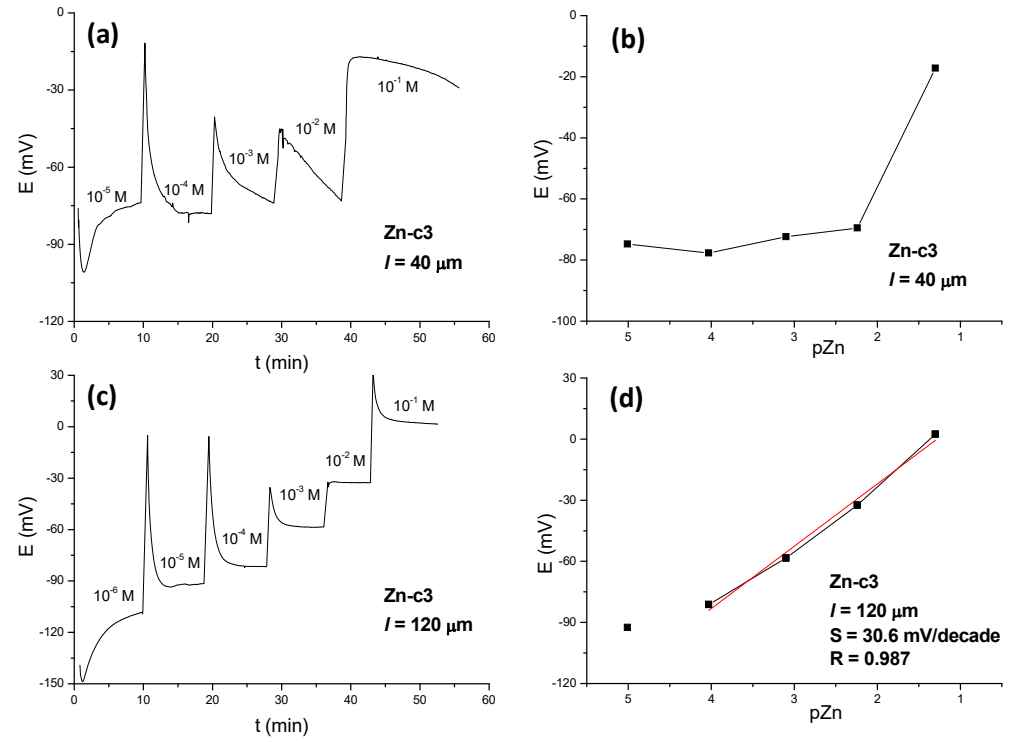

Figure 54. Response of Zn^{2+}-SME based on membrane cocktail Zn-c3 with different column length (40 µm and 120 µm).

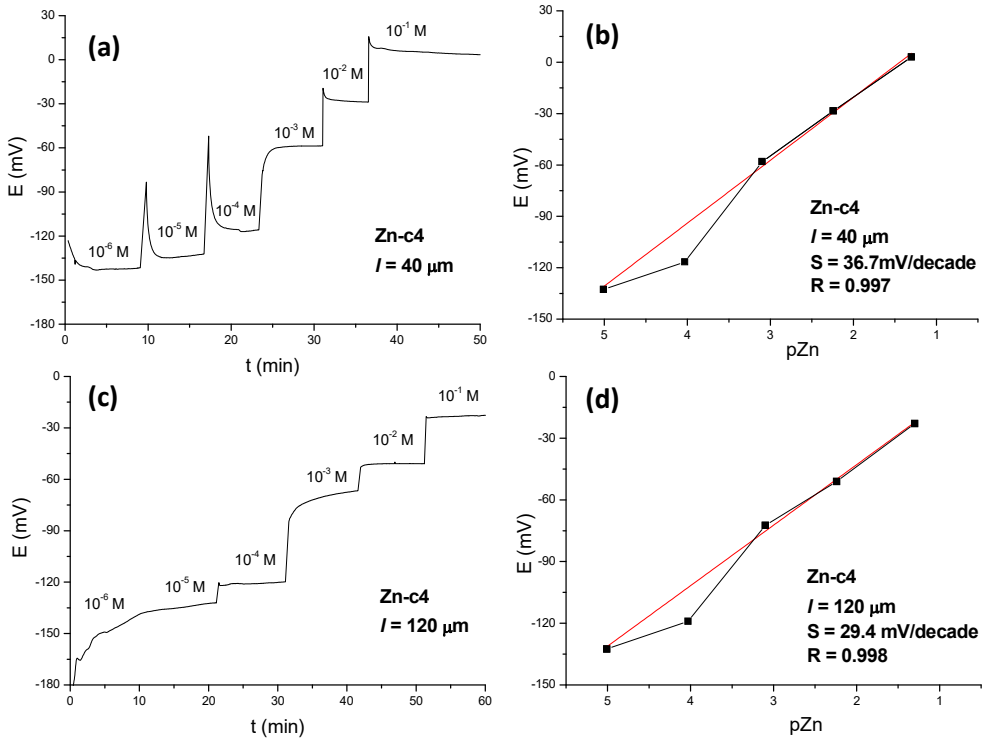

Figure 55. Response of Zn^{2+}-SME based on membrane cocktail Zn-c4 with different column length (40 µm and 120 µm).

Table 10. Comparison of response of Zn^{2+}-SMEs based on preparead cocktails.

Cocktail	Column length, *l* = 40 µm		Column length, *l* = 120 µm	
	S, mV/decade	linear range, pZn	S, mV/decade	linear range, pZn
Zn-c1	31.8*	1-5*	31.8	1-5
Zn-c2	35.2	1-5	34.2	1-5
Zn-c3	-	not detectable*	30.6	1-4
Zn-c4	36.7	1-5	29.4	1-5

*- with potential drift

According to the dynamic calibration plots, Zn^{2+}-SMEs with larger column length of the cocktail have more stable potential (Figures 52 c and 54 c) in contrast to Zn^{2+}-SMEs with smaller column length of the cocktail (Figures 52 a and 54 a).

Comparing cocktails Zn-c3, Zn-c1 and Zn-c2, which have 5 wt.%, 7 wt.% and 10 wt.% of the ionophore respectively (Table 10 and Figures 54 b, 52 b and 53 b) one can say that higher concentration of the TBTDS provides faster response and wider linear range of Zn^{2+}-SME. The presence of ion-exchanger (KTClPhB) also affects the performance of Zn^{2+}-SMEs. The higher is the content of KTClPhB, the closer is the slope of the microelectrodes to the theoretical value (compare cocktails with larger column length in Table 10). Thus,

Zn^{2+}-SME based on Zn-c4 with 75 mol.% of KTClPhB has slope of 29.4 mV/decade and Zn^{2+}-SME based on Zn-c2 with 25 mol.% of KTClPhB has slope of 34.2 mV/decade.

The sensitivity for Zn^{2+} in the presence of Na^{+} ions was tested for all cocktails, but only a microelectrode based on the cocktail Zn-c2, that has 10 wt.% of TBTDS, worked in 0.05M NaCl background having narrow linear range from 10^{-1} to 10^{-3} M of $ZnCl_2$ and slope of 25.4 mV/decade (Figure 56). This means that the high selectivity of Zn^{2+}-ISE against Na^{+} ions claimed in [296] could not be reproduced. The other cocktails did not show reliable potenial values in 0.05M NaCl solution. Moreover, the prepared microelectrodes often showed unstable potential and could not be used for localized measurements.

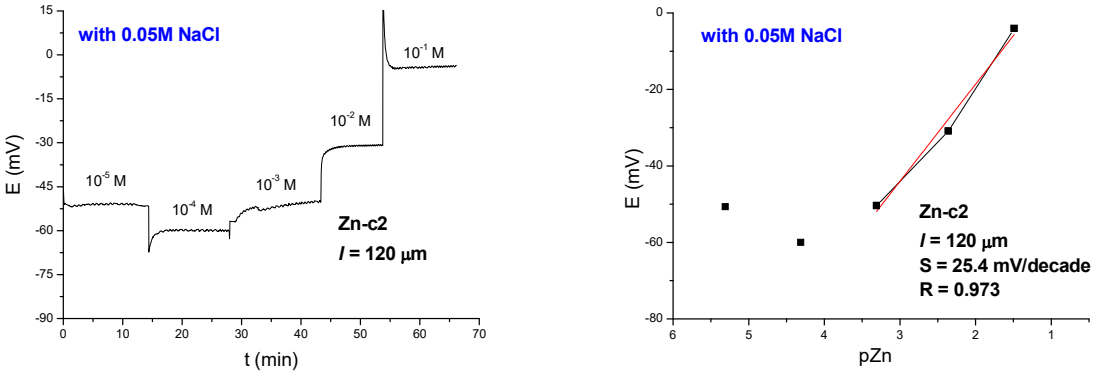

Figure 56. Response of Zn^{2+}-SME based on membrane cocktail Zn-c2 with 120 µm of column length in the presence of 0.05M NaCl.

An attempt of improvement was made in close collaboration with IST (Lisbon, Portugal) where after several trials and discussion it was decided to modify the cocktail by using highly lipophilic ion exchangers – sodium tetrakis[3,5-bis(trifluoro-methyl)-phenyl]borate (NaFMPhB) and tetrakis(4-chlorophenyl)borate tetradodecyl ammonium (ETH 500) [297]. They were introduced into the membrane composition in order to decrease the membrane resistance and stabilize the electrode potential, what was found to work well for Ca^{2+}-SME [224]. The developed cocktail, Zn-c5, consisted of 7.0 wt.% of TBTDS, 22.8 wt.% (150 mol.%) of NaFMPhB, 1.4% of ETH500 and 68.8 wt.% of NPhOE. The concentration of Zn^{2+} in the internal solution was decreased to provide lower detection limit [298]. The internal solution was 0.1M KCl + 0.01M KH_2PO_4 + 10^{-5}M $ZnCl_2$.

Calibration plots of Zn^{2+}-SME, based on Zn-c5, are shown in Figure 57. The response was linear in the range 1.3-5.5 pZn in pure Zn^{2+} solutions and 1.3-3.5 pZn in 5mM NaCl background having slopes of 34.8 and 30.4 mV/decade respectively. The measured time of response was τ_{95} = 2.6 s and τ_{lim} = 4.6 s.

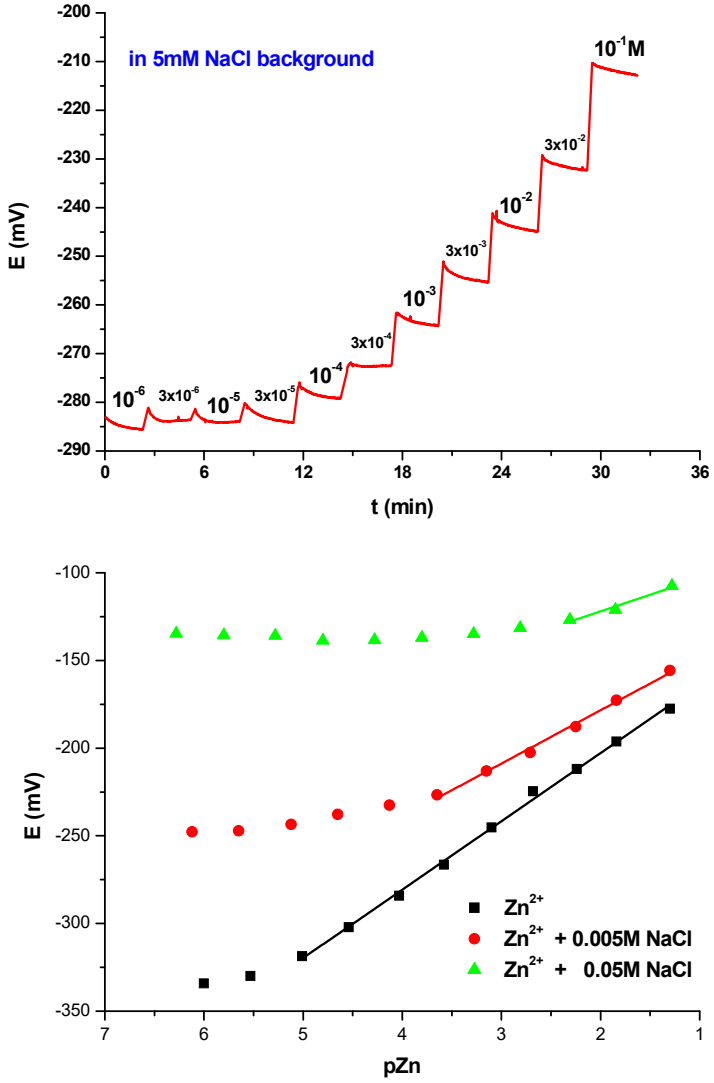

Figure 57. The dynamic response (upper) and calibration plots (lower) of Zn^{2+} -SME based on membrane cocktail Zn-c5.

It becomes clear from Figure 57 that NaCl influences the electrode response what is confirmed by the selectivity coefficient $logK_{Zn2+,Na+}^{Pot} = -1.4$ measured by modified SSM as described in Section 4.7.1.3.

In spite of the limited selectivity, the Zn^{2+}-SME based on cocktail Zn-c5 was successfully applied for investigation of zinc electrodeposition, corrosion in defects of coated galvanised steel [297]; galvanic corrosion of Zn-Fe couple (next Section 7.2.1) and pure zinc corrosion (next Section 7.2.2).

7.2 Application of Zn^{2+}-SME to corrosion studies

7.2.1 Galvanically coupled Zn-Fe electrodes

The distribution of Zn^{2+} activity over a corroding Zn-Fe galvanic couple (cell shown in Figure 31) was measured in distilled H_2O and in 5mM NaCl. The time of data acquisition in each point was 3 seconds. The distance between points was 100-120 µm. The obtained maps of pZn distribution are presented in Figures 58 and 59.

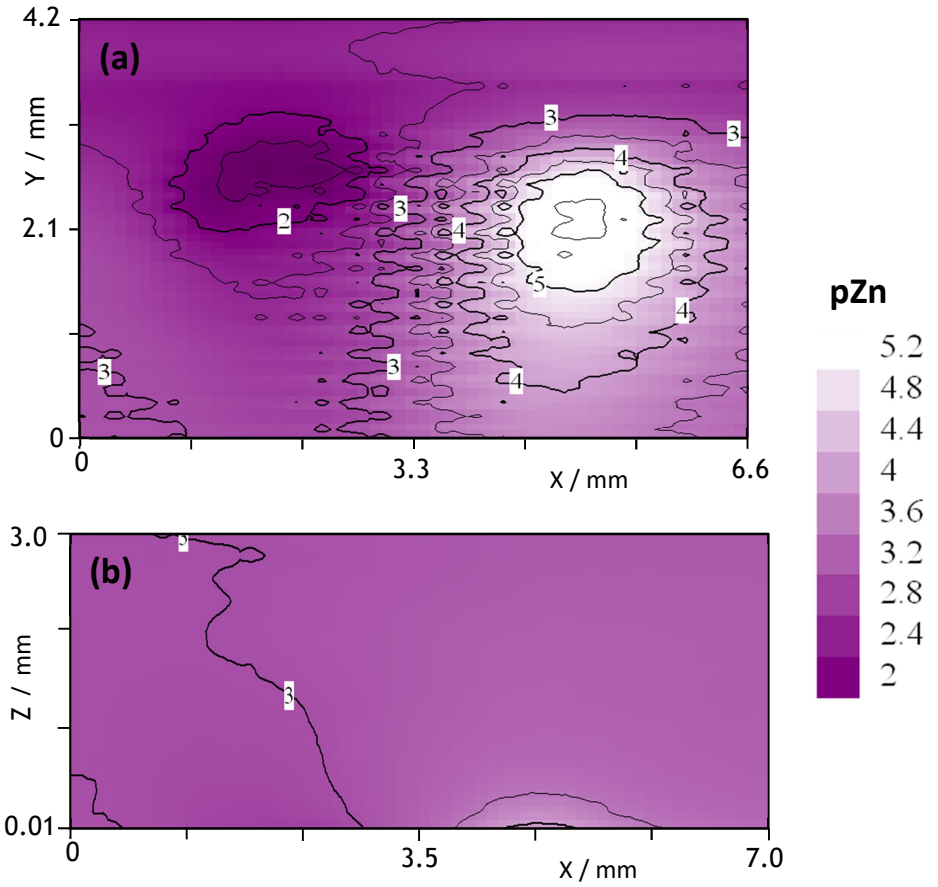

Figure 58. Distribution maps of Zn^{2+} activity in XY (height 10 µm) (a) and XZ (b) planes near the Zn-Fe galvanic couple after 15h of immersion in distilled H_2O.

Figure 58 (a) shows the distribution of pZn measured in the XY plane 10 µm above the surface of galvanically connected zinc and iron in distilled water. The highest Zn^{2+} activity (ca pZn 1.5) was detected above the zinc wire due to zinc dissolution according to the reaction 5.1 (anodic zone). The lowest values were measured upon the iron (ca. pZn 5.2), i.e in a cathodic zone, where the oxygen reduction (reaction 1.2) produces OH^-, which combines with Zn^{2+} and form $Zn(OH)_2$ reducing the content of free zinc ions in solution.

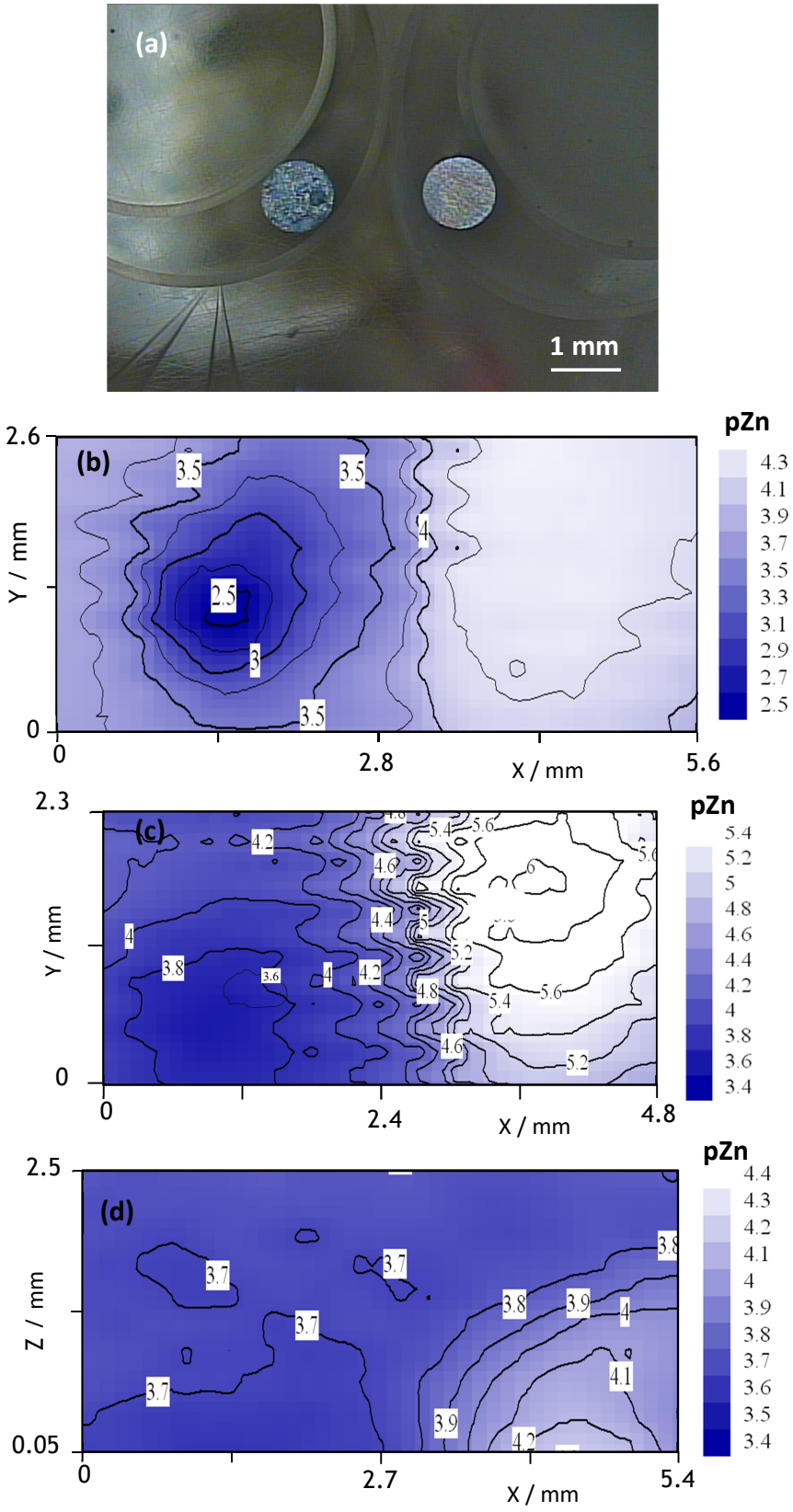

Figure 59. Optical image of the Zn-Fe couple (a). Distribution of pZn in XY (b, c) and in XZ planes (d) near Zn-Fe galvanic couple immersed in 5mM NaCl during 2h (b), 36h (c) and 48h (a, d).

The same character of Zn^{2+} distribution was found in XZ map (Figure 58 b). The changes in Zn^{2+} concentration were observed till ca. 1000 µm above the surface of the galvanic couple. The bulk value was around pZn 3 in both maps.

The mapping of Zn^{2+} 100 µm over the Zn-Fe galvanic couple after 2 hours of immersion in 5mM NaCl is shown in Figure 59 (b). Two regions of high (up to pZn 2) and low (to pZn 4.3) zinc activity were detected over the zinc and iron surfaces correspondingly. The bulk value was around pZn 4. The Zn^{2+} activity measured after 36 hours of immersion was lower, above the zinc surface, above the iron and in the bulk (Figure 59 c), due to formation of zinc corrosion products, that are slightly observed between the metal wires (closer to the iron) as a wide gray band on Figure 59 (a). Still two distinct areas of high and low pZn were detected. The local distribution of zinc ions in XZ map is coeherent with that in XY maps, i.e. more Zn^{2+} (pZn 3.5) was detected above the zinc and less (pZn 4.5) above the iron wire (Figure 59 d), and the concentration changes happen mainly till ca. 1300 µm from the sample surface.

The maps of spatial distribution of zinc ions in water and in 5mM NaCl showed above Zn and Fe wires galvanically connected are well defined, and allow visualize the corrosion of the zinc-iron galvanic couple.

The pZn maps are also in good agreement with current densities, pH and dissolved oxygen concentration maps measured above the Zn-Fe couple in 5mM NaCl and shown in Section 5.1.

7.2.2 Zinc wire corroding in chloride media

In this section the Zn^{2+}-SME based on cocktail Zn-c5 and the pH microelectrode based on Hydrogen ionophore I cocktail B (Fluka, Germany) were applied for characterization of localized corrosion of zinc wire immersed in 5mM NaCl.

Figure 60 (a) presents a zinc wire embedded in an epoxy matrix after 24 hours of immersion in 5mM NaCl. Three distinct regions are easily observed: an anodic pit (dark spot), where zinc oxidizes, a cathodic region (bright metallic surface) where oxygen reduction takes place and a “wall” of precipitated corrosion products, separating them. This localized form of corrosion (pitting) is typical for zinc in mild chloride aqueous solutions [299,300].

Values of electrode potential, pH and pZn (measured with dual head stage, Figure 30) were mapped 100 µm above the surface. The electrode potential was measured using a homemade electrode Ag/AgCl, 0.05MNaCl (Figure 22 b). Data were taken at selected points of the sample and in the bulk solution. The results are shown in Figure 60 (b) and summarized in Table 11 together with the corresponding reactions.

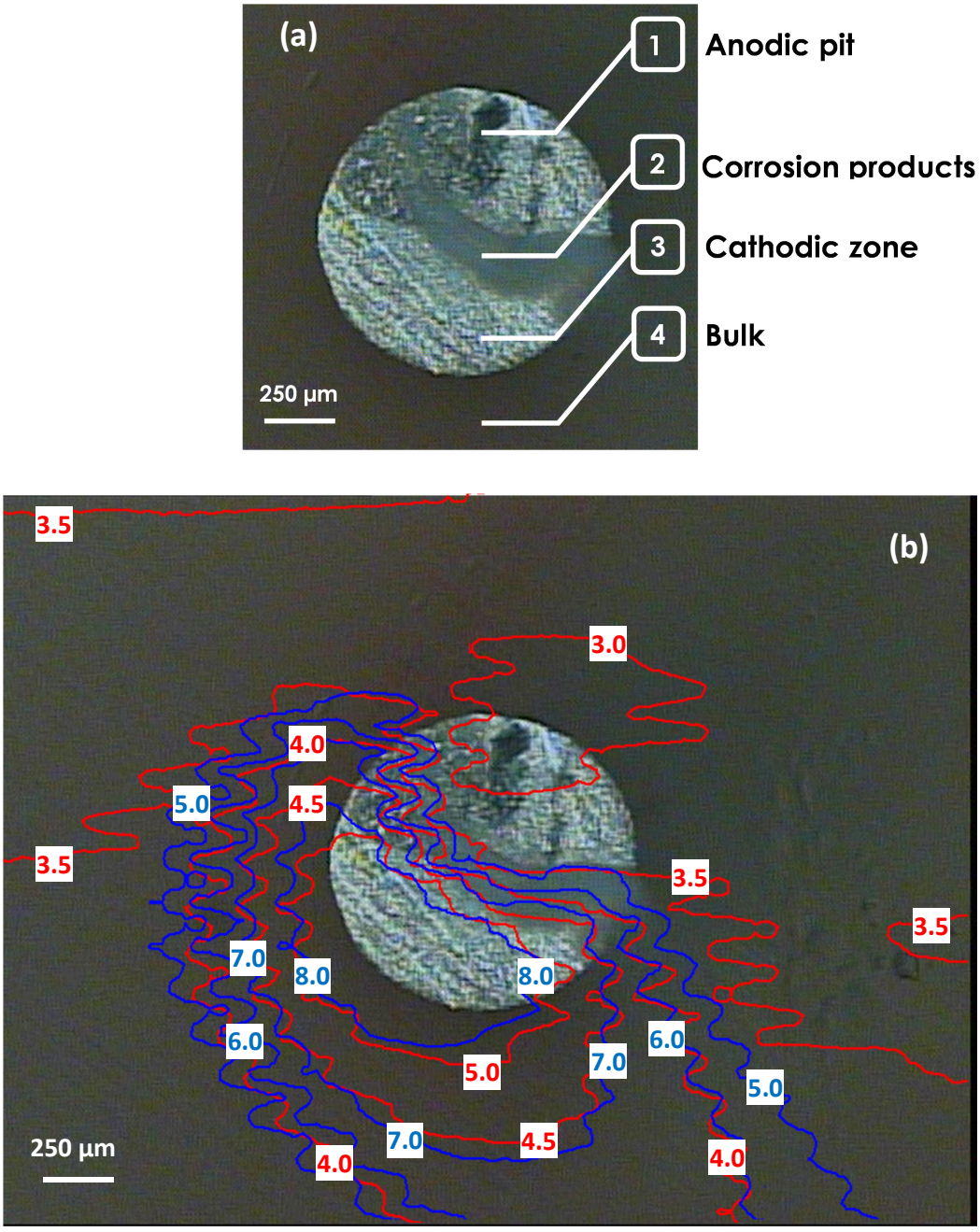

Figure 60. Photograph of zinc wire after 24 hours of immersion in 5mM NaCl (a). Maps of pH (blue lines and labels) and of pZn (red lines and labels) taken 100 µm above the surface and ploted over the sample photograph (b).

The anodic site (site 1), where the zinc dissolution takes place, has the most negative potential, the highest zinc activity and the lowest pH, while the cathodic site (site 3) is characterized by the lowest pZn, highest pH values and less negative potential. The bulk solution (site 4) and the zone of corrosion products (site 2) have intermediate values. It should be noticed, that each analyzed site belongs to the corresponding zone of the corrosion process, which has rather an interval than a single value of measured

parameters. For example, the precipitation of corrosion products is observed between the anodic and cathodic regions in the pH interval from 5 till approximately 7, where pZn changes from 3.5 to 4.5.

Table 11. Results of potential, pH and pZn measurements in single sites above Zn wire immersed in 5mM NaCl.

Site	E*, mV	pH	pZn	Reaction
1	-991.0	4.09	2.78	$Zn \rightarrow Zn^{2+} + 2e^{-}$
2	-985.2	6.85	3.89	$Zn^{2+} + 2OH^{-} \rightarrow Zn(OH)_2 \downarrow$
3	-983.4	8.89	5.48	$2H_2O + O_2 + 4e^{-} \rightarrow 4OH^{-}$
4	-986.4	4.41	3.52	no reaction

*vs Ag/AgCl,0.05M NaCl

An interesting point, still object of debate, concerns the initial zinc corrosion product in aqueous medium, oxide or hydroxide [301–305]. Some authors defend that the first product formed is ZnO followed by $Zn(OH)_2$ and the $ZnO/Zn(OH)_2$ ratio depends on temperature and time of exposure [303]. Others support that ZnO only appears first in dry atmospheres, with a slow constant of formation [302]. The surface layer of ZnO may reach a thickness of 100 Å, but only after a few weeks [302]. For these authors, after the formation of zinc hydroxide, which is the initial corrosion product of zinc according to,

$$Zn^{2+} + 2OH^{-} \rightarrow Zn(OH)_2 \downarrow \quad (7.1)$$

two processes may occur. Either the dehydration of $Zn(OH)_2$ and its transformation into ZnO,

$$Zn(OH)_2 \rightarrow ZnO + H_2O \quad (7.2)$$

or the reaction with CO_2 to form hydrozincite $Zn_5(CO_3)_2(OH)_6$,

$$5Zn(OH)_2 + 2CO_2 \rightarrow Zn_5(CO_3)_2(OH)_6 \quad (7.3)$$

ZnO may also react with CO_2 to form $Zn_5(CO_3)_2(OH)_6$,

$$5ZnO + 3H_2O + 2CO_2 \rightarrow Zn_5(CO_3)_2(OH)_6 \quad (7.4)$$

In the presence of chlorides $Zn_5(OH)_8Cl_2 \cdot H_2O$ (simonkolleite) is formed either from ZnO or $Zn(OH)_2$,

$$4Zn(OH)_2 + ZnCl_2 \rightarrow Zn_5(OH)_8Cl_2 \quad (7.5)$$

$$4ZnO + 4H_2O + ZnCl_2 \rightarrow Zn_5(OH)_8Cl_2 \quad (7.6)$$

The inter-conversion between $Zn_5(OH)_8Cl_2$ and $Zn_5(CO_3)_2(OH)_6$ is also possible [301]:

$$Zn_5(CO_3)_2(OH)_6 + 2Cl^- + 2H^+ \rightarrow Zn_5(OH)_8Cl_2 + 2CO_2 \uparrow \quad (7.7)$$

The following scheme can be advanced to summarize the sequence of formation and interrelation of the zinc corrosion products in aqueous environments in the presence of chlorides:

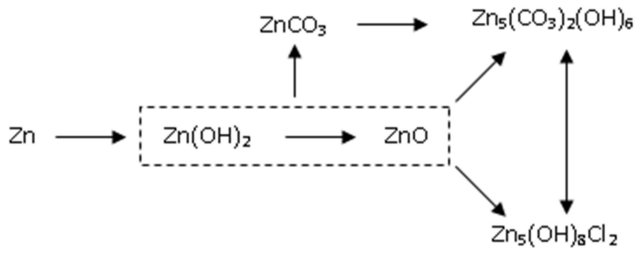

An interpretation of the local chemical environment can be done using Geochemical Modeling Software (GMS). The types of interactions between species near the corroding system are geochemical in nature; that is, the reactions are the same as those found in natural waters, high-temperature, or magmatic systems. When chemical systems are simple, with few possible reactions likely to occur, the geochemistry of a local environment may be described rather easily. When the geochemistry of an environment is more complex, however, quantitative models of aqueous and solid state chemistry are required. With the expansion of desktop computers and a wide variety of both commercial and freeware software it becomes possible to almost every scientist and engineer to predict the result of a real system.

In this work three GMS programs PHREEQC [306], Medusa&Hydra [307] and Geochemist's Workbench Pro 8 (GWB) [308] were used to generate diagrams of Zn^{2+} chemical speciation. Several species (Zn^{2+}, Na^+, Cl^-, H^+ and CO_2) with different concentrations and/or activities were used as initial input data. Experimental data were then added to the diagrams enabling the comparison between theory and experiments.

The diagram of Zn^{2+} species fractions generated by PHREEQC for $C(Zn^{2+}) = 10^{-3}$ M is shown in Figure 61. According to it, free Zn^{2+} exists in acidic medium until pH 7, where the points 1 and 4 arise, and then its fraction decreases and formation of several hydroxyl containing species begins. At the pH value of the region 2 (corrosion products region) the content of free Zn^{2+} decreases, while two species ($ZnOH^+$ and $Zn(OH)_2$) start to form and their fractions grow as the pH increases until reaching the pH of area 3 (cathodic zone). Then a new species become stable, $Zn(OH)_3^-$, and the fraction of $ZnOH^+$ begins to decrease. PHREEQC program generated similar diagrams of zinc speciation, with and without NaCl or CO_2, and for different initial concentrations of zinc with the following prevailing species: Zn^{2+}, $Zn(OH)^+$, $Zn(OH)_2$, $Zn(OH)_3^-$ and $Zn(OH)_4^{2-}$ in all cases.

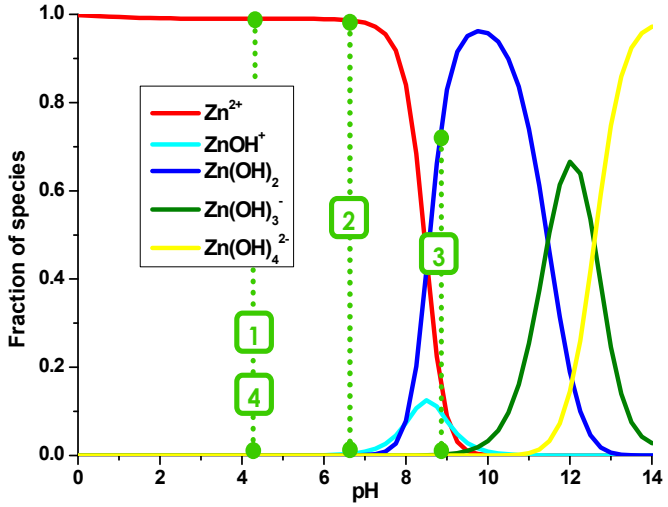

Figure 61. Diagram of distribution Zn^{2+} species in H_2O generated by PHREEQC for 1m M of Zn^{2+}. 1, 2, 3 and 4 correspond to the sites in Figure 60 (a) and Table 11.

Figure 62 presents fraction diagrams generated by Hydra & Medusa made for pZn = 3.89 in the presence of 5mM NaCl with (b) and without dissolved CO_2 (a) (considered as $[CO_3^{2-}]$ =1.5x10^{-4}M). The main differences with respect to the previous diagrams are noticed after pH 7, i.e. in the region of formation of corrosion products. Thus, in the absence of carbonates, Zn^{2+}, $ZnOH^+$ and $Zn_5(OH)_8Cl_2$ can be found in solution within the region with pH borders of 6.85 and 8.89 (pH of regions 2 and 3) (Figure 62 a). In the case of CO_2 less content of $ZnOH^+$ exists, and $Zn_5(OH)_6(CO_3)_2$ is present together with Zn^{2+} and $Zn_5(OH)_8Cl_2$.

Hydra&Medusa also produces variant graphs for different initial activities of Zn^{2+}. In the case of pZn = 1, Zn^{2+}, $ZnOH^+$ and $Zn_5(OH)_8Cl_2$ have lower fractions compared to the diagram in Figure 62 and are present in the pH between 6.85 and 8.89 (Figure 63). An increasing content of $Zn_4(OH)_4^{4+}$ can be seen as well.

Diagrams in Figure 64 were generated by GWB for 1M (blue lines) and 10^{-5}M (red lines) initial concentration of Zn^{2+} considering presence of 5mM NaCl and dissolved carbon dioxide (fugacity 3.54x10^{-4} bar) in solution. It shows that, at low concentrations, zinc is in solution in the free form (Zn^{2+}) up to pH 8. It precipitates as ZnO from pH 8 to 12 and dissolves after pH 12 in the form of $Zn(OH)_4^{2-}$ or $Zn(OH)_3^-$. Increasing the Zn^{2+} concentration (up to 1 M) gives origin to several stable chlorides containing species in acidic medium, making the free form to correspond to a fraction of nearly 0.6. Higher total content of zinc also enlarges the pH region where precipitation occurs. For 1M it is from 6 to 14.

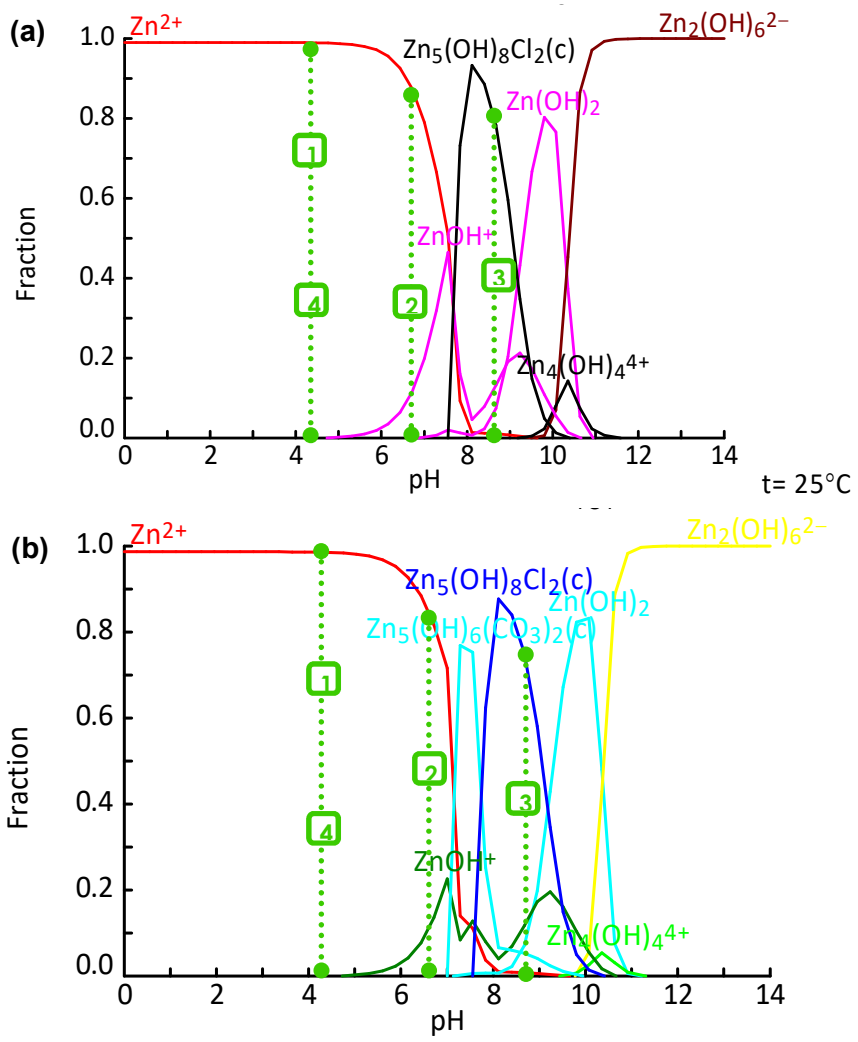

Figure 62. Diagram of Zn^{2+} species (pZn 3.89) in 5mM NaCl without CO_2 (a) and with CO_2 (b) generated by Hydra&Medusa.

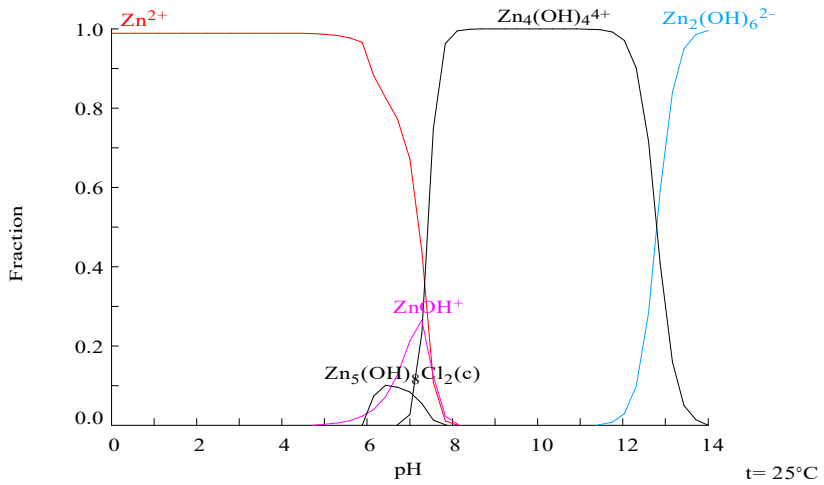

Figure 63. Diagram of Zn^{2+} species for initial pZn 1 in 5mM NaCl generated by Hydra&Medusa.

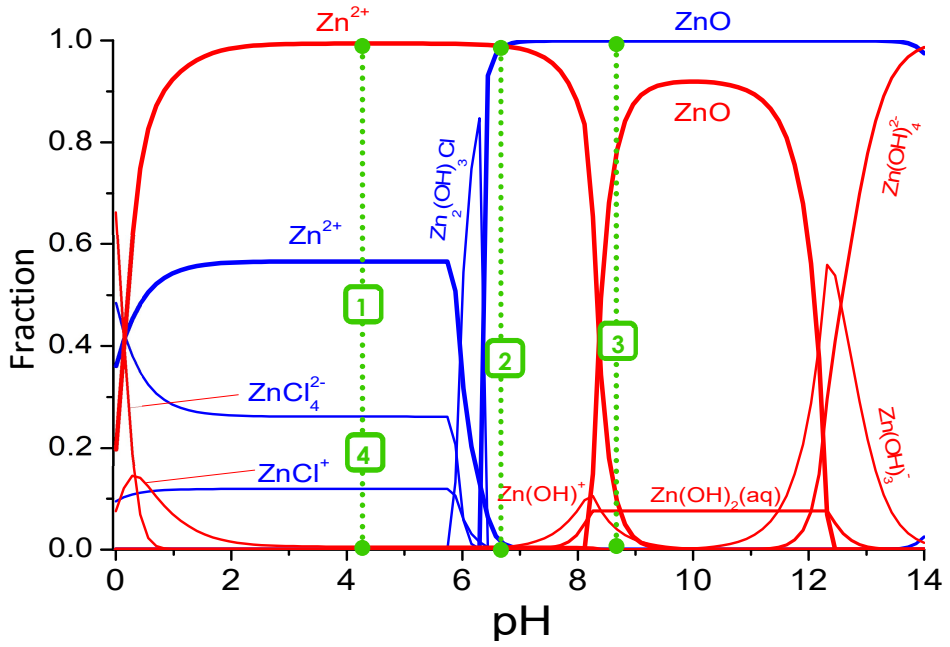

Figure 64. Stability diagram of Zn^{2+} containing species in 5mM NaCl with 1M (blue) or 10^{-5}M (red) of total zinc concentration in presence of dissolved CO_2 generated by GWB.

The added experimental data indicate, that for low initial zinc concentration, which will correspond closely to the case of 10^{-5}M Zn^{2+} (red lines in Figure 64), the main species existing in the border of cathodic and anodic regions, i.e. near the corrosion products zone, will be Zn^{2+}, $Zn(OH)^{+}$ $Zn(OH)_2$ (aq) and ZnO.

The obtained diagrams revealed the presence of the main corrosion ptoducts from the scheme mentioned above (page 136 of the thesis). However, predicted zinc species vary noticeably qualitatively and quantitatively. The differences in diagrams come from different databases used by the programs, with different species and reactions contemplated. Also kinetics is not considered here; only the most stable species appear on the results. The systems are then considered steady-state and the first moments of immersion may not be well characterized. This makes difficult to choose the most reliable model without experimental validation. This type of programs is still rare in corrosion research. Regarding this Mattens wrote in ASM Handbook Corrosion [309]: “Geochemical modeling software is now being used to understand and predict scaling, susceptibility to corrosion, atmospheric corrosion rates, acid rain, corrosion film solubility, and environmental impacts of aqueous species in runoff. Ironically, GMS systems are seldom used by corrosion scientists and engineers, even though geochemical modeling may provide greater insight into the causes and results of corrosion reactions and processes”.

7.2.3 Final remarks

The first attempts for development of Zn^{2+}-SME described in Section 7.1 resulted in a cocktail based on neutral carrier – tetra-n-butyl thiuram disulfide. The Zn^{2+}-SME was made with the cocktail Zn-c5 (7.0 wt.% of TBTDS, 22.8 wt.% of NaFMPhB, 1.4 wt.% of ETH500 and 68.8 wt.% of NPhOE).

This microlelectrode was successfully applied for investigation of several important cases of zinc corrosion. The quasi simultaneous mapping of pH and pZn resulted from the localized corrosion of Zn wire showed that spatial distribution of Zn^{2+} ions was immediately affected by OH^-, i.e. as soon as zinc cations were released from the surface, the formation of Zn^{2+} containing species was iniciated and insoluble precipitates appeared close to the pit. The use of GMS programs with input data from SIET results allowed estimating the chemical composition of the corrosion products.

These examples have demonstrated the suitability of the fabricated Zn^{2+}-SME for materials science and corrosion research. But in spite of the reported attractive analytical characteristics and the promising results this Zn^{2+}-SME has reduced selectivity against Na^+. Selectivity to Na^+ should be improved to extend the linear response in NaCl solutions and decrease the detection limit of Zn^{2+}-SME.

7.3 Optimization of the membrane composition for Zn^{2+}-SME applicable for corrosion related studies

In this section the rationalization of membrane composition for Zn^{2+}-selective microelectrode is presented. The most important requirement of a selective sensor for zinc is an ionophore with high affinity for Zn^{2+} and poor for other species. That is why it was decided to look for other ionophores apart from TBTDS. Together with ionophore influence, the effect of the membrane solvent and the ion-exchanger was also studied.

The membrane optimization followed the procedure for traditional macro ISEs based on polymeric (PVC) membranes. First, because conventional ISEs are much more stable and robust during daily experiments, giving more confident and reproducible results, and second, because the PVC membranes preparation technique is simple, easy and relatively fast. The best membrane compositions were then used to produce cocktails for Zn^{2+}-SMEs.

7.3.1 Selection of Zn^{2+} ionophores

A large number of compounds has been explored as ionophores for fabrication of ion-selective sensors for Zn(II) ions [210]. These compounds are macrocyclic or non-cyclic

molecules, containing electron donor atoms of O, N, S, etc., which are capable to form electronic rich cavities and possess the affinity to complex zinc ions. For instance, O and N-based macrocycles, as crown ethers [310–312], 2,2,2-cryptand [313], calixarene [314], porphyrins [315–317], tetraazamacrocycle [318], etc. have been investigated for the construction of PVC membrane electrodes. Compounds containing nitrogen donors have attracted wide attention, as the stability of their complexes with transition metal ions was higher compared to either alkali or alkaline earth metals [319]. Among them are also non-cyclic N,N'-Bis(2-dimethylaminoethyl)-N,N'-dimethyl-9,10-anthracenedimethanamine (bis(TMEDA)-anthracene) [319] and ligands containing both N and O atoms in the cavities: derivative of 1,3,4-thiadiazole [320], benzo-substituted macrocyclic diamide derivative [321], macrocyclic compound 1,12,14-triaza-5,8-dioxo-3(4),9(10)-dibenzoylcyclo-pentadeca-1,12,14-triene [322], pendant armed macrocyclic ligand [323], Schiff's bases [324] and non-cyclic N,N'-bis(acetylacetone)ethylediamine [325]. The complexing ability of O and N rich coordination centres towards soft heavy metals, like zinc, can be improved by S atoms, which possess high bonding affinity to cations of heavy metals. The examples of such ionophores are dithizone [326], sulpiride drug [327], 3-[(2-furylmethylene)amino]-2-thioxo-1,3-thiazolidin-4-one [328], disulfide derivatives [296,329] and substituted thioimidazole and pyrazole derivatives [330].

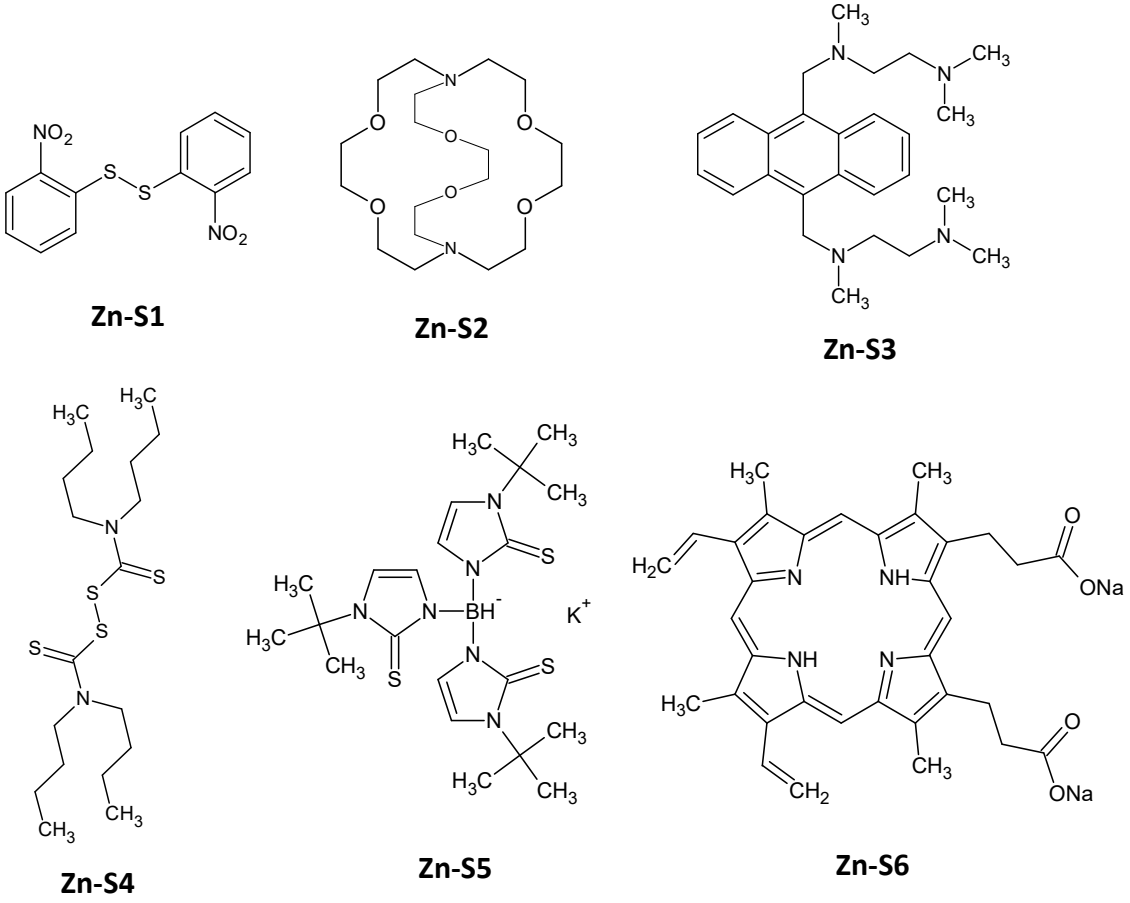

Figure 65. Studied zinc-ionophores structures.

The selection of zinc ionophores was based on the reported detection limit, working pH range, response time and selectivity against sodium ions of ISE prepared with them. The commercial availability was also an essential factor, as many of the structures were synthesized by the respective authors.

The chosen ionophores were bis(2-nitrophenyl) disulfide (BNDS, Zn-S1), 4,7,13,16,21,24-Hexaoxa-1,10-diazabicyclo[8.8.8]hexacosane (2,2,2-cryptand, Zn-S2), N,N'-Bis(2-dimethylaminoethyl)-N,N'-dimethyl-9,10-anthracenedimethanamine (bis(TMEDA)-anthracene, Zn-S3), tetrabutylthiuram disulfide (TBTDS, Zn-S4), potassium hydrotris(N-tert-butyl-2-thioimidazolyl)borate ($KTt^{t\text{-}Bu}$, Zn-S5) and protoporphyrin IX disodium salt (protoporphyrin IX, Zn-S6). The ionophores belong to different classes of compounds and their structures are presented in Figure 65.

Table 12 contains characteristics of Zn^{2+}-SEs prepared with the chosen ionophores. The electrodes based on membranes № 4 and 5 (with ionophores Zn-S4 and Zn-S5 correspondingly) have higher selectivity coefficients against Na^{+} and lowest detection limits, while the electrodes based on membranes № 1, 2, 3 and 6 with Zn-S1, Zn-S2, Zn-S3 and Zn-S6 ionophores correspondingly demonstrate wider working pH region (Table 12).

Table 12. Characteristics of chosen Zn^{2+}-selective electrodes.

№	Membrane composition, wt. %	Characteristics					Reference
		S, mV/dec	DL, M	$logK^{Pot}_{Zn2+,Na+}$	τ, s	pH range	
1	1.0% BNDS, 66.5% DBP, 32.5% PVC	29.9	$0.2\cdot10^{-6}$	-2.41 (FIM)	<15	2.0-9.0	[329]
2	5.6% 2,2,2-cryptand 11.1% DBP, 83.3% PVC	22.0	$3.2\cdot10^{-5}$	1.25 (FIM), -0.75 (FIM*)	<10	2.8-7.0	[313]
3	2% bis(TMEDA)anthracene, 65% NPhOE, 33% PVC	30.0	$1.5\cdot10^{-6}$	-1.8 (FIM)	15	3.0-7.5	[319]
4	5.4% TBTDS, 0.8% KTClPhB, 53.6% NPhOE, 40.2% PVC	28.0	$4.2\cdot10^{-7}$	-3.3 (SSM)	2	3.5-6.5	[296]
5	3.4% $KTt^{t\text{-}Bu}$, 0.9% NaTPhB, 61.9% DBP, 33.4 % PVC	29.4	$9.5\cdot10^{-8}$	-3.77 (FIM)	12	3.5-7.8	[330]
6	2.8% protoporphyrin IX, 0.6% NaTPhB, 55.2% dibutyl(butyl)phosphonate, 41.4 % PVC	30.0	-	1.4 (FIM), -0.6 (FIM*)	10	3.0-7.4	[316]

(* – value for $logK^{pot}$ without power ($z_i/z_j = 2$) in Equation 3.8)

7.3.2 Screening of Zn^{2+}-SEs

7.3.2.1 Membrane compositions

Membranes for preliminary screening of Zn^{2+}-SEs were prepared as described in Section 4.6 and are summarized in Table 13. The best membranes of references in Table 12 were made according to the composition described in those papers (compositions Zn-S1-B, Zn-S2-B, Zn-S3-A, Zn-S4-2A, Zn-S5-2B). Taking into account, that the ionophores Zn-S1, Zn-S2 and Zn-S3 are uncharged carries (see the structures in Figure 65) a membrane based on any of them should contain an ion-exchanger. This is why KTClPhB was added to the membranes (compositions Zn-S1-2B, Zn-S2-2B and Zn-S3-2A). Apart from NPhOE and DBP, used for PVC-based membranes, TEHP was chosen as possible solvent for cocktails of microelectrodes. Membranes based on TEHP without ionophores and with two ion-exchangers ($Ca(TOBS)_2$ and KTClPhB) were also prepared (Zn-1C and Zn-2C respectively).

Table 13. Prepared membranes for preliminary screening of Zn^{2+}-selective electrodes.

Membrane	Ionophore		Ion exchanger		PVC, wt. %	Plasticizer, up to 100 wt. %	Ref.
	Substance	wt. %	Substance	Content			
Zn-S1-B	Zn-S1	1	-	-	33	DBP	[329]
Zn-S1-2B	Zn-S1	1	KTClPhB	50 mol.%	33	DBP	-
Zn-S2-B	Zn-S2	5.6	-	-	83	DBP	[313]
Zn-S2-2B	Zn-S2	2	KTClPhB	50 mol.%	30	DBP	-
Zn-S3-A	Zn-S3	2	-	-	33	NPhOE	[319]
Zn-S3-2A	Zn-S3	2	KTClPhB	50 mol.%	33	NPhOE	-
Zn-S4-2A	Zn-S4	5.4	KTClPhB	12.5 mol.%	40	NPhOE	[296]
Zn-S5-2B	Zn-S5	3.4	KTClPhB	40 mol.%	33	DBP	[330]
Zn-C	-	-	-	-	33	TEHP	-
Zn-1C	-	-	$Ca(TOBS)_2$	2 wt.%	33	TEHP	-
Zn-2C	-	-	KTClPhB	2 wt.%	33	TEHP	-

Here and further membranes were labeled according to their composition using an appropriate designation for each component. Components in membrane were named in the following order: ionophore – ion-exchanger – solvent. Labels for used ionophores correspond to their chemical structures. Labels for ion-exchangers and solvents are indicated in Table 7. For example, membrane Zn-S1-2B is consisted of zinc ionophore Zn-S1, ion-exchanger 2 – KTClPhB and solvent B – DBP.

7.3.2.2 Testing response of Zn^{2+}-SEs at different pH

Preliminary screening was started from evaluating pH dependence of Zn^{2+}-SEs. Taking into account, that this parameter is important for functioning of Zn^{2+}-SEs (Section 3.6), electrodes response was measured in 10^{-2}M and 10^{-3}M $Zn(NO_3)_2$ solutions at different pH, as described in Section 4.7.2.1. When it was considered relevant the electrodes function in zinc calibration solutions from 10^{-5}M to 10^{-1}M was also recorded.

Response of Zn^{2+}-SEs to pH at concentrations of Zn^{2+} 10^{-2}M and 10^{-3}M is shown in Figures 66 and 67, where the recorded electrode potential is plotted versus pH, in order to reveal the pH range (pH plateau), where the tested electrode responds to zinc ions and not to H^+ ions, i.e. where it is pH independent. At low pH (high H^+ concentration), the electrode response can be caused by membrane components containing N atoms, which can be protonated. As pH of solution increases, i.e. H^+ content decreases, the state of zinc ions will change due to formation of hydroxy complexes and precipitation of $Zn(OH)_2$. This process will reduce the concentration of free Zn^{2+} in solution and the potential of the tested ISE should decrease.

According to the results (Figure 66), the electrodes with membrane compositions based on the ionophores Zn-S1, Zn-S2 and Zn-S3 could not recognize zinc ions in solution, as no meaningful (i.e. corresponding to theoretical Nernst slope of 29 mV/activity decade) difference between potential plots for two zinc concentrations were obtained. While electrodes with membranes Zn-S1-B, Zn-S1-2B, Zn-S2-2B and Zn-S3-2A have pH plateau, but do not show function toward Zn^{2+} (Figure 66 (a), (b), (d) and (f)), Zn-S2-2B-based electrode reveals anionic function (Figure 66 (d), slope with opposite sign, ca.–20 mV/dec) and Zn-S2-B-based one, which has 83% PVC, shows strong potential drift (Figure 66 (c)). For the electrode with membrane Zn-S3-A the potential difference between plots obtained in 10^{-2}M and 10^{-3}M of Zn^{2+} was about 50 mV (Figure 66 (e)), what is much higher than the theoretical value. The performance of Zn^{2+}-SEs based on the ionophores Zn-S1, Zn-S2 and Zn-S3 with KTClPhB in the membrane compositions was not much better than that without the ion-exchanger.

The membrane composition Zn-S4-2A was based on the same ionophore as the cocktail Zn-c5 and is a replica of the membrane reported by Kojima and Kamata [296]. The pH response of Zn^{2+}-SE based on this composition measured at 10^{-2}M $Zn(NO_3)_2$ background is shown in Figure 67 (a). The expected trend of electrode potential was obtained. At low pH (lower than 5) the response of membrane components is present, pH region from pH 5 to pH 7 is a small plateau, where the potential of the tested Zn^{2+}-SE is almost constant and starting from pH 7 the electrode potential goes down, as the concentration of Zn^{2+} decreases due to formation of $Zn(OH)_2$.

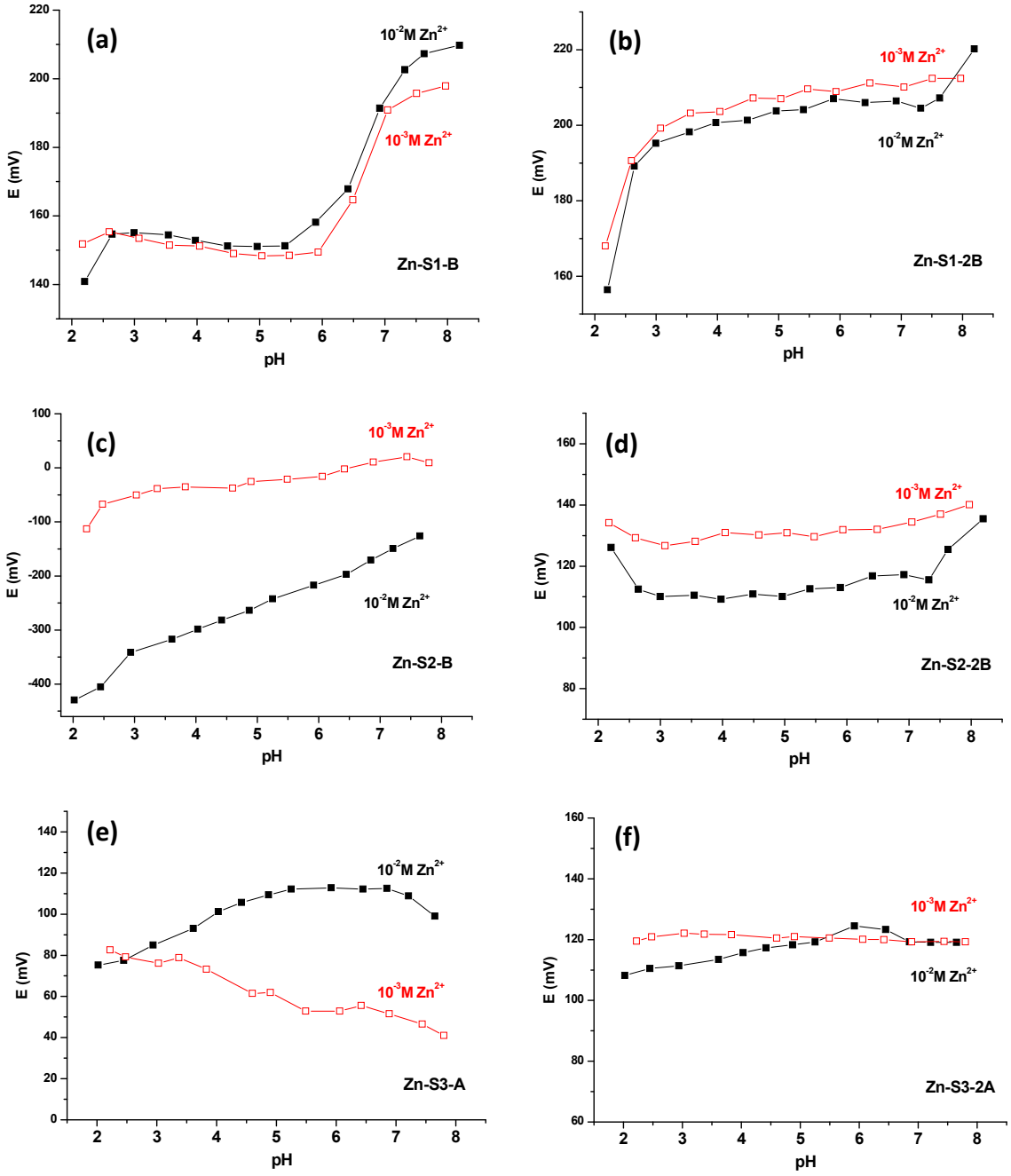

Figure 66. Response to pH of Zn^{2+}-SEs with different ionophores measured in 10^{-2}M $Zn(NO_3)_2$ (black solid symbols) and 10^{-3}M $Zn(NO_3)_2$ (red open symbols).

The response to pH of Zn^{2+}-SE based on the membrane Zn-S5-2B is shown in Figure 67 (a). Its trend is similar to the one of Zn^{2+}-SE based on the membrane Zn-S4-2A, i.e. three regions of electrode behaviour exist: decreasing potenial at pH lower than 3 due to response of the membrane components, slightly increasing potential from pH 3 to pH 7 instead of plateau, and decreasing potential after pH 7 due to formation of $Zn(OH)_2$.

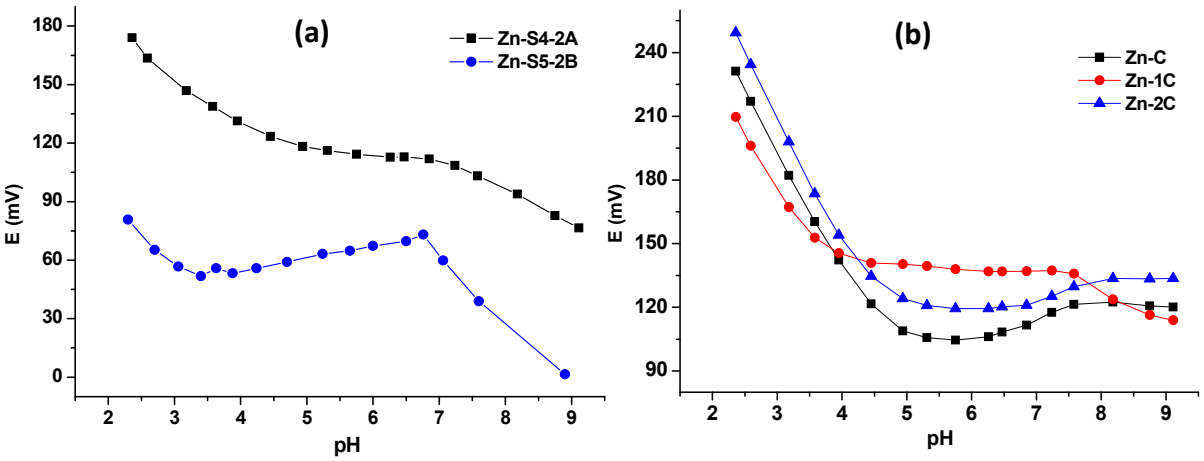

Figure 67. Response of Zn^{2+}-SEs to pH at 10^{-2}M $Zn(NO_3)_2$ background.

Figure 67 (b) shows the behaviour of Zn^{2+}-SEs based on the TEHP plasticized membranes without any ionophore present. As one can notice, the potential of Zn^{2+}-SE based on the membrane containing $Ca(TOBS)_2$ (Zn-1C) is similar to that of Zn-S4-2A: it is stable from pH 4 to pH 7.5 and also decreases due to $Zn(OH)_2$ formation. The electrode with membrane composition, Zn-2C, containing KTClPhB, has the same pH response as electrode with the membrane containing only PVC and TEHP (Zn-C).

Thus, Zn^{2+}-SEs with the membranes Zn-S4-2A and Zn-1C were chosen for further tests. Figure 68 shows calibration plots of Zn^{2+}-SEs based on membranes Zn-S4-2A and Zn-1C. Both electrodes respond to Zn^{2+} in solution, and the last one, which is based on the ion-exchanger $Ca(TOBS)_2$, is somehow better (Zn-S4-2A with slope ≈13 mV/dec and Zn-1C with slope ≈23 mV/dec).

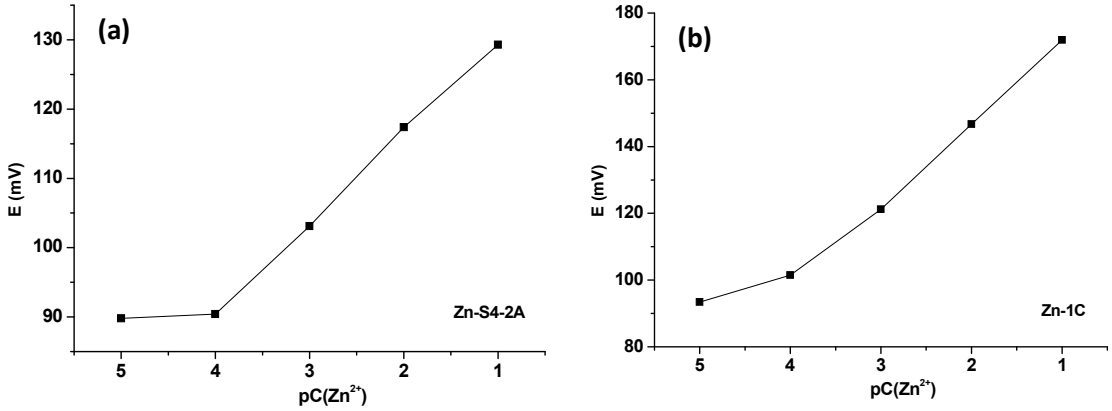

Figure 68. Calibrations plots of Zn^{2+}-SEs based on Zn-S4-2A and Zn-1C membranes.

Among the membranes based on commercially available ionophores Zn-S1, Zn-S2, Zn-S3 and Zn-S4 in presence of KTClPhB as the ion-exchanger the membrane based on Zn-

S4 was the only operable giving clear Zn^{2+}-response in solutions with practical relevant pH region. The membrane plasticized with TEHP and containing $Ca(TOBS)_2$ displayed pronounced response to Zn^{2+} ions as well. Membranes based on the ionophores Zn-S1, Zn-S2 and Zn-S5 plasticized with DBP were found to have the worst pH response.

7.3.3 Study of Zn^{2+}-SEs response at natural pH and in 0.05M NaCl

The simultaneous testing of electrodes sensitivity to Zn^{2+} and to H^+ in previous section was not very successful. The method was based on recording the ISEs potential when pH was changing from to 2 to almost 9 at presence of zinc ions. However, this experiment takes time, during which the electrodes are continuously immersed in solution and exposed to aggressive conditions (addition of concentrated KOH solutions). Such conditions could cause alterations in membrane composition, what obviously would affect the electrodes response. This approach also did not consider the presence of sodium chloride in solution. That is why, for further studies another methodology, based on measuring potential in solutions, containing at least Zn^{2+}, Na^+ and H^+, as it happens in corrosion studies, should be used.

7.3.3.1 Membrane compositions

It was decided, on the one hand, to investigate Zn-S4 ionophore in combination with other ion-exchangers and plasticizers and, on the other hand, to investigate the performance of the membranes plasticized with TEHP and containing $Ca(TOBS)_2$ as the ion-exchanger in combination with different ionophores. In addition to Zn-S1, Zn-S2, Zn-S3, Zn-S4 and Zn-S5 ionophores studied previously one more commercially available ionophore Zn-S6 was tested. Membranes were prepared according to Section 4.6 and their compositions are presented in Table 14.

Table 14. Studied membranes of Zn^{2+}-selective electrodes.

Membrane	Ionophore		Ion exchanger		PVC, wt. %	Plasticizer, up to 100 wt. %
	Substance	wt. %	Substance	Content		
Zn-1C	-	-	$Ca(TOBS)_2$	2 wt.%	33	TEHP
Zn-2C*	-	-	KTClPhB	0.5 wt.%	33	TEHP
Zn-2A	-	-	KTClPhB	0.5 wt.%	33	NPhOE
Zn-S1-1C	Zn-S1	2	$Ca(TOBS)_2$	50 mol.%	33	TEHP
Zn-S2-1C	Zn-S2	2	$Ca(TOBS)_2$	50 mol.%	33	TEHP
Zn-S3-1C	Zn-S3	2	$Ca(TOBS)_2$	50 mol.%	33	TEHP

Zn-S4-1C	Zn-S4	2	$Ca(TOBS)_2$	50 mol.%	33	TEHP
Zn-S5-1C	Zn-S5	2	$Ca(TOBS)_2$	50 mol.%	33	TEHP
Zn-S6-1C	Zn-S6	2	$Ca(TOBS)_2$	50 mol.%	33	TEHP
Zn-S4-1A	Zn-S4	5	$Ca(TOBS)_2$	50 mol.%	33	NPhOE
Zn-S4-2A*	Zn-S4	5	KTClPhB	50 mol.%	33	NPhOE
Zn-S4*-2A*	Zn-S4	12	KTClPhB	50 mol.%	33	NPhOE
Zn-S4-3A	Zn-S4	5	NaFMPhB	50 mol.%	33	NPhOE
Zn-S4*-3A*	Zn-S4	12	NaFMPhB	150 mol.%	33	NPhOE
Zn-S4*-2C	Zn-S4	12	KTClPhB	50 mol.%	33	TEHP
Zn-S5-C	Zn-S5	2	-	-	33	TEHP
Zn-S5-A	Zn-S5	2	-	-	33	NPhOE
Zn-S5-2A	Zn-S5	2	KTClPhB	50 mol.%	33	NPhOE

* – here and further component in a different amount.

7.3.3.2 Effect of ionophore, ion-exchanger and plasticizer

The response of the produced Zn^{2+}-selective electrodes was investigated towards zinc ions as described in Section 4.7.2.2.

The data illustrating the influence of the plasticizer nature and ion-exchanger, as well as the influence of the concentration of ion-exchanger and ionophore on the selectivity against Na^+ are presented in Table 15.

Figure 69 shows calibration plots of Zn^{2+}-SEs. It demonstrates that the membranes plasticized with TEHP and containing $Ca(TOBS)_2$ in combination with various ionophores actually display good Zn^{2+}-response in the concentration range 10^{-5}M – 10^{-1}M. However, among the membranes containing $Ca(TOBS)_2$ only the one based on Zn-S5 ionophore (membrane Zn-S5-1C) showed the ability to recognize Zn^{2+} in the presence of 0.05M NaCl background (Table 15). All other membranes based on Zn-S1, Zn-S2, Zn-S3, Zn-S4 and Zn-S6 ionophores performed from this point of view similarly to pure ion-exchanger-based membrane (membrane Zn-1C) which contains $Ca(TOBS)_2$ only, without ionophore.

From Table 15 one can see that presence of Zn-S4 ionophore greatly improves the selectivity towards Zn^{2+} against Na^+ in comparison with pure ion-exchanger-based membranes plasticized with NPhOE (compare the membranes Zn-2A, Zn-S4*-2A* and Zn-S4*-3A*). It's clear as well that for tetraphenyl borate derivatives the nature of the ion-exchanger does not influence significantly Zn^{2+}—Na^+ selectivity (compare the membranes Zn-S4*-2A* and Zn-S4*-3A*). The concentration of the ion-exchanger does not essentially affect the selectivity as well (membranes Zn-S4*-3A* and Zn-S4-3A).

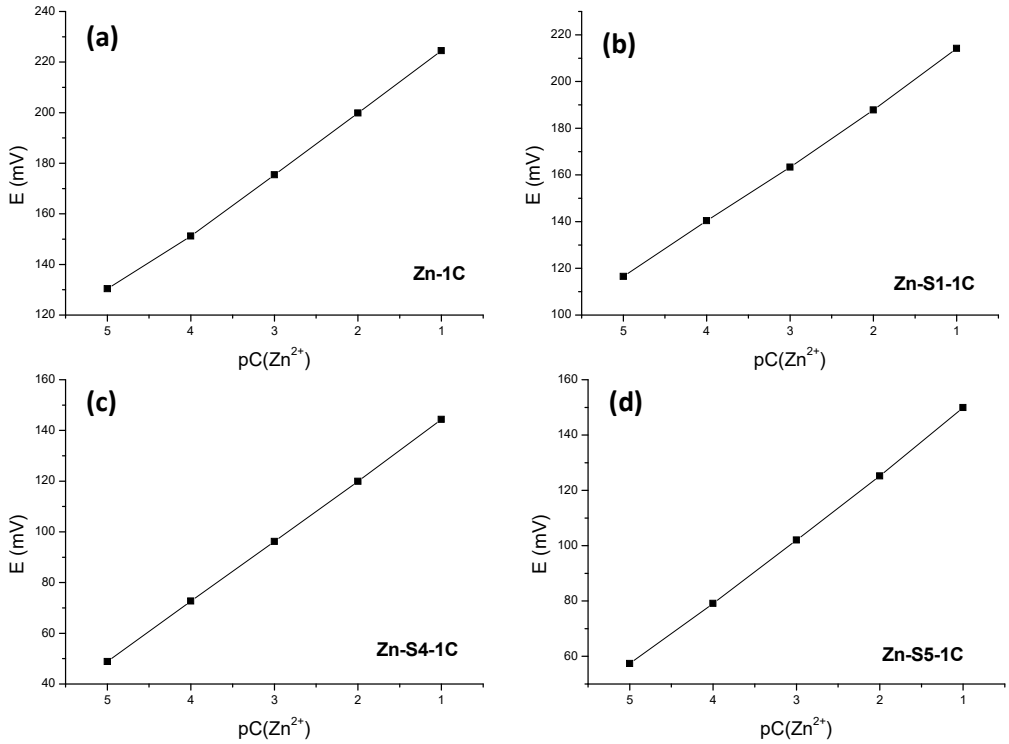

Figure 69. Electrode function of the Zn^{2+}-selective electrodes with different Zn ionophores.

On the contrary, concentration of the ionophore exerts significant influence on the selectivity: the higher is Zn-S4 concentration the better is the selectivity to Zn^{2+} against Na^+ (compare the membranes Zn-S4*-2A* and Zn-S4-2A*, Zn-S4*-3A* and Zn-S4-3A).

It was found that use of $Ca(TOBS)_2$ as the ion-exchanger instead of KTClPhB or NaFMPhB leads to drastic deterioration of Zn^{2+}-Na^+ selectivity (compare the membranes Zn-S4-1C, Zn-S4-2A* and Zn-S4-3A), while for pure ion-exchanger-based membranes the opposite result was obtained (Table 15, membranes Zn-1C and Zn-2C*). The observed effect can be explained by $TOBS^-$-anion ability to form complexes with metal cations, including Na^+. As far as in the membrane under study Zn^{2+} is bound into more stable complex with Zn-S4 ionophore, it can't interact effectively with $TOBS^-$ anion, while complexation $TOBS^-$-Na^+ does take place. The presence of Na^+ ions resulted from the complexation in the membrane fase makes it sensitive to Na^+ as well, so resulted Zn^{2+} selectivity against Na^+ becomes worse.

As it follows from the data obtained for the membranes Zn-S4*-2C and Zn-S4*-2A*, the nature of the plasticizer dramatically influences the selectivity of Zn-S4-based membranes. Evidently, the selectivity of the membranes plasticized with NPhOE is much better in comparison with the membranes plasticized with TEHP (ΔE_{12}(Zn-S4*-2C)≈-67 mV, and ΔE_{12}(Zn-S4*-2A*)≈50 mV). The selectivity of the Zn-S4*-2C is very close to the selectivity of pure KTClPhB-based membrane without ionophore (membrane Zn-2C*).

Table 15. The effect of the membrane composition on the selectivity of Zn^{2+}-SEs, where E_1 – potential in 0.01 M $Zn(NO_3)_2$ with pH=5.14; E_2 – potential in 0.05 M NaCl with pH=5.22.

Membrane	E_1, mV	E_2, mV	ΔE_{12}, mV
Zn-1C	210.6	204.9	5.7
Zn-2C*	214.8	292.4	-77.6
	224.4	301.6	-77.2
Zn-2A	173.0	194.2	-21.2
	180.5	200.2	-19.7
Zn-S1-1C	206.0	202.7	3.3
	221.2	215.4	5.8
Zn-S2-1C	203.5	202.4	1.1
	208.8	209.3	-0.5
Zn-S3-1C	186.1	178.5	7.6
	203.0	194.4	8.6
Zn-S4-1C	197.8	197.0	0.8
	217.8	214.7	3.1
Zn-S5-1C	189.6	122.3	67.3
	229.3	155.1	74.2
Zn-S6-1C	212.6	215.5	-2.9
	218.5	218.0	0.5
Zn-S5-C	152.3	125.0	27.3
	165.9	113.2	52.7
Zn-S4-1A	214.8	214.2	0.6
Zn-S4*-2C	201.2	268.6	-67.4
	209.6	275.6	-66.0
Zn-S4*-2A*	209.8	159.4	50.4
	219.8	163.0	56.8
Zn-S4-2A*	204.6	189.7	14.9
	216.2	181.3	34.9
Zn-S4*-3A*	211.0	159.1	51.9
	219.0	165.9	53.1
Zn-S4-3A	196.0	181.5	14.5
	206.3	193.7	12.6

The obtained results give evidence that the effect of Zn-S4 ionophore does not reveal itself in the membranes plasticized with TEHP, possibly due to very strong Lewis' basicity of TEHP and its high ability to solvate metal cations.

The selectivity of Zn-S4- and Zn-S5-based membranes depends on the nature of the ion-exchanger and the plasticizer in different ways. While for Zn-S5-based membranes the ion-exchanger and plasticizer nature doesn't affect significantly Zn^{2+}—Na^{+} selectivity (slightly better selectivity is achieved for the membranes plasticized with TEHP), the selectivity of Zn-S4-based membranes drastically depends on the nature of both plasticizer and ion-exchanger and the best selectivity is achieved for the membranes plasticized with NPhOE and containing tetraphenyl borate derivatives as the ion-exchangers. The membranes based on the compositions of Zn-S4 ionophore with either KTClPhB or NaFMPhB as the ion-exchanger also give rather good Zn^{2+}-responses (Figure 70).

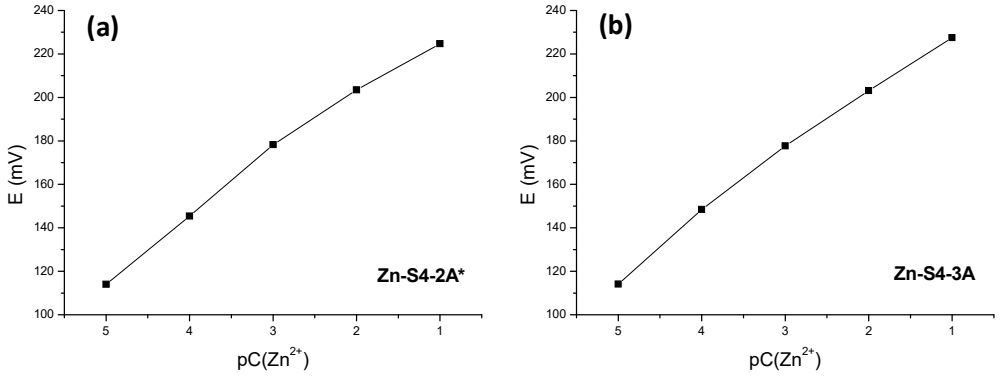

Figure 70. Electrode functions of the Zn^{2+}-selective electrodes based on the Zn-S4 inophore with two ion exchangers: KTClPhB (Zn-S4-2A*) and NaFMPhB (Zn-S4-3A).

The obtained results show that both Zn-S4-based and Zn-S5-based membranes can be considered as promising ones for fabrication of Zn^{2+}-selective microelectrodes for corrosion studies. With respect to selectivity to Zn^{2+} against Na^{+}, Zn-S5 ionophore looks slightly better (compare the membranes Zn-S5-1C, Zn-S4*-2A* and Zn-S4*-3A* in Table 15).

For membranes based on Zn-S4 ionophore, the results considered above allow to propose the following ways to improve the selectivity to Zn^{2+} with respect to Na^{+}:

a) use of tetraphenyl borate as ion-exchangers;
b) use of high concentration of Zn-S4 ionophore in the membrane;
c) use of solvents with low solvation ability in relation to cations (for example, 1,2-dimethyl-3-nitrobenzene, 2-fluorophenyl 2-nitrophenyl ether and benzyl 2-nitrophenyl ether).

The screening method based on single potential measurements in solutions of target (Zn^{2+}) and influencing ions (Na^+ and H^+) resembles the separate solution method for determination of potentiometric selectivity coefficients (Equation 3.9). However, this equation was not followed because the result is mainly dictated by the potential difference (E_i-E_j), reason why it was decided to evaluate the ability of the Zn^{2+}-SEs to recognize the Zn^{2+} by direct comparison of the ΔE values. Such approach is fast and simple, especially when a lot of compositions have to be studied and no information about the Nernstian response of the tested Zn^{2+}-SEs toward interfering ions is known. Nevertheless, further experiments (calibrations with and without NaCl background) were carried out for the membrane compositions that seemed more promising for the use in microelectrodes.

7.3.4 Cocktails for Zn^{2+}-SMEs

Cocktail compositions for Zn^{2+}-selective microelectrodes were prepared as described in Section 4.5.2.1 and are shown in Table 16. According to the above mentioned recommendations the content of ionophore Zn-S4 in membrane cocktail was increased. A new cocktail Zn-c6 was based on the cocktail Zn-c5 (see Section 7.1), but had 10% of the ionophore Zn-S4. Two cocktails based on the ionophore Zn-S5 with $Ca(TOBS)_2$ and KTClPhB, Zn-c7 and Zn-c8 correspondingly, were prepared. The internal reference solution consisted of 0.1M KCl + 0.01M KH_2PO_4 + 10^{-5}M $ZnCl_2$.

Table 16. Membrane cocktail compositions for Zn^{2+}-SME being studied.

Cocktail	Ion exchanger		Ionophore		Solvent, up to 100 wt.%
	Substance	mol.%	Substance	wt. %	
Zn-c6	NaFMPhB	150	Zn-S4	10	NPhOE
	ETH500	55			
Zn-c7	$Ca(TOBS)_2$	50	Zn-S5	2	NPhOE
Zn-c8	KTClPhB	50	Zn-S5	2	NPhOE

The calibration plots of Zn^{2+}-SMEs are presented in Figures 71 and 72.

Comparing graphs on Figure 71 in the presence of 5mM NaCl background, one can see that the linear range is ca. 0.3 pZn wider for Zn^{2+}-ISME with higher inophore content (Zn-c6) in the membrane cocktail.

The Zn^{2+}-SME with Zn-c8 cocktail without NaCl background shows near Nernstian response (S = 25.3 mV/decade) towards Zn^{2+} in 10^{-5}-10^{-2}M concentration range (Figure 72

b). The Zn^{2+}-SME with Zn-c7 cocktail has the same linear range, but with slope of only 15.5 mV/decade (Figure 72 a).

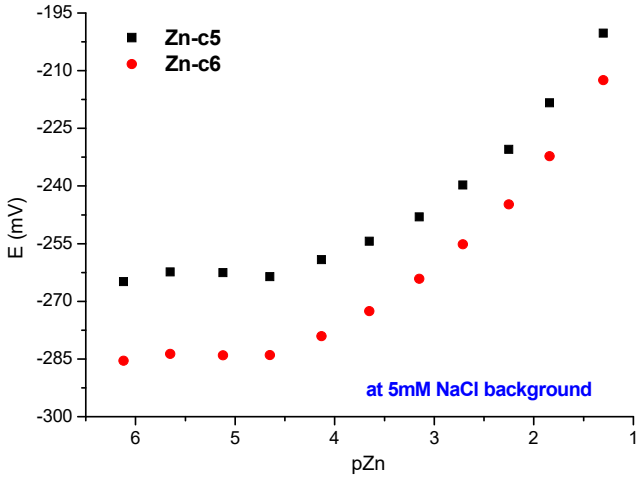

Figure 71. Calibrations plots of Zn^{2+} -SME based on membrane cocktails with different content of the ionophore Zn-c5 (7% of Zn-S4) and Zn-c6 (10% of Zn-S4) at 5mM NaCl background.

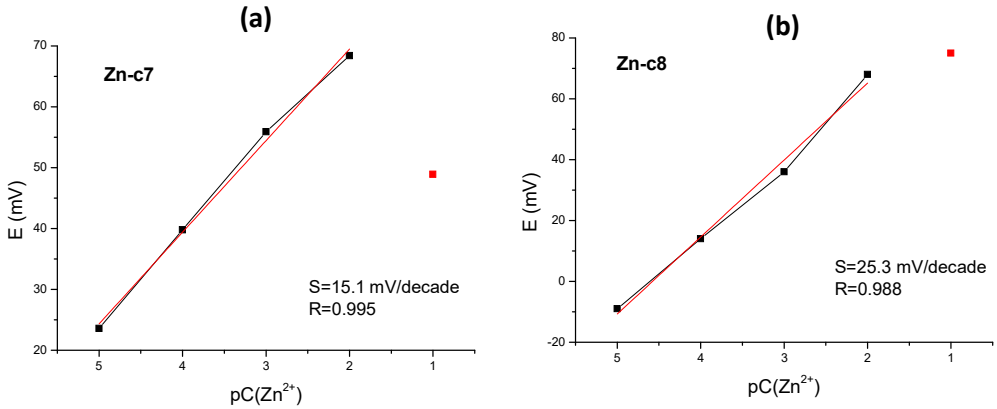

Figure 72. Response of the developed Zn^{2+}-SMEs based on Zn-S5 ionophore with different ion exchangers: (a) - $Ca(TOBS)_2$ and (b) - KTClPhB.

Unfortunately, calibrations of the microelectrodes based on the cocktails Zn-c7 and Zn-c8 in the presence of 0.05M NaCl were not successful, because of unstable potential, sometimes impossible to be measured due to high microelectrode resistance. Thus, the Zn-S5 ionophore based membranes need to be further developed. One of the possible solutions for lowering cocktail resistance based on the Zn-S5 ionophore could be the use of the same highly lipophilic additivie as in the cocktail based on Zn-S4 ionophore, namely ETH 500, providing the reasonable Zn^{2+}/Na^{+} selectivity.

7.3.5 Concluding remarks

Six zinc ionophores, three ion-exchangers and three solvents were used to fabricate 29 PVC membrane compositions (macroelectrodes) and 8 liquid cocktails (microelectrodes) for Zn^{2+} ions. The screening tests revealed that the most promising ionophores were Zn-S4 (TBTDS) and Zn-S5 ($KTt^{t\text{-}Bu}$), the latter found to possess better selectivity against Na^{+}. Ways for improvement of Zn^{2+} versus Na^{+} selectivity for Zn-S4-based membranes were proposed.

The performance of Zn^{2+}-selective microelectrodes based on Zn-S4 and Zn-S5 ionophores was also tested. However, the measurements on the microlevel did not reveal a Zn^{2+}-SME with high selectivity against Na^{+}. Further studies are needed in order to find more appropriate cocktail composition.

Chapter 8

8 Development of a membrane cocktail for Al^{3+}-SME

The detection and quantification of aluminium is important in areas as diverse as health and life sciences, environmental and pollution research, industrial production, surface engineering and materials degradation. In all, aluminium can be found in aqueous media in ionic form. For such conditions potentiometry would be the simplest and straightforward analytical method. Over the years, dozens of procedures, most of them based on PVC membranes, have been proposed for fabricating Al^{3+}-selective electrodes. In spite of all that work and the existent body of knowledge, no ion selective electrode for aluminium is available in the market.

In corrosion, and in the context of this thesis, the development of a microelectrode sensitive to Al^{3+} would be a great achievement with high practical interest for the better characterization of the corrosion of aluminium alloys and the application of adequate preventive actions. This chapter describes the attempts made to fabricate such Al^{3+}-SME.

As for Zn^{2+}-SMEs, the development of membrane composition suitable for Al^{3+}-SME also started with traditional ISE based on PVC membranes, in order to simplify the measurements and enhance the reliability of the results. The work included screening experiments to evaluate the influence of the membrane components on the electrode sensitivity to aluminium ion under relevant pH and NaCl background conditions.

8.1 Aluminium ions in solution

During the anodic dissolution of aluminium due to pitting corrosion (Figure 3, Section 1.2.2), a large number of species is produced depending on pH, concentration, temperature and time. After the attack of the oxide layer, the bare metal starts to react and aluminium ions go into solution. According to Foley and Nguyen [331], the hydrated aluminium ion, $Al(OH)_6^{3+}$ is rapidly formed (equilibrium is being achieved in about 1 μs) and hydrolyzed, producing acidic conditions within the pit. At the begining, in microsecond range, two species are available for reaction, Al^{3+} and $Al(OH)^{2+}$. In the presence of chloride ions the reaction has two alternative paths, through $AlCl^{2+}$ and $Al(OH)Cl^{+}$, both leading to formation of reasonably stable basic aluminium chloride $Al(OH)_2Cl$, which is slowly transformed to $Al(OH)_3$, and finally to $Al_2O_3{\cdot}H_2O$ creating a cap over the pit [331].

For the potentiometric detection of Al^{3+} produced during corrosion process, the hydrolysis reactions are very important, as they directly affect the state of aluminium ions. The iteraction of Al^{3+} with water forms hydrolytic species according to the following reactions [332]:

$$Al^{3+} + H_2O \rightleftarrows Al(OH)^{2+} + H^+ \qquad \log K_1 = -4.97 \qquad (8.1)$$

$$Al(OH)^{2+} + H_2O \rightleftarrows Al(OH)_2^{+} + H^+ \qquad \log K_2 = -8.70 \qquad (8.2)$$

$$Al(OH)_2^{+} + H_2O \rightleftarrows Al(OH)_3\,(aq) + H^+ \qquad \log K_3 = -15.0 \qquad (8.3)$$

$$Al(OH)_3 + H_2O \rightleftarrows Al(OH)_4^{-} + H^+ \qquad \log K_4 = -23.85 \qquad (8.4)$$

In addition to mononuclear species, it is believed that polynuclear $Al_2(OH)_2^{4+}$, $Al_3(OH)_4^{5+}$ and $Al_{13}O_4(OH)_{24}^{7+}$ species should also be formed in Al^{3+} hydrolysis [333].

The stability of aluminium species as a function of pH can be estimated from the equilibrium constants of hydrolysis reactions. Figure 73 shows diagrams of equilibrium composition of Al(III) solutions with different initial concentrations. At concentrations of Al(III) less than 10^{-3}M, and at a pH lower than 4, only a few hydrolytic species are present, namely, $Al(OH)^{2+}$, $Al(OH)_2^{+}$ and $Al_2(OH)_2^{4+}$, that means that the percentage of free Al^{3+} is the highest (Figure 73a and b). As the total Al(III) concentration increases, the concentration of dimeric species becomes more important and higer than that of $Al(OH)^{2+}$, which becomes insignificant for total Al(III) ≥ 0.1M (Figure 73c and d). In solutions with high total concentration of Al^{3+}, the fraction of Al^{3+} begins to decrease already at pH > 3, mainly due to formation of $Al(OH)^{2+}$, $Al(OH)_2^{+}$, $Al_2(OH)_2^{4+}$, $Al_3(OH)_4^{5+}$ and $Al_{13}O_4(OH)_{24}^{7+}$ (Figure 73 c and d). $Al(OH)_3$ and $Al(OH)_4^{-}$ are present significantly only at pH ≥ 6 (this region is not included in the diagrams). In general, the tendency of formation of trimeric species $Al_3(OH)_4^{5+}$ and polymeric species, $Al_{13}O_4(OH)_{24}^{7+}$, increases with the increase of total Al(III) concentration. In concentrated solutions of Al(III) and at pH 4 the

concentration of free Al^{3+} species is aproximatly one order smaller than the total concentration of Al(III) (Figure 73 c and d).

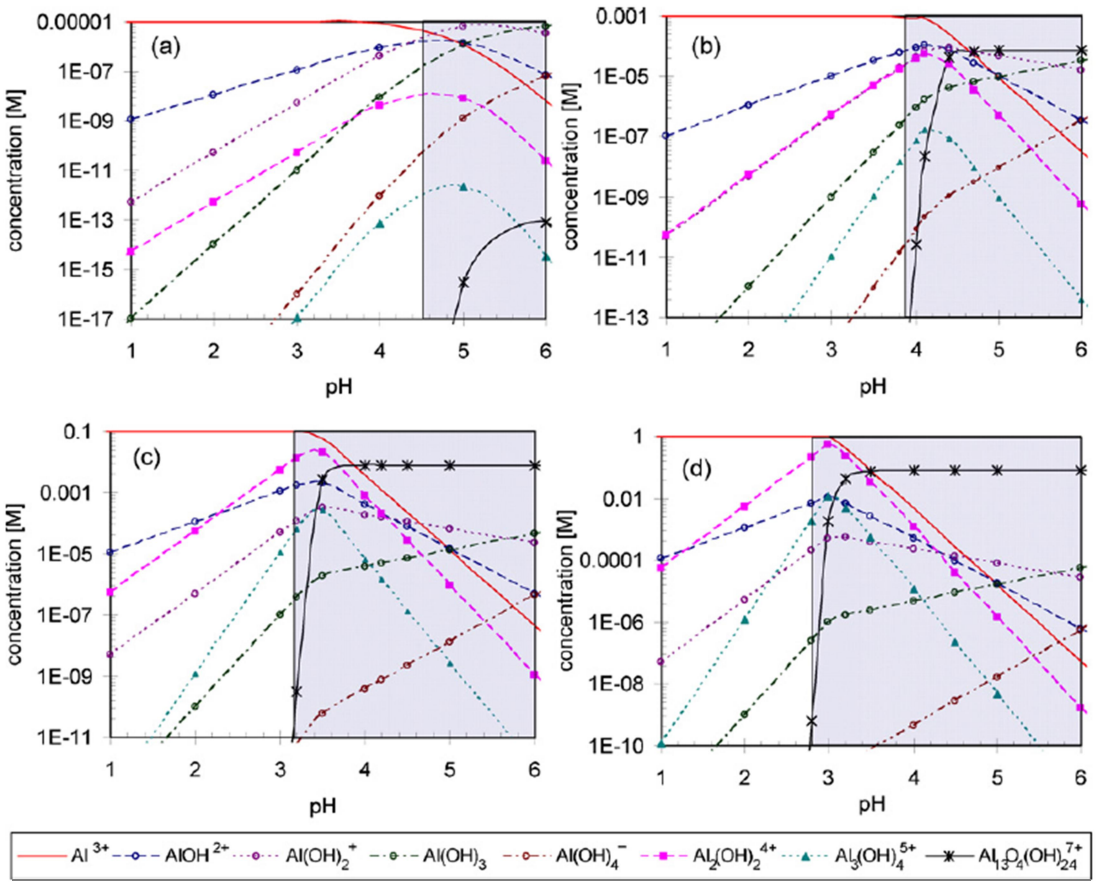

Figure 73. Distribution of Al(III) species in 10^{-5}M (a), 0.001M (b), 0.1M (c) and 1M (d) hypothetically homogeneous Al(III) solution as a function of pH. The shaded area indicates the approximate pH range of oversaturation with regard to gibbsite, $Al(OH)_3$(s). Taken from [334].

The pH value, at which the aluminium starts to precipitate from solution, can be estimated through the solubility product for $Al(OH)_3$, K_{sp}. If its dissociation reaction is written as follow:

$$Al(OH)_3 \leftrightarrow Al^{3+} + 3OH^- \tag{8.5}$$

then the K_{sp} expression is

$$K_{sp} = [Al^{3+}]\,[OH^-]^3 \tag{8.1}$$

Knowing the value for $K_{sp}(Al(OH)_3)$=1.3x10^{-33} [233] and assuming $[Al^{3+}] = C(Al^{3+})$, the equation can be solved for $[OH^-]$. The pH for beginning of precipitation of $Al(OH)_3$ can then be easily calculated from the dissociation constant of water, K_w=1.0·10^{-14} at 25°C, yielding in the following expression:

$$pH = 14 + \frac{1}{3}lgK_{sp} - \frac{1}{3}lgC(Al^{3+}) \quad (8.2)$$

The obtained pH values for different initial concentrations of aluminium Al^{3+} are shown in Table 17 and at Figure 74.

Table 17. The pH of beginning of $Al(OH)_3$ precipitation for different initial concentrations of total Al^{3+} in solution calculated from Equation 8.2.

$C(Al^{3+}), M$	$[OH^-]$, M	pH
$1.0 \cdot 10^{-1}$	$3.16 \cdot 10^{-3}$	3.37
$1.0 \cdot 10^{-2}$	$6.81 \cdot 10^{-3}$	3.70
$1.0 \cdot 10^{-3}$	$1.47 \cdot 10^{-2}$	4.04
$1.0 \cdot 10^{-4}$	$3.16 \cdot 10^{-2}$	4.37
$1.0 \cdot 10^{-5}$	$6.81 \cdot 10^{-2}$	4.70
$1.0 \cdot 10^{-6}$	$1.47 \cdot 10^{-1}$	5.04

The precipitation of metal ions is considered fully in analytical chemistry, if their final concentration in solution is ≤ 10^{-6} M. For aluminium ions the pH of full precipitation is 5.04, i.e. if the pH of solution is higher than 5, the content of free Al^{3+} is almost negligible.

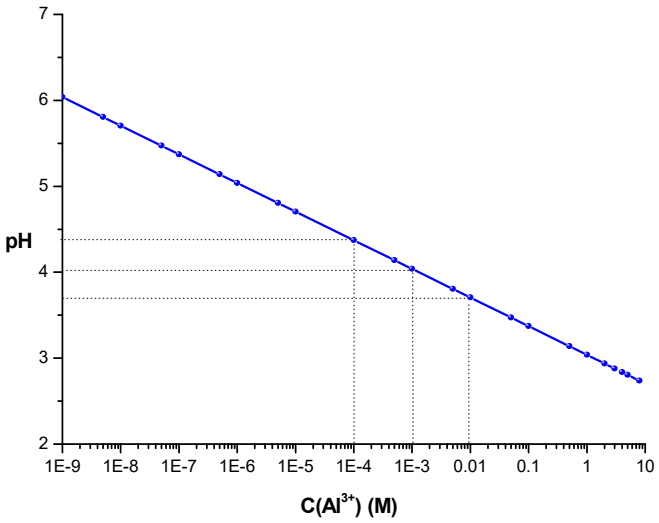

Figure 74. The pH of beginning of $Al(OH)_3$ precipitation for different initial concentrations of total Al^{3+} in solution calculated from Equation 8.2.

This speciation analysis shows that for any concentration of Al(III), the Al^{3+} species in a significant quantity exists only at pH ≤ 4, i.e. in a narrow pH range. Moreover and

considering the functioning of ISE, at low concentration of Al^{3+} and low pH values, the ISE potential will strongly be influenced by the competitive interference of H^+ ions.

8.2 Overview of Al^{3+}-SEs

In addition to narrow working pH range, the sensitivity of an ISE for Al^{3+} is very small, the theoretical value being 19.7 mV per decade of activity, since it is a trivalent ion, compared to 29.5 mV for divalent and 59 mV for univalent ions, as depicted in Figure 75. This is probably the reason why there is little published work on ISE for trivalent ions such as Bi (III), Ce (III), Fe (III), Cr (III) and Al (III) [209,335,336].

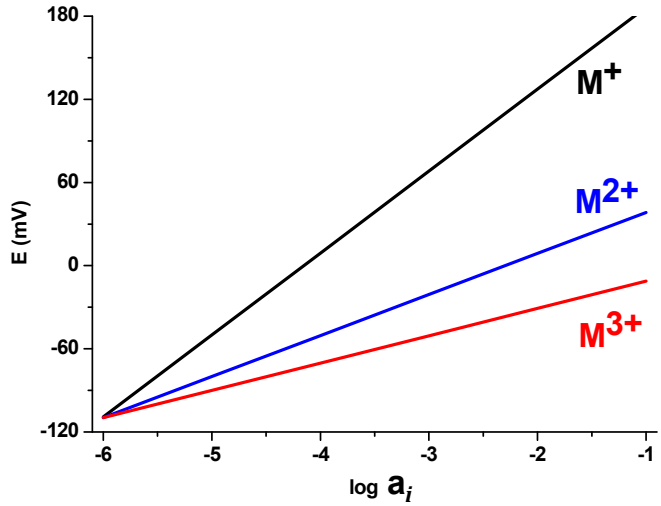

Figure 75. Ideal response of selective electrodes to one-charged (M^+), two-charged (M^{2+}) and three-charged (M^{3+}) cations.

Nontheless, over the years, several procedures, most of them based on PVC membranes, have been proposed for fabrication of Al^{3+}-selective electrodes [262,337–351]. A revision of Al^{3+}-SEs found in the literature is made in Table 18, where the best electrodes from each paper are present. Apart from the main requirements for ISMEs (linear concentration range, slope, working pH range, response time and selectivity to Na^+, see Section 3.6) the conditions of calibration procedure were also taken into consideration.

The response of the Al^{3+}-SEs described in Table 18 is linear in rather wide concentration range, for instance electrodes based on N,N'-bis(salicylidene)-1,2-phenylenediamine [341], 2-(1H-benzo[d]imidazole-1-yl)-1-phenylethanoneoxime [345], E-N'-(2-hydroxy-3-methoxybenzylidene) benzohydrazine [350] and on 2-((3-silylpropylimino)methyl)phenol [351] can work from 10^{-7} to 10^{-2} M, while based on morin [262], N,N'-

Table 18. Comparison of found Al^{3+}-selective electrodes.

Ionophore	Linear concentration range, M	S, mV/pAl	Conditions of calibration	Working pH range	Resp. time, s	$logK^{Pot}_{Al3+,Na+}$	Ref.
7-ethylthio-4-oxa-3-phenyl-2-thioxa-1,2-dihydropyrimido-[4,5-d]pyrimidine	10^{-5}–10^{-1}	19.5*	n/m	2.2–3.2	20	-4.34 (SSM)	[337]
di-2(furyl)	$1.0\cdot10^{-6}$–$1.0\cdot10^{-2}$	18.5*	in 10^{-2}M HNO_3	0.5–3.0	70	-2.79 (MPM)	[338]
bis(5-phenyl azo salicylaldehyde) 2,3-naphthalene diamine	$5.0\cdot10^{-6}$–$1.0\cdot10^{-2}$	19.3	n/m	2.9–5.0	<10	-2.54 (FIM)	[339]
1-hydroxy-3-methyl-9*H*-xanthen-9-one	$1.0\cdot10^{-6}$–$1.6\cdot10^{-2}$	20.0	n/m	3.0–8.5	<5	-0.37 (FPM)	[340]
N,N'-bis(salicylidene)-1,2-phenylenediamine	$8.0\cdot10^{-7}$–$3.0\cdot10^{-2}$	19.8	n/m	3.2–4.5	<12	-3.06 (MPM)	[341]
morin	$5.0\cdot10^{-7}$–$1.0\cdot10^{-1}$	19.7	between pH 4.0 and 5.0	3.5–5.0	~5	-2.77 (MPM)	[262]
6-(4-nitrophenyl)-2-phenyl-4-(thiophen-2-yl)-3,5-diaza-bicyc-lo[3.1.0]hex-2-ene	$1.0\cdot10^{-6}$–$1.0\cdot10^{-1}$	19.6	n/m	3.0–6.0	~10	-3.05 (FIM)	[342]
glyoxal-bis-thiosemicarbazone	$1.8\cdot10^{-5}$–$1.0\cdot10^{-1}$	20.1	pH=3	2.5–4.5	~10	-2.26 (SSM)	[343]
N,N'-bis(salicylidene)-1,2-cyclohexane-diamine	$1.0\cdot10^{-8}$–$1.0\cdot10^{-1}$	20.3	pH=3.7	2.0–9.0	<5	-3.15 (MPM)	[344]
2-(1H-benzo[d]imi-dazole-1-yl)-1-phe-nylethanoneoxime	$4.3\cdot10^{-7}$–$5.0\cdot10^{-2}$	19.4	n/m	3.1–5.5	~10	-3.46 (MPM)	[345]
N,N'-propane-diamide bis(2-salicylideneimine)	$7.9\cdot10^{-7}$–$1.0\cdot10^{-1}$	19.4	pH=3 (HNO_3)	2.5–4.0	8	-4.92 (SSM)	[346]
2-(4,5-dihydro-1,3-imidazol-2-yl)phenol	$1.0\cdot10^{-6}$–$1.0\cdot10^{-1}$	19.3	n/m	3.0–8.0	10	-3.17 (MPM)	[347]
salicylaldehyde salicyloyl hydrazone	$9.0\cdot10^{-6}$–$1.0\cdot10^{-1}$	20.0	pH=3.5	2.5–4.0	9	-3.30 (SSM)	[348]
N,N'-bis(benzoin)-1,2-phenylenediamine	$3.0\cdot10^{-7}$–$1.0\cdot10^{-1}$	19.7	n/m	2.5–4.0	8	-3.55 (SSM)	[349]
E-N'-(2-hydroxy-3-methoxybenzylidene) benzohydrazine	$1.0\cdot10^{-7}$–$1.0\cdot10^{-2}$	19.7	n/m	3.0–7.0	<10	n/m	[350]
2-((3-silylpropylimi-no)methyl)phenol	$1.0\cdot10^{-7}$–$5.0\cdot10^{-2}$	19.9	at constant pH	3.5–7.0	~5	-2.66 (MPM)	[351]

* - mV per decade of Al^{3+} concentration; n/m - not mentioned

propanediamide bis(2-salicylideneimine) [346] and bis(benzoin)-1,2-phenylenediamine [349] can work from 10^{-7} to 10^{-1} M. The electrode based on N,N'-bis(salicylidene)-1,2-cyclohexanediamine demonstrates the largest concentration range form 10^{-8} to 10^{-1} M of Al^{3+} [344].

Following the previous section about hydrolysis of aluminium ions, it is expected that in order to guarantee that aluminium species in calibration solutions exist mainly in the form of Al^{3+}, one should adjust the pH of calibration solution to values below 4. In spite of the fact that this precaution has not always been taken (see column "Conditions of calibration" in Table 18), the described Al^{3+}-SEs have slopes close to theoretical value, i.e. 18-20 mV per decade of activity or concentration.

Another important electrode characteristic is the nonsensitivity to pH. When a tested electrode and a pH-SE are placed in aluminium solution of known concentration (usually from 10^{-2} to 10^{-4} M), small amount of NaOH or KOH is added to change pH. The recorded electrode potential is than plotted versus pH, in order to reveal the pH range, where the tested electrode responds to primary ions and not to H^+ ions, i.e. where it is pH independent. In the beginning of experiment, i.e. at low pH (high H^+ concentration), the electrode response can be caused by membrane components containing N atoms, which can be protonated. As pH of solution increases, i.e. H^+ content decreases, the state of aluminium ions will change due to formation of hydroxy complexes and precipitation of $Al(OH)_3$ until all aluminium from solution is consumed. This process will reduce the concentration of free Al^{3+} in solution and the tested ISE should respond by giving lower potential values.

This means that the pH range where Al^{3+} can be detected in solution is very narrow, and the working pH range (pH plateau) of an Al^{3+}-SE also should be narrow, i.e. not reaching pH 6. This is true for many referred Al^{3+}-SEs (see Table 18), but in some cases the electrode potential remains stable at pH as high as 7 [340,344,347,350,351], 8 [340,344,347] or even 9 [344]. Nonetheless, the pH in solutions of real samples tested with reported Al^{3+}-SEs was kept in the range 3-4 in all papers.

The evaluation of response times of the Al^{3+}-SEs in Table 18 is somehow limited, as not always authors presented graphs and indicated the conditions of its determination. Thus, τ_{90} was measured in references [344,345,351], while τ_{95} in [339,343,350], τ_{lim} in [338,340,342,346,348,349] and the time characteristic measured was not indicated in papers [262,337,341,347]. A time response of less than 10 seconds was considered as acceptable from practical point of view.

The majority of the Al^{3+}-SEs reveals good selectivity against Na^+ ions, as can be seen from values of selectivity coefficients in Table 18, which are in the order of 10^{-3} or 10^{-4}. However, it should be noticed that $K^{Pot}_{Al3+,Na+}$ determined by SSM and FIM might not have

physical significance as these methods were found to be not well suited for ions of different charge (Na^+ and Al^{3+}), because they result in unrealistically large or small selectivity coefficients [232]. For example, the lowest values of $logK^{Pot}_{Al3+,Na}$ were obtained by SSM for electrodes based on 7-ethylthio-4-oxa-3-phenyl-2-thioxa-1,2-dihydropyrimido-[4,5-d]pyrimidine [337] and on N,N'-propanediamide bis(2-salicylideneimine) [346], which are –4.34 and –4.92 respectively. The highest value of $logK^{Pot}_{Al3+,Na}$, determined by the Fixed Primary ion method (FPM), was –0.37 for an electrode based on 1-hydroxy-3-methyl-9*H*-xanthen-9-one [340].

Hence, only 9 from 16 of found Al^{3+}-SEs from the following papers [262,341,342,344–346,348,349,351] possess at least 4 acceptable characteristics of the 6 presented in Table 18, i.e. have at least linear range from $1\cdot10^{-6}$ to $5\cdot10^{-2}$M, working pH range from 3 to 5, response time < 10 s and calibration with adjusted pH. One is based on commercially available ionophore [262], one is based on custom synthesized ionophore [342], two electrodes have intricate fabrication procedures dealed with carbon composite membrane materials [345,351] and others are made from PVC membranes with Schiff base ionophores [341,344,346,348,349], which are possibly suitable for further work.

8.3 Selection of Al^{3+} ionophores

Given the commercial availability of morin (Al-M) and the simple synthesis of N,N'-bis(salicylidene)-1,2-cyclohexanediamine (Al-S0) and N,N'-bis(salicylic-dene)-1,2-phenylenediamine (Al-S1) according to, respectively, references [344] and [341], these ionophores were used for first trials made on microlevel. The results, however, were not satisfactory. But Schiff bases are known to form stable complexes with transition metals and the complexation ability of Al-S0 to Al^{3+} was found to be the strongest compared to other metals [344]. These Schiff bases act as carriers in the polymeric membranes due to two tertiary N atoms and two O atoms from hydroxyl groups in the ligand cavity (Figure 76). According to the Pearson's HSAB (hard-soft acid-base) theory, these oxygen and nitrogen containing groups are hard and nearly hard bases respectively. They should favourably react with hard and nearly hard acids, such as Al^{3+}, Fe^{3+}, Zn^{2+} or Cu^{2+}. Among them Al^{3+} is the hardest as it has higher charge density and therefore is more preferable by Schiff base ligand than other metal ions. Thus, it was decided to design new ionophores based on similar coordination center. Such structures are Al-S2 to Al-S10 (Figure 76). They were synthesized and purified in IST, Lisbon, Portugal, by Dr. M.Kopylovich in the frame of SISET project. Different radicals in lateral benzene rings were used for modulation of ionophores lipophilicity. Thus substances Al-S5, Al-S6, Al-S7, Al-S8, Al-S9 and Al-S10 are considered more lipophilic than Al-S2, Al-S3 or Al-S4. The geometric control of host-guest cavity was provided by separation of two N-O chelating sites by chains of 2 (Al-S3, Al-S7), 3 (Al-S10) or 4 (AlS-4) carbon atoms.

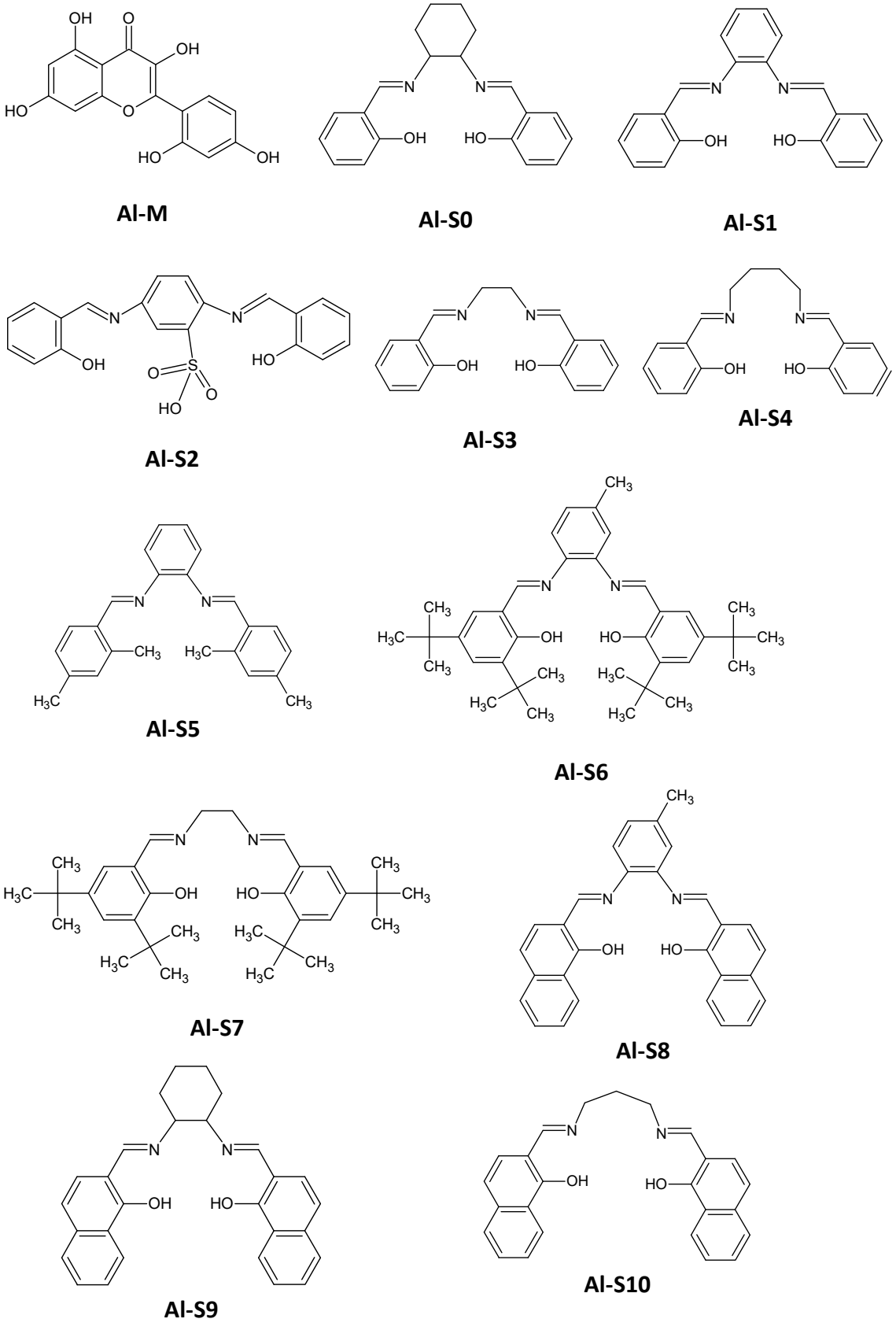

Figure 76. Structures of the studied Al^{3+} ionophores.

8.4 Screening of Al^{3+}-SEs

Screening experiments with Al^{3+}-SEs were similar to that for Zn^{2+}-SEs. They were carried out in parallel to Zn^{2+}-SEs tests and were also started from identification of membrane composition with an appropriate selectivity against H^+ ions (pH dependence, Section 3.6).

8.4.1 Membranes compositions

Membranes for preliminary screening of Al^{3+}-SEs, prepared as described in Section 4.6, are presented in Table 19. Two compositions, Al-M-0C and Al-S0-0A, were based on those described in references [262] and [344] respectively. Other membranes based on custom synthesized inophores Al-S0, Al-S1, Al-S3 to Al-S9 (see Figure 76 for structures) were prepared by varying membrane components. Membranes with KTClPhB and $Ca(TOBS)_2$ were prepared based on Al-S6, Al-S8 and Al-S9 ionophores. The influence of plasticizer nature (NPhOE, TEHP, DBP and NPhPE) was studied on membranes based on Al-S9 ionophore.

Table 19. Prepared membranes for preliminary screening of Al^{3+}-selective electrodes.

Membrane	Ionophore		Ion exchanger		PVC, wt. %	Plasticizer, up to 100 wt. %	Reference
	Substance	wt. %	Substance	Content			
Al-M-0C	Al-M	1.6	NaTPhB	1.6 wt.%	48	TEHP	[262]
Al-S0-0A	Al-S0	1.6	NaTPhB	1.6 wt.%	48	NPhOE	[344]
Al-S0-2C	Al-S0	1.0	KTClPhB	50 mol.%	33	TEHP	-
Al-S1-2C	Al-S1	1.0	KTClPhB	50 mol.%	33	TEHP	-
Al-S3-2C	Al-S3	1.0	KTClPhB	50 mol.%	33	TEHP	-
Al-S4-2C	Al-S4	1.0	KTClPhB	50 mol.%	33	TEHP	-
Al-S5-1C	Al-S5	2.0	$Ca(TOBS)_2$	25 mol.%	33	TEHP	-
Al-S6-1C	Al-S6	2.0	$Ca(TOBS)_2$	25 mol.%	33	TEHP	-
Al-S6-A	Al-S6	2.0	-	-	33	NPhOE	-
Al-S6-1A	Al-S6	2.0	$Ca(TOBS)_2$	25 mol.%	33	NPhOE	-
Al-S6-2A	Al-S6	2.0	KTClPhB	25 mol.%	33	NPhOE	-
Al-S7-1C	Al-S7	2.0	$Ca(TOBS)_2$	25 mol.%	33	TEHP	-
Al-S8-1C	Al-S8	2.0	$Ca(TOBS)_2$	50 mol.%	33	TEHP	-
Al-S8-2C	Al-S8	2.0	KTClPhB	50 mol.%	33	TEHP	-

Al-S9-1C	Al-S9	2.0	$Ca(TOBS)_2$	50 mol.%	33	TEHP	-
Al-S9-2C	Al-S9	2.0	KTClPhB	50 mol.%	33	TEHP	-
Al-S9-1E	Al-S9	2.0	$Ca(TOBS)_2$	37 mol.%	33	NPhPE	-
Al-S9-1B	Al-S9	1.7	$Ca(TOBS)_2$	50 mol.%	33	DBP	-
Al-S9-1CE	Al-S9	2.0	$Ca(TOBS)_2$	50 mol.%	33	TEHP:NPhPE=1:1	-
Al-S9-1CE*	Al-S9	2.0	$Ca(TOBS)_2$	50 mol.%	33	TEHP:NPhPE=1:3	-
Al-1A	-	-	$Ca(TOBS)_2$	2.0 wt.%	33	NPhOE	-
Al-1C	-	-	$Ca(TOBS)_2$	2.0 wt.%	33	TEHP	-
Al-2C	-	-	KTClPhB	1.2 wt.%	33	TEHP	-

The response of Al^{3+}-SEs was tested for pH and Al^{3+} activity. The electrodes potentials were recorded at two constant concentrations of $Al(NO_3)_3$ (10^{-2}M and 10^{-3}M) with different pH values as described in Section 4.7.2.1. The calibrations of selected Al^{3+}-SEs were measured at fixed pH as also described in the same section.

8.4.2 Response of Al^{3+}-SEs at different pH

The response of Al^{3+}-SEs to pH is shown in Figure 77. The potential of Al^{3+}-SE based on the ionophore Al-M (Al-M-0C) is almost stable in pH region 3.7-5, and starts to decrease due to decrease of Al^{3+} concentration caused by formation of aluminium hydroxy-complexes and aluminium hydroxide (Figure 77a). Such electrode behaviour is close to the the expected (Section 8.2) and reported in Table 18. The response of electrode based on Al-S0 ionophore (Al-S0-0A) is pH influenced (Figure 77 a), what is different from the expected and from that indicated in Table 18. Based on the potential behaviour, the other Al^{3+}-SEs can be divided into 3 groups: i) without distinctive plateau, i.e. pH dependent – electrodes with membranes Al-S1-2C and Al-S5-1C (c and f); ii) with almost constant potential values at pH ≥ 4, independently of Al^{3+} concentration – Al-S0-2C, Al-S3-2C and Al-S4-2C (b, d and e); and iii) with regions of nearly constant at pH 3-5 and then decreasing potential, but with slope between two plots far from the theoretical value – Al-S6-1C, Al-S6-A, Al-S6-1A, Al-S6-2A, Al-S7-1C and Al-1A (g, h, I, j, k and l).

Nonetheless, the calibration of selected Al^{3+}-SEs in $Al(NO_3)_3$ solutions from 10^{-5}M to 10^{-1}M with pH adjusted in each solution was carried out. Results are shown in Figures 78. The Al^{3+}-SEs based on Al-M ionophore (Al-M-0C) and on Al-S0 (Al-S0-0A), could not recognize the aluminium in calibration solutions at pH≈3.7 (Figure 78 a and b) as well as the electrode based on Al-S5 ionophore (Al-S5-1C) at pH≈4 (Figure 78 c). The electrodes with Al-S6 and Al-S7 ionophores (Al-S6-1C and Al-S7-1C) were sensitive to Al^{3+} with slopes of linear part 15.7 and 23.8 mV per concentration decade respectively (Figure 78 c).

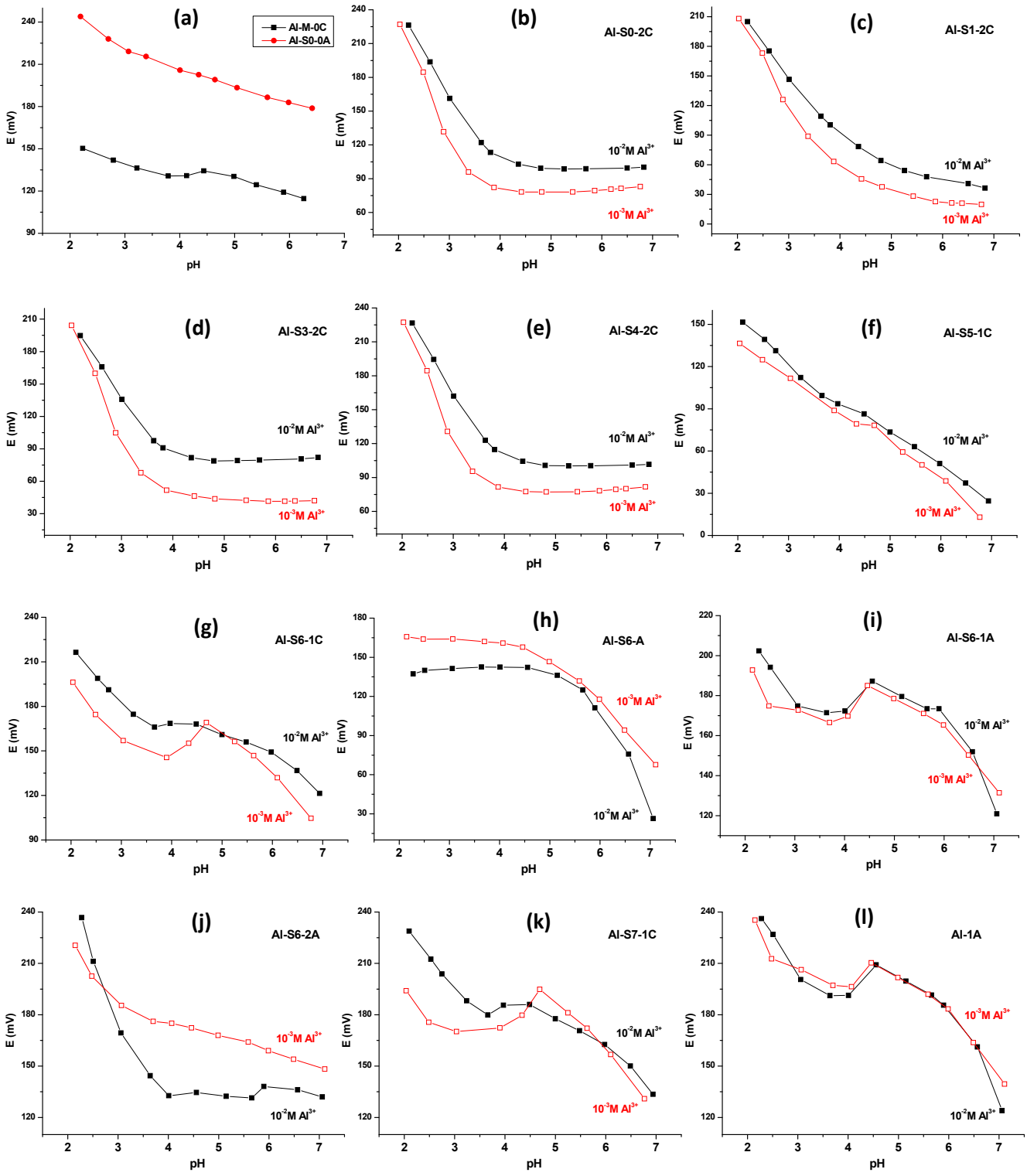

Figure 77. Response of Al^{3+}-ISEs to pH at 10^{-2}M $Al(NO_3)_3$ (solid black symbols) and at 10^{-3}M $Al(NO_3)_3$ (open red symbols) background.

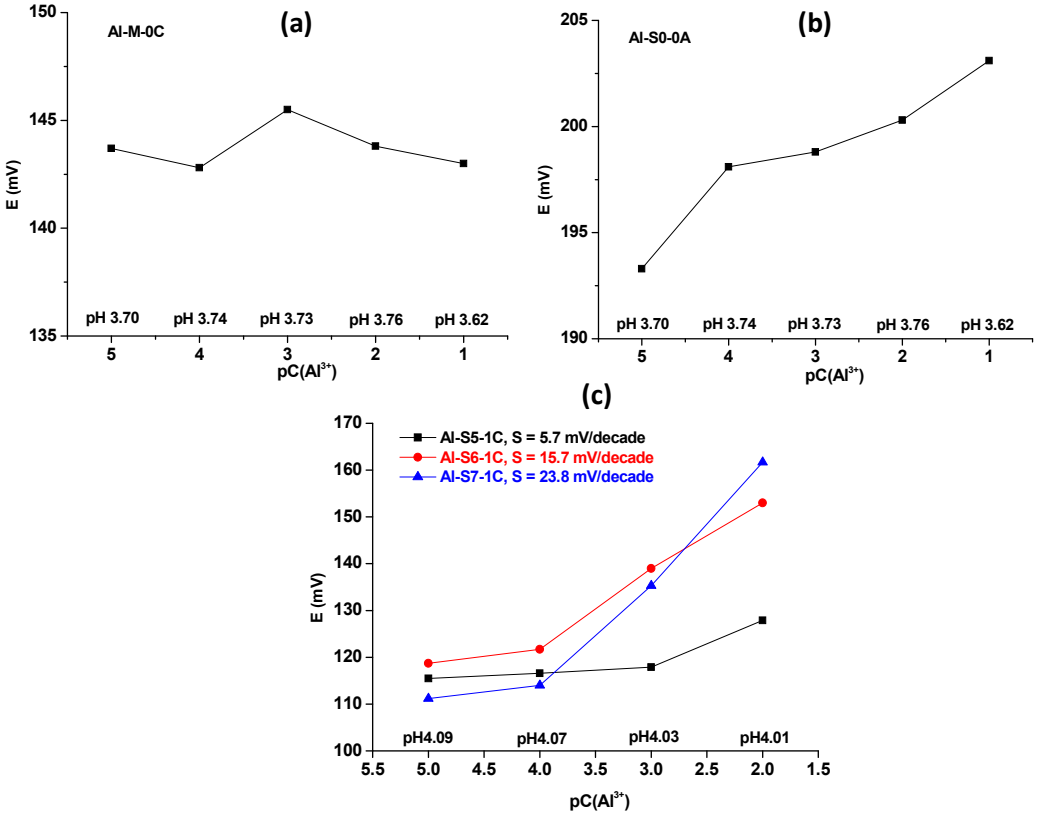

Figure 78. Electrode functions of Al^{3+}-SEs based on Al-M, Al-S0, Al-S5, Al-S6 and Al-S7 ionophores.

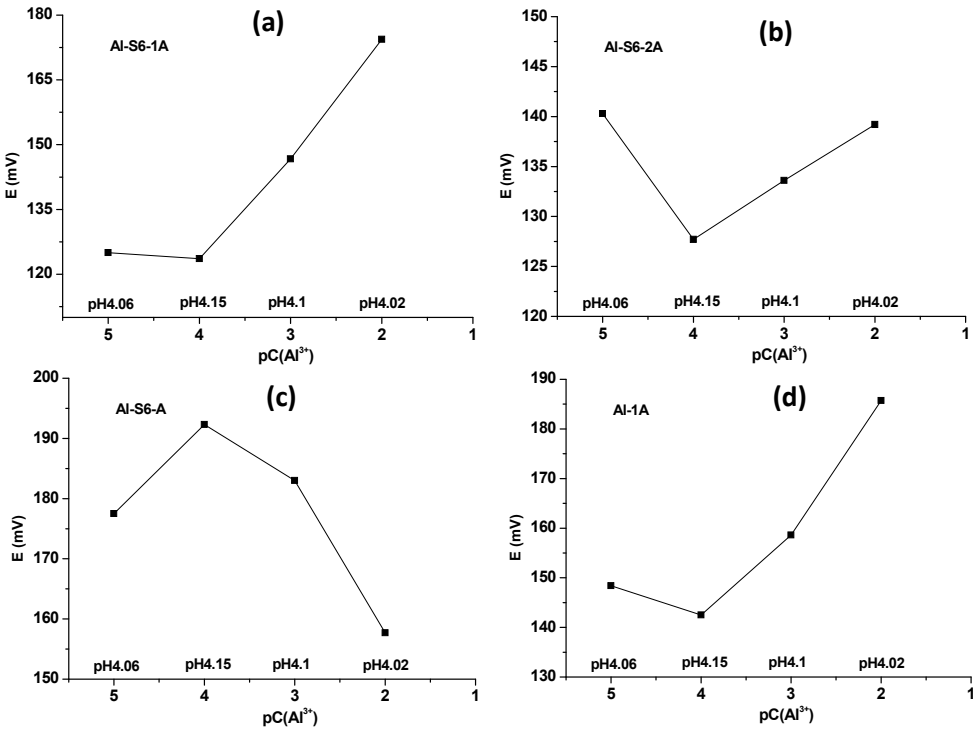

Figure 79. Effect of ion-exchanger on electrode functions of the Al^{3+}-SEs based on the Al-S6 ionophore and plasticized by NPhOE.

8.4.2.1 Influence of ion-exchanger nature

The response of Al^{3+}-SEs based on Al-S6 ionophore with and without ion-exchangers is shown in Figure 79. The electrodes based on NPhOE membranes with KTClPhB (Al-S6-2A) or without ion exchanger (Al-S6-A) do not respond to aluminium ions (Figure 79 b and c). It is also easy to notice that presence of Al-S6 ionophore in the membrane plasticized by NPhOE almost doesn't change the electrode response (compare Al-S6-1A and Al-1A) (Figure 79 a and d). Better performance is given by electrodes with membrane containing $Ca(TOBS)_2$ as ion-exchanger and plasticized by NPhOE (Al-S6-1A, Figure 79 a) or TEHP (Al-S6-1C, Figure 78 c).

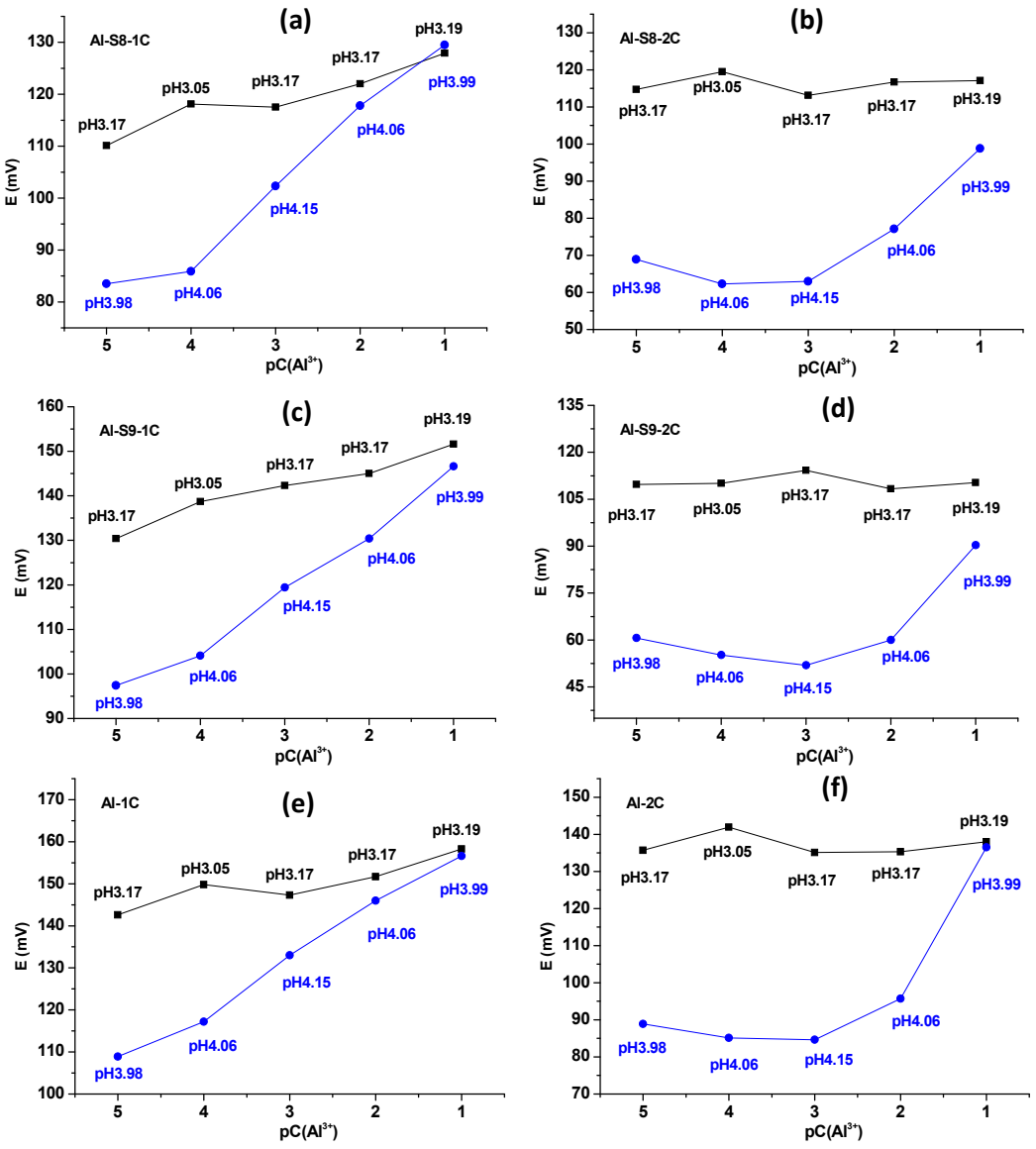

Figure 80. Influence of ion-exchanger on response of the Al^{3+}-SEs based on Al-S8 and Al-S9 ionophores to aluminium calibration solutions at pH≈3 (black squares) and at pH≈4 (blue circles). (Exact pH values are shown on graphs).

The same effect of $Ca(TOBS)_2$ was observed on Al^{3+}-SEs with membranes based on Al-S8 and Al-S9 ionophores plasticized with TEHP (Figure 80). One can see, that membranes containing $Ca(TOBS)_2$ as ion-exchanger with or without ionophores (Al-S8-1C, Al-S9-1C and Al-1C) show response to aluminum ions at pH≈4, which become worse with increasing the H^+ content in solution, i.e at pH≈3 (Figure 80 a, c and e). The presence of KTClPhB in membrane compositions (Al-S8-2C, Al-S9-2C and Al-2C) deteriorates significantly the performance of Al^{3+}-SEs in both series of calibration solutions (Figure 80 b, d and f). These results also allow assuming that both ionophores, Al-S8 and Al-S9, are not sensitive enough to recognize Al^{3+} at presence of H^+ ions, as electrodes response is similar to that without ionophores.

8.4.2.2 Influence of plasticizer nature on response of the Al^{3+}-SEs

In order to select a plasticizer for Al^{3+}-selective electrode, the membranes plasticized with DBP, NPhPE, as well as with mixtures of TEHP/NPhPE in ratios 1:1 and 1:3 were studied (Table 19). Influence of plasticizer nature on response of the Al^{3+}-SEs based on Al-S9 ionophore to aluminium calibration solutions at pH≈4 is shown in Figure 81.

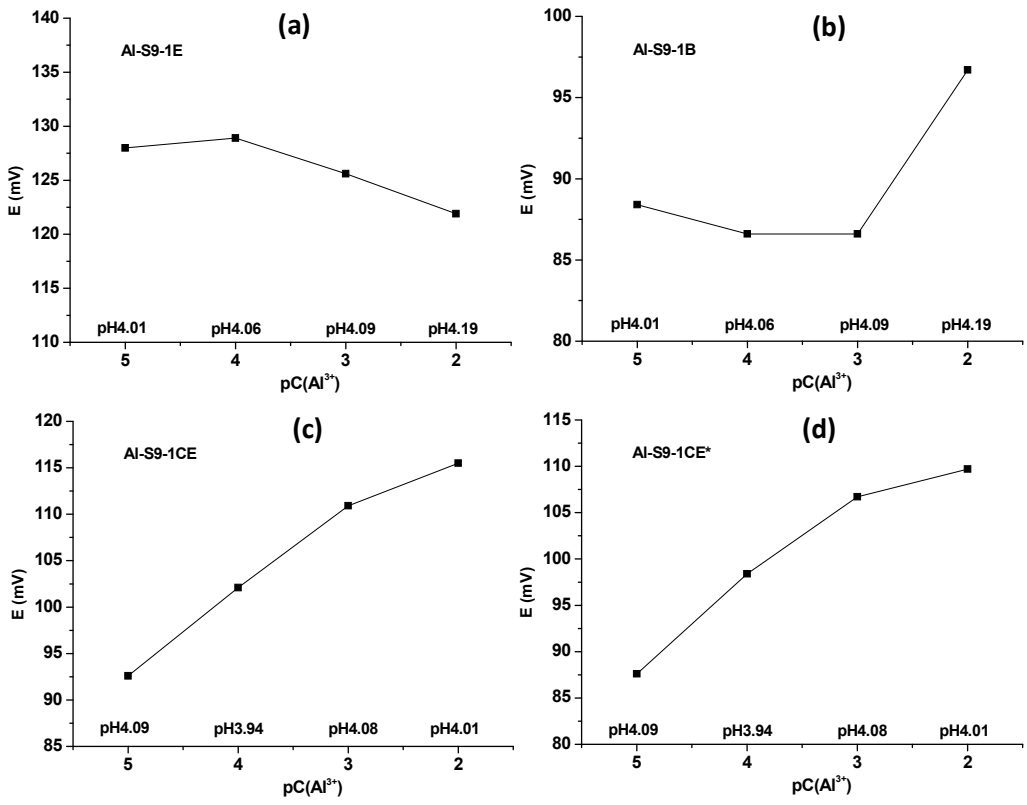

Figure 81. Influence of plasticizer on response of the Al^{3+}-SEs based on Al-S9 ionophore to aluminium calibration solutions at pH≈4 (exact pH values are indicated on graphs).

Comparing response of Al^{3+}-SEs based on Al-S9 ionophore and the ion-exchanger $Ca(TOBS)_2$, one can see that electrodes with the membranes plasticized by TEHP (Al-S9-1C, Al-S9-1CE and Al-S9-1CE*) respond to aluminium ions at pH≈4 (Figure 80 c, Figure 81 c and d), while electrodes with DBP (Al-S9-1B) and NPhPE (Al-S9-1E) plasticized membranes don't feel the presence of Al^{3+} in solution (Figure 81 a and b).

Summarising, one can notice that as in the case of Zn^{2+}-SEs, the simultaneous testing of electrodes sensitivity to Al^{3+} and to H^+ was not very conclusive. The same problem of electrodes performance caused by addition of solutions with high pH could be present. It was found, that electrodes with membranes plasticized by TEHP and containing $Ca(TOBS)_2$ as ion-exchanger seemed to be the most promising. However, according to the preliminary results, none of the tested compositions, including that based on Al-M ionophore, provided Al^{3+}-response in the concentration range from 10^{-5}M to 10^{-1}M independent on pH. At low Al^{3+} concentration and low pH values the potential was strongly influenced by H^+-ions, which were competitively combining with Schiff base ionophores by protonation of N atoms in their structure. At high Al^{3+} concentrations and pH values about 5 precipitation of aluminium hydroxide took place. So taking into account that actual variations of Al^{3+} concentration and pH values provoked by corrosion reactions are interconnected, i.e. the higher is Al^{3+} concentration the lower is pH value in solution, it was decided to investigate the electrodes response under less rigid conditions, i.e. at natural pH values caused by Al^{3+} partial hydrolysis and in presence of sodium chloride.

8.5 Effect of membrane components on Al^{3+}-SEs response at natural pH and in 0.05M NaCl

The strategy was to continue the investigation the influence of all membrane components (ionophore, ion-exchanger and solvent) on the sensitivity to aluminium ions under natural pH caused by Al^{3+} partial hydrolysis and in 0.05M NaCl.

8.5.1 Membranes compositions

According to the previous results the membranes plasticized by TEHP and containing $Ca(TOBS)_2$ as ion-exchanger seemed to be the most promising, so the corresponding set of membranes based on commercially available Al-M ionophore as well as on custom synthesized ionophores Al-S1 to Al-S10 was investigated. Two more components, i.e., ion-exchanger BEHP, and plasticizer BBPA, were tested. The membranes compositions are shown in Table 20.

The response of produced Al^{3+}-selective electrodes was tested according to the procedures described in Section 4.7.2.2.

Table 20. Prepared membranes for Al^{3+}-SEs.

Membrane	Ionophore		Ion-exchanger		PVC,	Plasticizer,
	Substance	wt. %	Substance	Content	wt. %	up to 100 wt.%
Al-1C	-	-	$Ca(TOBS)_2$	2 wt.%	33	TEHP
Al-2C	-	-	KTClPhB	0.5 wt.%	33	TEHP
Al-4C	-	-	BEHP	0.4 wt.%	33	TEHP
Al-M-1C	Al-M	2	$Ca(TOBS)_2$	50 mol.%	33	TEHP
Al-S1-1C	Al-S1	2	$Ca(TOBS)_2$	50 mol.%	33	TEHP
Al-S2-1C	Al-S2	2	$Ca(TOBS)_2$	50 mol.%	33	TEHP
Al-S3-1C	Al-S3	2	$Ca(TOBS)_2$	50 mol.%	33	TEHP
Al-S4-1C	Al-S4	2	$Ca(TOBS)_2$	50 mol.%	33	TEHP
Al-S5-1C	Al-S5	2	$Ca(TOBS)_2$	50 mol.%	33	TEHP
Al-S6-1C	Al-S6	2	$Ca(TOBS)_2$	50 mol.%	33	TEHP
Al-S7-1C	Al-S7	2	$Ca(TOBS)_2$	50 mol.%	33	TEHP
Al-S8-1C	Al-S8	2	$Ca(TOBS)_2$	50 mol.%	33	TEHP
Al-S9-1C	Al-S9	2	$Ca(TOBS)_2$	50 mol.%	33	TEHP
Al-S10-1C	Al-S10	2	$Ca(TOBS)_2$	50 mol.%	33	TEHP
Al-S7-2C	Al-S7	2	KTClPhB	50 mol.%	33	TEHP
Al-M-2C	Al-M	2	KTClPhB	50 mol.%	33	TEHP
Al-S7-4C	Al-S7	2	BEHP	50 mol.%	33	TEHP
Al-M-4C	Al-M	2	BEHP	50 mol.%	33	TEHP
Al-S7-C	Al-S7	2	-	-	33	TEHP
Al-M-C	Al-M	2	-	-	33	TEHP
Al-S7-1A	Al-S7	2	$Ca(TOBS)_2$	50 mol.%	33	NPhOE
Al-S7-1AC	Al-S7	2	$Ca(TOBS)_2$	50 mol.%	33	NPhOE:TEHP=1:1
Al-S7-1D	Al-S7	2	$Ca(TOBS)_2$	50 mol.%	33	BBPA
Al-S7-1CD	Al-S7	2	$Ca(TOBS)_2$	50 mol.%	33	BBPA:TEHP=1:1
Al-S7*-1C*	Al-S7	6	$Ca(TOBS)_2$	50 mol.%	33	TEHP
Al-S7*-1D	Al-S7	6	$Ca(TOBS)_2$	16.7 mol.%	33	BBPA
Al-S7-1AD	Al-S7	6	$Ca(TOBS)_2$	16.7 mol.%	33	NPhOE:BBPA=1:1
Al-S7-2AD	Al-S7	6	KTClPhB	16.7 mol.%	33	NPhOE:BBPA=1:1

8.5.2 Effect of ionophore nature

Response of Al^{3+}-SEs to aluminium calibration solution with natural pH values caused by Al^{3+} partial hydrolysis (Table 8) is presented in Figure 82 (red circles). One can see that a lot of Al^{3+}-SEs reveals pronounced cation response versus the logarithm of aluminium total concentration. Such response, however, can be caused not only by Al^{3+} concentration change but by pH change as well. To elucidate the origin of the response (whether is the membrane sensitive to Al^{3+} or to H^+) the potential values in solutions without Al^{3+} with pH values strictly adjusted by HNO_3 to the values in Al^{3+} solutions with concentrations 10^{-1}, 10^{-2}, 10^{-3}, 10^{-4} and 10^{-5} M were measured. The data are plotted in Figure 82 (black squares). Comparison of the potentials measured in presence and in the absence of Al^{3+} gives direct information on the membranes response to Al^{3+} or H^+ ions. Similarly to ΔE calculations made in Section 4.7.2.2, the larger is the potential diference measured in solutions with Al^{3+} or H^+ ions (the higher is a plot on the graph), the better is electrode sensitivity to the target ion. It follows from the obtained data that only few membranes manifest pronounced Al^{3+}-response, and the most promising in this sense are membranes based on Al-M ionophore and on custom ionophores Al-S2, Al-S4, Al-S7 and Al-S10 (Figure 82 d, f, h, k and n).

Taking into account the proximity of the electrodes slope to Nernstian value and solubility of ionophores in different plasticizers Al-M and Al-S7 ionophores were chosen for further studies.

8.5.3 Influence of ion-exchanger nature

Membranes based on Al-M and Al-S7 ionophores both with ion-exchangers such as $Ca(TOBS)_2$, KTClPhB, BEHP and without ion-exchanger were investigated in terms of Al^{3+}-response in the 0.05M NaCl background. The results of potential measurements are presented in Table 21.

One can see that only the set of membranes containing $Ca(TOBS)_2$ (membranes Al-1C, Al-M-1C and Al-S7-1C) give pronounced response to Al^{3+} while neither pure ionophore-based membranes without ion-exchangers (Al-M-C and Al-S7-C) nor the membranes containing KTClPhB or BEHP (both with and without ionophores, i.e. Al-2C, Al-M-2C, Al-S7-2C, Al-4C, Al-M-4C and Al-S3-4C) can distinguish Al^{3+} at 0.05M NaCl background. It follows from the values of ΔE_{12} and ΔE_{13}, that both ionophores, Al-M and Al-S7 improve the membrane selectivity to Al^{3+} against Na^+ in comparison with pure ion-exchanger membrane. The electrode based on Al-M ionophore (Al-M-1C) is superior, as values of ΔE_{12} and ΔE_{13} for it are the biggest.

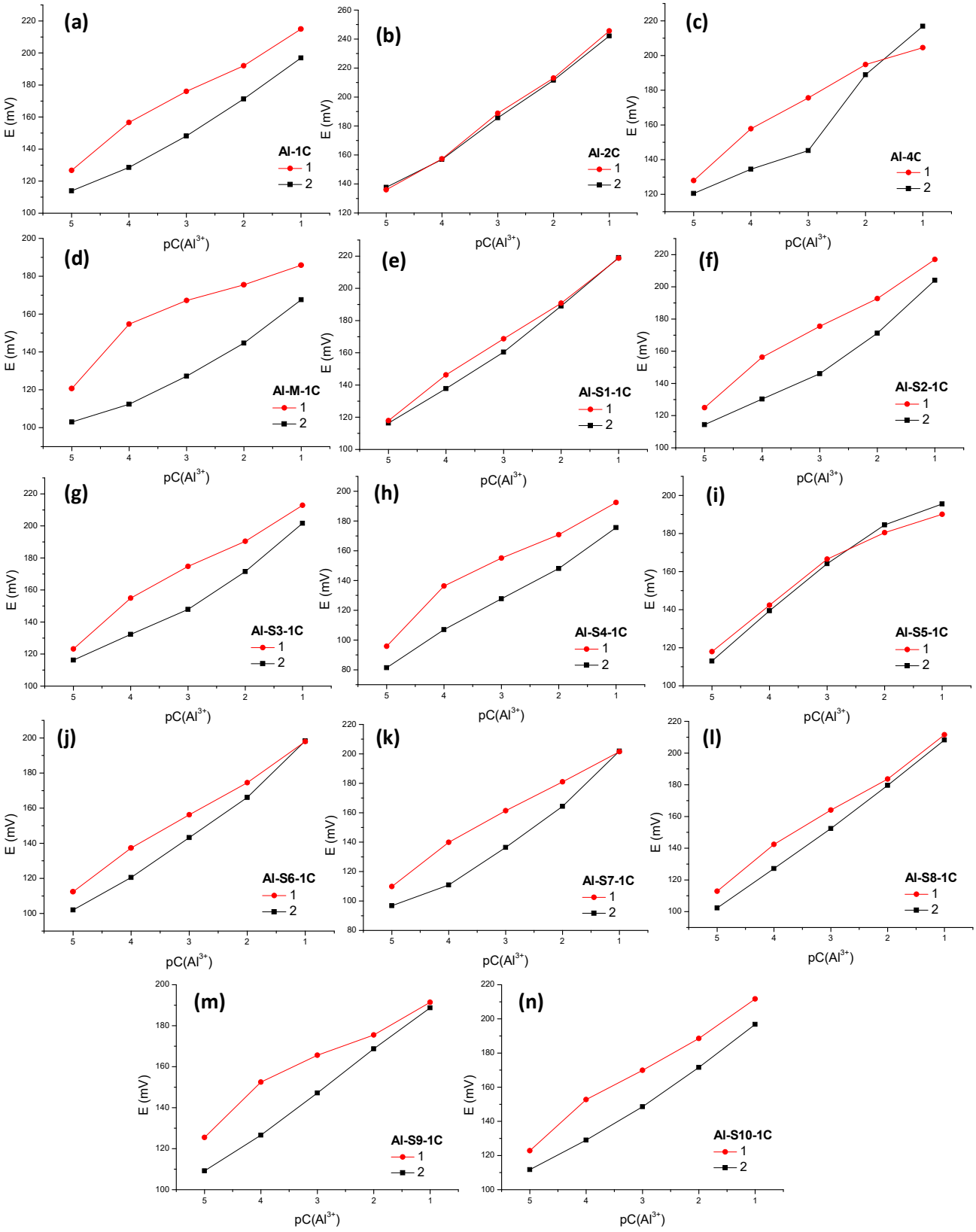

Figure 82. Response of the Al^{3+}-SEs: 1- in solutions with Al^{3+} ions, 2 – in solutions without Al^{3+} ions but with corresponding pH (pH values are listed in Table 8, Section 4.7.2.2).

Table 21. The effect of the ion-exchanger on the selectivity of Al^{3+}-selective electrodes, where E_1 – potential in solution of 0.01 M Al^{3+} with pH=3.70; E_2 – potential in HNO_3 solution with pH=3.68; E_3 – potential in 0.05 M NaCl solution with pH=3.67.

Membrane	E_1, mV	E_2, mV	E_3, mV	ΔE_{12}, mV	ΔE_{13}, mV
Al-1C	201.2	181.0	194.0	20.2	7.2
	209.8	187.8	200.8	22.0	9.0
Al-M-1C	199.1	147.7	159.8	51.4	39.3
	205.7	155.1	149.2	50.6	56.5
Al-S7-1C	199.8	174.7	184.1	25.1	15.7
	206.5	183.3	177.2	23.2	29.3
Al-2C	211.8	212.4	231.2	-0.6	-19.4
	212.8	212.7	232.4	0.1	-19.6
Al-M-2C	209.9	209.8	233.4	0.1	-23.5
	217.2	217.7	239.9	-0.5	-22.7
Al-S7-2C	208.4	210.8	232.1	-2.4	-23.7
	217.0	218.8	239.0	-1.8	-22.0
Al-4C	189.2	199.9	178.9	-10.7	10.3
	197.8	183.5	190.2	14.3	7.6
Al-M-4C	199.3	224.8	212.2	-25.5	-12.9
	203.0	220.1	219.4	-17.1	-16.4
Al-S7-4C	184.3	195.6	169.9	-11.3	14.4
	182.7	197.6	182.8	-14.9	-0.1
Al-M-C	193.8	195.9	195.9	-2.1	-2.1
	211.7	217.2	213.4	-5.5	-1.7
Al-S7-C	160.5	170.6	169.9	-10.1	-9.4
	173.2	191.6	177.0	-18.4	-3.8

8.5.4 Effect of plasticizer and ionophore content

The next step was to investigate the influence of plasticizer on the performance of Al^{3+}-selective electrode. The expediency of such investigation proceeds from the fact that ionophore-based electrodes reveal their best selectivity in the solvents or membrane plasticizers with poor solvation abilities [209]. The reason is that the solvent with good

solvation ability usually solvates uncomplexed ions much better than complexed ones, so the selectivity against interfering ions which are not bound into complexes with ionophore should deteriorate [209]. TEHP possesses very strong Lewis' basicity and can intensively solvate cations. One can assume that replacement of TEHP for a solvent with lower solvation abilities would be advantageous. So other membrane solvents with higher dielectric constants and lower basicity are of interest. It turned out unfortunately that Al-M ionophore does not dissolve in the solvents with less basicity. So this part of investigation was carried out with the Al-S7-based membranes only. With this purpose the membranes plasticized with BBPA, NPhOE, as well as with mixtures of BBPA/NPhOE, TEHP/BBPA and TEHP/NPhOE (Table 20) were studied. Moreover the influence of the ionophore concentration on the Al^{3+} – H^+ selectivity and Al^{3+} – Na^+ selectivity was tested. The results of potential measurements of E_1 – potential in 0.01 M Al^{3+} with pH=3.70; E_2 – potential in HNO_3 solution with pH=3.68; and E_3 – potential in 0.05 M NaCl solution with pH=3.67 are presented in Table 22**.**

Table 22. The effect of the plasticizer on the response of Al^{3+}-SEs, where E_1 – potential in solution of 0.01 M Al^{3+} with pH=3.70; E_2 – potential in HNO_3 solution with pH=3.68; E_3 – potential in 0.05 M NaCl solution with pH=3.67.

Membrane	E_1, mV	E_2, mV	E_3, mV	ΔE_{12}, mV	ΔE_{13}, mV
Al-S7-1A	173.4	168.2	146.3	5.2	27.1
	177.4	178.5	157.3	-1.1	20.1
Al-S7-1AC	209.2	192.0	192.2	17.2	17.0
	207.3	192.3	195.5	15.0	11.8
Al-S7-1D	195.0	172.5	159.1	22.5	35.9
	199.6	177.2	165.7	22.4	33.9
Al-S7-1CD	198.7	173.1	170.3	25.6	28.4
	201.7	174.6	177.9	27.1	23.8
Al-S7*-1C*	224.3	204.4	203.7	19.9	20.6
	212.2	189.2	189.1	23.0	23.1
Al-S7*-1D	187.0	160.2	152.1	26.8	34.9
	200.0	174.0	149.5	26.0	50.5
Al-S7-1AD	220.9	209.1	202.7	11.8	18.2
	225.3	213.6	210.3	11.7	15.0
Al-S7-2AD	204.7	201.3	207.2	3.4	-2.5
	229.8	225.2	208.5	4.6	21.3

One can see that the membrane with 2.0 wt.% of Al-S7 plasticized with NPhOE (Al-S7-1A) reveals the worst response to Al^{3+} over H^+. The membrane Al-S7-1AC plasticized with TEHP/NPhOE mixture has somewhat better selectivity to Al^{3+} against H^+, but its selectivity against Na^+ is poor. The membrane Al-S7-1CD plasticized with the mixture TEHP/BBPA has better characteristics in comparison with two previuos membranes with respect to both H^+ and Na^+, and the membrane Al-S7-1D plasticized with BBPA is the best. The membranes Al-S7-1AD and Al-S7-2AD plasticized with NPhOE/BBPA mixtures showed poor H^+ and Na^+ selectivity independently of the ion-exchanger, either $Ca(TOBS)_2$ or KTClPhB. Plasticizer BBPA was the best as well for the membranes containing 6 wt.% of Al-S7, and Al^{3+} against Na^+ selectivity for the membrane Al-S7*-1D almost achieved that for the membrane Al-M-1C. One can see that increase of the Al-S7 ionophore content in the membrane improves its selectivity to Al^{3+} (compare the membranes Al-S7-1C and Al-S7*-1C*, Al-S7-1D and Al-S7*-1D).

Dependences of electrodes potential versus the logarithms of total aluminum concentration in solutions containing 0.05M NaCl are presented in Figure 83 in red lines with circles. Corresponded electrodes dependences for NaCl solutions with adjusted pH values (without Al^{3+}) are shown as black line with squares (Figure 83).

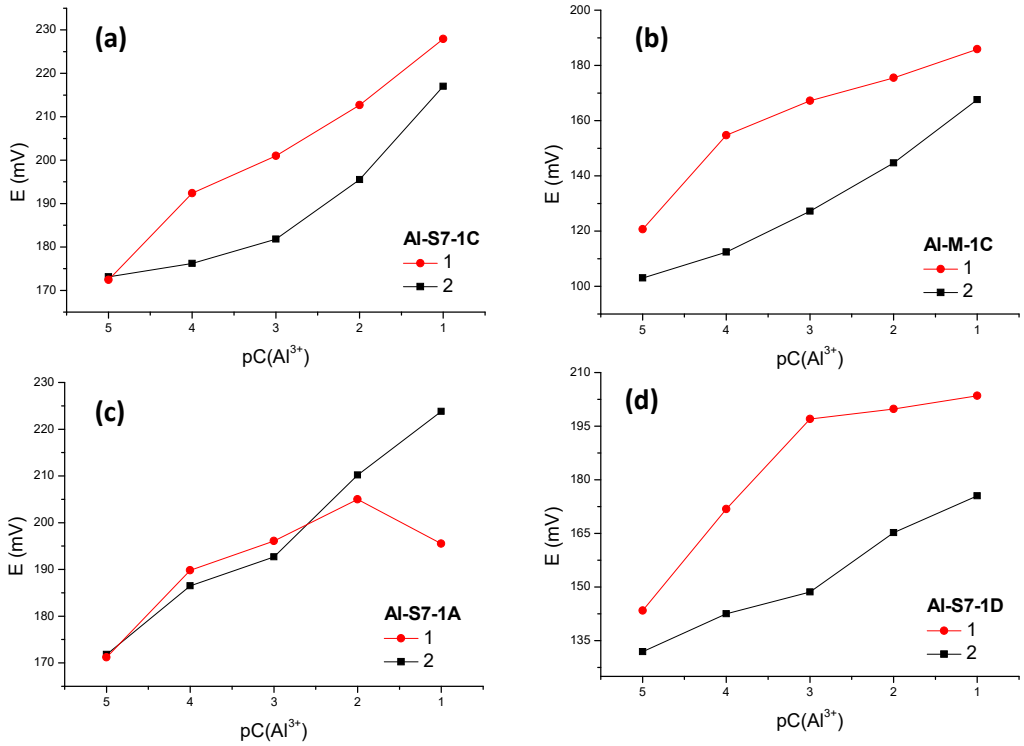

Figure 83. Response of the Al^{3+}-SEs at 0.05 M NaCl background: 1- in solutions of Al^{3+} ions, 2 – in solutions without Al^{3+} ions but with corresponding pH value listed in Table 8, Section 4.7.2.2.

It is clear that the electrode with the membrane Al-S7-1A plasticized with NPhOE does not distinguish the presence of Al^{3+} in solutions (Figure 83 c), while the electrode based on Al-M ionophore, plasticized with TEHP (Al-M-1C, Figure 83 b), as well as one based on Al-S7 plasticized with BBPA (Al-S7-1D, Figure 83 d) reveals the best response to Al^{3+} of all tested formulations.

8.6 Cocktails for Al^{3+}-SME

According to the previous results, the electrodes with membranes Al-M-1C and Al-S7-1D reveal the best sensitivity to Al^{3+} against Na^+ and H^+ ions. Thus, cocktails with the corresponding compositions were prepared for the fabrication of microelectrodes (Table 23). Internal solution for fabricated Al^{3+}-ISMEs was 10^{-3}M $Al(NO)_3$+10^{-2}M KCl.

Table 23. Membrane cocktail compositions for Al^{3+}-SMEs being studied.

Cocktail	Ion exchanger		Ionophore		Solvent, up to 100 wt.%
	Substance	Content	Substance	wt. %	
Al-c-M-1C	$Ca(TOBS)_2$	50 mol.%	Al-M	2	TEHP
Al-c-S7-1D	$Ca(TOBS)_2$	50 mol.%	Al-S7	6	BBPA
Al-c-M-1AC	$Ca(TOBS)_2$	50 mol.%	Al-M	2	NPhOE:TEHP=1:1
Al-c-S7-1AD	$Ca(TOBS)_2$	50 mol.%	Al-S7	6	NPhOE:BBPA=1:1
Al-c-S7-2AD	KTClPhB	50 mol.%	Al-S7	6	NPhOE:BBPA=1:1

The performance of obtained Al^{3+}-SMEs was tested in aluminium calibration solutions with and without pH adjustments. ISMEs with cocktails based on sole TEHP or BBPA, as well as based on mixtures of solvents, NPhOE/TEHP and NPhOE/BBPA, were not responding. All attempts to acquire the analytical characteristics of these microelectrodes failed because of very strong drift and irreproducibility of potential values (most probably caused by high ME resistance), so a reliable microelectrode response was never attained.

8.7 Concluding remarks

12 ionophores, 4 ion-exchangers and 5 solvents were used to fabricate 49 PVC membrane compositions for macroelectrodes and 5 liquid cocktails for microelectrodes used for Al^{3+} ion detection. In spite of all this work and many tested conditions, desired results were not acquired yet. An optimal membrane composition for Al^{3+}-SME remains unreachable due to:

- Narrow pH range for Al^{3+} determination;
- Competitive interference of H^{+} onto Al^{3+} interaction with Schiff base ionophores;
- Solvents with higher dielectric constants and lower basicity are of interest to provide better selectivity. Unfortunately, Al-M ionophore does not dissolve in the solvents with less basicity;
- The microelectrodes for their functioning require solvents with high dielectric constant, such as NPhOE, but this solvent drastically decreases the selectivity of studied ionophores to Al^{3+}.

Based on the results in this part of the work the best approach is to find a solvent (or a mixture with carefully selected qualitative and quantitative composition) capable of substantially increase the conductivity of the cocktail without decreasing the selectivity of Al^{3+}-selective microelectrode.

However, some of produced Al^{3+}-SEs, which are based on membranes Al-M-1C (morin, $Ca(TOBS)_2$, TEHP and PVC) and Al-S7*-1D (ionophore Al-S7, $Ca(TOBS)_2$, BBPA and PVC) work in particular narrow conditions (at adjusted pH solution) and may be used in others analytical purposes.

Chapter 9

9 Two potentiometric sensors for Cu^{2+} determination in corrosion processes

This chapter describes the developments and testing of the two ISMEs for Cu^{2+} detection, one based on a liquid membrane cocktail and another based on a metal/metal salt electrode. The chapter is devided in 3 parts: the first presents some generalities about copper corrosion and inhibition and the other two present the response of each microelectrode and its application to some idealized corrosion conditions.

9.1 Generalities about copper corrosion and inhibition

Copper is an important industrial material. It is used in electrical industry, construction, transportation, industrial machinery, telecommunications, and also in metallurgy as one of intermetallics.

Copper is a relatively noble metal (in the absence of complexing species at least) as it follows from Pourbaix diagram [352]. According to Zoubov *et al.* [352], copper also will not corrode in solutions free of oxidizing agents. Oxygen dissolved in water causes the copper to become covered with a layer of oxides (Cu_2O and CuO), which could be eventually protective [2]. Practically neutral or slightly alkaline solutions passivate the metal also due to the formation of oxides film [352]. Copper becomes susceptible to corrosion in aerated acidic medium and/or in presence of chloride ions [2,352–354]; even though some authors have reported about the passivation effects of chloride ions [355–357].

The copper dissolution mechanism is variously interpreted depending on the pH of the solution as well as the chloride ions. According to Mattsson and Bockris [358] and some others works [359,360], the mechanism of anodic dissolution in acidic aerated medium takes place in two continuous steps [360]:

$$Cu \rightleftarrows Cu(I)_{ads.} + e^- \text{ (fast step)} \quad (9.1)$$

$$Cu(I)_{ads.} \rightarrow Cu^{2+} + e^- \text{ (the rate-determining step)} \quad (9.2)$$

where $Cu(I)_{ads.}$ is an adsorbed species at the copper surface and does not diffuse into the bulk solution. The dissolution of copper is controlled by the diffusion of soluble Cu^{2+} species from the outer Helmholtz plane to the bulk solution. This indicates that the redox process between Cu^{2+} and Cu^{+} is rate-controlling whilst Cu^{+} exists in reversible equilibrium with Cu at the electrode surface.

Also, Cu^{+} ions can undergo disproportionation according to reaction 9.3 [361]:

$$2Cu^+ \rightleftarrows Cu^{2+} + Cu \quad (9.3)$$

In near neutral and slightly alkaline solutions the formation of Cu_2O, as described by reaction 9.4, is followed by its further oxidation to CuO, or to $Cu(OH)_2$ [362,363]:

$$2Cu + H_2O \rightleftarrows Cu_2O + 2H^+ + 2e^- \quad (9.4)$$

$$Cu_2O + H_2O \rightleftarrows 2CuO + 2H^+ + 2e^- \quad (9.5)$$

$$Cu_2O + 3H_2O \rightleftarrows 2Cu(OH)_2 + 2H^+ + 2e^- \quad (9.6)$$

The influence of chloride ions on copper corrosion was investigated by several authors [353,354,361,362,364–368]. Due to the activation effect of chloride ions copper dissolution can proceed according to the following equations [365,366]:

$$Cu + Cl^- \rightleftarrows CuCl_{ads} + e^- \quad (9.7)$$

$$CuCl_{ads} + Cl^- \rightleftarrows CuCl_2^- \quad (9.8)$$

In near neutral or slightly alkaline solutions hydrolysis of $CuCl_2^-$ can happen resulting in the formation of poorly protective surface film of Cu_2O [369]:

$$2CuCl_2^- + H_2O \rightleftarrows Cu_2O + 2H^+ + 4Cl^- \quad (9.9)$$

As far as copper corrosion products are concerned, the authors have mainly observed the formation of the following types, apart from copper oxides and hydroxide: CuCl [361,365,366,368], $Cu_2(OH)_3Cl$ [367], $CuCl_2^-$ [364–366]; $CuCl_3^{2-}$ [366,368] and $CuCl_4^{3-}$ [368] at Cl^- concentration > 1 M.

Because of limited passivation offered by copper corrosion products [123,352,370], inhibitors are used to control copper degradation. One of them is benzotriazole ($C_6H_5N_3$, BTAH), a heterocyclic compound containing three nitrogen atoms in the ring. It has been successfully used for over 60 years in the prevention of Cu corrosion in packaging, storage

and transport, in the reduction of thermal oxidation and, in particular, in the protection of copper under atmospheric and immersed conditions [371–373]. Its effectiveness is accounted for by the presence of unfilled *d* orbitals in the Cu atom which forms coordinated bonds with the atoms able to give up electrons, such as nitrogen. BTAH can also act as a mixed type inhibitor, but its predominant effect is on inhibition of anodic reaction [362].

In most studies [353,361,362,364,370,373,374] the influence of BTAH inhibitor on the corrosion behaviour of copper and its alloys is reflected in the formation of a protective barrier layer, consisting of a complex between copper and BTAH, Cu(I)-BTA, on the surface of the metal. The relevant literature is abundant but not unified in its teaching about bonding mechanism, thickness, composition and structure of the resulting film and the nature of its protection. The major disagreement between different research groups consists in whether molecular adsorption or polymeric complex formation takes place. It is recognised, that Cu(I)BTA surface complex involves Cu-N bonds, while BTAH molecule orientation in the complex has been described as perpendicular, tilted, or parallel relative to the metal surface [362]. Film growth kinetics and thickness depends on pH and the state of the copper surface prior to the contact with BTAH [370]. BTAH has been reported to adsorb only on copper oxide surface, to adsorb faster on copper oxides than on pure Cu, and to adsorb only on a clean Cu surface ([362] and references cited therein). According to Finsgar's review [362], the most probable mechanism of inhibition by BTAH is the one, proposed by Morito and Suetaka [375–377] and improved by Youda *et al.* [378]. They suggested existence of equilibrium between the BTAH adsorption and the Cu-BTA complex formation according to the reaction 9.10:

$$n(BTAH)_{ads} + nCu \;\rightleftarrows\; [Cu(BTA)]_n + nH^+ + ne^- \tag{9.10}$$

It was deduced that the complex formation is unfavourable at low BTAH concentration because of decrease of the $(BTAH)_{ads}$ content. Moreover, as seen from the reaction 9.10, at low pH and negative potential, adsorption rather than complex formation is expected to occur [362].

Mechanism of inhibition due to formation of Cu-BTA protective layer on a oxide-free copper surface in chloride solution containing BTAH can be described by the following reactions [379]:

$$Cu + BTAH \;\rightarrow (Cu - BTAH)_{ads} \tag{9.11}$$

$$nCuCl_2^- + nBTAH \;\rightleftarrows (CuBTA)_n + \; nH^+ + 2nCl^- \tag{9.12}$$

$$(Cu - BTAH)_{ads} + \; (CuBTA)_n \;\rightarrow\; [(Cu - BTAH) - (CuBTA)_n]_{ads} \tag{9.13}$$

Similarly, Modestov *et al.* [364] proposed a reversible mechanism of BTAH action on Cu in chloride media, according to reactions 9.14 and 9.15:

$$Cu + 2Cl^- - e^- \rightleftarrows CuCl_2^- \quad (9.14)$$

$$CuCl_2^- + BTAH \rightleftarrows CuBTA + 2Cl^- + H^+ \quad (9.15)$$

At the early stage, the growth of a Cu-BTA film is controlled by the diffusion of $CuCl_2^-$ into the pores of the film. This reaction is accompanied by the formation of a Cu_2O under-layer. Later, the film growth is controlled by the volume diffusion of Cu(I) ions through the film. The enhanced corrosion resistance of Cu in the presence of BTAH was attributed to the stabilizing action of the Cu_2O by the Cu-BTA over-layer (like a membrane) and not because of the Cu-BTA action alone. They claimed that this surface film prevents the doping of Cu_2O by Cl^- ions that leads to solid CuCl formation.

9.2 Glass-capillary Cu^{2+}-SME based on TBTDS ionophore

As referred in Section 3.7.4, no reports about Cu^{2+}-sensitive potentiometric microelectrodes based on liquid membrane cocktails were found in literature. A chelating agent, TBTDS, used as ionophore for PVC-membrane of Zn^{2+}-selective electrode by Kojima and Kamata [296], together with its derivatives were initially tested by Kamata *et al.* as neutral carriers for copper (II) ions [380]. It has been demonstrated that these neutral carriers have almost ideal C-shaped cavities to fit the Cu^{2+} ion, and form a 1:1 cation-inophore coordination sphere, and hence provide a highly selective sensor [210,380]. The higher selectivity toward Cu^{2+}, compared to Zn^{2+} ions is confirmed by $K^{pot}_{Zn2+,Cu2+} = 9.2$ (for Zn^{2+}-SE based on TBTDS, KTClPhB, NPhOE, PVC) [380]. It became obvious, the possibility to prepare the same cocktail composition for fabrication of both Zn^{2+} and Cu^{2+}-SMEs from glass micropipettes provided both ions do not coexist in the analysing system.

9.2.1 Caracterization of Cu^{2+}-SME

The glass capillary Cu^{2+}-SME was prepared from the cocktail Zn-c5 described in Section 7.1. The cocktail consists of 7.0 wt. % of TBTDS, 22.8 wt. % of NaFMPhB, 1.4 wt. % of ETH500 and 68.8 wt. % of NPhOE. The internal solution was 0.1M KCl + 0.01M KH_2PO_4 + 10^{-5}M $CuCl_2$.

Calibration plots of the Cu^{2+}-SME, based on TBTDS ionophore, are shown in Figure 84. The microelectrode response was linear in the range 1.3-5.5 pCu in pure Cu^{2+} solutions and 1.3-4.0 pCu at 5mM NaCl background having slopes of 34.9 and 34.6 mV/activity decade correspondingly. The microelectrode linearity at 0.05M NaCl background was from 1.5 to 3.0 pCu, what clearly indicates limited selectivity of the TBTDS based microsensor against Na^+ ions.

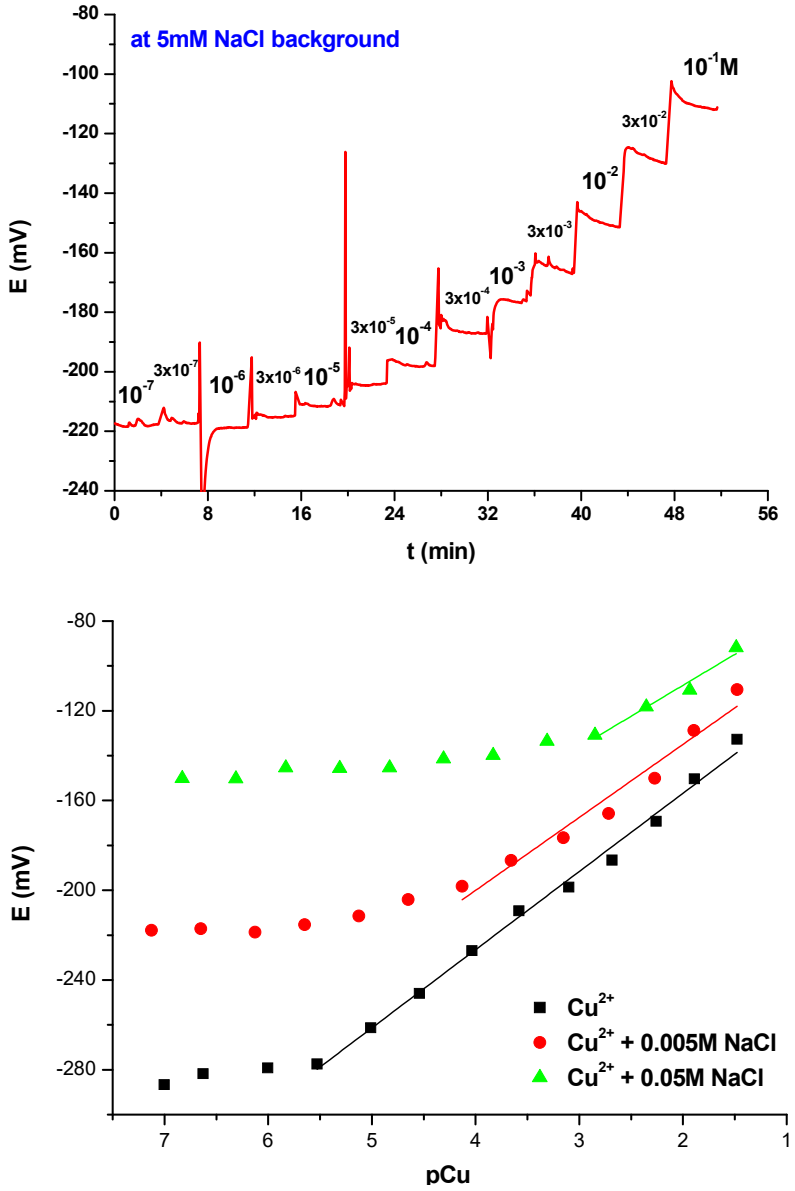

Figure 84. The dynamic response (upper) and calibration plots (lower) of glass-capillary Cu^{2+}-SME in different media.

9.2.2 Probing copper inhibition by BTAH with Cu^{2+}-SME

In this section the Cu^{2+}-SME based on TBTDS ionophore was applied for studying corrosion and inhibition by BTAH of a copper wire connected to a platinum wire and immersed in 5mM NaCl.

Tests performed on a Cu disk showed no quantifiable results, and to provide higher dissolution the copper wire was coupled to a more noble metal, namely platinum, and immersed in chloride containing solution. A cell is shown in Figure 85. Platinum provides an extra cathodic area where O_2 can react forcing the oxidation of copper. The copper

dissolution corresponds to the anodic process; the cathodic is oxygen reduction at the platinum wire according to the reaction 1.2.

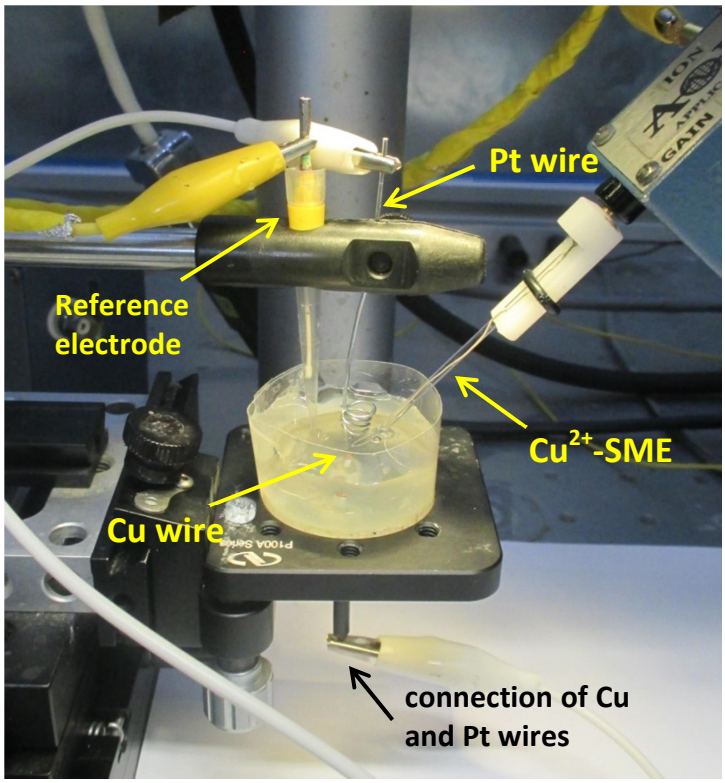

Figure 85. Photograph of the cell composed by Cu-Pt galvanic couple, reference electrode and a Cu^{2+}-selective microelectrode.

The copper activity was monitored along a 5 mm line, which is shown on Figure 87 (a), and at 10 µm distance from the sample surface. Figure 86 (b) presents obtained profiles (consisted of at least 100 points) of Cu^{2+} activity. Copper activity up to $4.1 \cdot 10^{-3}$ M was detected close to the centre of the Cu wire almost immediately, i.e. 5 minutes after the couple had been immersed in 5mM NaCl (black line on Figure 86 (b)), when the surface was still shiny and salmon-pink in colour. Then a decrease of $a_{Cu^{2+}}$ was observed (red line) and after next 1.5 hour the dissolution became more intense. Values of Cu^{2+} activity, ca. $5.7 \cdot 10^{-3}$M (green line) were measured. After 2.5 hour of immersion, Cu^{2+} activity in the order of $3 \cdot 10^{-5}$M was detected (yellow line); they were almost the same as above the epoxy matrix, likely due to formation of corrosion products. At this stage the wire surface turned tarnish, dark and slightly greenish brown (Figure 86 (c)). According to previous studies [2,123,352], such colour of the metal surface relates mainly to a mixture of copper oxides.

Thus, the effect of BTAH on copper dissolution in 5 mM NaCl was also investigated by the Cu^{2+}-SME. In the beginning the copper-platinum couple was immersed in 5 mM

NaCl for 3 hours. Then the crystals of BTAH were added into solution in order to get 1 mM concentration of the inhibitor. The copper activity profiles were measured in the same way as described above. After 30 minutes of immersion in 5mM NaCl + 1mM BATH solution $a_{Cu^{2+}}$ was $4.8 \cdot 10^{-5}$M along the whole scanned line (Figure 87 (b), emerald green line). No active spots were found at the metal surface.

Before the addition of BTAH, the copper surface was covered by corrosion products (more likely by Cu_2O, CuCl and $Cu(OH)_2$) and Cu^{2+} ions were present in the solution. Thus, benzotriazole could interact with the bulk solution and at the sample surface. The form of BTAH molecule in an aqueous solution depends on the pH and can be neutral (BTAH), dissociated (BTA^-) or protonated ($BTAH_2^+$):

$$BTAH_2^+ \rightleftarrows BTAH + H^+, \; pK_1 \approx 1 \tag{9.16}$$

$$BTAH \rightleftarrows BTA^- + H^+, \quad pK_2 = 8.2 \tag{9.17}$$

Cotton and Scholes reported that BTAH forms insoluble precipitates with both cuprous and cupric ions, Cu(I)BTA and Cu(II)BTA, respectively [374]. The composition of the Cu(II)BTA compound obtained in the presence of cupric chloride or cupric sulphate was assumed to be $(BTA_2Cu)_2 \cdot CuCl_2 \cdot H_2O$ or $(BTA_2Cu)_3 \cdot 2H_2O$ correspondingly [374]. Eventually, BTAH dissolved in the cell solution would react with Cu^{2+} with formation of such precipitates. However, Cu(II)BTA was found to be formed at Cu_2O surface only after removal of the liquid phase due to oxidation of Cu(I)BTA till Cu(II)BTA by air; and no Cu(II) species were observed in corrosion products after immersion of Cu in BTAH containing 3% NaCl [362]. It should be noticed, that in those experiments BTAH was present in the solution from the beginning and, hence, would react from the first moments of corrosion process, while in this work the inhibitor was added after some time of immersion, when the metal dissolution was already on going.

Next, after 30 minutes of immersion, an artificial scratch on the copper surface was made by a sharp knife (Figure 87 (a)), and immediately a peak of Cu^{2+} activity was detected above the scribe (Figure 87 (b), pink line). The shiny scratch exposed pure copper to the solution, which started to dissolve instantly. Later the measured values of $a_{Cu^{2+}}$ become smaller (blue line), ca. $3.7 \cdot 10^{-4}$M comparing to $5.7 \cdot 10^{-4}$M (pink line), and after further 30 minutes (immersion time of 1h 20 minutes) the copper activity become low (ca. $4.8 \cdot 10^{-5}$M) and almost constant along the whole measured profile (orange line).

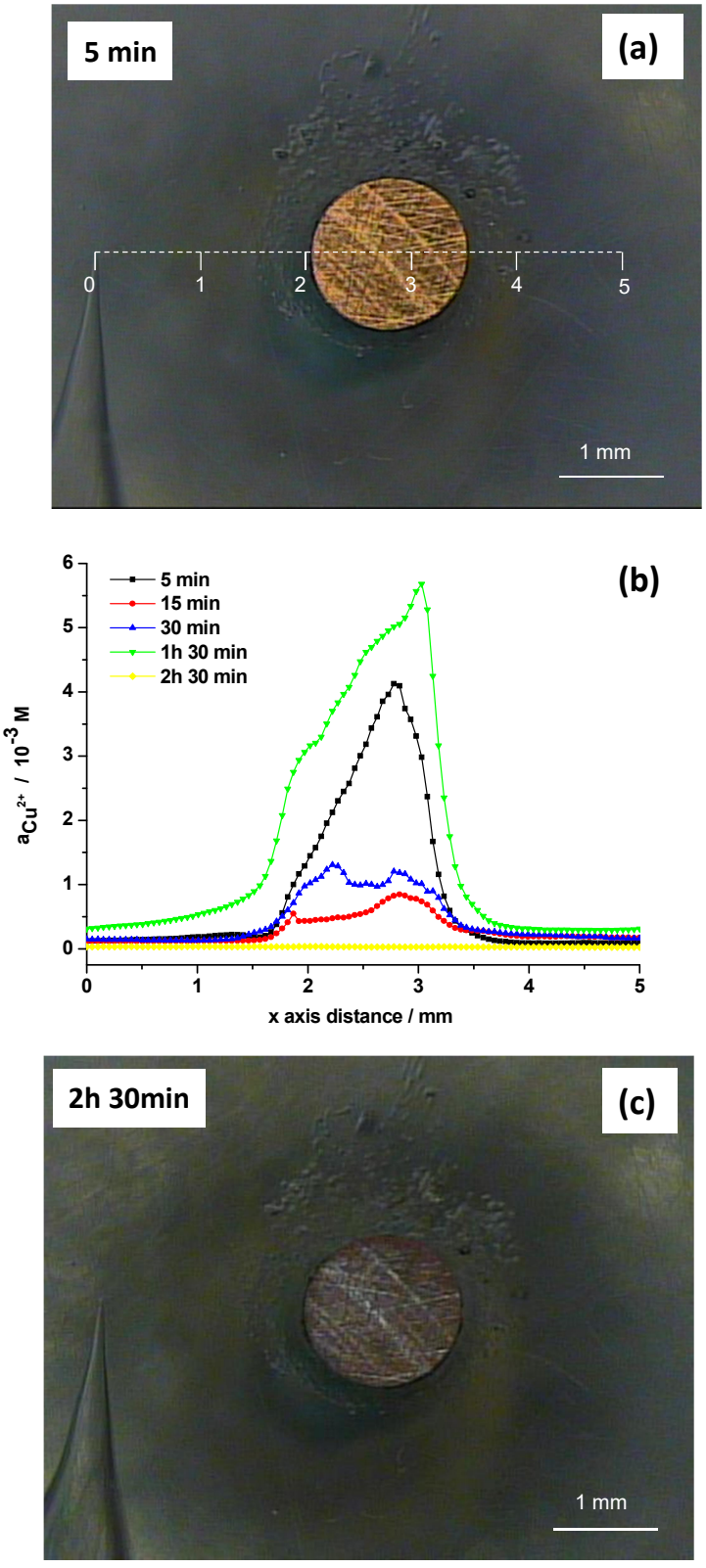

Figure 86. Optical photographs of Cu wire that is connected to Pt after 5 minutes (a) and up to 2 hours 30 minutes (c) of immersion in 5 mM NaCl. Activity of Cu^{2+} measured by Cu^{2+}-SME 10 µm above the surface at different times of immersion (b).

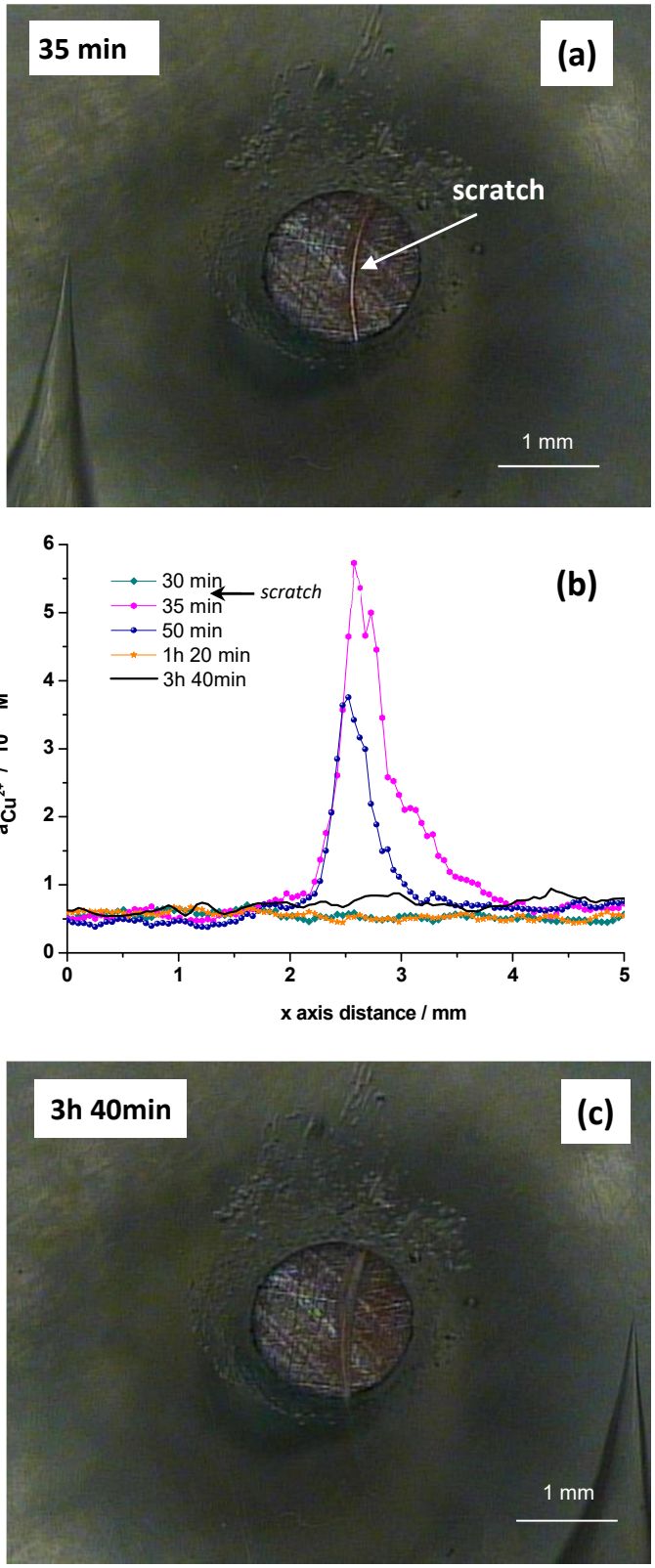

Figure 87. Optical photographs of Cu wire that is connected to Pt with an artificial scratch after 35 minutes (a) and up to 3 hours 40 minutes (c) of immersion in 5 mM NaCl + 1 mM BTAH. Activity of Cu^{2+} measured 10 µm above the surface at different times of immersion (b).

The BTAH inhibitive effect could be clearly observed. Its action was still occurring even after ca. 3.5 hours from the beginning of immersion (black line). The scratch area became tarnish as the rest of the sample surface (Figure 87 (c)).

9.3 Copper(II) ion sensitive solid state microelectrode based on copper selenide

An alternative to the glass microelectrode and in order to overcome the small selectivity towards Na^+, a different Cu^{2+}-SME was produced. Based on reports of Papeschi *et al.* [255,256] a Cu{CuSe} microelectrode for use in detecting copper(II) fluxes along Olea europaea roots was developed. The described ME for Cu^{2+} detection possesses good analytical characteristics, easy in fabrication and being all solid state provides mechanical robustness, essential for performing measurements close to metallic surfaces.

9.3.1 Response of the Cu{CuSe} microelectrode

The produced Cu{CuSe} microsensor shows near Nernstian slopes in calibration graphs (Figure 88). The Cu^{2+} selective microsensor is linear in the concentration range from $3 \cdot 10^{-2}$ M to $3 \cdot 10^{-6}$M in pure copper (II) solutions and from $3 \cdot 10^{-2}$ M to 10^{-5}M at 0.05M NaCl background with slopes of 34.1 and 33.1 mV per activity decade correspondingly. The influence of Na^+ on response of the copper (II) microsensor is almost negligible, as can be seen from the graphs. The Cu{CuSe} microsensor has lower detection limit around $3 \cdot 10^{-6}$ M.

It should be mentioned, that in previous works [255,256,381], calibrations of copper selenide based ISEs were done in solutions with constant high ionic strength, i.e. in 0.1 M KNO_3. Indeed, as one can notice on Figure 88, the calibration points of the Cu{CuSe} microsensor in solutions with 0.05M NaCl background (ionic strength is around 0.05) are less scaterred, than in pure Cu^{2+} solutions, where the ionic strength is dictated only by $CuCl_2$, even though the response of the microelectrode in 10^{-1}M Cu^{2+} solutions, in both with and without 0.05M NaCl (ionic strength > 0.3), is out of the linear range. Such electrode behaviour is caused by alterations in surface composition of the microelectroe tip, probably, due to Cu^{2+} adsorption and possible further diffusion inside the membrane material [382].

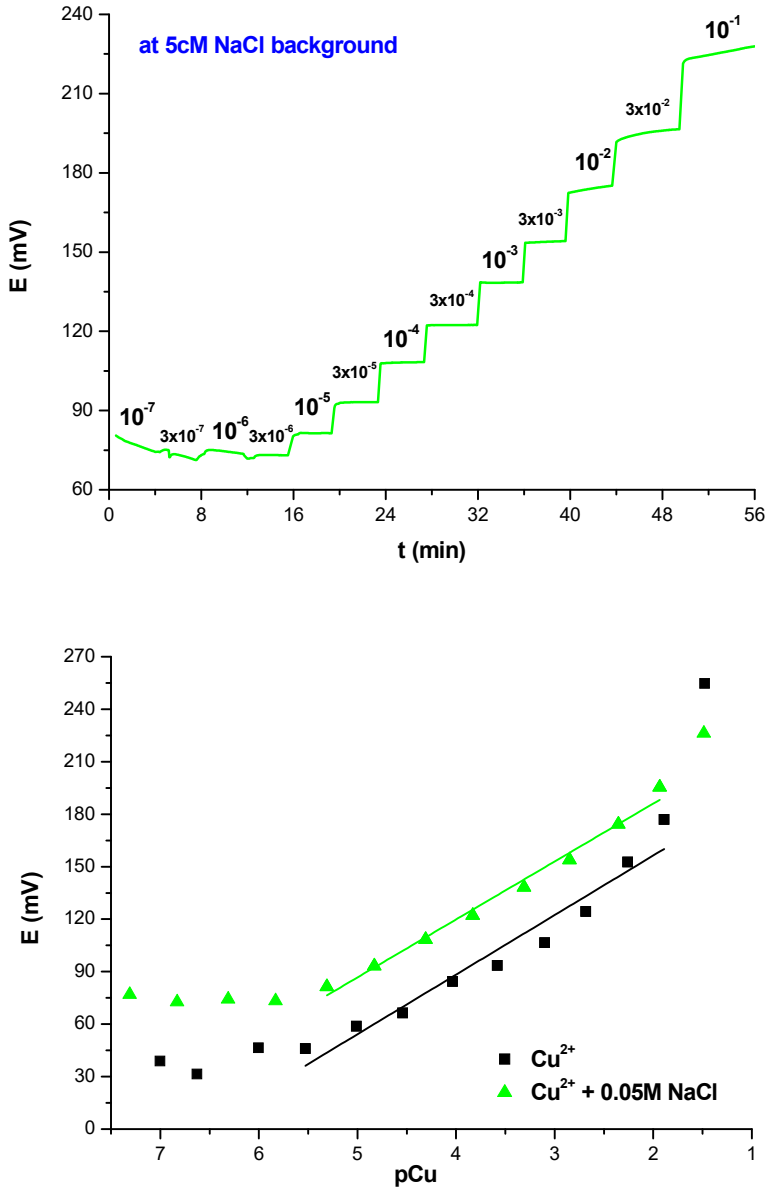

Figure 88. The dynamic response (upper) and calibration plots (lower) of Cu{CuSe} microsensor in different mediums.

9.3.2 A word about working mechanism

As referred in Section 4.5.3, the microelectrode was produced by copper plating on a Pt tip followed by the cathodic deposition of copper selenide at -100 nA for 30 minutes from 0.1M Na_2SeO_3 solution adjusted to pH 6 with sulphuric acid [255].

Depending on the current density, the copper to selenium ratio and pH of the solution, copper selenide of four possible stoichiometries could be deposited electrolytically: CuSe, Cu_2Se, Cu_3Se_2 and $Cu_{2-x}Se$ and very often the coatings comprises a

mixture of them [381]. Thus, during a co-deposition on Pt substrate of Se (IV) and Cu (II) from corresponding solution a coating with formula of $Cu_{2-x}Se$ (x≈0.2) was obtained [381], the same as that of the monocrystal described elsewhere [382]. While Papeschi *et al.* had reported about a microsensor with chemical composition Cu/CuSe [255,256]. As also some spots of uncovered copper can appear during deposition in acidic medium due to pitting corrosion [256] and no chemical surface analyses of the coating was made, it is better to refer to this microelectrode as a Cu{CuSe}, omitting assumptions about the stoichiometry.

Copper selenide is a type of chalcogenide compounds, which are well known for their Cu^{2+} sensing properties [381,382]. It was proved that usually the copper in chalcogenide materials is mainly monovalent and it does not change its valence after soaking an ISE in copper (II) solutions [254,382]. Several models had been considered by chemists to explain the Cu^{2+} sensing mechanism of copper (II) selective chalcogenide glasses of different composition, including monocrystalline $Cu_{1.8}Se$ one [382]. Vlasov *et al.* showed that ionic sensitivity of such sensors is related to the exchange of copper (II) ions between solution and modified surface layer of the glass (so called "modified surface layer model") [382]. It is admitted, that the modified layer is formed on the glass surface as a result of interaction with solution and partial glass network destruction. A considerable content of exchange sites for Cu (II) appears in the modified surface layer. A potential-generating process in this case is the direct copper (II) ion exchange between solution and the modified surface layer of the glass

$$Cu^{2+}\ (solution) \leftrightarrow\ Cu^{2+}\ (modified\ surface\ layer) \tag{9.18}$$

The equilibrium at the modified surface layer/glass bulk boundary is achieved according to the reaction

$$Cu^{2+}\ (modified\ surface\ layer) \leftrightarrow Cu^{+} +\ h^{+} \tag{9.19},$$

where h^{+} is a positively charged hole. Copper (II) ions in the surface layer are generated as a result of the copper (I) disproportionation reaction

$$2Cu^{+} \leftrightarrow\ Cu^{2+} +\ Cu^{0} \tag{9.20}$$

and a subsequent metallic copper oxidation, as well as Cu^{2+} diffusion from solution.

Thus, (and as it was empirically established [382]) the Nernst equation for the copper selenide based sensor can be written as:

$$E = constant + 29.6\ loga_{Cu^{2+}} \tag{9.1}.$$

9.3.3 Probing copper corrosion and inhibition with Cu{CuSe} microelectrode

The Cu{CuSe} microelectrode was applied for mapping copper dissolution above a copper wire connected to a Pt wire and immersed in 0.05M NaCl. The cell configuration was the same as in the previous experiment with glass capillary Cu^{2+}-SME, described in section 9.2.2 (Figure 85). The microelectrode was placed 50 µm above the sample surface. The scan consisted of a 46x32 points grid; time of data acquisition in each point was 2 seconds. Figure 89 presents a map of pCu distribution obtained after 3 hours of immersion of Cu-Pt galvanic couple.

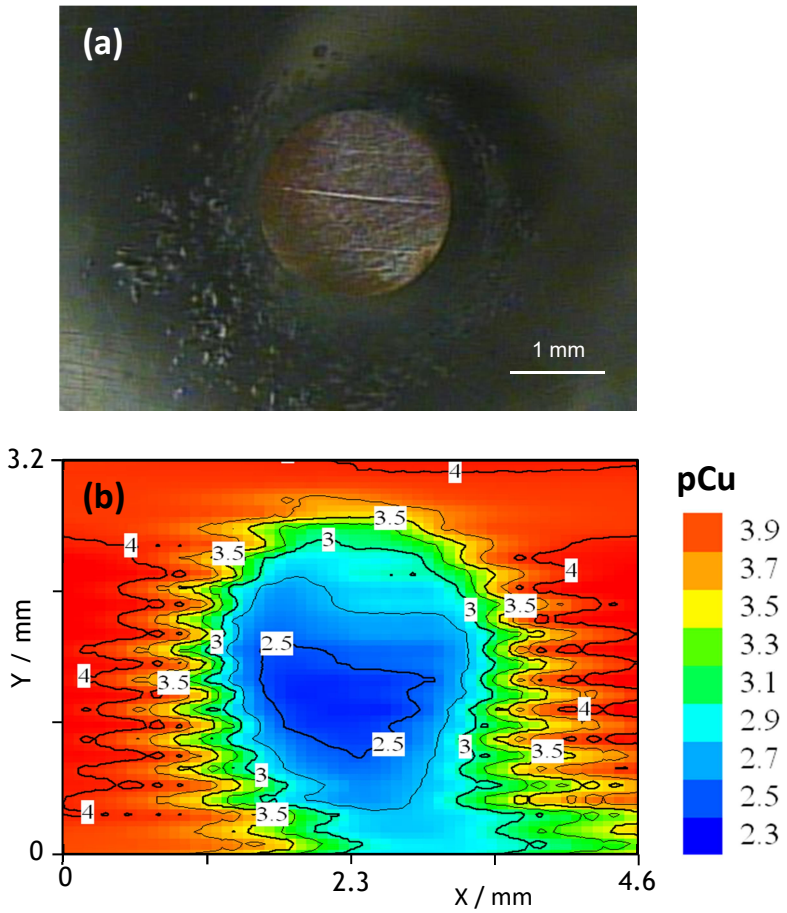

Figure 89. Optical image of Cu wire connected to Pt wire beneath the holder (a) and distribution of pCu 50 µm above the surface (b) after 3 hours of immersion in 0.05M NaCl.

According to the map, the copper (II) ions are located mainly above the copper wire, with higher content (up to $5 \cdot 10^{-3}$M) at the bottom of the metal disk, where it turned greenish brown due to corrosion products (most probably Cu_2O, CuCl and $Cu_2(OH)_3Cl$). The Cu^{2+} activity in the bulk solution is smaller and is close to 10^{-4}M. Slight spreading of Cu^{2+} is observed in the very bottom of the scan.

Before measurements of $a_{Cu^{2+}}$ during inhibition process, some preliminary tests were done, in order to estimate the influence of BTAH on the response of the Cu{CuSe} microsensor. The response of the microsensor was monitored in 0.05M NaCl with and without BTAH (Figure 90). As one can see, the microelectrode potential started to increase, when crystals of BTAH (to get 1mM concentration) were added into the 0.05M NaCl solution (Figure 90 a). A steady state was reached in approximately 80 minutes. Then the solution was changed to 0.05M NaCl, and the potential started to decrease (Figure 90 b). Such changes in potential correspond to adsorption / increase of potential and desorption / decrease of potential processes of the BTAH on/from the microelectrode surface. This means, that measurements of Cu^{2+} content in a solution containing BTAH can not be carried out by the Cu{CuSe} microsensor.

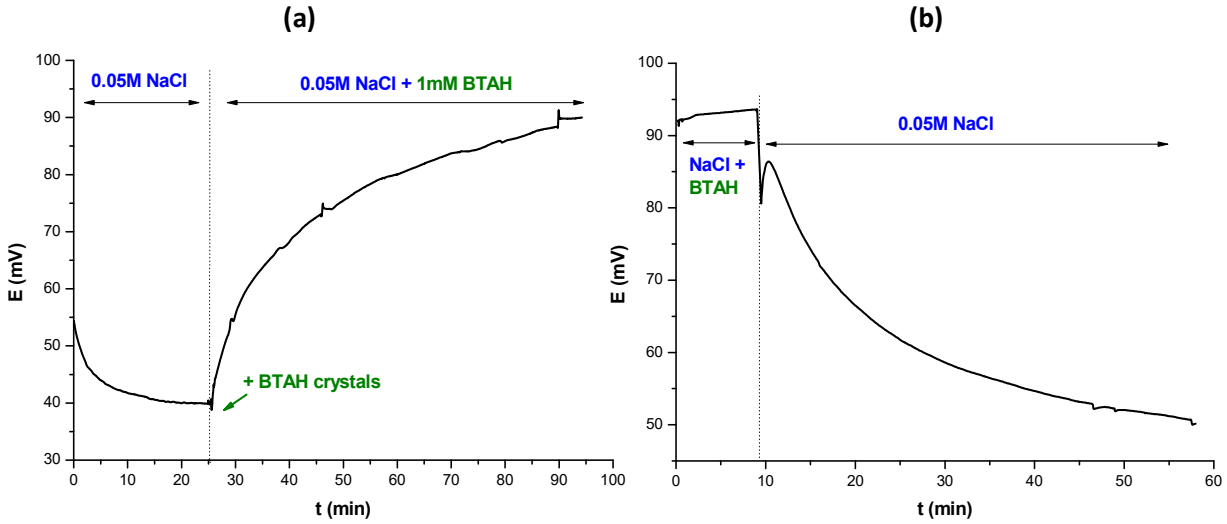

Figure 90. Influence of BTAH on the response of Cu{CuSe} microelectrode at 0.05M NaCl background.

Therefore, the measurement was done in 0.05M NaCl after a period of pre-exposure of the sample to the inhibitor solution. The sequence of tests is summarized in Table 24. The results are presented in Figures 91 and 92.

After 30 minutes of immersion in 0.05M Cu^{2+} profiles were measured above the not coupled copper wire and neither $a_{Cu^{2+}}$ changes (black line, Figure 91 a) nor visible changes on the metal surface (photo (b)) were detected. But in a galvanic couple with platinum, corrosion started very fast and after 1h and 20 minutes of immersion the copper began to dissolve rather intensively (red line, Figure 91 a, photo (c)). Some decrease in the copper activity was observed after 3h and 45 minutes of immersion (blue line in Figure 91 a), which could be explained by formation of corrosion products.

Table 24. Tests made during corrosion and inhibition of copper connected to platinum.

Parameter	Stage			
	1	2	3	4
Solution	0.05M NaCl	1mM BTAH + 0.05M NaCl	0.05M NaCl	0.05M NaCl
Time of immersion	18h 45 min	45 min	55 min	4h 40 min
State of the surface	from pink to reddish brown (Figures 91 b to f)	dark reddish brown (no figure)	dark reddish brown (no figure)	scratched, slightly brown (Figure 92 a)
$a_{Cu^{2+}}$ **profile**	Figure 91 a, lines from black to yellow	not measured	Figure 91 a, magenta line	Figure 92 b

After almost 19 hours of immersion the copper surface was completely attacted and covered by dark reddish brown corrosion products (Figure 91 f); the $a_{Cu^{2+}}$ profile revealed at least one active side of the copper wire (yellow line, Figure 91 a). Then BTAH crystals were added into the 0.05M NaCl solution in order to obtain 1 mM concentration. The sample was left during 45 minutes in contact with the inhibitor. Then the solution was replaced by new 0.05M NaCl solution and the activity profile was measured after 55 minutes of immersion. The observed values of $a_{Cu^{2+}}$ were very low and were the same above the wire and in the solution bulk, i.e. $1.3 \cdot 10^{-5}$M (magenta line, Figure 91 a), because a protective layer containing BTAH was formed at the copper surface, which blocked the metal dissolution.

The inhibition of copper corrosion still took place, even after the wire surface was intentionally scratched by a glass stick after 3 hours and 15 minutes of immersion in 0.05M NaCl (Figure 92 a). Thus, the measured Cu^{2+} activity was in the order of $3 \cdot 10^{-3}$M immediately after the scratch was made and decreased nearly one order of magnitude, i.e. till $2.9 \cdot 10^{-4}$M after 4 hours and 40 minutes of immersion in 0.05M NaCl solution (Figure 92 b).

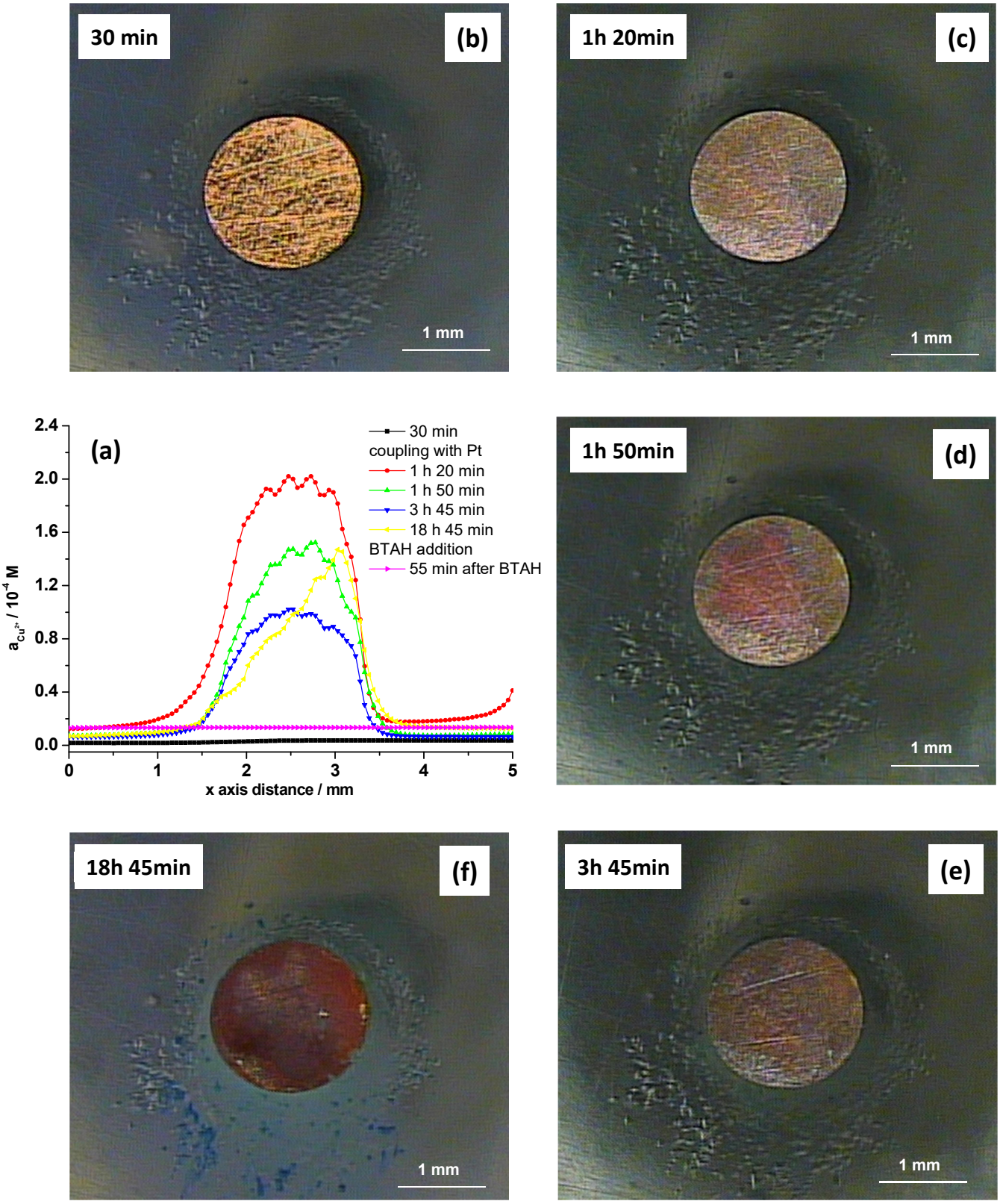

Figure 91. Copper activity measured 100 µm above the surface at different immersion times in 0.05M NaCl (a) and corresponding optical images of the copper wire (b, c, d, e and f).

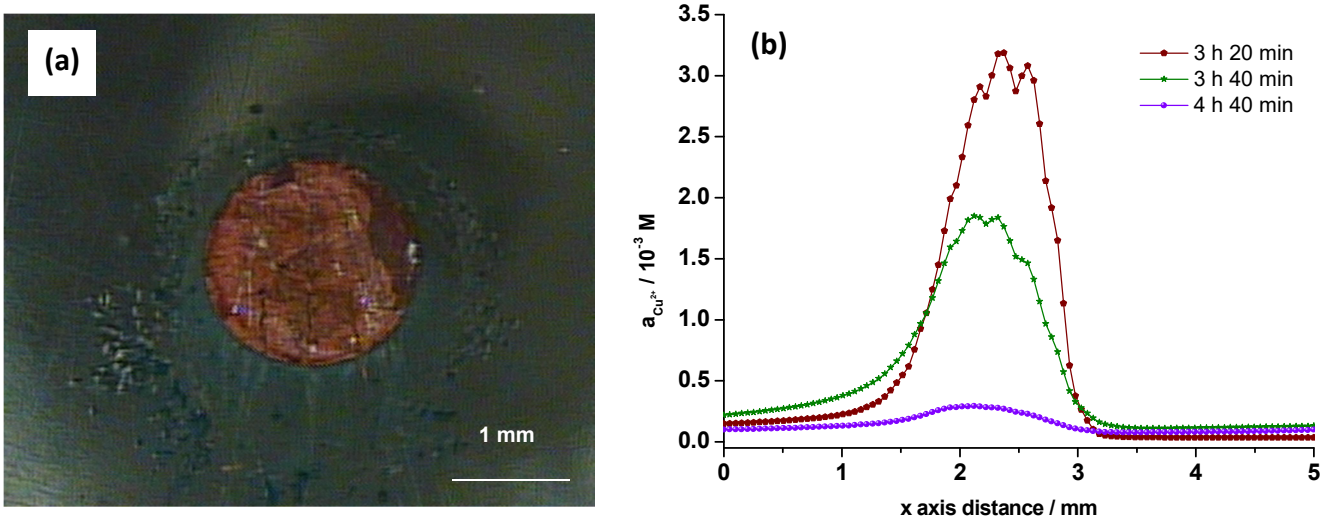

Figure 92. Optical photograph of Cu wire with scratched surface (a) and copper activity measured 100 µm above the surface at different times of immersion in 0.05M NaCl after the pre-exposure in 1 mM BTAH + 0.05M NaCl solution (b).

9.4 Concluding remarks

Two Cu^{2+} selective microelectrodes, a glass TBTDS based cocktail Cu^{2+}-SME and a 2nd kind metal/metal salt Cu{CuSe} microsensor, were developed. Their main characteristics (linear range, slope and sensitivity at NaCl background) were determined. Both microsensors showed good sensitivity for Cu^{2+} ions giving linear response in the range of 10^{-2}-10^{-6}M for TBTDS based Cu^{2+}-SME and $3{\cdot}10^{-2}$-10^{-6}M for Cu{CuSe} microsensor in pure Cu (II) solutions. The Cu{CuSe} microsensor possessed better selectivity against Na^{+} ions as was shown on calibration graphs.

Both microelectrodes were applied for investigation of corrosion processes of a copper wire connected to Pt and immersed in NaCl solution with and without BTAH. Obviously, the solid state Cu{CuSe} microelectrode is mechanically more robust, but it is affected by BTAH and can not be used in its presence. Moreover, the spatial resolution for the Cu{CuSe} microsensor is lower than for the other ME, as its tip diameter is likely to be more than 10 µm comparing to 1.5-2 µm for the TBTDS based Cu^{2+}-SME. Moreover, further investigation of the Cu{CuSe} microsensor tip surface (exact coating composition and its thickness) are desirable.

Chapter 10

10 Discussion

10.1 Work overview

The present PhD work was mainly dedicated to the development and application of microelectrode techniques, namely the Scanning Vibrating Electrode Technique (SVET) and the Scanning Ion Selective Electrode Technique (SIET), as experimental tools capable to assess local electrochemical reactions on metallic substrates immersed in aggressive solutions.

In order to demonstrate the applicability of SVET and SIET for the investigation of corrosion processes the following tasks were addressed:

- Definition and description of localized corrosion types;
- Evaluation of capabilities of existing microelectrochemical techniques;
- Search for sensitive microelectrodes suitable for SIET;
- Study of fabrication procedure for MEs based on glass capillaries;
- Screening of PVC-based Zn^{2+} and Al^{3+}-SEs;
- Development of liquid membrane cocktails for Zn^{2+},Cu^{2+} and Al^{3+} ISMEs;
- Fabrication of ISMEs for pH, Mg^{2+}, Zn^{2+},Cu^{2+} and Al^{3+} detection;
- Validation of the obtained ISMEs by determination of their linear concentration range, slope, time of response and selectivity to H^{+} and Na^{+};
- Application of SVET and SIET for investigation of model and real corrosion cases.

A schematic summary of the implemented work is shown in Figure 93. The SVET was used for local measurements of ionic currents in solution (red frame). The dissolved oxygen concentration was determined by an amperometric microsensor (purple frame). The SIET was utilized for the analysis of the chemical species involved in the corrosion process (green frames). The spatiotemporal distribution of pH, activity of Mg^{2+}, Zn^{2+} and Cu^{2+} ions were measured by appropriate microsensors during corrosion and inhibition of model (Zn, Zn-Fe and Cu-Pt couples) and real (defects on coated magnesium alloy AZ31 and coated aluminium alloy AA2024) systems. Attempts for producing an Al^{3+}-SME were made.

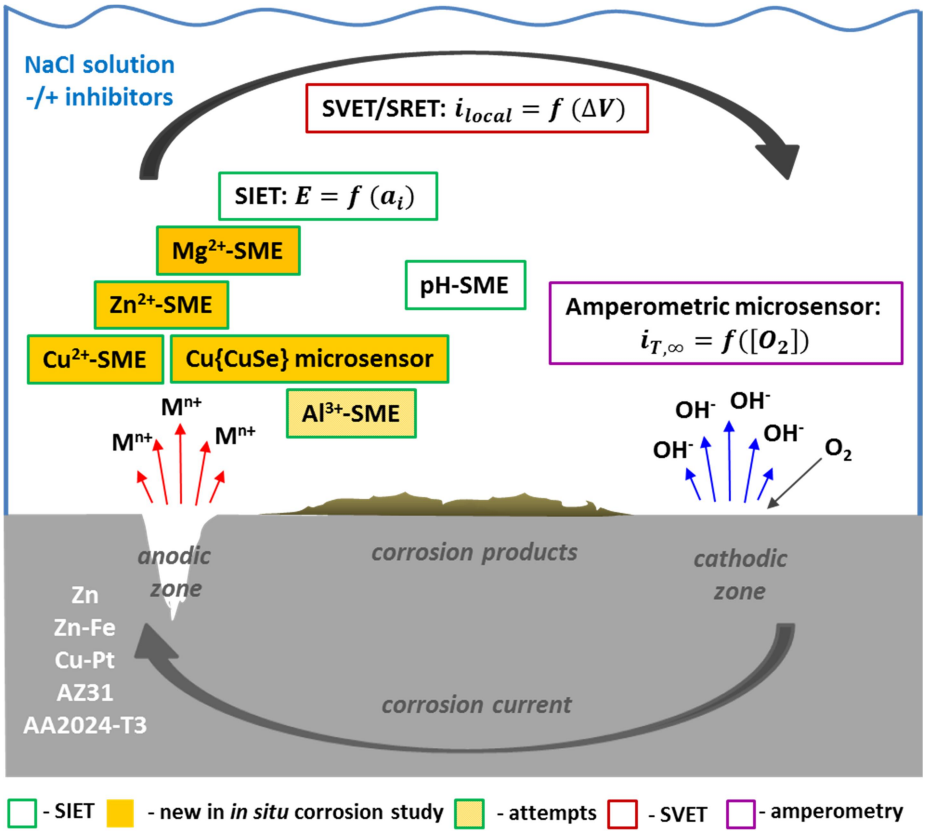

Figure 93. Summary of realizations made during this PhD work.

10.2 SVET/SRET and SIET applications in corrosion studies

The application of SVET/SRET and SIET for investigation of corrosion and inhibition processes permitted to conclude the following:

i) The SVET provided important information regarding the localization of currents and their magnitudes. Because SVET uses a lock in amplifier to amplify and filter the signal, the current density map measured above Zn-Fe galvanic couple had higher resolution and lower noise compared to the map calculated from SRET data. Together

with the map of dissolved oxygen concentration determined amperometrically and maps of pH and Zn^{2+} activity measured by SIET the spatiotemporal distribution of species taking part in the galvanic corrosion of the Zn-Fe couple was characterized. All four maps were in good agreement.

ii) Localized measurements of pH and O_2 reduction current at defects on coated aluminium alloy AA2024-T3 complemented SVET results in the characterization of the anodic and cathodic processes. It was found cathodic activity in defects that were thought to be only anodic according to the current density map.

iii) The combination of SVET measurements and SIET mapping of pH and Mg^{2+} activity to study corrosion and inhibition processes inside the coating microdefects on AZ31 was used to identify the most efficient inhibitor among those tested. According to the results, 1,2,4-triazole was able to keep the corrosion activity on a very low level, that was confirmed by the small values of current density, pH and pMg in the defects.

iv) The quasi-simultaneous mapping of pH and pZn during the localized corrosion of Zn wire showed that spatial distribution of Zn^{2+} ions in solution was immediately affected by OH^- resulting from oxygen reduction, i.e. as soon as zinc cations were released from the surface, the formation of Zn^{2+} containing species was initiated and insoluble precipitates appeared close to the pit. The use of GMS (Geochemical Modelling Software) programs with input data obtained from SIET measurements allowed predicting the chemical composition of the corrosion products.

v) The dissolution of Cu wire connected to Pt and copper inhibition due to the presence of benzotriazole were addressed by Cu^{2+}-selective microsensors. It was possible to visualize and quantify the distribution of Cu^{2+} ions in space and time with high resolution.

vi) Potentiometric and amperometric microsensors were found to be good devices with high spatial resolution to assess chemical information during localized corrosion and inhibition processes, but the careful choice of the electrode material and type is necessary, as some of them can be strongly affected by the analyzed medium (as it happened in the case of solid state Cu{CuSe} microsensor).

vii) In spite of the fact, that corrosion processes evolve relatively fast, change location and the appearance of corrosion products interferes with the approximation of the probes to the metal surface, it was possible to perform *in situ* mapping of Mg^{2+}, Zn^{2+} and Cu^{2+} cations by potentiometric microsensors in corroding systems for the first time (Figure 93, yellow rectangles).

10.3 Development of membrane compositions for the ISMEs

The membrane cocktails used for pH- and Mg^{2+}-SMEs fabrication from glass micropipettes were commercially available (Section 4.5.2.1). Cocktail compositions for Zn^{2+} and Cu^{2+}-SMEs were based on the previously described in the literature PVC membranes (Sections 7.1 and 9.2, correspondingly). New membrane compositions for Zn^{2+} and membranes for Al^{3+}-SMEs were produced (Figure 93). The development of these membrane compositions for Zn^{2+} and Al^{3+}-SMEs was carried out through the following steps:

- Searching for ISEs with membrane compositions meeting the requirements for the application in corrosion studies and availability of components;
- Reproduction at the microlevel of PVC based compositins found in the literature and preliminary characterization of the ISMEs response;
- Searching for new membrane components (possible structures and their availability) and fabrication of ISEs with PVC membranes based on the new components;
- Analysis of the response (effects of ionophore, ion-exchanger and plasticizer) of the newly fabricated macroelectrodes at required pH and NaCl background in order to find the best selective membranes to be tested in microelectrodes;
- Recreation of the most promising PVC membrane compositions in the form of cocktails for microelectrodes and acquisition of the corresponding analytical characteristics.

The main practical achievements of the PhD thesis are related with the development of membrane compositions for ISMEs. Some aspects, for example, selection of ionophores, ME fabrication procedures and microelectrodes characteristics, were already mentioned in the previous chapters. Now a short discussion about the screening tests of ISEs, membrane resistance and evaluatuion of ISMEs performance is presented.

10.3.1 Screening tests of ISEs

Investigating the response of membrane compositions made of new components (especially ionophores) at the microlevel can lead to less confident decisions due to larger probability of artefacts occurrence and lower results reproducibility caused by different issues, from technical (air bubbles in the tip, inappropriate cocktail length, degree of silnization, cocktail leaking, etc.) to chemical (substance deterioration) ones. That is why such screening tests should be carried out on macroelectrodes with PVC based membranes.

The fact that during SIET mapping of localized corrosion processes an ISME is moved from one point of measurement to another one, where primary and interfering ions (e.g. H^+ and Na^+) with variable content always coexist together, means that the composition of analysed solution continuously changes qualitatively and quantitatively. While in traditional potentiometric methods of analysis sample preparation procedures can help mask, remove or decrease the effect of the interfering species, this is not possible in *in situ* corrosion studies. That is why screening tests with ISEs should be done with maximum approximation to reality, because at least two things are likely to happen in a non-conditioned matrix: i) chemical speciation of the metal cations at varying pH and concentration of anions in solution can change the state of the target ion and part of it might not be free to be detected (for example, hydrolysis of Al^{3+}); ii) interaction of ionophore with interfering ions in the case of poor membrane selectivity. Since these reactions are competitive, the electrode response was evaluated at pH values caused by partial hydrolysis of metal ions (Sections 7.3.3 and 8.5 for Zn^{2+}-SEs and Al^{3+}-SEs correspondingly) with and without Na^+ ions. Such approach permitted to reveal rapidly Zn^{2+}-SEs and Al^{3+}-SEs with the best selectivity for the given conditions.

10.3.2 Membrane resistance of ISMEs

The reformulation of the promising polymeric membranes in the form of cocktails for microelectrodes was mainly based on removing PVC and replacing it for the plasticizer which worked as matrix for the remaining cocktail components. However, this method did not always provide ISMEs working properly. All Al^{3+}-SMEs and some Zn^{2+}-SMEs produced by this way were not able to detect any potential values, meaning that their resistance was too high, while pH-SMEs and Mg^{2+}-SMEs never possessed such problems. It is well known, that the electrical membrane resistance of a microelectrode, R_m (Ω), is related to the membrane solution resistivity, ρ (Ω cm), as well as to the tip radius, r, (cm), according to the following equation [76,191]:

$$R_m \approx \frac{2\rho}{\pi r \theta}\,, \tag{10.1}$$

where θ – angle of the taper of the microelectrode (in radians).

Since a programmed pulling machine with the same adjustments was used for the micropipettes fabrication, the tip diameter was very reproducible, i.e. 1.5 ± 0.3 µm for all microelectrodes used including those with good response. This means the composition of the membrane cocktail is the most determinant factor, and particularly the solvent because its content is more than 80 wt.%. In this work the cocktail solvent was kept the same as the plasticizer used in the corresponding ISE to maintain the desired selectivity, which, obviously, also resulted from the optimized ionophore and ion-exchanger content. Plasticizers can have distinct physico-chemical properties, like, resistivity, dielectric

constant and viscosity even though meeting the general requirements for using in PVC membranes [76,222]. It is already known that solvents with high dielectric constants are to be preferred for cocktails of ISMEs in order to provide lower membrane resistance [76]. One of such solvents is NPhOE (ε=23.9 [222]), which has been used in the cocktails for pH-SMEs, Mg^{2+}-SMEs and Zn^{2+}-SMEs. However, the cocktails for the Al^{3+}-SMEs were based on pure TEHP or BBPA (Section 8.6) with much lower dielectric constant (4.8 and ≈4, respectively [76,222]). An attempt of decreasing R_m by mixing TEHP and BBPA with NPhOE didn't solve the problem. Typical solvents for these membranes exhibit resistivities in the range of 10^6 to 10^{10} Ω cm [76], that is a variation of 4 orders of magnitude, which is critical for the ISMEs. Meanwhile, viscosity of NPhOE and TEHP, characteristic essential for preventing the cocktail leaking from the micropipettes, are very close – 1380 and 1250 g cm^{-1} s^{-1}, respectively [76]. That is why initially TEHP seemed to be an appropriate solvent for ISMEs; also earlier cocktails for Mg^{2+} and Li^{+}-SMEs were based on it [76].

As all membrane components contribute to the electrical resistance, it is possible to tune it by changing their nature and content. Thus, the addition of the ion exchanger ETH500 into the cocktail for Zn^{2+} greatly improved the performance of the Zn^{2+}-SME (Section 7.1). This approach has limitations. As reported before for Ca^{2+}-SME [76], this additive only had beneficial effect on membrane resistance if the polarity of the solvent was significantly increased at the same time (for example, propylene carbonate with dielectric constant of 64.9). However, a more polar solvent can result in worsening of detection limit and/or selectivity [76].

The membrane resistance of a microelectrode is also influenced by the composition of adjacent solutions [76]. This fact explains why the Zn^{2+}-SMEs with the same cocktail composition based on NPhOE worked in calibration solutions, which contain only Zn^{2+} ions, and failed in the presence of 0.05M NaCl background (Sections 7.1 and 7.3.4).

For future work with cocktail mixtures, as in the case of Al^{3+}-SME, a fast and reliable way of R_m determination would be advisable. Another approach that might be used for testing membrane resistances of ISMEs based on new components is to fabricate mini-ISEs, i.e. with sensing tip size in the range of several milimeters with liquid membranes without PVC.

10.3.3 ISMEs response evaluation

The response of the obtained ISMEs was evaluated according to the IUPAC recommendations for ISEs [228]. It should be mentioned that these recommendations were published in the 1990s, since then new descoveries concerning, for instance

detection limit and selectivity coefficients, have been made [383], but also new types of MEs, for example microfabricated ISEs, gained ground both as research tools as well as detectors in commercial blood gas analyzers [298]. Unfortunately, there are no IUPAC recommendations for evaluation of the working characteristics of ISMEs taking into account some specific conditions of their application like continuous usage in the field.

As important working characteristics of the ISMEs were already described in the previous chapters, here in attention will be given to time dependent parameters of ISMEs, as lifetime and response time.

Usually lifetime of the obtained ISMEs was around 1 day, i.e. it was possible to make mapping measurements with the same ISME during this time. As no manipulations with the ME were made during the mapping, except its first positioning on a sample surface, lifetime of the sensor was mostly dictated by the cocktail state and not by technical or mechanical reasons. Thus, sometimes after continuous usage (from three to six scans depending on experiment) during monitoring of corrosion or inhibition processes, an ISME gave a signal but lost its sensitivity toward the target ions, as its slope deviated far from the theoretical value, for example, 44 mV/activity decade for the pH-SME. Such microelectrodes behaviour means, that leaching and/or decomposition (for instance, due to membrane poisoning by corrosion products) of the cocktail components happened, which changed an optimal ionophore – ionic additive ratio, consequently provoking loss of sensitivity. It also can be accompanied by increased membrane resistance, worse detection limit and increased noise [298].

Determination of response time (τ_{95} and τ_{lim}) of ISMEs using a ‘‘dual drop cell”, as described in the Section 4.7.1.2, was based on the recording potential while moving the microelectrode from one drop of less concentrated solution to other drop of more concentrated solution, for example, from pH 9 to pH 8 in the case of the pH-SME. Based on the obtained value of τ_{95}, the time of data acquisition during mapping by ISME was chosen to be close to it. However, in some maps the activity profiles did not always correspond to the shape of ions source (Figures 37 a, 48 b, 59 b, 60 b and 89 b) resulting in blurry counter lines of ion activity. The orientation for values of τ_{lim}, which are bigger than τ_{95}, instead would slightly reduce this effect, but could increase the time of measurement significantly. Still another issue could be present. When an ISME scans an area with a source of ions (like a wire or a coating defect), it continuously moves from places with low content to places with high content of the target ions and vice versa. Taking into account that response time of the ISMEs was determined by increasing concentration of solutions in drops, different response speed might exist when concentration of solutions decreases. The term *recovery time* is frequently used in this case [229]. It seemed that the determination of it would be useful for mapping by SIET. Whatever the value for data aquisition during scanning is used, the response time of an

electrode is not a univocal parameter, as it depends not only whether it was determined after increasing or decreasing the target ion concentration, but also on other particular working conditions. These are, for instance, if it was measured in the middle of the dynamic response range or near the detection limit; if the primary ion was alone or in the presence of interferents; on solution in which electrode is initially conditioned and on conditioning time [229].

Besides the IUPAC protocols, there are also some common practices in the methodology of using ISEs, which, however, can be irrelevant for the ISMEs. For example, conditioning of freshly prepared electrodes with polymeric neutral carrier based membranes in a relatively concentrated solution of primary ions overnight in reality does not make sense if the ISME lifetime is around 1 day, as in the case of glass micropippettes based microsensors. Another example is the concentration of inner filling solution that is widely accepted to be in the order of 10^{-2}-10^{-3}M [298]. A concentrated inner solution may contribute to primary ion leaching across the membrane into the sample solution due to salt co-extraction, thus being the major source of biased detection limit and selectivity coefficients values. Thus, the usage of less concentrated inner filing solution of 10^{-5}M of Zn^{2+} ions for Zn^{2+}-SME favoured the better performance of the microelectrode. To avoid ion fluxes across the ISE membrane, the use of inner filling solution that exactly matches the concentration of a sample solution would be ideally [298,383]. Unfortunatelly, matching the concentration of the sample solution is not a realistic alternative for the measurements with high variability in analyte concentrations, like during the mapping above an ion source in SIET.

10.4 SIET particularities regarding to corrosion studies

SIET mapping, or *in situ* micro-potentiometry, close to corroding metals has at least two particularities compared to the potentiometric measurements in analytical chemistry or in the life sciences, which pose challenges difficult to overtake and leading sometimes to poor or unreliable data:

1) Ionic currents flowing between anodes and cathodes

During SIET measurements in the frame of the PhD studies no current or potential was applied to the systems under investigation, yet, the electric field in solution associated to the ionic currents flowing between anodes and cathodes exists. Consequently, this potential is felt by the scanning microelectrode which works like a SRET plus a potentiometric sensor [93,99,198,215,297]. For example, in the simple case of Zn-Fe galvanic couple immersed in 5mM NaCl the measured potential in solution varied from 5 mV in anodic to –4 mV in cathodic sites (Figure 33). This is small compared to the potential changes usually found in the pH measurements (≈250 mV or more are typical).

Nevertheless, for metal cations the concentration changes are not so sharp, therefore the corresponding potential variations of the ISME are also small and in this case the contribution of potential caused by the electric field is significant. This is even more important, if an ISME is for double-charged species, which ideal response is only 29.5 mV/activity decade (at 25°C). Different approaches can be used in order to compensate or overcome it. One way is to put the RE and the ISME close together, as in double-channel glass micropipettes, where one channel is for a Ag/AgCl reference microelectrode and the other is for an ISME [99,136,198,384]. But in some cases the surface geometry does not allow the entrance of two tips, therefore, Luo *et al.* applied a current-interrupt technique while determining Cl^- activity and pH in the induced pits on nickel [93].

2) Dissimilar chemical composition near anodes and cathodes

Dissimilar chemical composition near anodes and cathodes, caused particularly by pH changes, dictates the chemical speciation of the metal ions. The latter may not be in a free form, the one sensed by an ISE, but rather hydrolysed, complexed or precipitated. Thus, resulting from the anodic dissolution metal cations are immediately hydrated and undergo hydrolysis reactions. The latter effect is more pronounced in the case of transition metal cations (such as Zn^{2+}, Cu^{2+} and Al^{3+}), than for alkali-earth metal cations (such as Mg^{2+}) [181]. Then, as metal ions diffuse further in the bulk solution, they meet species formed at cathodic sites and react with the precipitation of corrosion products, or might interact with inhibitors, if present, with formation of complexes. Consequently, the different local composition formed in the solution alters the ionic strength, one of the important parameters for ions activity determination by ISEs. It would be better if corrosion scientists are able to determine full metal content in solution, as it can be easily converted into corrosion rate. However, the ISE will only detect the activity of free form of the target ion.

In addition, other, more trivial issues relating with the *in situ* measurements by ISMEs in corrosion applications are the fragility of the glass microelectrodes close to the metallic surface and the eventual tip contamination and blocking by corrosion products, which can reduce microsensor lifetime and the stability of response over time (see section 10.3.3).

Chapter 11

11 Conclusions and future work

Scanning Vibrating Electrode Technique and Scanning Ion-selective Electrode Technique together with microamperometry are powerful localized electrochemical techniques based on the use of microelectrodes to study corrosion.

SVET detects the potential distribution in solution associated to ionic currents and can provide valuable information regarding the localization of currents and their magnitudes as well as vizualisation of the temporal and spatial evolution of active sites. Comparing to SRET, data given by SVET are characterized by higher spatial resolution and less noise.

SIET permits to obtain chemical information about the nature and concentration of many species involved in the corrosion process. An important and key step in this technique is the search of ISME with required analytical characteristics. ISMEs produced from glass micropipettes and based on neutral carrier membranes are attractive tools due to their universal fabrication procedure. For their successful application in localized corrosion studies high selectivity towards H^+ and Na^+ ions is essential.

In this work the search and development of membrane compositions suitable for ISMEs was carried out on traditional ion-selective electrodes with PVC membranes. Preliminary tests with ISEs based on commercially available membrane components revealed deficient response in the desired pH range and in the presence of Na^+ ions.

ISEs based on custom synthesized ionophores and ionic additives possessed better selectivity properties provided the optimized ratio of membrane components was achieved.

Some of the compositions showed responses that may be used with success in regular analytical applications, even commercial electrodes. Some of those compositions are: for Zn^{2+} , Zn-S4*-2A* (TBTDS, KTClPhB, NPhOE and PVC), Zn-S4*-3A* (TBTDS, NPhOE, NaFMPhB and PVC) and Zn-S5-1C (KTt^{t}-Bu, $Ca(TOBS)_2$, TEHP and PVC) and for Al^{3+} , Al-M-1C (morin, $Ca(TOBS)_2$, TEHP and PVC) and Al-S7*-1D (ionophore Al-S7, $Ca(TOBS)_2$, BBPA and PVC).

Following the most promising PVC composition determined in the screening tests, liquid membrane cocktails for Zn^{2+} and Al^{3+} ISMEs were prepared and tested. The most efficient Zn^{2+}-SME was made with TBTDS, NaFMPhB, NPhOE and ETH 500 (a highly lipophilic ion-exchanger added to stabilize microelectrode response by lowering cocktail resistance). Work done with microelectrodes sensitive to Al^{3+} had less success, due to several limitations caused by the nature of Al^{3+} ions and the cocktail properties.

The cocktail solvent, which was the same as PVC plasticizer to maintain selectivity, was found to be critical for ISMEs performance. Not all PVC plasticizers were suitable for micropipette cocktails due to their high influence on the membrane resistance (increasing it) and consequently on the ISME possibility to sense the signal. When moving from macro to micro level the membrane resistance should be a key parameter to evaluate.

Two Cu^{2+} selective microsensors, a glass micropipette with TBTDS based cocktail, and a Cu{CuSe} microsensor, were successfully produced and characterized. The Cu{CuSe} microsensor possessed better selectivity against Na^{+} ions and was considered a good alternative for SIET due to its higher mechanical robustness. Microelectrodes sensitive to pH and to Mg^{2+} were also fabricated from glass micropipettes. They were based on commercially available cocktails and were employed in SIET without modifications.

The new microelectrodes were used for investigating the reactivity on defects and corrosion inhibition on coated aluminium and magnesium alloys in NaCl solution, detecting micro-distribution of chemical species in solution close to the corroding surface of Zn, Cu and a Zn-Fe galvanic couple. *In situ* mapping of local activity of Mg^{2+}, Zn^{2+} and Cu^{2+} ions was performed by potentiometric microsensors in corroding systems for the first time.

Limitations and difficulties exist for the use of these techniques in corrosion research due to the inherent reactivity of corroding metals, with the formation of corrosion products and sharp changes of pH, O_2 and ionic strength along the samples surface, which are responsible for chemical speciation of analyte ions. In spite of these factors, that influence the measurements, still it's possible to count with micro-

potentiometry for studies in corrosion provided the microelectrodes responses and characteristics are well known and the measurements performed with care and discernment.

The results presented here demonstrate that the SVET/SIET mapping could give useful information for the quantification of electrochemical processes at the micro-level. These techniques can be used for *in situ* detection, observation and monitoring of corrosion and inhibition processes. The data are of prime importance for the modeling and simulation of corrosion mechanisms, selection of new corrosion inhibitors and development of ‘‘smart” coatings that suppress the corrosion processes.

Future work

At the end of this Thesis four lines of research are identified as the most promising for continuation of the work:

1) Microelectrodes with lower resistance

The development of membrane cocktails for microelectrodes was first implemented with macroelectrodes because these are easier to handle and the reproducibility is better. The best compositions were then modified for use in microelectrodes. The main modification was the replacement of the PVC by a viscous solvent, typically the plasticizer used in the macroelectrode composition. Despite this modification the microelectrodes resistance was still too high. This factor alone seems to be the greatest obstacle to pass from the macroelectrode compositions to microelectrodes. Future work should focus on strategies to decrease the resistance in order to obtain at the micro level similar response as that found with macroelectrodes. The first option would be, as an example, to test solvents with high dielectric constant.

2) Further testing with the macroelectrodes

Some macroelectrode compositions revealed good response for Zn^{2+} and Al^{3+}. Since the focus of this Thesis was microelectrodes, the work did not explore further the response of the macroelectrodes. The full characterisation should be carried out. If the properties are indeed very good, the possible commercialisation of membrane compositions can be attempted. This is particularly important for Al^{3+} since no such ISE exists in the market.

3) Search for ISE and ISME for other chemical species

Apart from the metal cations, other chemical species are of interest to corrosion research, namely anions in solution (e.g. from the electrolyte) and organic species (e.g. inhibitors). ISME for such species should be developed.

4) Overcome the fragility of glass microelectrodes

The microelectrodes targeted in this work were based on liquid-membranes in glass body. One of the main drawbacks is the mechanical fragility resulting in breakage upon contact with the metal surface or some corrosion products. If the potentiometric response is good and the main drawback is mechanical robustness, it is worth to try to overcome the problem with polymeric transparent micropipettes and/or flexible tips.

References

[1] D.A. Jones, Principles and Prevention of Corrosion, 2nd ed., Prentice Hall, New Jersey, 1996.

[2] L.L. Shreir, R.A. Jarman, G.T. Burstein, eds., Corrosion V.1- Metal/Environment Reactions, 3d ed., Butterworth-Heinemann, Oxford, 1994.

[3] P.R. Roberge, Handbook of Corrosion Engineering, McGraw-Hill, New York, 1999.

[4] M.G. Fontana, Corrosion Engineering, 3d ed., McGraw-Hill, New York, 1986.

[5] K.E. Heusler, D. Landolt, S. Trasatti, Electrochemical corrosion nomenclature, Pure Appl. Chem. 61 (1989) 19–22.

[6] L.L. Shreir, R.A. Jarman, G.T. Burstein, eds., Corrosion V.2 - Corrosion Control, 3d ed., Butterworth-Heinemann, Oxford, 2000.

[7] R.W. Revie, H.H. Uhlig, eds., Corrosion and Corrosion Control: An Introduction to Corrosion Science and Engineering, 4th ed., John Wiley & Sons, New Jersey, 2008.

[8] P.A. Schweitzer, Fundamentals of Corrosion: Mechanisms, Causes, and Preventative Methods, Taylor & Francis Group, Boca Raton, 2010.

[9] H.P. Hack, Corrosion Testing Made Easy: Galvanic Corrosion Test Methods v.2, NACE International, Houston, TX, 1993.

[10] D. Landolt, Corrosion and Surface Chemistry of Metals, EPFEL Press, Lausanne, 2007.

[11] G. Frankel, N. Sridhar, Understanding localized corrosion, Mater. Today 11 (2008) 38–44.

[12] Z. Szklarska-Smialowska, Pitting Corrosion of Metals, National Association of Corrosion Engineers, Houston, TX, 1986.

[13] R.G. Kelly, Small scale corrosion, Electrochem. Soc. Interface 6 (1997) 18–23.

[14] H.P. Hack, Evaluation Galvanic Corrosion, in: Corrosion: Fundamentals, Testing, and Protection, Vol 13A, ASM Handbook, ASM International, Materials Park, OH, 2003: pp. 562–567.

[15] R.G. Buchheit, Local dissolution phenomena associated with S phase (Al2CuMg) particles in aluminum alloy 2024-T3, J. Electrochem. Soc. 144 (1997) 2621.

[16] J.O. Park, Influence of Fe-rich intermetallic inclusions on pit initiation on aluminum alloys in aerated NaCl, J. Electrochem. Soc. 146 (1999) 517.

[17] N. Birbilis, R.G. Buchheit, Electrochemical characteristics of intermetallic phases in aluminum alloys, J. Electrochem. Soc. 152 (2005) B140.

[18] W. Zhang, G.. Frankel, Transitions between pitting and intergranular corrosion in AA2024, Electrochim. Acta 48 (2003) 1193–1210.

[19] D. Battocchi, J. He, G.P. Bierwagen, D.E. Tallman, Emulation and study of the corrosion behavior of Al alloy 2024-T3 using a wire beam electrode (WBE) in conjunction with scanning vibrating electrode technique (SVET), Corros. Sci. 47 (2005) 1165–1176.

[20] G. Song, A. Atrens, Corrosion mechanisms of magnesium alloys, Adv. Eng. Mater. 1 (1999) 11–33.

[21] A.E. Coy, F. Viejo, P. Skeldon, G.E. Thompson, Susceptibility of rare-earth-magnesium alloys to micro-galvanic corrosion, Corros. Sci. 52 (2010) 3896–3906.

[22] R.G. Buchheit, N. Birbilis, Electrochemical microscopy : An approach for understanding localized corrosion in microstructurally complex metallic alloys, Electrochim. Acta 55 (2010) 7853–7859.

[23] K.B. Deshpande, Numerical modeling of micro-galvanic corrosion, Electrochim. Acta 56 (2011) 1737–1745.

[24] C.A. Nunez-Lopez, H. Habazaki, P. Skeldon, G.E. Thompson, H. Karimzadeh, P. Lyon, T.E. Wilks, An investigation of microgalvanic corrosion using a model magnesium-silicon carbide metal matrix composite, Corros. Sci. 38 (1996) 1721–1729.

[25] H. Kalb, A. Rzany, B. Hensel, Impact of microgalvanic corrosion on the degradation morphology of WE43 and pure magnesium under exposure to simulated body fluid, Corros. Sci. 57 (2012) 122–130.

[26] N.D. Tomashov, Development of the electrochemical theory of metallic corrosion, Corrosion 20 (1964) 7t–14t.

[27] J.R. Galvele, Transport processes and the mechanism of pitting of metals, J. Electrochem. Soc. Electrochem. Sci. Technol. 123 (1976) 464–474.

[28] G. Wranglén, An Introduction to Corrosion and Protection of Metals, Chapman and Hall, London, 1985.

[29] G.S. Frankel, Pitting corrosion of metals, J. Electrochem. Soc. 145 (1998) 2186–2198.

[30] R.G. Kelly, Crevice Corrosion, in: Corrosion: Fundamentals, Testing, and Protection, Vol 13A, ASM Handbook, ASM International, Materials Park, OH, 2003: pp. 242–247.

[31] V.S. Sastri, E. Ghali, M. Elboujdaini, Corrosion Prevention and Protection. Practical Solutions, John Wiley & Sons, West Sussex, 2007.

[32] J.R. Davis, ed., Surface Engineering for Corrosion and Wear Resistance, ASM International, Materials Park, OH, 2001.

[33] A. Forsgren, Corrosion Control Through Organic Coatings, CRC, Taylor&Francis Group, LLC, Boca Raton, 2006.

[34] D. Wang, G.P. Bierwagen, Sol–gel coatings on metals for corrosion protection, Prog. Org. Coat. 64 (2009) 327–338.

[35] M.L. Zheludkevich, I.M. Salvado, M.G.S. Ferreira, Sol–gel coatings for corrosion protection of metals, J. Mater. Chem. 15 (2005) 5099.

[36] A.F. Galio, S.V. Lamaka, M.L. Zheludkevich, L.F.P. Dick, I.L. Müller, M.G.S. Ferreira, Inhibitor-doped sol–gel coatings for corrosion protection of magnesium alloy AZ31, Surf. Coatings Technol. 204 (2010) 1479–1486.

[37] K.A. Yasakau, M.L. Zheludkevich, O.V. Karavai, M.G.S. Ferreira, Influence of inhibitor addition on the corrosion protection performance of sol–gel coatings on AA2024, Prog. Org. Coat. 63 (2008) 352–361.

[38] S.V. Lamaka, M.L. Zheludkevich, K.A. Yasakau, R. Serra, S.K. Poznyak, M.G.S. Ferreira, Nanoporous titania interlayer as reservoir of corrosion inhibitors for coatings with self-healing ability, Prog. Org. Coat. 58 (2007) 127–135.

[39] M. Zheludkevich, Self-Healing Anticorrosion Coatings, in: S.K. Ghosh (Ed.), Self-Healing Materials: Fundamentals, Design Strategies, and Applications, Wiley-VCH Verlag GmbH & Co. KGaA, Weinheim, Germany, 2008: pp. 101–139.

[40] L. Fedrizzi, W. Fürbeth, F. Montemor, eds., Self-Healing Properties of New Surface Treatments (EFC 58), Maney Publishing, 2011.

[41] M.L. Zheludkevich, J. Tedim, M.G.S. Ferreira, “Smart” coatings for active corrosion protection based on multi-functional micro and nanocontainers, Electrochim. Acta 82 (2012) 314–323.

[42] C.G. Munger, L.D. Vincent, Corrosion Prevention by Protective Coatings, 2nd ed., National Association of Corrosion Engineers, Houston, TX, 1999.

[43] G. Grundmeier, W. Schmidt, M. Stratmann, Corrosion protection by organic coatings: electrochemical mechanism and novel methods of investigation, Electrochim. Acta 45 (2000) 2515–2533.

[44] O. Schneider, R.G. Kelly, Localized coating failure of epoxy-coated aluminium alloy 2024-T3 in 0.5M NaCl solutions: Correlation between coating degradation, blister formation and local chemistry within blisters, Corros. Sci. 49 (2007) 594–619.

[45] P.A. Schweitzer, P.E, Paint and Coatings: Applications and Corrosion Resistance, CRC Press, Boca Raton, FL, 2006.

[46] C. Hahin, R.G. Buchheit, Filiform Corrosion, in: Corrosion: Fundamentals, Testing, and Protection, Vol 13A, ASM Handbook, ASM International, Materials Park, OH, 2003: pp. 248–256.

[47] T. Nguyen, B. Hubbard, J.M. Pommersheim, Unified model for the degradation of organic coatings on steel in a neutral electrolyte, J. Coat. Technol. 68 (1996) 45–56.

[48] A. Bautista, Filiform corrosion in polymer-coated metals, Prog. Org. Coat. 28 (1996) 49–58.

[49] G.S. Frankel, Pitting Corrosion, in: Corrosion: Fundamentals, Testing, and Protection, Vol 13A, ASM Handbook, ASM International, Materials Park, OH, 2003: pp. 236–241.

[50] R.X. Li, M.G.S. Ferreira, Chemical and electrochemical dissolution mechanism for the initiation of localized corrosion, Mater. Sci. Forum 192–194. E (1995) 237–252.

[51] M. Forslund, C. Leygraf, P.M. Claesson, C. Lin, J. Pan, Micro-galvanic corrosion effects on patterned copper-zinc samples during exposure in humidified air containing formic acid, J. Electrochem. Soc. 160 (2013) C423–C431.

[52] N. Sato, 1989 Whitney Award Lecture: Toward a more fundamental understanding of corrosion processes, Corrosion 45 (1989) 354–368.

[53] H.S. Isaacs, G. Adzic, C.S. Jeffcoate, 2000 W.R. Whitney Award Lecture: Visualizing corrosion, Corrosion 56 (2000) 971–978.

[54] A.T. Kuhn, M. Hayes, Techniques in electrochemistry, corrosion, and metal finishing: a handbook, John Wiley & Sons, Chichester, 1987.

[55] A. Bard, L. Faulkner, Electrochemical Methods: Fundamentals and Applications, 2d ed., J. Wiley & Sons Inc., New York, 2001.

[56] R. Kelly, J. Scully, D. Shoesmith, R. Buchheit, Electrochemical Techniques in Corrosion Science and Engineering, CRC Press, 2002.

[57] P. Marcus, F. Mansfeld, eds., Analytical Methods in Corrosion Science and Engineering, Taylor & Francis Group, Boca Raton, FL, 2006.

[58] G. Grundmeier, K.-M. Juttner, M. Shtratmann, Novel electrochemical techniques in corrosion research, in: M. Schutze (Ed.), Corrosion and Environmental Degradation. V.1., Wiley-VCH, Weinheim, 2000: pp. 285–381.

[59] R. Oltra, V. Maurice, R.Akid, P. Marcus, eds., European Federation of Corrosion Publications, № 45. Local probe techniques for corrosion research, Woodhead Publishing Limited, Cambridge, 2007.

[60] Y. Tan, An overview of techniques for characterizing inhomogeneities in organic surface films and underfilm localized corrosion, Prog. Org. Coat. 76 (2013) 791–803.

[61] S. Rossi, M. Fedel, F. Deflorian, M.C. Vadillo, Localized electrochemical techniques: Theory and practical examples in corrosion studies, Comptes Rendus Chim. 11 (2008) 984–994.

[62] D.E. Tallman, M.B. Jensen, Application of Scanning Electrochemical Microscopy in Corrosion Research, in: A.J. Bard, M. V Mirkin (Eds.), Scanning Electrochemical Microscopy, 2d Ed., CRC, Taylor & Francis Group, Boca Raton, Florida, 2012: pp. 451–488.

[63] J.P.H. Sukamto, W.H. Smyrl, N. Casillas, M. Al-Odan, P. James, W. Jin, L. Douglas, Microvisualization of corrosion, Mater. Sci. Eng. A 198 (1995) 177–196.

[64] T. Suter, H. Bohni, The Microcell Technique, in: P. Marcus, F. Mansfeld (Eds.), Analytical Methods in Corrosion Science and Engineering, Taylor & Francis Group, Boca Raton, Florida, 2006: pp. 649–696.

[65] G.K. Binnig, C.F. Quate, Atomic Force Microscope, Phys. Rev. Lett. 56 (1986) 930–933.

[66] G.K. Binnig, Atomic force microscope and method for imaging surfaces with atomic resolution, United States Patent 4724318, 1988.

[67] V. Maurice, P. Marcus, Scanning Tunneling Microscopy and Atomic Force Microscopy, in: F. Mansfeld, P. Marcus (Eds.), Analytical Methods in Corrosion Science and Engineering, CRC, Taylor & Francis Group, Boca Raton, Florida, 2006: pp. 133–168.

[68] H.S. Isaacs, M.W. Kending, Determination of surface inhomogeneities using a Scanning Probe Impedance Technique, Corrosion 36 (1980) 269–274.

[69] R.S. Lillard, P.J. Moran, H.S. Isaacs, A novel method for generating quantitative local Electrochemical Impedance Spectroscopy, J. Electrochem. Soc. 139 (1992) 1007–1012.

[70] V.M. Huang, S.-L. Wu, M.E. Orazem, N. Pébère, B. Tribollet, V. Vivier, Local electrochemical

impedance spectroscopy: A review and some recent developments, Electrochim. Acta 56 (2011) 8048–8057.

[71] H. Bohni, T. Suter, A. Schreyer, Micro- and nanotechniques to study localized corrosion, Electrochim. Acta 40 (1995) 1361–1368.

[72] T. Suter, H. Böhni, Microelectrodes for corrosion studies in microsystems, Electrochim. Acta 47 (2001) 191–199.

[73] A.J. Bard, M. V Mirkin, eds., Scanning Electrochemical Microscopy, 2nd ed., CRC Press, Taylor & Francis Group, Boca Raton, Florida, 2012.

[74] A.J. Bard, F.F. Fan, J. Kwak, O. Lev, Scanning Electrochemical Microscopy. Introduction and principles, Anal. Chem. 61 (1989) 132–138.

[75] J. Kwak, A.J. Bard, Scanning Electrochemical Microscopy. Theory of the feedback mode, Anal. Chem. 61 (1989) 1221–1227.

[76] D. Ammann, Ion-Selective Microelectrodes: Principles, Design and Application, Springer-Verlag, Berlin, 1986.

[77] G. Denuault, G. Nagy, K. Toth, Potentiometric Probes, in: A.J. Bard, M. V. Mirkin (Eds.), Scanning Electrochemical Microscopy, 2d Ed., 2nd ed., CRC Press, Taylor & Francis Group, Boca Raton, Florida, 2012: pp. 275–316.

[78] M. Stratmann, The investigation of the corrosion properties of metals, covered with adsorbed electrolyte layers - a new technique, Corros. Sci. 27 (1987) 869–827.

[79] S. Yee, Application of a Kelvin Microprobe to the corrosion of metals in humid atmospheres, J. Electrochem. Soc. 138 (1991) 55–61.

[80] M. Rohwerder, F. Turcu, High-resolution Kelvin probe microscopy in corrosion science: Scanning Kelvin probe force microscopy (SKPFM) versus classical scanning Kelvin probe (SKP), Electrochim. Acta 53 (2007) 290–299.

[81] M. Nonnenmacher, M.P. O'Boyle, H.K. Wickramasinghe, Kelvin probe force microscopy, Appl. Phys. Lett. 58 (1991) 2921–2923.

[82] H.S. Isaacs, B. Vyas, Scanning Reference Electrode Techniques in localized corrosion, in: F. Mansfield, U. Bertocci (Eds.), Electrochemical Corrosion Testing. ASTM STP 727, American Society for Testing and Materials, Philadelphia, Pensilvania, USA, 1981: pp. 3–33.

[83] H.R. Copson, Distribution of galvanic corrosion, Trans. Electrochem. Soc. 84 (1943) 71–81.

[84] R.S. Lillard, Scanning electrode techniques for investigating nearsurface solution current densities, in: P. Marcus, F. Mansfeld (Eds.), Analytical Methods in Corrosion Science and Engineering, CRC, Taylor & Francis Group, Boca Raton, FL, 2006: pp. 571–604.

[85] H.S. Isaacs, Y. Ishikawa, Applications of the Vibrating Probe to localized current measurements, in: R. Baboian (Ed.), Electrochemical Techniques for Corrosion Engineering, NACE, Houston, TX, 1986.

[86] Y.-J. Tan, The effects of inhomogeneity in organic coatings on electrochemical measurements using a wire beam electrode. Part I., Prog. Org. Coat. 19 (1991) 89–94.

[87] Y.-J. Tan, S. Yu, The effects of inhomogeneity in organic coatings on electrochemical measurements using a wire beam electrode. Part II., Prog. Org. Coat. 19 (1991) 257–263.

[88] Y.-J. Tan, Wire beam electrode: a new tool for studying localised corrosion and other

heterogeneous electrochemical processes, Corros. Sci. 41 (1998) 229–247.

[89] G. Nagy, L. Nagy, Electrochemical sensors developed for gathering microscale chemical information, Anal. Lett. 40 (2007) 3–38.

[90] M.I. Montenegro, A. Queirós, J.L. Daschbach, eds., Microelectrodes: Theory and Applications. NATO ASI Series, Series E: Applied Sciences - Vol.197, Kluwer Academic Press, Dordrecht, The Netherlands, 1991.

[91] P.J.S. Smith, R.H. Sanger, M.A. Messerli, Principles, Development and Applications of Self-Referencing Electrochemical Microelectrodes to the Determination of Fluxes at Cell Membranes, in: A.C. Michael, L.M. Borland (Eds.), Electrochemical Methods for Neuroscience, CRC Press, Boca Raton, Florida, 2007.

[92] C.E. Reimers, Applications of microelectrodes to problems in chemical oceanography., Chem. Rev. 107 (2007) 590–600.

[93] J.L. Luo, Y.C. Lu, M.B. Ives, Microelectrodes for the study of localized corrosion, J. Electroanal. Chem. 326 (1992) 51–68.

[94] Y.C. Lu, J.L. Luo, M.B. Ives, The influence of chlorination of saline environments on localized corrosion of stainless steel, ISIJ Int. 31 (1991) 210–215.

[95] E. Tada, K. Sugawara, H. Kaneko, Distribution of pH during galvanic corrosion of a Zn/steel couple, Electrochim. Acta 49 (2004) 1019–1026.

[96] A.C. Bastos, O.V. Karavai, M.L. Zheludkevich, K.A. Yasakau, M.G.S. Ferreira, Localised measurements of pH and dissolved oxygen as complements to SVET in the investigation of corrosion at defects in coated aluminum alloy, Electroanalysis 22 (2010) 2009–2016.

[97] A.C. Bastos, O.V. Karavai, S.V. Lamaka, M.L. Zheludkevich, M.G.S. Ferreira, Micro-sensores potenciométricos e amperométricos para o estudo da corrosão, Corrosão E Protecção Mater. 28 (2009) 1–6.

[98] E. Klusmann, J.W. Schultze, pH-microscopy - theoretical and experimental investigations, Electrochim. Acta 42 (1997) 3123–3134.

[99] C.-J. Lin, R.-G. Du, T. Nguyen, In-situ imaging of chloride ions at the metal/solution interface by scanning combination microelectrodes, Corrosion 56 (2000) 41–47.

[100] B.R. Horrocks, M. V. Mirkin, D.T. Pierce, A.J. Bard, G. Nagy, K. Toth, Scanning electrochemical microscopy. 19. Ion-selective potentiometric microscopy, Anal. Chem. 65 (1993) 1213–1224.

[101] F.J. Maile, T. Schauer, C.D. Eisenbach, Evaluation of corrosion and protection of coated metals with local ion concentration technique (LICT), Prog. Org. Coat. 38 (2000) 111–116.

[102] J.O. Park, C.-H. Paik, R.C. Alkire, Scanning microsensors for measurement of local pH distributions at the microscale, J. Electrochem. Soc. 143 (1996) L174–L176.

[103] K. Ogle, V. Baudu, L. Garrigues, X. Philippe, Localized electrochemical methods applied to cut edge corrosion, J. Electrochem. Soc. 147 (2000) 3654–3660.

[104] S. Lamaka, R.M. Souto, M.G.S. Ferreira, In-situ visualization of local corrosion by Scanning Ion-selective Electrode Technique (SIET), in: A. Mendez-Vilas, J. Diaz (Eds.), Microscopy: Scince, Technology Application and Education. Vol.3, Formatex, Badajoz, 2010: pp. 2162–2173.

[105] H. Ding, L.H. Hihara, Localized corrosion currents and pH profile over B4C, SiC, and Al2O3

reinforced 6092 aluminum composites, J. Electrochem. Soc. 152 (2005) B161-167.

[106] J.G. Kunkel, S. Cordeiro, Y.J. Xu, A. Shipley, J.A. Feijó, Use of Non-Invasive Ion-Selective Microelectrode Techniques for the Study of Plant Development, in: A. Volkov (Ed.), Plant Electrophysiology. Theory and Methods., Springer-Verlag, Berlin Heidelberg New York, 2006: pp. 109–137.

[107] M. Küpper, J.W. Schultze, SLCP—The scanning diffusion limited current probe: A new method for spatially resolved analysis, Electrochim. Acta 42 (1997) 3085–3094.

[108] E. Tada, S. Satoh, H. Kaneko, The spatial distribution of Zn2+ during galvanic corrosion of a Zn/steel couple, Electrochim. Acta 49 (2004) 2279–2285.

[109] A.C. Bastos, A.M. Simões, S. González, Y. González-García, R.M. Souto, Imaging concentration profiles of redox-active species in open-circuit corrosion processes with the scanning electrochemical microscope, Electrochem. Commun. 6 (2004) 1212–1215.

[110] M. Rohwerder, E. Hornung, M. Stratmann, Microscopic aspects of electrochemical delamination: an SKPFM study, Electrochim. Acta 48 (2003) 1235–1243.

[111] E. Klusmann, J.W. Schultze, pH-Microscopy: technical application in phosphating solutions, Electrochim. Acta 48 (2003) 3325–3332.

[112] D.O. Wipf, F. Ge, T.W. Spaine, J.E. Baur, Microscopic measurement of pH with iridium oxide microelectrodes, Anal. Chem. 72 (2000) 4921–4927.

[113] S. V. Lamaka, M.L. Zheludkevich, K.A. Yasakau, M.F. Montemor, P. Cecílio, M.G.S. Ferreira, TiOx self-assembled networks prepared by templating approach as nanostructured reservoirs for self-healing anticorrosion pre-treatments, Electrochem. Commun. 8 (2006) 421–428.

[114] I.M. Zin, S.B. Lyon, A. Hussain, Under-film corrosion of epoxy-coated galvanised steel: An EIS and SVET study of the effect of inhibition at defects, Prog. Org. Coat. 52 (2005) 126–135.

[115] D.G. Shchukin, M. Zheludkevich, K. Yasakau, S. Lamaka, M.G.S. Ferreira, H. Möhwald, Layer-by-Layer assembled nanocontainers for self-healing corrosion protection, Adv. Mater. 18 (2006) 1672–1678.

[116] G.P. Bierwagen, D. Battocchi, A.M. Simões, A. Stamness, D. Tallman, The use of multiple electrochemical techniques to characterize Mg-rich primers for Al alloys, Prog. Org. Coat. 59 (2007) 172–178.

[117] M.L. Zheludkevich, D.G. Shchukin, K.A. Yasakau, H. Möhwald, M.G.S. Ferreira, Anticorrosion coatings with self-healing effect based on nanocontainers impregnated with corrosion inhibitor, Chem. Mater. 19 (2007) 402–411.

[118] I.A. Newman, Ion transport in roots: measurement of fluxes using ion-selective microelectrodes to characterize transporter function, Plant, Cell Environ. 24 (2001) 1–14.

[119] M. Marenzana, A.M. Shipley, P. Squitiero, J.G. Kunkel, A. Rubinacci, Bone as an ion exchange organ: evidence for instantaneous cell-dependent calcium efflux from bone not due to resorption, Bone 37 (2005) 545–554.

[120] L. Shabala, T. Ros, I. Newman, T. McMeekin, S. Shabala, Measurements of net fluxes and extracellular changes of H+, Ca2+, K+, and NH4+ in Escherichia coli using ion-selective microelectrodes, J. Microbiol. Methods 46 (2001) 119–129.

[121] R.S. Tornhill, U.R. Evans, The electrochemistry of the rusting process along a scrtach-line on iron, J. Chem. Soc. (1938) 614–621.

[122] R.S. Tornhill, U.R. Evans, Th electrochemistry of the corrosion of partly immersed zinc, J. Chem. Soc. (1938) 2109–2114.

[123] U.R. Evans, The corrosion and oxidation of metals: scientific principles and practical applications, Edward Arnold Publishers, Ltd., London, 1960.

[124] H.S. Isaacs, G. Kissel, Surface preparation and pit propagation in stainless steels, J. Electrochem. Soc. 119 (1972) 1628–1632.

[125] G.V. Akimov, A.I. Golubev, Issledovanie protsessov korozii na modeli lokalnogo elementa I (in russian), Zhurnal Fiz. Khimii 20 (1946) 303–308.

[126] A.I. Golubev, G.V. Akimov, Issledovanie protsessov korozii na modeli lokalnogo elementa II (in russian), Zhurnal Fiz. Khimii 20 (1946) 309–314.

[127] I.L. Rosenfeld, I.S. Danilov, Electrochemical aspects of pitting corrosion, Corros. Sci. 7 (1967) 129–142.

[128] C.D.S. Tuck, The use of micro-electrodes in the study of localised corrosion in aluminium alloys, Corros. Sci. 23 (1983) 379–389.

[129] K.R. Trethewey, D.A. Sargeant, D.J. Marsh, A.A. Tamimi, Applications of the scanning reference electrode technique to localized corrosion, Corros. Sci. 35 (1993) 127–134.

[130] J. V. Standish, H.J. Leidheiser, The electrical properties of organic coatings on a local scale-relationship to corrosion, Corrosion 36 (1980) 390–395.

[131] L.J. Gainer, G.R. Wallwork, An apparatus for the examination of localized corrosion behavior, Corrosion 35 (1979) 61–67.

[132] R.J. O'Halloran, L.F.G. Williams, C.P. Lloyd, A microprocessor based isopotential contouring system for monitoring surface corrosion, Corrosion 40 (1984) 344–349.

[133] R.A. Cottis, D. Holt, A semi-automatic device for the rapid measurement of pit-depths and positions, Corros. Sci. 27 (1987) 103–106.

[134] D.A. Sargeant, J.G.C. Hainse, S. Bates, Microcomputer controlled scanning reference electrode technique apparatus developed to study pitting corrosion of as turbine disc materials, Mater. Sci. Technol. 5 (1989) 487–491.

[135] N. Hsu, J.D. Garber, R. Brunel, R.D. Braun, A scanning reference electrode for use during corrosive measurements, Corrosion 43 (1987) 606–610.

[136] A.C. Bastos, S.A.S. Dias, T.C. Diamantino, M.G.S. Ferreira, Uma introdução à técnica SVET, Corrosão E Protecção Mater. 32 (2013) 50–67.

[137] O. Blüh, B.I.H. Scott, Vibrating probe electrometer for the measurement of bioelectric potentials, Rev. Sci. Instrum. 21 (1950) 867–868.

[138] P.W. Davies, Membrane potential and resistance of perfused skeletal muscle fibers with control of membrane current, Fed. Proc. 25 (1966) 332.

[139] L.F. Jaffe, R. Nuccitelli, An ultrasensitive vibrating probe for measuring steady extracellular currents, J. Cell Biol. 63 (1974) 614–628.

[140] J. Ferrier, W.J. Lucas, Ion transport and the vibrating probe, Biophys. J. 49 (1986) 803–807.

[141] C. Scheffey, Electric Fields and the Vibrating Probe for the Uninitiated, in: R. Nuccitelli

(Ed.), Ionic Currents in Development, Alan R. Liss Inc., New York, USA, 1986: pp. xxv–xxxvii.

[142] Applicable Electronics Inc., Forestdale, MA, USA, www.applicableelectronics.com, (1999).

[143] C. Scheffey, Two approaches to construction of vibrating probes for electrical current measurement in solution, Rev. Sci. Instrum. 59 (1988) 787–792.

[144] Sciencewares, East Falmouth, MA, USA, www.sciencewares.com, (1991).

[145] J.A. Freeman, P.B. Manis, P.C. Samson, J.P. Wikswo Jr., Microprocessor controlled two- and three-dimensional vibrating probes with video graphics: biological and electro-mechanical applications, in: R. Nuccitelli (Ed.), Ionic Currents in Development, A.R. Liss Inc., New York, USA, 1986: p. 21.

[146] R.G. Kasper, C.R. Crowe, Comparison of localized ionic currents as measured from 1-D and 3-D vibrating probes with finite-element predictions for an iron-copper galvanic couple) in Galvanic corrosion (H.P. Hack, ed.), , p. 118 (1988)., in: H.P. Hack (Ed.), Galvanic Corrosion. ASTM STP 978, ASTM International, Philadelphia, Pensilvania, USA, 1988: p. 118.

[147] D.A. Worsley, A. Belghazi, S.M. Powell, Study of corrosion mechanism occurring at cut edges of organically coated galvanised steels, Ironmak. Steelmak. 26 (1999) 387–392.

[148] Hokuto Denko Corp. www.hokuto-denko.co.jp/epages/top/index.html, (2014).

[149] Uniscan Instruments Ltd., http://www.uniscan.com/electrochemistry-instruments/scanning-vibrating-electrode/, (1997).

[150] Ametek Inc., Electrochemical Scanning l Princeton Applied Research http://www.princetonappliedresearch.com/Our-Products/Electrochemical-Scanning-System/index.aspx, (2010).

[151] Bio-Logic, Science Instruments http://www.bio-logic.info/scanning-systems-scan-lab/instruments/, (2014).

[152] H.S. Isaacs, The use of the Scanning Vibrating Electrode Technique for detecting defects in ion vapor-deposited aluminum on steel, Corrosion 43 (1987) 594–596.

[153] H.S. Isaacs, Limitations of in-situ current density mapping for vibrating electrode close to metal surfaces, Corrosion 46 (1990) 677–679.

[154] H.S. Isaacs, The effect of height on the current distribution measured with a vibrating electrode probe, J. Electrochem. Soc. 138 (1991) 722–728.

[155] C. Scheffey, Pitfalls of the Vibrating probe Technique, and What to Do About Them, in: R. Nuccitelli (Ed.), Ionic Currents in Development, A.R. Liss Inc., New York, USA, 1986: pp. 3–12.

[156] R. Akid, M. Garma, Scanning vibrating reference electrode technique: a calibration study to evaluate the optimum operating parameters for maximum signal detection of point source activity, Electrochim. Acta 49 (2004) 2871–2879.

[157] B.P. Wilson, J.R. Searle, K. Yliniemi, D. a. Worsley, H.N. McMurray, Effect of probe tip inclination on the response of the Scanning Vibrating Electrode Technique to an idealised pit-like feature, Electrochim. Acta 66 (2012) 52–60.

[158] H. Kaesche, Galvanic Corrosion Cells, in: Corrosion of Metals: Physicochemical Principles and Current Problems, Springer, Berlin Heidelberg New York, 2003: p. 594.

[159] M. Anderson, E. Bowdan, J.G. Kunkel, Comparison of defolliculated oocytes and intact

follicles of the cockroach using the vibrating probe to record steady currents, Dev. Biol. 162 (1994) 111–122.

[160] P. Somieski, W. Nagel, Localizing transepithelial conductive pathways using a vibrating voltage probe, J. Exp. Biol. 201 (1998) 2489–95.

[161] J.H. Lee, T. Chiba, D.C. Marcus, P2X2 receptor mediates stimulation of parasensory cation absorption by cochlear outer sulcus cells and vestibular transitional cells., J. Neurosci. 21 (2001) 9168–74.

[162] H.S. Isaacs, The localized breakdown and repair of passive surfaces during pitting, Corros. Sci. 29 (1989) 313–323.

[163] H.S. Isaacs, The measurement of the galvanic corrosion of soldered copper using the scanning vibrating electrode technique, Corros. Sci. 28 (1988) 547–558.

[164] S. Kallip, A.C. Bastos, K.A. Yasakau, M.L. Zheludkevich, M.G.S. Ferreira, Synergistic corrosion inhibition on galvanically coupled metallic materials, Electrochem. Commun. 20 (2012) 101–104.

[165] A.J. Aldykiewicz Jr., H.S. Isaacs, A.J. Davenport, The investigation of cerium as a cathodic inhibitor for aluminum-copper alloys, J. Electrochem. Soc. 142 (1995) 3342–3350.

[166] A.C. Bastos, M.G. Ferreira, A.M. Simões, Corrosion inhibition by chromate and phosphate extracts for iron substrates studied by EIS and SVET, Corros. Sci. 48 (2006) 1500–1512.

[167] A.C. Bastos, M.G.S. Ferreira, A.M. Simões, Comparative electrochemical studies of zinc chromate and zinc phosphate as corrosion inhibitors for zinc, Prog. Org. Coat. 52 (2005) 339–350.

[168] S. Kallip, A.C. Bastos, M.L. Zheludkevich, M.G.S. Ferreira, A multi-electrode cell for high-throughput SVET screening of corrosion inhibitors, Corros. Sci. 52 (2010) 3146–3149.

[169] J. He, V.J. Gelling, D.E. Tallman, G.P. Bierwagen, A Scanning Vibrating Electrode study of chromated-epoxy primer on steel and aluminum, J. Electrochem. Soc. 147 (2000) 3661–3666.

[170] M.L. Zheludkevich, K.A. Yasakau, A.C. Bastos, O.V. Karavai, M.G.S. Ferreira, On the application of electrochemical impedance spectroscopy to study the self-healing properties of protective coatings, Electrochem. Commun. 9 (2007) 2622–2628.

[171] M. Taryba, S.V. Lamaka, D. Snihirova, M.G.S. Ferreira, M.F. Montemor, W.K. Wijting, S. Toews, G. Grundmeier, The combined use of scanning vibrating electrode technique and micro-potentiometry to assess the self-repair processes in defects on “smart” coatings applied to galvanized steel, Electrochim. Acta 56 (2011) 4475–4488.

[172] F. Thébault, B. Vuillemin, R. Oltra, K. Ogle, C. Allely, Investigation of self-healing mechanism on galvanized steels cut edges by coupling SVET and numerical modeling, Electrochim. Acta 53 (2008) 5226–5234.

[173] J. Kwak, A.J. Bard, Scanning electrochemical microscopy. Apparatus and two-dimensional scans of conductive and insulating substrates, Anal. Chem. 61 (1989) 1794–1799.

[174] R.C. Engstrom, M. Weber, D.J. Wunder, R. Burgess, S. Winquist, Measurements within the diffusion layer using a microelectrode probe, Anal. Chem. 58 (1986) 844–848.

[175] R.C. Engstrom, T. Meaney, R. Tople, R.M. Wightman, Spatiotemporal description of the diffusion layer with a microelectrode probe, Anal. Chem. 59 (1987) 2005–2010.

[176] R.C. Engstrom, R.M. Wightman, E.W. Kristensen, Diffusional distortion in the monitoring of dynamic events, Anal. Chem. 60 (1988) 652–656.

[177] A.J. Bard, M.V. Mirkin, eds., Scanning Electrochemical Microscopy, Marcel Dekker, Inc., Basel, Switzerland, 2001.

[178] M. Fleischmann, S. Pons, D.R. Rolinson, P.P. Schmidt, Ultramicroelectrodes, Datatech Systems, Inc., Morganton, 1986.

[179] G. Wittstock, M. Burchardt, S.E. Pust, Y. Shen, C. Zhao, Scanning electrochemical microscopy for direct imaging of reaction rates., Angew. Chem. Int. Ed. Engl. 46 (2007) 1584–1617.

[180] L. Niu, Y. Yin, W. Guo, M. Lu, R. Qin, S. Chen, Application of scanning electrochemical microscope in the study of corrosion of metals, J. Mater. Sci. 44 (2009) 4511–4521.

[181] R.M. Souto, S. V Lamaka, S. González, Uses of Scanning Electrochemical Microscopy in Corrosion Research, in: A. Mendez-Vilas, J. Diaz (Eds.), Microscopy: Scince, Technology Application and Education. Vol.3, Formatex, Badajoz, 2010: pp. 1769–1780.

[182] M.B. Jensen, D.E. Tallman, Application of Scanning Electrochemical Microscopy in Corrosion Studies, in: A.J. Bard, C.G. Zoski (Eds.), Electroanalytical Chemistry: A Series of Advances, Vol. 24, CRC Press, Boca Raton, Florida, 2012: pp. 171–286.

[183] A. Schramm, Microsensors for the study of microenvironments and processes in the intestine of invertebrates, in: H. König, A. Varma (Eds.), Soil Biology, V.6. Intestinal Microorganisms of Soil Invertebrates, Springer-Verlag, Berlin, 2006: pp. 465–473.

[184] L.C. Clark, R. Wolf, D. Granger, Z. Taylor, Continuous recording of blood oxygen tensions by polarography., J. Appl. Physiol. 6 (1953) 189–193.

[185] N.P. Revsbech, An oxygen microsensor with a guard cathode, Limnol. Oceanogr. 34 (1989) 474–478.

[186] M. Sosna, G. Denuault, R.W. Pascal, R.D. Prien, M. Mowlem, Development of a reliable microelectrode dissolved oxygen sensor, Sensors Actuators B Chem. 123 (2007) 344–351.

[187] W. Xu, W. Ma, K. Li, J. Hu, L. Shen, H. Li, L. Cao, A needle-electrochemical microsensor for in vivo measurement of the partial pressure of oxygen in acupuncture points, Sensors Actuators B Chem. 86 (2002) 174–179.

[188] Z. Lewandowski, W.C. Lee, W.G. Characklis, B. Little, Dissolved oxygen and pH microelectrode measurements at water-immersed metal surfaces, Corrosion 45 (1989) 92–98.

[189] E.L. Silva, A.C. Bastos, M.A. Neto, R.F. Silva, M.L. Zheludkevich, M.G.S. Ferreira, F.J. Oliveira, Boron doped nanocrystalline diamond microelectrodes for the detection of Zn2+ and dissolved O2, Electrochim. Acta 76 (2012) 487–494.

[190] J.L. Walker, Ion Specific Liquid Ion Exchanger Microelectrodes, Anal. Chem. 43 (1971) 89A–93A.

[191] D. Ogden, ed., Microelectrode techniques: the Plymouth Workshop handbook, 2d ed., Company of Biologists Limited, Cambridge, UK, 1994.

[192] A.G. Volkov, ed., Plant Electrophysiology. Theory and Methods, Springer-Verlag, Berlin Heidelberg New York, 2006.

[193] K.T. Brown, D.G. Flaming, Advanced micropipette techniques for cell physiology, John

Wiley & Sons, Chichester, 1995.

[194] Y. Xu, T. Sun, L.-P. Yin, Application of non-invasive microsensing system to simultaneously measure both H+ and O2 fluxes around the pollen tube, J. Integr. Plant Biol. 48 (2006) 823–831.

[195] S. Tong, L. Peng, Y. Liping, X. Yue, Y. Shangguan, Non-invasive scanning ion-selective electrode technique and its applications to the research of higher plants, Prog. Nat. Sci. 17 (2007) 625–629.

[196] W.-R. Schlue, W. Kilb, D. Giinzel, Ultramicroelectrodes for membrane research, Electrochim. Acta 42 (1997) 3197–3205.

[197] P.J.S. Smith, K. Hammar, D.M. Porterfield, R.H. Sanger, J.R. Trimarchi, Self-referencing , non-invasive , ion selective electrode for single cell detection of trans-plasma membrane calcium flux, Microsc. Res. Tech. 46 (1999) 398–417.

[198] C. Wei, A.J. Bard, G. Nagy, K. Toth, Scanning Electrochemical Microscopy. 28. Ion-selective neutral carrier-based microelectrode potentiometry, Anal. Chem. 67 (1995) 1346–1356.

[199] S.V. Lamaka, G. Knörnschild, D.V. Snihirova, M.G. Taryba, M.L. Zheludkevich, M.G.S. Ferreira, Complex anticorrosion coating for ZK30 magnesium alloy, Electrochim. Acta 55 (2009) 131–141.

[200] A. Alvarez-Pampliega, M.G. Taryba, K. Van den Bergh, J. De Strycker, S.V. Lamaka, H. Terryn, Study of local Na+ and Cl− distributions during the cut-edge corrosion of aluminum rich metal-coated steel by scanning vibrating electrode and micro-potentiometric techniques, Electrochim. Acta 102 (2013) 319–327.

[201] S.V. Lamaka, M. Taryba, M.F. Montemor, H.S. Isaacs, M.G.S. Ferreira, Quasi-simultaneous measurements of ionic currents by vibrating probe and pH distribution by ion-selective microelectrode, Electrochem. Commun. 13 (2011) 20–23.

[202] M. Cremer, Uber die ursache der Über die Ursache der elektromotorischen Eigenschaften der Gewebe, zugleich ein Beitrag zur Lehre von den polyphasischen Elektrolytketten., Z. Biol. 47 (1906) 562–569.

[203] G. Eisenman, D.O. Rudin, J.U. Casby, Glass electrode for measuring sodium ion, Science 126 (1957) 831–834.

[204] M.S. Frant, J.W. Ross, Electrode for sensing fluoride ion activity in solution, Science 154 (1966) 1553–1555.

[205] A. Craggs, G.J. Moody, J.D.R. Thomas, PVC matrix membrane ion-selective electrodes. Construction and laboratory experiments, J. Chem. Educ. 51 (1974) 541–544.

[206] R. Bloch, A. Shatkay, H.A. Saroff, Fabrication and evaluation of membranes as specific electrodes for calcium ions., Biophys. J. 7 (1967) 865–77.

[207] L.A.R. Pioda, V. Stankova, W. Simon, Highly selective potassium ion responsive liquid-membrane electrode, Anal. Lett. 2 (1969) 665–674.

[208] R.A. Durst, Ion-selective electrodes - The early years, Electroanalysis 24 (2012) 15–22.

[209] E. Bakker, P. Bühlmann, E. Pretsch, Carrier-based ion-selective electrodes and bulk optodes. 1. General characteristics, Chem. Rev. 97 (1997) 3083–3132.

[210] P. Bühlmann, E. Pretsch, E. Bakker, Carrier-based ion-selective electrodes and bulk optodes. 2. Ionophores for potentiometric and optical sensors, Chem. Rev. 98 (1998)

1593–1688.

[211] E. Pretsch, The new wave of ion-selective electrodes, Trends Anal. Chem. 26 (2007) 46–51.

[212] G. Eisenman, Glass electrodes for hydrogen and other cations: principles and practice, Marcel Dekker, Inc., 1967.

[213] P. Bergveld, Development of an ion-sensitive solid-state device for neurophysiological measurements, IEEE Trans. Biomed. Eng. BME-17 (1970) 70–71.

[214] J.H. Saunders, Liquid and solid-state Cl- -sensitive microelectrodes. Characteristics and application to intracellular Cl- activity in Balanus photoreceptor, J. Gen. Physiol. 70 (1977) 507–530.

[215] G. Denuault, M.H.T. Frank, L.M. Peter, Scanning electrochemical microscopy: potentiometric probing of ion fluxes, Faraday Discuss. 94 (1992) 23–35.

[216] C. Zuliani, D. Diamond, Opportunities and challenges of using ion-selective electrodes in environmental monitoring and wearable sensors, Electrochim. Acta 84 (2012) 29–34.

[217] J. Bobacka, A. Ivaska, A. Lewenstam, Potentiometric ion sensors., Chem. Rev. 108 (2008) 329–51.

[218] E. Lindner, R.P. Buck, Microfabricated potentiometric electrodes and their in vivo applications, Anal. Chem. 72 (2000) 336A–345A.

[219] Fluka ionophores catalogue. http://www.sigmaaldrich.com/analytical-chromatography/analytical-reagents/sensoric-applications.html, (n.d.).

[220] P. Buhlmann, L.D. Chen, Ion-Selective Electrodes With Ionophore-Doped Sensing Membranes, Wiley-VCH, 2012.

[221] W.E. Morf, The principles of ion-selective electrodes and of membrane transport, Elsevier, Budapest, 1981.

[222] R. Eugster, T. Rosatzin, B. Rusterholz, B. Aebersold, U. Pedrazza, D. Rüegg, A. Schmid, U.E. Spichiger, W. Simon, Plasticizers for liquid polymeric membranes of ion-selective chemical sensors, Anal. Chim. Acta 289 (1994) 1–13.

[223] R.D. Armstrong, G. Horvai, Properties of PVC based membranes used in ion-selective electrodes, Electrochim. Acta 35 (1990) 1–7.

[224] D. Ammann, E. Pretsch, W. Simon, E. Lindner, a. Bezegh, E. Pungor, Lipophilic salts as membrane additives and their influence on the properties of macro- and micro-electrodes based on neutral carriers, Anal. Chim. Acta 171 (1985) 119–129.

[225] D. Harvey, Modern Analytical Chemistry, 1st ed., McGraw-Hill, 2000.

[226] C.A.M. Brett, A.M. Oliveira Brett, Electroanalysis (Oxford Chemistry Primers 64), Oxford University Press, Oxford, 1998.

[227] R.W. Cattrall, Chemical sensors (Oxford Chemistry Primers 52), Oxford University Press, Oxford, 1997.

[228] R.P. Buck, E. Lindner, Recommendations for nomenclature of ion-selective electrodes (IUPAC Recomendations 1994), Pure Appl. Chem. 66 (1994) 2527–2536.

[229] C. Maccà, Response time of ion-selective electrodes. Current usage versus IUPAC recommendations., Anal. Chim. Acta 512 (2004) 183–190.

[230] S. V. Lamaka, M.G. Taryba, M.L. Zheludkevich, M.G.S. Ferreira, Novel solid-contact ion-

selective microelectrodes for localized potentiometric measurements, Electroanalysis 21 (2009) 2447–2453.

[231] E. Bakker, E. Pretsch, P. Bühlmann, Selectivity of potentiometric ion sensors., Anal. Chem. 72 (2000) 1127–33.

[232] Y. Umezawa, K. Umezawa, H. Sato, Selectivity coefficients for ion-selective electrodes: Recommended methods for reporting KA,Bpot values (Technical Report), Pure Appl. Chem. 67 (1995) 507–518.

[233] J.A. Dean, Lange's Handbook of Chemistry, 15th ed., McGraw-Hill, New York, 1999.

[234] G.L. Long, J.D. Winefordner, Limit of detection. A closer look at the IUPAC definition, Anal. Chem. 55 (1983) 712A–724A.

[235] D. Ammann, F. Lanter, R. a Steiner, P. Schulthess, Y. Shijo, W. Simon, Neutral carrier based hydrogen ion selective microelectrode for extra- and intracellular studies., Anal. Chem. 53 (1981) 2267–2269.

[236] P. Schulthess, Y. Shijo, H.V. Pham, E. Pretsch, D. Ammann, W. Simon, A hydrogen ion-selective liquid-membrane electrode based on tri-n-dodecylamine as neutral carrier, Anal. Chim. Acta 131 (1981) 111–116.

[237] Fluka Chemika, Selectophore. Ionophores. Membranes. Mini-ISE, Fluka Chemie AG, Buchs, 1996.

[238] Y. Kim, Y. Lee, B. Sohn, J. Lee, C. Kim, A novel pH microsensor with a built-in reference electrode, J. Korean Phys. Soc. 43 (2003) 769–772.

[239] E.E.-D.M. El-Giar, D.O. Wipf, Microparticle-based iridium oxide ultramicroelectrodes for pH sensing and imaging, J. Electroanal. Chem. 609 (2007) 147–154.

[240] R. Oltra, B. Malki, F. Rechou, Influence of aeration on the localized trenching on aluminium alloys, Electrochim. Acta 55 (2010) 4536–4542.

[241] M. Winter, WebElements Periodic Table. Abundance in Earth's crust/periodicity, (n.d.).

[242] H.E. Friedrich, B.L. Mordike, eds., Magnesium Technology: Metallurgy, Design Data, Applications, Springer Science & Business Media, Berlin Heidelberg, 2006.

[243] R.W. Murray, J.E. Hillis, Magnesium Finishing: Chemical Treatment and Coating Practices, 1990.

[244] F. Lanter, D. Erne, D. Ammann, W. Simon, Neutral carrier based ion-selective electrode for intracellular magnesium activity studies, Anal. Chem. 52 (1980) 2400–2402.

[245] Z.M. Hu, T. Bührer, M. Müller, B. Rusterholz, M. Rouilly, W. Simon, Intracellular magnesium ion selective microelectrode based on a neutral carrier., Anal. Chem. 61 (1989) 574–576.

[246] U. Schaller, U.E. Spichiger, W. Simon, Novel magnesium ion-selective microelectrodes based on a neutral carrier, Pflugers Arch. - Eur. J. Physiol. 423 (1993) 338–342.

[247] Y. González-García, Degradation of anticorrosive polymeric coatings applied on metallic materials: Electrochemical and nanoscopic research, University of La Laguna (Tenerife, Spain), 2007.

[248] K. Tóth, G. Nagy, C. Wei, A.J. Bard, Novel application of potentiometric microelectrodes: Scanning potentiometric microscopy, Electroanalysis 7 (1995) 801–810.

[249] Á. Varga, L. Nagy, J. Izquierdo, I. Bitter, R.M. Souto, G. Nagy, Development of solid contact

micropipette Zn-ion selective electrode for corrosion studies, Anal. Lett. 44 (2011) 2876–2886.

[250] C.T. Baker, I. Trachtenberg, Ion selective electrochemical sensors - Fe+3, Cu+2, J. Electrochem. Soc. 118 (1971) 571–576.

[251] R. Jasinski, I. Trachtenberg, G. Rice, A Chalcogenide Glass Electrode Sensitive to Cupric Ions, J. Electrochem. Soc. 121 (1974) 363–370.

[252] S.P. Awasthi, N.S. Shenoy, T.P. Radhakrishnan, Copper ion-selective electrode based on a chalcogenide glass membrane, Analyst 119 (1994) 1361–1362.

[253] G. Taillades, O. Valls, A. Bratov, C. Dominguez, A. Pradel, M. Ribes, ISE and ISFET microsensors based on a sensitive chalcogenide glass for copper ion detection in solution, Sensors Actuators B Chem. 59 (1999) 123–127.

[254] E.A. Bychkov, M. Bruns, G. Pfennig, W. Hoffmann, H.J. Ache, Cu2+ -selective thin films for chemical microsensors based on sputtered copper-arsenic-selenium glass, Sensors Actuators B Chem. 24–25 (1995) 733–736.

[255] G. Papeschi, S. Mancuso, A.M. Marras, Electrochemical behaviour of a Cu/CuSe microelectrode and its application in detecting temporal and spatial localisation of copper (II) fluxes along Olea europaea roots, J. Solid State Electrochem. 4 (2000) 325–329.

[256] G. Papeschi, S. Pinzauti, P. Gratteri, M. Larini, Copper(II) ion-selective sensor with electrolytically plated chalcogenide coating, Sensors Actuators B Chem. 7 (1992) 544–548.

[257] G. Papeschi, Evidence of silver(I) adsorption processes on the electroactive surface of the silver/silver selenide electrode, Sensors Actuators B Chem. 24 (1995) 336–340.

[258] M. Kupper, J.W. Schultze, A new copper ion selective microelectrode for electrochemical applications, J. Electroanal. Chem. 427 (1997) 129–135.

[259] I.A. Marques de Oliveira, M. Pla-Roca, L. Escriche, J. Casabó, N. Zine, J. Bausells, F. Teixidor, E. Crespo, A. Errachid, J. Samitier, Novel all-solid-state copper(II) microelectrode based on a dithiomacrocycle as a neutral carrier, Electrochim. Acta 51 (2006) 5070–5074.

[260] R. Mlika, I. Dumazet, H. Ben Ouada, N. Jaffrezic-Renault, R. Lamartine, M. Gamoudi, G. Guillaud, Cu2+-ISFET type microsensors based on thermally evaporated p-tert-butylcalix[9 and 11]arene thin films, Sensors Actuators B. Chem. 62 (2000) 8–12.

[261] S. Wakida, N. Sato, K. Saito, Copper(II)-selective electrodes based on a novel charged carrier and preliminary application of field-effect transistor type checker, Sensors Actuators B Chem. 130 (2008) 187–192.

[262] V.K. Gupta, A.K. Jain, G. Maheshwari, Aluminum(III) selective potentiometric sensor based on morin in poly(vinyl chloride) matrix., Talanta 72 (2007) 1469–1473.

[263] S. Szunerits, D.R. Walt, Aluminum surface corrosion and the mechanism of inhibitors using pH and metal ion selective imaging fiber bundles, Anal. Chem. 74 (2002) 886–894.

[264] MatWeb: Material Property Data, www.matweb.com, (1996).

[265] K.A. Yasakau, Active corrosion protection of AA2024 by sol-gel coatings with corrosion inhibitors, Universidade de Aveiro, 2011.

[266] S.V. Lamaka, M.F. Montemor, A.F. Galio, M.L. Zheludkevich, C. Trindade, L.F. Dick, M.G.S. Ferreira, Novel hybrid sol–gel coatings for corrosion protection of AZ31B magnesium alloy, Electrochim. Acta 53 (2008) 4773–4783.

[267] MicroProbes Inc., USA, www.microprobes.com, (n.d.).

[268] D.A. Dudek, P.S. Fedkiw, Electrodeposition of copper from cuprous cyanide electrolyte I . Current distribution on a stationary disk, 474 (1999) 16–30.

[269] E.A. Starke, J.T. Staley, Application of modern aluminum alloys to aircraft, Prog. Aerosp. Sci. 32 (1996) 131–172.

[270] O.V. Karavai, a. C. Bastos, M.L. Zheludkevich, M.G. Taryba, S.V. Lamaka, M.G.S. Ferreira, Localized electrochemical study of corrosion inhibition in microdefects on coated AZ31 magnesium alloy, Electrochim. Acta 55 (2010) 5401–5406.

[271] M.L. Hitchman, Measurement of Dissolved Oxygen, Wiley, New York, 1978.

[272] I. Fatt, Polarographic Oxygen Sensors: Its Theory of Operation and Its Application in Biology, Medicine, and Technology, 1982.

[273] F.M. Seon, Rare earths for materials corrosion protection, J. Less Common Met. 148 (1989) 73–78.

[274] J.H. Osborne, K.Y. Blohowiak, S.R. Taylor, C. Hunter, G. Bierwagon, B. Carlson, D. Bernard, M.S. Donley, Testing and evaluation of nonchromated coating systems for aerospace applications, Prog. Org. Coat. 41 (2001) 217–225.

[275] B.F. Rivera, B.Y. Johnson, M.J. O'Keefe, W.G. Fahrenholtz, Deposition and characterization of cerium oxide conversion coatings on aluminum alloy 7075-T6, Surf. Coatings Technol. 176 (2004) 349–356.

[276] M. Dabalà, E. Ramous, M. Magrini, Corrosion resistance of cerium-based chemical conversion coatings on AA5083 aluminium alloy, Mater. Corros. 55 (2004) 381–386.

[277] A.E. Hughes, J.D. Gorman, P.R. Miller, B.A. Sexton, P.J.K. Paterson, R.J. Taylor, Development of cerium-based conversion coatings on 2024-T3 Al alloy after rare-earth desmutting, Surf. Interface Anal. 36 (2004) 290–303.

[278] B.R.W. Hinton, D.R. Arnott, N.E. Ryan, The inhibition of alumninum alloys corrosion by cerous cations, Met. Forum 7 (1984) 211.

[279] K. Aramaki, The inhibition effects of cation inhibitors on corrosion of zinc in aerated 0.5 M NaCl, Corros. Sci. 43 (2001) 1573–1588.

[280] A.J. Aldykiewicz, A.J. Davenport, H.S. Isaacs, Studies of the formation of cerium-rich protective films using X-Ray absorption near-edge spectroscopy and rotating disk electrode methods, J. Electrochem. Soc. 143 (1996) 147–154.

[281] R. Supplit, T. Koch, U. Schubert, Evaluation of the anti-corrosive effect of acid pickling and sol–gel coating on magnesium AZ31 alloy, Corros. Sci. 49 (2007) 3015–3023.

[282] L. Wang, L. Chen, Z. Yan, H. Wang, J. Peng, Effect of potassium fluoride on structure and corrosion resistance of plasma electrolytic oxidation films formed on AZ31 magnesium alloy, J. Alloys Compd. 480 (2009) 469–474.

[283] K.Y. Chiu, M.H. Wong, F.T. Cheng, H.C. Man, Characterization and corrosion studies of fluoride conversion coating on degradable Mg implants, Surf. Coatings Technol. 202 (2007) 590–598.

[284] H. Ardelean, I. Frateur, P. Marcus, Corrosion protection of magnesium alloys by cerium, zirconium and niobium-based conversion coatings, Corros. Sci. 50 (2008) 1907–1918.

[285] M.F. Montemor, W. Trabelsi, S.V. Lamaka, K. a. Yasakau, M.L. Zheludkevich, a. C. Bastos, M.G.S. Ferreira, The synergistic combination of bis-silane and CeO2·ZrO2 nanoparticles on the electrochemical behaviour of galvanised steel in NaCl solutions, Electrochim. Acta 53 (2008) 5913–5922.

[286] Y.H. F. Kazunori, Y. Yuhua, K. Masaya, H. Hiroshi, H. Takashi, Rust preventive for magnesium and/or magnesium alloy, EP 1683894 A1, 2006.

[287] M.L. Zheludkevich, K.A. Yasakau, S.K. Poznyak, M.G.S. Ferreira, Triazole and thiazole derivatives as corrosion inhibitors for AA2024 aluminium alloy, Corros. Sci. 47 (2005) 3368–3383.

[288] B. Mernari, H. El Attari, M. Traisnel, F. Bentiss, M. Lagrenee, Inhibiting effects of 3,5-bis(n-pyridyl)-4-amino-1,2,4-triazoles on the corrosion for mild steel in 1 M HCl medium, Corros. Sci. 40 (1998) 391–399.

[289] E.-S.M. Sherif, R.M.M. Erasmus, J.D.D. Comins, Corrosion of copper in aerated synthetic sea water solutions and its inhibition by 3-amino-1,2,4-triazole, J. Colloid Interface Sci. 309 (2007) 470–477.

[290] G.S. Frankel, A. Samaniego, N. Birbilis, Evolution of hydrogen at dissolving magnesium surfaces, Corros. Sci. 70 (2013) 104–111.

[291] G. Baril, N. Pébère, The corrosion of pure magnesium in aerated and deaerated sodium sulphate solutions, Corros. Sci. 43 (2001) 471–484.

[292] M.G. López-Buisán-Natta, Evidence of two anodic processes in the polarization curves of magnesium in aqueous media, Corrosion 57 (2001) 712–720.

[293] G. Baril, G. Galicia, C. Deslouis, N. Pébère, B. Tribollet, V. Vivier, An impedance investigation of the mechanism of pure magnesium corrosion in sodium sulfate solutions, J. Electrochem. Soc. 154 (2007) C108–C113.

[294] A. Atrens, W. Dietzel, The negative difference effect and unipositive Mg+, Adv. Eng. Mater. 9 (2007) 292–297.

[295] S. Thomas, N.V. Medhekar, G.S. Frankel, N. Birbilis, Corrosion mechanism and hydrogen evolution on Mg, Curr. Opin. Solid State Mater. Sci. 19 (2015) 85–94.

[296] R. Kojima, S. Kamata, Zinc-selective membrane electrode using tetrabutyl thiuram disulfide neutral carrier, Anal. Sci. 10 (1994) 409–412.

[297] A.C. Bastos, M.G. Taryba, O.V. Karavai, M.L. Zheludkevich, S.V. Lamaka, M.G.S. Ferreira, Micropotentiometric mapping of local distributions of Zn2+ relevant to corrosion studies, Electrochem. Commun. 12 (2010) 394–397.

[298] E. Lindner, Y. Umezawa, Performance evaluation criteria for preparation and measurement of macro- and microfabricated ion-selective electrodes (IUPAC Technical Report), Pure Appl. Chem. 80 (2008) 85–104.

[299] I. Suzuki, The behavior of corrosion products on zinc in sodium chloride solution, Corros. Sci. 25 (1985) 1029–1034.

[300] R. Venkatesan, Study of corrosion product of zinc in natural sea water, Br. Corros. J. 33 (1998) 77–80.

[301] X.G. Zhang, Corrosion and Electrochemistry of Zinc, Springer, 1996.

[302] W. Feitknecht, Studies on the influence of chemical factors on the corrosion of metals,

Chem. Ind. 36 (1959) 1102–1109.

[303] Internal Corrosion of Water Distribution Systems, 2d ed., American Water Works Association&DVGW-TEW, 1996.

[304] S. Thomas, N. Birbilis, M.S. Venkatraman, I.S. Cole, Corrosion of zinc as a function of pH, Corrosion 68 (2012) 1–9.

[305] M. Pourbaix, Atlas of electrochemical equilibria in aqueous solutions, NACE, Houston, TX, 1966.

[306] PHREEQC http://wwwbrr.cr.usgs.gov/projects/GWC_coupled/phreeqc/, (1998).

[307] I. Puigdomenech, Medusa&Hydra http://www.kemi.kth.se/medusa/, (n.d.).

[308] The Geochemist's Workbench. https://www.gwb.com/, (n.d.).

[309] S.A. Matthes, Geochemical Modeling, in: Corrosion: Fundamentals, Testing, and Protection, Vol 13A, ASM Handbook, ASM International, 2003: pp. 34–41.

[310] V.K. Gupta, A PVC-based 12-crown-4 membrane potentiometric sensor for zinc (II) ions, Sensors Actuators B Chem. 55 (1999) 195–200.

[311] M.A. Akl, M.H. Abd El-Aziz, Polyvinyl chloride-based 18-crown-6, dibenzo18-crown-6 and calix-[6]-arene zinc(II)-potentiometric sensors, Arab. J. Chem. (2011) doi:10.1016/j.arabjc.2011.09.009.

[312] V.K. Gupta, M. Al Khayat, a. K. Minocha, P. Kumar, Zinc(II)-selective sensors based on dibenzo-24-crown-8 in PVC matrix, Anal. Chim. Acta 532 (2005) 153–158.

[313] S.K. Srivastava, V.K. Gupta, S. Jain, PVC-based 2,2,2-cryptand sensor for zinc ions, Anal. Chem. 68 (1996) 1272–5.

[314] V.K. Gupta, R.N. Goyal, M. Al Khayat, P. Kumar, N. Bachheti, A new Zn(II)-selective potentiometric sensor based on 4-tert-butylcalix[4]arene in PVC matrix, Talanta 69 (2006) 1149–55.

[315] A.K. Jain, S.M. Sondhi, S. Rajvanshi, A PVC based hematoporphyrin IX membrane potentiometric sensor for zinc(II), Electroanalysis 14 (2002) 293–296.

[316] V.K. Gupta, D.K. Chauhan, V.K. Saini, S. Agarwal, M.M. Antonijevic, H. Lang, A porphyrin based potentiometric sensor for Zn2+ determination, Sensors 3 (2003) 223–235.

[317] A.R. Fakhari, M. Shamsipur, K. Ghanbari, Zn(II)-selective membrane electrode based on tetra(2-aminophenyl) porphyrin, Anal. Chim. Acta 460 (2002) 177–183.

[318] A.K. Singh, A.K. Jain, P. Saxena, S. Mehtab, Zn(II)-selective membrane electrode based on tetraazamacrocycle [Bzo2Me2Ph2(16)hexaeneN4], Electroanalysis 18 (2006) 1186–1192.

[319] N.R. Gupta, S. Mittal, S. Kumar, S.K. Ashok Kumar, Potentiometric studies of N,N'-Bis(2-dimethylaminoethyl)-N,N'-dimethyl-9,10 anthracenedimethanamine as a chemical sensing material for Zn(II) ions, Mater. Sci. Eng. C 28 (2008) 1025–1030.

[320] R. Dumkiewicz, C. Wardak, S. Zar, S. Zaręba, Properties of the ion-selective electrode with a chelating pseudo-liquid membrane phase for zinc determination, Analyst 125 (2000) 527–530.

[321] M. Shamsipur, S. Rouhani, M.R. Ganjali, H. Sharghi, H. Eshghi, Zinc-selective membrane potentiometric sensor based on a recently synthesized benzo-substituted macrocyclic diamide, Sensors Actuators B Chem. 59 (1999) 30–34.

[322] S. Chandra, D.R. Singh, Zinc(II) selective poly(vinyl chloride) membrane ISE using a macrocyclic compound 1,12,14-triaza-5,8-dioxo-3(4),9(10)-dibenzoylcyclopentadeca-1,12,14-triene as neutral carrier, J. Saudi Chem. Soc. 14 (2010) 55–60.

[323] P. Singh, A.K. Singh, A.K. Jain, Electrochemical sensors for the determination of Zn2+ ions based on pendant armed macrocyclic ligand, Electrochim. Acta 56 (2011) 5386–5395.

[324] M. Hosseini, S.D. Abkenar, M.R. Ganjali, F. Faridbod, Determination of zinc(II) ions in waste water samples by a novel zinc sensor based on a new synthesized Schiff's base, Mater. Sci. Eng. C 31 (2011) 428–433.

[325] V.K. Gupta, S. Agarwal, A. Jakob, H. Lang, A zinc-selective electrode based on N,N'-bis(acetylacetone)ethylenediimine, Sensors Actuators B Chem. 114 (2006) 812–818.

[326] V.K. Gupta, A.K. Jain, G. Maheshwari, A new Zn2+ selective potentiometric sensor based on dithizone-PVC membrane, Chem. Anal. 51 (2006) 889–897.

[327] M.B. Saleh, A.A. Abdel Gaber, Novel zinc ion-selective membrane electrode based on sulipride drug, Electroanalysis 13 (2001) 104–108.

[328] M.R. Ganjali, H.A. Zamani, P. Norouzi, M. Adib, M. Rezapour, M. Aceedy, Zn2+ PVC-based membrane sensor based on 3-[(2-furylmethylene)amino]-2-thioxo-1,3-thiazolidin-4-one, Bull. Korean Chem. Soc. 26 (2005) 579–584.

[329] M.B. Gholivand, Y. Mozaffari, PVC-based bis(2-nitrophenyl)disulfide sensor for zinc ions., Talanta 59 (2003) 399–407.

[330] A.K. Singh, S. Mehtab, U.P. Singh, V. Aggarwal, Tripodal chelating ligand-based sensor for selective determination of Zn(II) in biological and environmental samples., Anal. Bioanal. Chem. 388 (2007) 1867–76.

[331] R.T. Foley, T.H. Nguyen, The chemical nature of aluminum corrosion, J. Electrochem. Soc. Electrochem. Sci. Technol. 129 (1982) 464–467.

[332] D.W. Barnum, Hydrolysis of cations. Formation Constants and standard free energies of formation of hydroxy complexes, Inorg. Chem. 22 (1983) 2297–2305.

[333] C.F. Baes, Jr., R.E. Mesmer, The thermodynamics of cations hydrolysis, Am. J. Sci. 281 (1981) 935–962.

[334] O. Guseva, P. Schmutz, T. Suter, O. von Trzebiatowski, Modelling of anodic dissolution of pure aluminium in sodium chloride, Electrochim. Acta 54 (2009) 4514–4524.

[335] B.J. Privett, J.H. Shin, M.H. Schoenfisch, Electrochemical sensors., Anal. Chem. 82 (2010) 4723–41.

[336] F. Faridbod, P. Norouzi, R. Dinarvand, M.R. Ganjali, Developments in the field of conducting and non-conducting polymer based potentiometric membrane sensors for ions over the past decade, Sensors 8 (2008) 2331–2412.

[337] M.B. Saleh, S.S.. Hassan, A.A. Abdel Gaber, N.A. Abdel Kream, Novel potentiometric membrane sensor for selective determination of aluminum(III) ions, Anal. Chim. Acta 434 (2001) 247–253.

[338] M.F. Mousavi, M. Arvand-Barmchi, M.A. Zanjanchi, Al(III)-selective electrode based on furil as neutral carrier, Electroanalysis 13 (2001) 1125–1128.

[339] A. Abbaspour, Aluminium(III)-selective electrode based on a newly synthesized tetradentate Schiff base, Talanta 58 (2002) 397–403.

[340] A. Yari, L. Darvishi, M. Shamsipur, Al(III)-selective electrode based on newly synthesized xanthone derivative as neutral ionophore, Anal. Chim. Acta 555 (2006) 329–335.

[341] M.B. Gholivand, F. Ahmadi, E. Rafiee, A novel Al(III)-selective electrochemical sensor based on N,N'-bis(salicylidene)-1,2-phenylenediamine complexes, Electroanalysis 18 (2006) 1620–1626.

[342] M. Arvand, S.A. Asadollahzadeh, Ion-selective electrode for aluminum determination in pharmaceutical substances, tea leaves and water samples, Talanta 75 (2008) 1046–1054.

[343] Y. Li, Y. Chai, R. Yuan, W. Liang, L. Zhang, G. Ye, Aluminium(III)-selective electrode based on a newly synthesized glyoxal-bis-thiosemicarbazone Schiff base, J. Anal. Chem. 63 (2008) 1090–1093.

[344] V.K. Gupta, R.N. Goyal, A.K. Jain, R.A. Sharma, Aluminium (III)-selective PVC membrane sensor based on a Schiff base complex of N,N'-bis (salicylidene)-1, 2-cyclohexanediamine, Electrochim. Acta 54 (2009) 3218–3224.

[345] A. Abbaspour, M. Refahi, A. Khalafi-nezhad, M.N. Soltani Rad, S. Behrouz, A selective and sensitive carbon composite coated platinum electrode for aluminium determination in pharmaceutical and mineral water samples., Anal. Chim. Acta 662 (2010) 76–81.

[346] Y.H. Ma, R. Yuan, Y.Q. Chai, X.L. Liu, A new aluminum(III)-selective potentiometric sensor based on N,N'-propanediamide bis(2-salicylideneimine) as a neutral carrier, Mater. Sci. Eng. C 30 (2010) 209–213.

[347] R.K. Bera, S.K. Sahoo, S.K. Mittal, K.S. Ashok Kumar, An imidazol based novel potentiometric PVC membrane sensor for aluminium(III) determination, Int. J. Electrochem. Sci. 5 (2010) 29–38.

[348] X.L. Liu, R. Yuan, W.J. Xu, Y.H. Ma, Y.Q. Chai, Aluminum(III)-selective PVC membrane electrode based on salicylaldehyde salicyloyl hydrazone, J. Chinese Chem. Soc. 58 (2011) 482–487.

[349] X.L. Liu, B. Xie, X.H. Pan, K.Q. Qiao, Y. Wang, New polymeric membrane sensor doped with N,N'-bis(benzoin)-1,2-phenylenediamine for selective determination of aluminum, in: Advanced Materials Research, 2012: pp. 336–341.

[350] S. Tajik, M.A. Taher, I. Sheikhshoaie, Potentiometric determination of trace amounts of aluminium utilizing polyvinyl chloride membrane and coated platinum sensors based on E-N'-(2-hydroxy-3-methoxybenzylidene) benzohydrazide, J. AOAC Int. 96 (2013) 204–211.

[351] M. Ghaedi, M. Montazerozohori, S. Khodadoust, M. Behfar, Chemically modified multiwalled carbon nanotubes as efficient material for construction of new Al(III) ion selective carbon paste electrode, IEEE Sens. J. 13 (2013) 321–327.

[352] N. Zoubov, C. Vanleugenhaghe, M. Pourbaix, Copper, in: Atlas of Electrochemical Equilibria in Aqueous Solutions. M. Pourbaix, NACE, Houston, TX, 1966: pp. 384–392.

[353] S.M. Milic, M.M. Antonijevic, Some aspects of copper corrosion in presence of benzotriazole and chloride ions, Corros. Sci. 51 (2009) 28–34.

[354] D.B. Harrison, D.M. Nicholas, G.M. Evans, Pitting corrosion of copper tubes in soft drinking waters: corrosion mechanism, J. Am. Water Assoc. 96:11 (2004) 67–76.

[355] S. Mamaş, T. Kıyak, M. Kabasakaloğlu, A. Koç, The effect of benzotriazole on brass corrosion, Mater. Chem. Phys. 93 (2005) 41–47.

[356] M. Kabasakaloğlu, T. Kıyak, O. Şendil, A. Asan, Electrochemical behavior of brass in 0.1 M NaCl, Appl. Surf. Sci. 193 (2002) 167–174.

[357] R.M. El-Sherif, K.M. Ismail, W.A. Badawy, Effect of Zn and Pb as alloying elements on the electrochemical behavior of brass in NaCl solutions, Electrochim. Acta 49 (2004) 5139–5150.

[358] E. Mattsson, J.O. Bockris, Galvanostatic studies of the kinetics of deposition and dissolution in the copper + copper sulphate system, Trans. Faraday Soc. 55 (1959) 1586–1601.

[359] G.G.O. Cordeiro, O.E. Barcia, O.R. Mattos, Copper electrodissolution mechanism in a 1M sulphate medium, Electrochim. Acta 38 (1993) 319–324.

[360] M.A. Amin, K.F. Khaled, Copper corrosion inhibition in O2-saturated H2SO4 solutions, Corros. Sci. 52 (2010) 1194–1204.

[361] T. Hashemi, C.A. Hogarth, The mechanism of corrosion inhibition of copper in NaCl solution by benzotriazole studied by electron spectroscopy, Electrochim. Acta 33 (1988) 1123–1127.

[362] M. Finsgar, I. Milosev, Inhibition of copper corrosion by 1,2,3-benzotriazole: A review, Corros. Sci. 52 (2010) 2737–2749.

[363] D. Tromans, Anodic behavior of copper in weakly alkaline solutions, J. Electrochem. Soc. 139 (1992) 1945–1951.

[364] A.D. Modestov, G.D. Zhou, Y.P. Wu, T. Notoya, D.P. Schweinsberg, A study of the electrochemical formation of Cu(I)-BTA films on copper electrodes and the mechanism of copper corrosion inhbition in aqeous chloride/benzotriazole solutions, Corros. Sci. 36 (1994) 1931–1946.

[365] D.-Q. Zhang, L.-X. Gao, G.-D. Zhou, Inhibition of copper corrosion by bis-(1-benzotriazolymethylene)-(2,5-thiadiazoly)-disulfide in chloride media, Appl. Surf. Sci. 225 (2004) 287–293.

[366] H.P. Lee, K. Nobe, A.J. Pearlstein, Film formation and current oscillations in the electrodissolution of copper in acidic chloride media, J. Electrochem. Soc. 132 (1985) 2159–2165.

[367] M. Chmielová, J. Seidlerová, Z. Weiss, X-ray diffraction phase analysis of crystalline copper corrosion products after treatment in different chloride solutions, Corros. Sci. 45 (2003) 883–889.

[368] H.P. Lee, Kinetics and mechanisms of Cu electrodissolution in chloride media, J. Electrochem. Soc. 133 (1986) 2035–2043.

[369] J.-H. Chen, Z.-C. Lin, S. Chen, L.-H. Nie, S.-Z. Yao, An XPS and BAW sensor study of the structure and real-time growth behaviour of a complex surface film on copper in sodium chloride solutions (pH=9), containing a low concentration of benzotriazole, Electrochim. Acta 43 (1998) 265–274.

[370] V. Brusic, M.A. Frisch, B.N. Eldridge, F.P. Novak, F.B. Kaufman, B.M. Rush, G.S. Frankel, Copper corrosion with and without inhibitors, J. Electrochem. Soc. 138 (1991) 2253–2259.

[371] Proctor and Gamble Ltd., Compositions for inhibiting metal tarnish, GB652339, 1947.

[372] R. Walker, The use of benzotriazole as a corrosion inhibitor for copper, Anti-Corrosion Methods Mater. 17 (1970) 9–15.

[373] R. Walker, Benzotriazole a corrosion inhibitor for antiques: Some practical surface chemistry, J. Chem. Educ. 57 (1980) 789–791.

[374] J.B. Cotton, I.R. Scholes, Benzotriazole and related compounds as corrosion inhibitors for copper, Br. Corros. J. 2 (1967) 1–5.

[375] N. Morito, W. Suëtaka, Infrared and ultraviolet-visible reflection spectra of the surface films on copper treated with benzotriazole, J. Japan Inst. Met. Mater. 35 (1971) 1165–1170.

[376] N. Morito, W. Suëtaka, Infrared reflection studies of the oxidation of copper and the inhibition by benzotriazole, J. Japan Inst. Met. Mater. 36 (1972) 1131–1140.

[377] N. Morito, W. Suëtaka, in situ Ultraviolet high sensitivity reflection studies on the corrosion ihibition of copper by benzotriazole, J. Japan Inst. Met. Mater. 37 (1973) 216–221.

[378] R. Youda, H. Nishihara, K. Aramaki, SERS and impedance study of the equilibrium between complex formation and adsorption of benzotriazole and 4-hydroxybenzotriazole on a copper electrode in sulphate solutions, Electrochim. Acta 35 (1990) 1011–1017.

[379] D. Tromans, R. Sun, Anodic polarization behavior of copper in aqueous chloride/benzotriazole solutions, J. Electrochem. Soc. 138 (1991) 3235–3244.

[380] S. Kamata, A. Bhale, Y. Fukunaga, H. Murata, Copper (II)-selective electrode using thiuram disulfide neutral carriers, Anal. Chem. 60 (1988) 2464–2467.

[381] M. Neshkova, H. Sheytanov, Ion-selective electrodes with sensors of electrolytically plated chalcogenide coatings, J. Electroanal. Chem. 102 (1979) 189–198.

[382] Y.G. Vlasov, E.A. Bychkov, Ion-selective chalcogenide glass electrodes, Ion-Selective Electrode Rev. 9 (1987) 5–93.

[383] E. Bakker, E. Pretsch, The new wave of ion-selective., Anal. Chem. 74 (2002) 420A–426A.

[384] V.A. Nazarov, M.G. Taryba, E.A. Zdrachek, K.A. Andronchyk, V. V Egorov, S. V Lamaka, Sodium- and chloride-selective microelectrodes optimized for corrosion studies, J. Electroanal. Chem. 706 (2013) 13–24.